Mechanical Behavior and Radiation Effects

2024 Principal Investigators Meeting

September 17-19, 2024

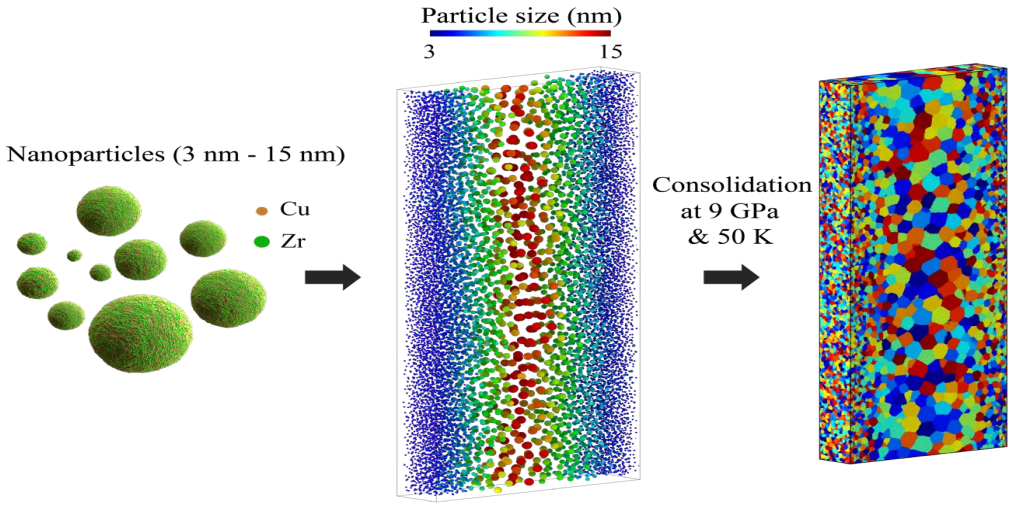

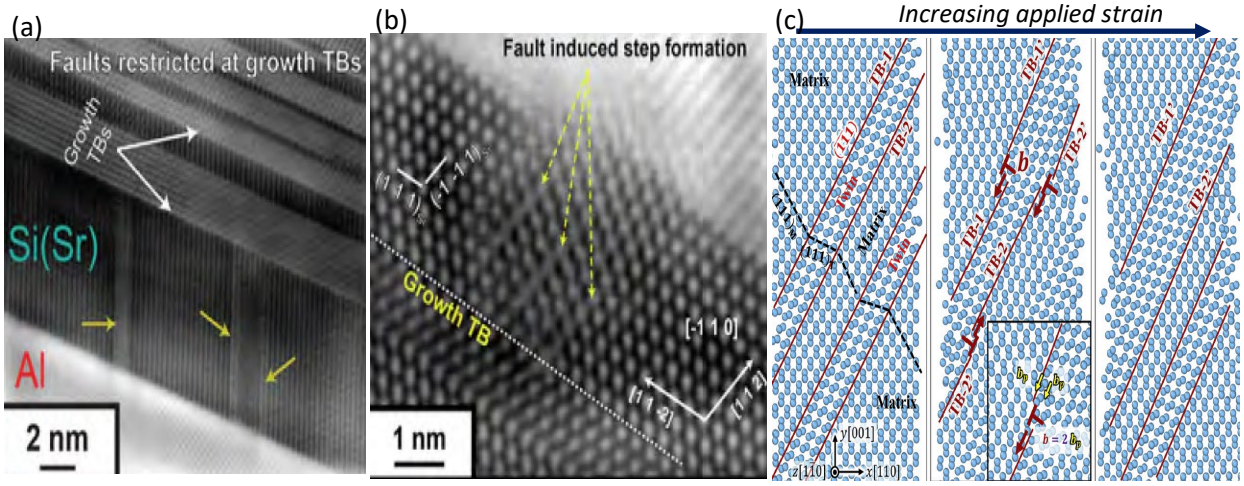

U.S. DEPARTMENT OF ENERGY | Office of Science

Materials Sciences and Engineering Division

Office of Basic Energy Sciences

Cover

Top: Synthesis of a double gradient GNG using nanoparticles of sizes ranging from 3 nm to 15 nm, consolidated at 9 GPa and 50 K. Colors in the last figure indicate distinct glassy grains. (Branicio, USC)

Bottom: (a-b)HR/STEM images showing deformation induced stacking faults (SFs) due to partial dislocation mediated plasticity in nano-twinned Si(Sr) fibers in Al-Si(Sr) nanoeutectics. c) MD simulation showing that the dislocation motion on twin boundary (TB) in the Si(Sr) fiber leads to TB migration. (Misra, Michigan)

Foreword

This volume comprises the scientific content of the 2024 Mechanical Behavior and Radiation Effects Principal Investigators' (PI) Meeting sponsored by the Division of Materials Science and Engineering (DMSE) in the Office of Basic Energy Sciences (BES) of the U. S. Department of Energy (DOE). The meeting, held on September 17-19 in person for the first time since 2019, is the ninth such meeting on this topic and is one among a series of research theme-based PI Meetings being held by DMSE. The meeting's focus is on research in mechanical behavior and radiation effects of materials.

The studies of mechanical behavior and radiation effects have a long and important history with respect to the generation, transmission, utilization and conservation of energy. It is a tribute to the researchers that they have continued to move the field forward into a number of important areas, as can be seen by the diversity of projects being presented at this meeting. Attendees will note a number of new projects and research directions since the previous meeting including several recipients of Early Career Research Program awards. These new projects add to the exciting areas of research and cutting-edge techniques that are a hallmark of this program.

The purpose of the Mechanical Behavior and Radiation Effects PI Meeting is to bring together researchers funded by DMS&E in this important area of research on a periodic basis (approximately every two years) in order to facilitate the exchange of new results and research highlights, to nucleate new ideas and collaborations among the participants, and to identify needs of the research community. The meeting will also help DMSE staff in assessing the state of the program, identifying new research directions and recognizing programmatic needs.

I would like to express my sincere thank all of the attendees for their active participation and for sharing their ideas and new research results. Of special note, I have greatly appreciated the help of Dr. Saryu Fensin from LANL, who is helping me as a detail to my program and helped tremendously with this meeting. I would also like to express my sincere gratitude to Ms. Teresa Crockett in DMSE, and staff at the Oak Ridge Institute of Science and Education (ORISE) for their dedicated and outstanding work in taking care of all the logistical aspects of the meeting

John Vetrano
Program Manager
Mechanical Behavior and Radiation Effects
Division of Materials Sciences and Engineering
Office of Basic Energy Sciences
U.S. Department of Energy

Table of Contents

Agenda

Tuesday, September 17, 2024	
8:20 – 8:30AM	**Intro and Welcome** – John Vetrano
Session Chair:	***Izabela Szlufarska***
8:30 – 8:50AM	**Blas Uberuaga, LANL** *Disorder and Diffusion in Complex Oxides: Towards Prediction and Control*
8:50 – 9:10AM	**Kelly Nygren, Cornell** *The Role of Subgrain Heterogeneous Processes in Slip Localization in Polycrystalline Metals During Cyclic Plasticity*
9:10 – 9:30AM	**David Simmons, USF** *Nanoscale origins of nonlinear energy dissipation and toughness in elastomeric nanocomposites*
9:30 – 9:50AM	**Chris Schuh, Northwestern** *Towards High-Throughput Computation of Phase-and Defect Diagrams*
9:50 – 10:10AM	**Break**
Session Chair:	***Michael Demkowicz***
10:10 – 10:30AM	**Laurent Capolungo, LANL** *Multi-Scale Study of the Role of Microstructure in the Deformation Behavior of Hexagonal Materials*
10:30 – 10:50AM	**Dan Schreiber, PNNL** *Crack-Tip Mechanisms Driving Environmental Degradation*
10:50 – 11:10AM	**Adrien Couet, Wisc** *Role of nanoscale heterogeneities on charged species transport in oxide*
11:10 – 11:30AM	**Mitra Taheri, JHU** *Grain Boundary Microstates: Exploring the Metastability of Sink Efficiency*

11:30 – 11:50AM	**Marie Charpagne, UIUC** *Dynamical grain-boundary phase diagrams in irradiated alloys*
11:50 – 1:30PM	**Lunch – Poster lightning talks**
1:30 – 3:30PM	**Poster Session**
Session Chair: Mitra Taheri	
3:30 - 3:50PM	**Arun Devaraj, PNNL** *Coupled Effects of Stress and Hydrogen on Stress Corrosion Cracking of Fe-based alloys*
3:50 - 4:10PM	**Wendy Gu, Stanford** *Deformation of Nano-Metallic Glasses Made using Colloidal Synthesis*
4:10 - 4:30PM	**Penghui Cao, UC-Irvine** *The Role of Local Chemical Order on Defect Kinetics in Alloys under Irradiation*
4:30 - 4:50PM	**Janelle Wharry, UIUC** *Irradiation Tailoring of Deformation-Induced Phase Transformation*
4:50 – 5:10PM	**Boopathy Kombaiah, INL** *Fundamental Mechanisms of Newtonian Diffusional Creep in Structural Alloys*
5:10 – 5:30PM	**Hyunseok Oh, Wisc** *Understanding Irradiation-Assisted Plasticity in Complex Concentrated Alloys*
End of Day 1	

Wednesday, September 18, 2024	
8:20 – 8:30AM	**Intro to Day 2** – John Vetrano
Session Chair:	***Frederic Sansoz***
8:30 – 8:50AM	**John Allison, Michigan** *Center for Predictive Integrated Structural Materials Science PRISMS Center*
8:50 – 9:10AM	**Maryam Ghazisaeidi, Ohio State** *Mechanisms of Deformation and Slip Transmission in Two Phase BCC/B2 Refractory High Entropy Alloys*
9:10 – 9:30AM	**Aeriel Leonard, Ohio State** *The Role of Strain Localization at Interfaces on Fatigue Crack Initiation in Highly Textured Magnesium Alloy*
9:30 – 9:50AM	**Ryan Sills, Rutgers** *Micromechanics of Migrating Interfaces*
9:50 – 10:10AM	**Break**
Session Chair:	***Amit Misra***
10:10 – 10:30AM	**John Vetrano, BES** *Programmatic Updates*
10:30 – 10:50AM	**Emmanuelle Marquis, Michigan** *Chemical Partitioning and Radiation Damage in Concentrated Alloys*
10:50 – 11:10AM	**Amanda Krause, Carnegie Mellon** *Elucidating Grain Growth in Thermo-Magnetic Processed Materials by Transfer Learning and Reinforcement Learning*
11:10 – 11:30AM	**Brian Sheldon, Brown** *Toughening Mechanisms in Ceramic Nanocomposites*
11:30 – 11:50AM	**Sarah Finkeldei, UC-Irvine** *Advancing clean energy through fundamental insights into defect generation and transport phenomena at grain boundaries in nuclear energy materials*
11:50 – 1:30PM	**Lunch – Dr. Andrew Schwartz and poster talks**
1:30 – 3:30PM	**Poster Session**

3:30-4:00PM	**Discussion Panel (Ashley Bucsek, Xuan Zhang, and Jason Trelewicz)** *Using BES-Supported Light Sources for MBRE-Related Research*
Session Chair: Mia Jin	
4:00 – 4:20PM	**Avinash Dongare, UConn** *Understanding the Mechanics of Reverse Phase Transformation and Detwinning in BCC Metal*
4:20 – 4:40PM	**Chris Weinberger, Colorado State** *Understanding the Competition between Plastic Flow and Fracture in BCC Transition Metals*
4:40 – 5:00PM	**Michael Tonks, Florida** *Mechanisms of Irradiation-Induced Grain Subdivision*
5:00 – 5:20PM	**Tim Rupert, JHU** *Structural Short-Range Order and the Damage Tolerance of Amorphous Grain Boundary Complexions*
End of Day 2	

Thursday, September 19, 2024	
8:20 – 8:30AM	**Intro to Day 3** – John Vetrano
Session Chair: Karl Sieradzki	
8:30 – 8:50AM	**Brad Boyce, SNL** *Nanomechanics and Nanometallurgy of Boundaries*
8:50 – 9:10AM	**Seok-Woo Lee, Uconn** *Mechanical Properties of Metals at the Micrometer Scale in Different Environments*
9:10 – 9:30AM	**Ashley Bucsek, Michigan** *Beyond Shear: Improving the Prediction of Plastic Deformation Activation in HCP Materials*
9:30 – 9:50AM	**Tevis D.B. Jacobs, Pitt** *Understanding the Role of Surface Energy in the Deformation of Metal Nanoparticles*
9:50 – 10:10AM	**Break**
Session Chair: Paulo Branicio	
10:10 – 10:30AM	**Rob Ritchie, LBNL** *Damage-Tolerance of Structural Materials*
10:30 – 10:50AM	**Yuri Mishin, GMU** *Metal-Ceramic Interfaces at High Temperatures*
10:50 – 11:10AM	**Jimmy Burns, UVA** *Elucidating the influence of bulk slip morphology on hydrogen environment-assisted cracking behavior in precipitation-hardened alloys*
11:10 – 11:30AM	**Maarten de Boer, CMU** *Understanding the effect of stress on complexion transitions and the interplay with creep in thermally stabilized nanocrystalline materials*
11:30 – 11:50AM	**Eric Homer, BYU** *Computational and Experimental Investigation of Cryogenic Grain Boundary Motion for Enhanced Mechanical Properties*
11:50	**Final Wrap-Up – John Vetrano**

Poster session 1
Tuesday, September 17, 2024

Lead PI: Laurent Capolungo, LANL
Presenter: Darshan Bamney
Multi-Scale Study of the Role of Microstructure in the Deformation Behavior of Hexagonal Materials

Lead PI: Michael Demkowicz, TAMU
Presenter: Michael Demkowicz
Improving Radiation Response of Solid‐State Interfaces via Control of Curvature

Lead PI: Sarah Finkeldei, UC-I
Presenter: William Nielson
Advancing Clean Energy through Fundamental Insights into Defect Generation and Transport Phenomena at Grain Boundaries in Nuclear Energy Materials

Lead PI: Mia Jin, PSU
Presenter: Mia Jin
Understanding the Interplay between Hydrogen and Chemical Short-Range Order in Multiple Principal Element Alloys

Lead PI: Amanda Krause, CMU
Presenter: Joel Harley
Elucidating Grain Growth in Thermo-Magnetic Processed Materials by Transfer Learning and Reinforcement Learning

Lead PI: Dane Morgan, UW - Madison
Presenter: Kevin Field
Mechanistic, Quantitative Understanding of the Dynamics of Many, Interacting Defect Clusters for Tailoring Irradiation Responses

Lead PI: Nitin Padture, Brown
Presenter: Nitin Padture
Fundamental Studies of the Mechanical Behavior of Charged Hetero-Interfaces

Lead PI: Olivier Pierron, GT
Presenter: Olivier Pierron
Fundamental Investigation of Grain Boundary Mediated Mechanisms in Ultrafine Grained Metallic Films

Lead PI: Rob Ritchie, LBNL
Presenter: Punit Kumar
Damage-Tolerance of Structural Materials

Lead PI: Frederic Sansoz, UVt
Presenter: Frederic Sansoz
Segregation and Shear Localization in Nanocrystalline Alloys

Lead PI: Karl Sieradzki, ASU
Presenter: Karl Sieradzki
Dynamic Fracture in Dealloying Induced Stress Corrosion Cracking

Lead PI: Jason Trelewicz, SBU
Presenter: Jason Trelewicz
Irradiation Defect Formation and Evolution in Doped Metallic Interfaces

Lead PI: Thomas O'Connor, CMU
Presenter: Thomas O'Connor
Modeling the Molecular Mechanisms of Interfacial Welding in Self-Healing Polymers

Lead PI: Mingwei Zhang, UC-Davis
Presenter: Mingwei Zhang
Understanding Elevated-Temperature Plasticity in Refractory Complex Concentrated Alloys

Poster session 2

Wednesday, September 18, 2024

Lead PI: John Allison, Michigan
Presenter: Liang Qi
Center for PRedictive Integrated Structural Materials Science PRISMS Center

Lead PI: Mohsen Asle Zaeem, CSM
Presenter: Mohsen Asle Zaeem
Understanding Multiscale Defect Formation Process and Phase-Switching Behavior in Shape Memory Functional Oxides

Lead PI: Pascal Bellon, UIUC
Presenter: Nicholas Saunders
Dynamical Grain-boundary Phase Diagrams in Irradiated Alloys

Lead PI: Irene Beyerlein, UCSB
Presenter: Justine Schulte
The Role of Subgrain Heterogeneous Processes in Slip Localization in Polycrystalline Metals During Cyclic Plasticity

Lead PI: Brad Boyce, SNL
Presenter: Doug Medlin
Nanomechanics and Nanometallurgy of Boundaries

Lead PI: Paulo Branicio, USC
Presenter: Paulo Branicio
Effect of Gradient Architectures on the Strength, Deformation and Failure of Nanoglasses

Lead PI: Eric Homer, BYU
Presenter: Greg Thompson
Computational and Experimental Investigation of Cryogenic Grain Boundary Motion for Enhanced Mechanical Properties

Lead PI: Qizhen Li, WSU
Presenter: Qizhen Li
Low Cycle Fatigue Crack Initiation and Growth in Fine-Grained Magnesium

Lead PI: Nathan Mara, UMN
Presenter: Nathan Mara
Influence of 3D Heterophase Interface Structure on Deformation Physics

Lead PI: Emmanuelle Marquis, Michigan
Presenter: Enrique Martinez
Chemical Partitioning and Radiation Damage in Concentrated Alloys

Lead PI: Amit Misra, Michigan
Presenter: Amit Misra
Plasticity of High-Strength Multiphase Metallic Composites

Lead PI: Daniel Schreiber, PNNL
Presenter: Pauline Simonnin
Crack-Tip Mechanisms Driving Environmental Degradation

Lead PI: Chris Schuh, NWU

Presenter: Chris Schuh
Microparticle Impacts for Extreme Mechanics

Lead PI: Izabela Szlufarska, Wisconsin
Presenter: Izabela Szlufarska
Radiation Effects in High Entropy Carbides

Lead PI: Mitra Taheri, JHU
Presenter: Michael Falk
Grain Boundary Microstates: Exploring the Metastability of Sink Efficiency

Lead PI: Blas Uberuaga, LANL
Presenter: Ellis Kennedy
Disorder and Diffusion in Complex Oxides: Towards Prediction and Control

Abstracts

Center for PRredictive Integrated Structural Materials Science – PRISMS Center

PI: J. Allison, University of Michigan (UM)
Co-PIs: A. Bucsek (UM), V. Gavini (UM), E. Holm (UM) A. Misra (UM), B. Puchala (UM), L. Qi (UM), V. Sundararaghavan (UM), K. Thornton (UM), A. Van der Ven (UCSB).
Keywords: Software, data repository, magnesium alloys, microstructural evolution, mechanical behavior**.**

Program Scope

The goal of the PRISMS Center is to establish a unique scientific platform that will enable accelerated predictive materials science. The platform has three key thrust areas:

1. **PRISMS Integrated Computational Software:** Develop and establish a suite of integrated, multi-scale, open-source computational tools for predicting the microstructural evolution and mechanical behavior of structural metals.
2. **The Materials Commons:** Develop and deploy "The Materials Commons," a knowledge repository and virtual collaboration space for curating, archiving and disseminating information from experiments and computations.
3. **PRISMS Integrated Science Use Cases:** The use cases demonstrate the application of the integrated PRISMS platform of experiments, theory and simulation for making major advances in the quantitative and predictive understanding of microstructural evolution and mechanical behavior of magnesium alloys.

Recent Progress and Future Plans

In addition to nine faculty members, the PRISMS Center currently has four full time software staff members and over the past two years has supported eighteen graduate students, post-doctoral fellows and part time staff. We hold an annual workshop to develop our external PRISMS collaborative community and to train external users of PRISMS software tools and Materials Commons and have trained more than 440 users. In addition, a PRISMS Center You-Tube channel has been established with training for PRISMS software. It currently has over 790 subscribers and over 42,000 combined views. Additional information can be found at http://prisms-center.org.

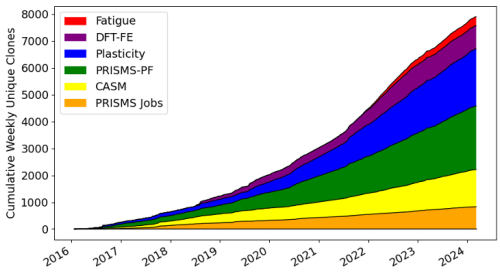

Figure 1. Cumulative clones of PRISMS codes since January 2016.

PRISMS Integrated Open-Source Computational Software

Currently four primary codes make up the PRISMS Open-Source Integrated software: *CASM, PRISMS-PF, PRISMS-Plasticity,* and *DFT-FE* are available on GitHub. The codes have major upgrades every year. Software GitHub pages have been viewed more than 300,000 times and over 8000 unique clones (copies) have been downloaded as shown in Figure 1. Each software package includes a substantial user manual, formulation notes, commented source code and unit tests.

CASM: CASM, a Clusters Approach to Statistical Mechanics, provides functionality for symmetry identification, enumeration of symmetrically unique supercells and configurations, use of automatically determined or custom reference states for formation energy calculation, and convex hull identification. CASM 2.0 was released in August 2024. This release contains a substantially improved user interface comprised of new Python packages for configuration enumeration, cluster expansion Hamiltonian construction, and Monte Carlo calculations. To support these, major updates have been made to the online documentation with examples and updated training materials. The CASM-Twinfinder application has been updated to enumerate structures for DFT calculation for the energetics of a wide variety of interfaces and interface growth mechanisms. *https://github.com/prisms-center/CASMCode.*

DFT-FE: *DFT-FE* is a massively parallel code for large-scale real-space DFT calculations using spatially adaptive higher-order finite-element basis. The current development version of DFT-FE incorporates several important updates on both performance and capability aspects and was released as the 1.2 version in August 2024. The benchmarking of DFT-FE on the Frontier exascale GPU machine shows excellent performance using almost the full machine on a 600,000 electrons system, that was awarded the 2023 ACM Gordon Bell prize. Key improvements include: (i) Extension of GPU porting to support AMD GPUs via the HIP language; (ii) Performance and scalability improvements for large-scale systems using implementation strategies such as mixed precision and overlap compute and communication, (iii) Development and implementation of advanced preconditioners for robust converge for large or inhomogeneous material systems. The GPU version of DFT-FE is over 100x faster than traditional DFT calculations. This has been used to make high precision calculations of c+a slip modes in Mg and Mg-Y alloys (Figure 2). *https://github.com/dftfeDevelopers/dftfe*

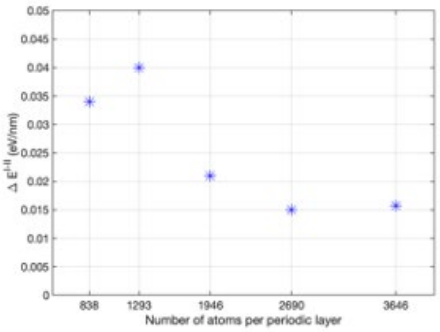

Figure 2. Dislocation core energetics calculated using DFT-FE showing convergence at 16meV/nm requiring at least 36,000 electron calculation which is not feasible using conventional DFT methods.

PRISMS-PF: The *PRISMS-PF* phase field code uses the deal.ii open-source finite element library and is a massively scalable numerical framework for implementing phase field models for the multiscale materials modeling effort of PRISMS. New developments of the PRISMS-PF framework consisted of the release of new applications, improvements in performance, ease of use, integration with other tools, and efforts to increase widespread adoption and development by the members of the phase-field community. A new version (v 2.3) of the framework was released. New applications were developed and released for static recrystallization, isothermal alloy solidification, conserved Allen-Cahn dynamics and fluid flow. Additional functionalities were added, including improved grain input from Dream3D/experimental microstructures, probabilistic nucleation of recrystallized grains, and compatibility with the latest version of deal.ii, as well as an improved suite of scripts for integration of PRISMS-PF with Materials Commons. An improved algorithm was developed for grain remapping. *https://github.com/prisms-center/phaseField*

PRISMS-Plasticity: The *PRISMS-Plasticity* code is a massively parallel numerical framework for implementing continuum and crystal plasticity finite element (CPFE) models using the deal.ii open source library. A variety of crystal and continuum plasticity material models have been

implemented. The PRISMS-Plasticity software includes two frameworks: one for crystal plasticity finite element (CPFE) and one for macroscale plasticity. Both frameworks are compatible with subroutines developed as a part of a new PRISMS-Indentation pipeline for virtual indentation experiments. A primal–dual active set strategy is incorporated to model the contact between the indenter and the sample. A pipeline for postprocessing GND distributions from PRISMS-Plasticity simulation output has been developed and will be released in Fall of 2024.
https://github.com/prisms-center/plasticity

PRISMS-MP: PRISMS-Multi-Physics: A new framework has been defined for integrating results from CASM, PRISMS-Plasticity and PRISMS-PF to simulate deformation and microstructural evolution. Algorithm and modifications in the existing frameworks necessary for concurrent solution of PRISMS-PF and PRISMS-plasticity have been finalized. In this coupled approach, the mechanical solver from PRISMS-Plasticity provides PRISMS-PF with the elastic and plastic strain energy distribution during the deformation while PRISMS-PF provides the morphological evolution of twins or recrystallized grains to PRISM-Plasticity. Twin boundary energy and mobilities are provided by CASM.

Materials Commons: The *Materials Commons 2.0* is a publicly available information repository and virtual collaboration space for curating, storing and disseminating materials information from experiments and computations. There are now over 780 registered users of Materials Commons. Published datasets have been viewed over 14,500 times and downloaded more than 7000 times. Materials Commons 2.0 now houses over 6.7 million files and 42TB of data in more than 721 projects. Published datasets have been viewed over 28,000 times and downloaded more than 14,000 times. Materials Commons was moved to a new storage backend that provides elastic storage and keeps multiple copies of user data. Many improvements were made so that users can customize their published data; support for computational data, relationships and exploration; deeper integration with Google Sheets; support for citation counts for datasets and the papers associated with them through Crossref; the ability for users to write custom python scripts that run on Materials Commons allowing for machine learning and computational workflows. *https://materialscommons.org*

PRISMS Use Cases

The PRISMS Use Cases serve as demonstrations and test beds for the development and demonstration of the PRISMS platform combining experiments, theory and simulation. Highlights from these use cases are summarized below.

Grain Boundary Effects Use Case: Segregation of solute atoms to grain boundaries (GB) can have profound effects on metals and in Mg alloys we are investigating this influence on twinning, <c+a> slip and recrystallization. A comprehensive framework for predicting GB segregation has been developed combining atomistic simulations, thermodynamic integration, and machine learning. This framework has been demonstrated and experimentally verified on GB segregation of Y. Importantly we have found that GB segregation of Y does not appear to depend on GB misorientation angle.

Using DFT-FE, the largest ab-initio simulation ever conducted was used to study the influence of solute (Y) atoms on the <c+a> pyramidal I/II screw dislocation cross-slip barrier in dilute binary Mg-Y alloys (this work was awarded the Gordon Bell Prize). These simulations

provided evidence of a new mechanism for explaining the important effect of Y on <c+a> slip. An improvement on Ashby's classic model for grain size dependence of flow stress was developed and calibrated for Mg-Al using nanoindentation testing. This model improvement incorporates both geometrically necessary dislocations (GNDs) and statistically stored dislocations (SSDs). Plans: Use DFT-FE to study pyramidal <c+a> screw dislocation cross-slip energy barrier in Mg-Ca-Zn ternary alloy. Validation of crystal plasticity-based prediction of GNDs using HREBSD data in Mg-Zn-Ca and Mg-Al, and use of GND densities within the back-stress evolution laws.

Alloying Effects on Twinning Use Case: We have applied a systematic framework to quantify the influence of alloying on the formation of twins and detwinning during monotonic and cyclic deformation. This framework involves the use of PRISMS-Plasticity simulations coupled with an array of advanced experimental tools including in-situ HEDM and in-situ EBSD to quantify twin evolution. We have determined that Al and Zn lead to low resistance to twinning, while Nd, Zn-Ca alloys and Y have increasingly high resistance to twinning. Using DFXM, an important in-situ twin evolution data set has been captured showing twin nucleation at grain boundary triple junctions (Figure 3). PRISMS-Plasticity simulations of this grain neighborhood are underway. Using MD simulation, alloy effects on competition between <c+a> slip and twin nucleation have been modeled. A {11-21} twin mechanism, uncommon in Mg alloys, has been discovered in Mg-7Y.

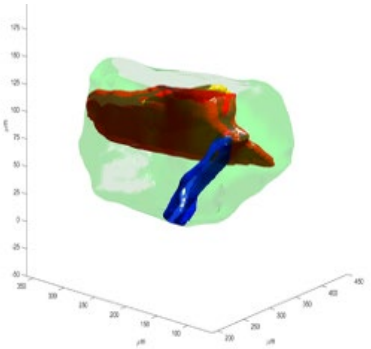

Figure 3. In-Situ Dark Field X-Ray Microscopy (DFXM) imaging of twin evolution in Mg-Al.

Plans: The PRISMS-MP coupled code twin model will be parameterized with CASM inputs and validated on unalloyed Mg and Mg-Al. Analysis of HEDM characterization of twinning and detwinning during cyclic deformation of Mg, Mg-Al and Mg-Y will be used to validate the coupled model. Twin embryo formation and propagation will be characterized in Mg-Al using multi-model HEDM.

Texture Evolution and Recrystallization Use Case: This Use Case is exploring the effect of processing and alloying on deformation and recrystallization textures in Mg-Zn-Ca alloys to produce isotropic textures and promote sheet formability. Using PRISMS-Plasticity TM coupled with thermo-mechanical testing and EBSD characterization of texture, we have demonstrated the ability to predict the influence of Ca, Zn and Ca/Zn in combination on deformation texture. We have determined that alloying with >1wt% Zn+Ca reduces the activity of basal slip and twinning while promoting <c+a> slip. This combination produces a weak basal deformation which is key for producing the highly desirable weak annular texture that is subsequently produced by recrystallization during annealing. To simulate the annealing phase, a probabilistic nucleation model has been established and incorporated into the PRISMS-PF recrystallization application. Alloy effects and segregation effects on grain boundary mobility are being characterized using MD simulation. Recrystallization experiments on Mg-Zn-Ca alloys have been completed to parameterize these models. Plans: The PRISMS-MP coupled code will be used to simulate dynamic recrystallization. Grain boundary segregation/co-segregation thermodynamics for different solute elements (e.g. Ca & Zn) will be investigated using atomistic simulations and DFT-FE calculations. Multi-modal (far field / intermediate field & near field / dark field) HEDM experiments on Mg-Zn-Ca samples will be used to characterize recrystallization kinetic processes.

2022-2024 Top Ten PRISMS Center Publications acknowledging DOE-BES support (out of a total of 20 publications in past two years).

1. S. Das, B. Kanungo, V. Subramanian, G. Panigrahi, P. Motamarri, D. Rogers, P. Zimmerman, V. Gavini, "Large-scale materials modeling at quantum accuracy: *Ab initio* simulations of quasicrystals and interacting extended defects in metallic alloys", ACM, SC'23 Denver Co, November 2023. NOTE: 2023 Gordon Bell Prize Winner.
2. A. Lakshmanan, M. Andani, M. Yaghoobi, J. Allison, A. Misra, V. Sundararaghavan, "A combined experimental and crystal plasticity study of grain size effects in magnesium alloys" Journal of Magnesium Alloys 11 (12) (2023) 4445-44.
3. K. Stopka, M. Yaghoobi, J. Allison, D. McDowell, "Microstructure-Sensitive Modeling of Surface Roughness and Notch Effects on Extreme Value Fatigue" International Journal of Fatigue, 166 (2023) 10725.
4. V. Goel, D. Montiel, K. Thornton "Understanding the Effect of Electrochemical Properties and Microstructure on the Microgalvanic Corrosion of Mg Alloys via Phase-Field Simulations", Journal of the Electrochemical Society, 170 (2023), 101502.
5. V. Menon, S. Das, V. Gavini, L. Qi, "Atomistic simulations and machine learning of solute grain boundary segregation in Mg alloys at finite temperatures", Acta Materialia, 264 (2024) 119515.
6. S. Lee, T. Berman, C. Yildirim, C. Detlefs, J. Allison, A. Bucsek "Multiscale and multimodal characterization of recrystallized and non-recrystallized grains during static recrystallization in a hot-compressed Mg-3.2Zn-0.1Ca wt.% alloy" Scientific Reports, 14,1 (2024) 6241.
7. D. A. Greeley, J. F. Adams, P. Kneissi, J. W. Jones, A. D. Spear, J. E. Allison "Use of Multi-modal HEDM for characterization of fatigue crack paths in Mg WE43", Fatigue and Fracture of Engineering Materials and Structures, 47 (2024) 1150-1171.
8. E. Song, M. Andani, A. Misra, "Investigation of grain size and geometrically necessary dislocation density dependence of flow stress in Mg-4Al by using nanoindentation" Acta Materialia, 265 (2024) 119633.
9. S. Sai Behara, J. C. Thomas, B. Puchala, and A. Van der Ven, "Chemomechanics in alloy phase stability", Phys. Rev. Materials 8, (2024) 033801.
10. B. Puchala, J. C. Thomas, A. Van der Ven, "CASM Monte Carlo: Calculations of the thermodynamic and kinetic properties of complex multicomponent crystals", in final edit Computational Materials Science (2024).

Understanding Multiscale Defect Formation Process and Domain Switching Behavior in Shape Memory Functional Oxides

Mohsen Asle Zaeem, Colorado School of Mines

Keywords: Ferroelasticity, Martensitic Transformation, Switching Mechanism, Molecular Dynamics, Phase Field Modeling

Research Scope

Shape memory functional oxides, including ferroelastic (FA) and ferroelectric (FE) types, exhibit recoverable domain switching and/or martensitic phase transformations (MPT) in response to various stimuli [1]. Depending on the application, specific hysteresis characteristics are often required [2-4]. While pure FA and FE materials exist, many materials demonstrate a coupling of both properties, which enhances performance through their interactive behaviors. Despite extensive research, several key questions regarding domain switching behavior in these ferroic oxides remain unresolved. These include: i) the mechanisms of nucleation and propagation in FE/FA materials under complex loading conditions; ii) the coupling between ferroelasticity and ferroelectricity under different loading conditions; iii) the interaction between FA and the shape memory effect; and, more importantly, iv) the impact of defects and inhomogeneities on various stages of the ferroic nucleation-growth-and-switching process. This research project primarily focuses on the ferroelastic behavior of zirconia-based ceramics to provide a multiscale understanding of FA domain formation, hysteresis responses, and nucleation/switching mechanisms, as well as their impact on deformation behavior. Additionally, we provide new atomistic insights into the effects of nanoscale defects on FE switching in specific functional oxides.

Research Progress

We have developed Molecular Dynamics (MD) and Phase-Field (PF) modeling frameworks to gain a multiscale understanding of ferroelastic (FA) domain switching in zirconia-based ceramics, specifically yttria-stabilized zirconia (YSZ). Following experimental procedures, we created the FA phase in tetragonal prime (t') YSZ by rapidly quenching the cubic phase in MD simulations. We then investigated the FA training steps and the hysteresis response of the t' phase through multiple cycles of mechanical loading and unloading. Additionally, we formulated a novel phase-field model to study the mechanisms of FA domain nucleation and switching, and we uncovered the effect of FA domain switching on the deformation behavior of t' YSZ.

For the nanoscale study of ferroelectric (FE) switching in specific functional oxides, we developed a novel MD approach utilizing a modified embedded-atom method with charge

equilibration (MEAM+QEq) interatomic potential. This approach provides new insights into how defects and dislocations in bulk can modulate the FE behavior of perovskite oxides.

Below we summarize findings from our recent works:

1) Both nanoscale and microscale studies have identified the reorientation of three crystallographic variants (c, a1, and a2 domains) in response to external stress in the t' phase of YSZ. Starting with experimentally observed microstructures containing all three variants, we have demonstrated that above a critical stress, domain walls (DWs) can propagate without the need for nucleation (Fig. 1a). However, the movement of DWs, approximately in the crystallographic direction <110>, requires energy, which is provided by the applied deformation. As the extent of FA switching increases, the stress-strain curve develops a plateau, and the stress at these plateaus depends on the net change in domain volume fractions [5].
2) Nucleation is a crucial step in domain switching and significantly influences ferroic behavior. Our MD simulations in $BiFeO_3$have shown that new domains nucleate at DWs. Similarly, PF simulations of FA domain switching in the t' phase have captured nucleation at DWs during reverse loading [6]. The PF simulations suggest that strain compatibility often results in non-smooth features, such as steps, crevices, or corners on the DW, where nucleation of new domains exclusively occurs. It was observed that stress concentrations at these sites are high enough to easily overcome the nucleation barrier. The PF simulations indicated the nucleation of triangular and oblate spheroid-shaped domains at the DW. Although these nuclei originate from slightly different switching reactions, the nucleation barrier remains on the order of $10^3 kT$.
3) In the absence of sufficient nucleation sites, domain switching proceeds through the movement of DWs, and the kinetics of domain switching should follow the Kolmogorov-Avrami-Ishibashi (KAI) model. However, our detailed microscale study has shown that single crystals of the t' phase in YSZ often deviate from this behavior. Analysis has revealed that sharp corners on the DW create a stress state that promotes localized back-switching, even while normal switching occurs elsewhere in the material under applied load. The tendency for back-switching increases as the applied strain rate decreases. Although back-switching is eventually overcome by normal re-switching behavior as the load increases, the switching→back-switching→re-switching cycle leads to greater energy absorption.

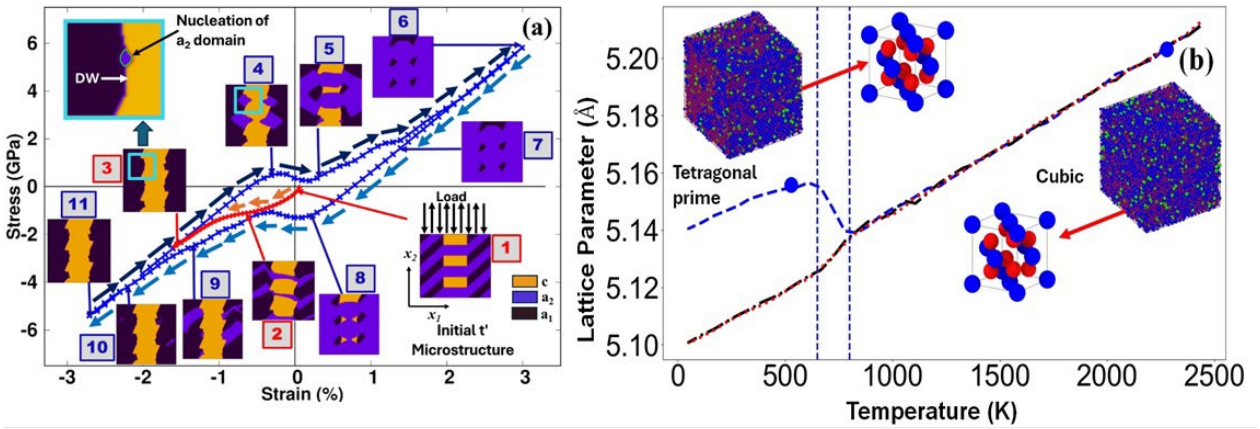

Fig. 1. (a) PF simulation of evolution of FA domains in stress-strain hysteresis loop in t′ phase in YSZ [5]. (b) MD simulation of formation of t′ phase during quenching of cubic YSZ phase [7].

4) MD simulations were employed to study the nanoscale mechanisms of FA training and switching in YSZ. To replicate the industrial approach, we quenched the material from the cubic phase to ensure the formation of the t' phase, a known ferroelastic phase of YSZ. The successful formation of the t' phase was confirmed through virtual XRD and lattice analysis. However, the rapid quenching process also introduced defects, such as oxygen vacancies, which initially hindered the system's ferroelastic behavior. This observation aligns with experimental findings. Our simulations demonstrated that by applying external stress, the defects within the material gained sufficient energy to relocate and adjust, thereby allowing ferroelasticity to emerge. Fig. 1b illustrates the quenching and training processes that reveal ferroelasticity [7]. This study underscores how defects within the system, influenced by production procedures, significantly affect the material's mechanical properties.

5) We also provided new insights into the role of dislocations in modulating the ferroelectric behavior of $BiFeO_3$ by MD simulations. Traditionally, dislocations in perovskites are believed to disrupt their ferroelectric properties. However, our findings reveal that the stress gradients induced by various dislocation configurations and densities significantly influence the polarization distribution pattern and the domain switching process, as illustrated in Fig. 2 (a)-(c). This modulation directly impacts the shape and energy characteristics of the hysteresis loop. Our study of the intrinsic charge-lattice coupling mechanism showed that changes in polarization during cyclic electrical loading are more pronounced in regions experiencing greater compressive or tensile stress. Furthermore, we uncovered the effect of dislocation density on the energy characteristics, offering valuable guidelines for material design in specific electronic applications.

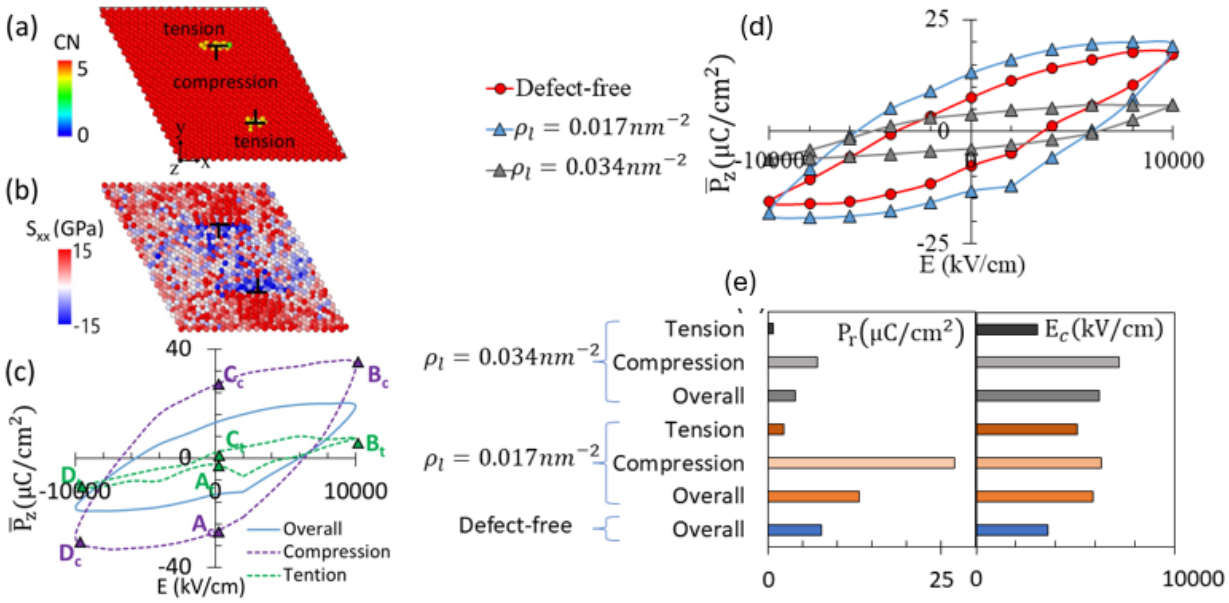

Fig. 2. Graphical representation system with dislocation density of 0.017 nm^{-2} given by (a) CN and (b) stress S_{xx}. (c) The overall hysteresis loop compared with the one for the regions under compression and tension stress system. The role of dislocation density on (d) hysteresis loop (e) remnant polarization $P_r(\mu C/cm^2)$ and coercive electric field $E_c(kV/cm)$ [6].

As shown in Fig. 2(d)-(e), lower dislocation densities widen the hysteresis response and improve the polarization and strain retention properties, which are desirable for random-access memory applications requiring long-term data preservation. In contrast, higher dislocation densities result in narrower hysteresis loops and sharper switching responses, optimizing the conditions for high-speed computing and power-sensitive logic devices [8].

Future Plans

There have been several experimental and computational studies on the mechanisms of toughening through MPT and FADS. While our contributions have significantly advanced the understanding of MPT in YSZ, the interactions between MPT and FADS have been less explored. We hypothesize that the interaction between MPT and FADS could enhance energy absorption by increasing back-switching events. To investigate this, we plan to develop a novel PF model incorporating both MPT and FADS. Additionally, we will create a surrogate machine learning (ML) model to predict microstructural evolution, which we anticipate will provide insights into features influencing back-switching behavior. Defects also play a crucial role in ferroic behaviors and MPT. Future MD studies will focus on identifying defects that obstruct ferroelasticity, understanding the interactions between different types of defects, and analyzing the movement of oxygen atoms/vacancies and dopant atoms.

In ABO_3 (perovskite) structures, the coupling between FEDS and FADS under electrical and/or mechanical stimuli results in hysteresis responses that are crucial for applications in

nanoelectronics, non-volatile memory devices, and logic devices. We plan to expand our study to explore the role of dislocations in improving FE material performance. This will include examining the effects of other defects (such as domain walls, vacancies, and grain boundaries) and their configurations and densities on FE domain switching. Additionally, nanoscale analysis of complex electromechanical loadings will help reveal the mechanisms governing the coupled interactions of ferroelastic and ferroelectric domain switching.

References

1. J.F. Scott, *Applications of modern ferroelectrics*, Science 315(5814) (2007) 954-959.
2. B.D. Poquette, T.A. Asare, J.P. Schultz, D.W. Brown, S.L. Kampe, *Domain reorientation as a damping mechanism in ferroelastic-reinforced metal matrix composites*, Metallurgical and Materials Transactions A 42(9) (2011) 2833-2842.
3. S.C. Hwang, C.S. Lynch, R.M. McMeeking, *Ferroelectric/ferroelastic interactions and a polarization switching model*, Acta Metallurgica et Materialia 43(5) (1995) 2073-2084.
4. Y. Hu, L. You, B. Xu, T. Li, S.A. Morris, Y. Li, Y. Zhang, X. Wang, P.S. Lee, H.J. Fan, J. Wang, *Ferroelastic-switching-driven large shear strain and piezoelectricity in a hybrid ferroelectric*, Nature Materials 20(5) (2021) 612-617.
5. A. Bhattacharya and M. Asle Zaeem, *A phase-field model for study of ferroelastic deformation behavior in yttria stabilized zirconia*, Acta Materialia 276, 120039 (2024).
6. A. Bhattacharya and M. Asle Zaeem, *Mechanism of nucleation in ferroelastic domain switching*, Scripta Materialia 252, 116273 (2024).
7. H. Li, M. Asle Zaeem, *Ferroelastic switching in yttria stabilized zirconia: A molecular dynamics study*, Computational Materials Science 244 (2024) 113187.
8. S. Kavousi, H. Nobarani, M. Asle Zaeem, *Can dislocations imprinted in bulk ferroelectric perovskites improve their polarization switching characteristics?*, Acta Materialia (2024).

Publications

1. A. Bhattacharya and M. Asle Zaeem, *A phase-field model for study of ferroelastic deformation behavior in yttria stabilized zirconia*, Acta Materialia 276, 120039 (2024).
2. A. Bhattacharya and M. Asle Zaeem, *Mechanism of nucleation in ferroelastic domain switching*, Scripta Materialia 252, 116273 (2024).
3. H. Li, M. Asle Zaeem, *Ferroelastic switching in yttria stabilized zirconia: A molecular dynamics study*, Computational Materials Science 244 (2024) 113187.
4. S. Kavousi, H. Nobarani, M. Asle Zaeem, *Can dislocations imprinted in bulk ferroelectric perovskites improve their polarization switching characteristics?*, Acta Materialia (2024).
5. A. Bhattacharya and M. Asle Zaeem, *Kinetics of Ferroelastic Domain Switching with and without Back-Switching Events: A Phase-Field Study*, Acta Materialia (2024).

Dynamical grain-boundary phase diagrams in irradiated alloys

Pascal Bellon, Robert S. Averback, Marie A. Charpagne

Department of Materials Science and Engineering, University of Illinois at Urbana-Champaign, Urbana, IL.

Keywords: Irradiation, self-organization, grain boundaries, correlative microscopy

Research Scope

Grain boundaries (GBs) play a determinant role in the properties of structural materials in nuclear applications. Furthermore, nanostructuring to length scales between 100 nm and 1 μm has been proposed to design future nuclear alloys with increased radiation resistance, by providing a large density of sinks for point defect elimination. Controlling the evolution of these interfaces in complex alloys under irradiation raises broad fundamental questions related to the structural and chemical evolution of these interfaces in such extreme non-equilibrium environments, presented by ballistic mixing, flux coupling of solute to defects, resulting in radiation-induced segregation (RIS) and precipitation (RIP), and interfacial complexions.

The two main objectives of the project are (i) to develop and construct dynamical phase diagrams at grain boundaries in irradiated alloys (GBs) in the presence of segregation and precipitation, and (ii) to develop a fundamental understanding of the stabilization of these nonequilibrium structures by evaluating the relevant kinetic processes and their synergies, including solute advection to GBs by defect-solute flux coupling, radiation-enhanced bulk diffusion, GB diffusion under irradiation and chemical mixing forced by nuclear collisions.

Recent Progress

1. Precipitation microstructures at GBs in ion-irradiated alloys

Three alloy systems were investigated, Ni-Si, Ni-Ge and Al-Sb. These three systems have been chosen in part because they make it possible to contrast the effects of the type of point defect responsible for solute drag, vacancy for Ni-Ge and Al-Sb, interstitial for Ni-Si, as well as the strength of this coupling at their respective homologous irradiation temperatures. Hypothesizing that solute diffusion along irradiated high energy GBs is similar to solute diffusion in an amorphous matrix, it is anticipated that GB diffusion is fast for Ni-Si owing to the negative size misfit of Si in Ni, but moderate to slow for Al-Sb and Ni-Ge. Based on these differences, the potential for self-organization of GB precipitates at TJs in Ni-Si is strong owing to strong solute drag and fast solute diffusion along GBs while it is weaker in Ni-Ge. Adding the Al-Sb alloy system to the two Ni-base alloys allows us to investigate whether the dominant factor for promoting GB precipitate self-organization is the strength of the solute drag or the defect coupling to solute species, since for Al-Sb the solute-vacancy binding is strong but solute GB diffusion is expected to be slow. The main recent results as summarized below.

1.1. Radiation-induced segregation and precipitation in Ni-Si and Ni-Ge thin-film alloys.

A first significant finding for Ni-Si nanocrystalline thin films irradiated with 2 MeV Ti ions to damage levels 1, 10 and 30 dpa is that RIS and RIP lead to significant re-organization of the microstructure. Irradiation at 550˚C and 500˚C resulted in the formation of a continuous network of GBs enriched in Si but without precipitation along these GBs. Irradiation at 450˚C, however, produced a novel microstructure with extensive Ni_3Si precipitation at TJs. At a dose of 30 dpa the microstructure has reached a steady state with 30-50 nm precipitates decorating most TJs, and little grain growth, see Fig. 1. It is hypothesized that RIP at TJs suppressed grain growth, resulting in a robust nanostructured microstructure that is at steady state, and thus stable, under irradiation. In addition, RIP on dislocation loops is observed for all three irradiation temperatures, similar to what is observed in large-grain alloys.

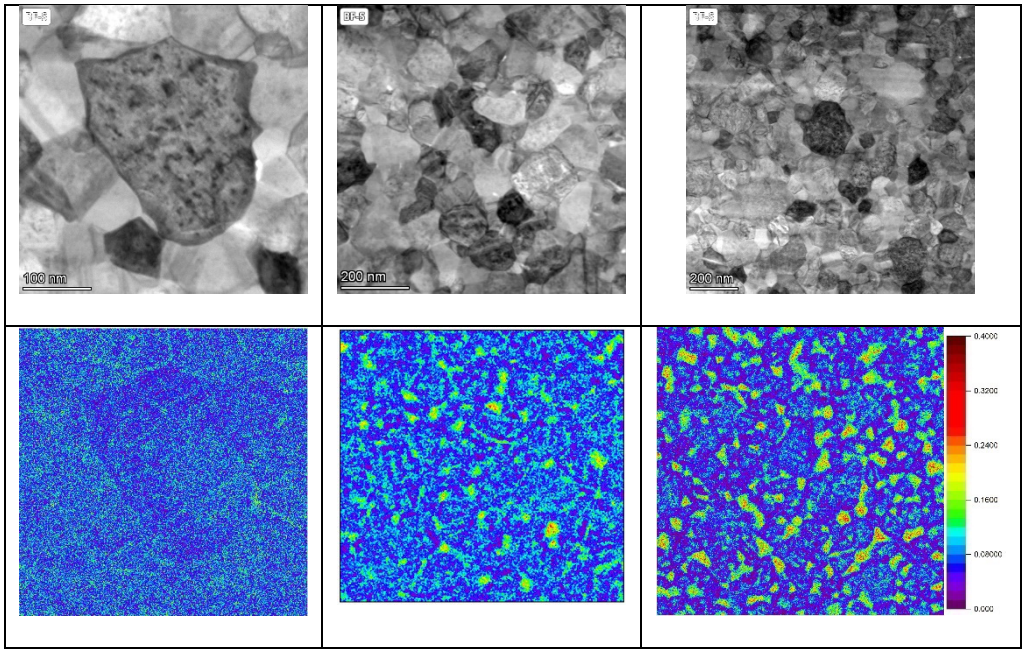

Figure 1: *Microstructure of Ni-8at.%Si thin films irradiated with 2 MeV Ti ions at 450 °C to a dose of (left) 1 dpa, (middle) 10 dpa, and (right) 30 dpa. Top row: Bright field STEM; bottom row: corresponding STEM-EDS maps of Si concentration.*

In the case of Ni-Ge alloys irradiated with 2 MeV Ti, RIS was observed on dislocation lines but no precipitation of the $L1_2$ Ni_3Ge phase was detected. Irradiation with 100 keV He ions, on the other hand, resulted in the formation of Ni_3Ge precipitates along dislocations and GBs, which were identified by correlative microscopy combining 4D-STEM and atom probe tomography, see Fig. 2. These different outcomes indicate that when solute-drag is not very strong, ballistic mixing can prevent RIP. These results are in excellent agreement with our phase-field simulations [1].

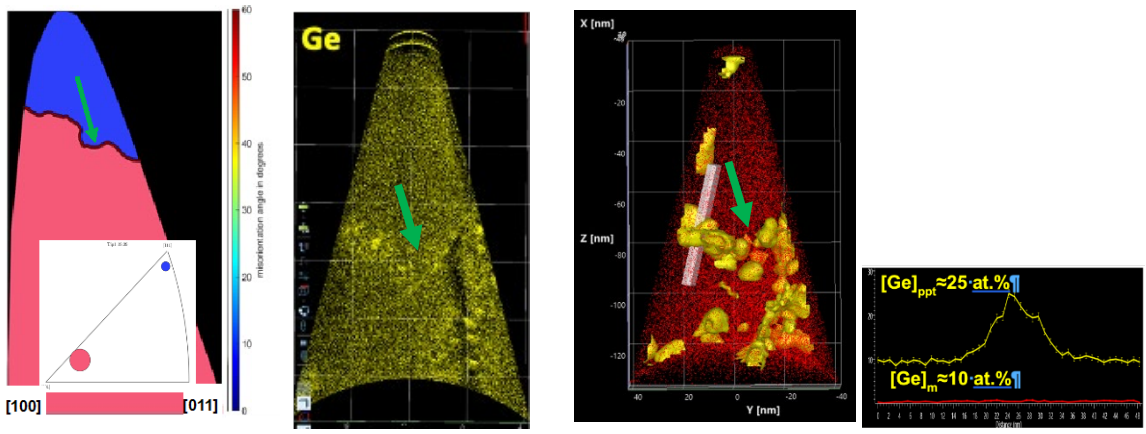

Figure 2: *Correlative microscopy of a Ni-Ge 8at.% alloy irradiated at 450 °C to 3.5 dpa with 100 keV He ions at CINT-LANL. Left to right: 4D-STEM orientation map; Atomic reconstruction, with green arrow pointing to GB; Iso-concentration contours of Ni_3Ge precipitates, along the GB and inside grains; concentration profile along the pink box, confirming the precipitate concentration of 25 at.% Ge.*

1.2 Global Self-organization of GB precipitates in Al-Sb alloy

Al-1.5at.% Sb thin films grown by magnetron sputtering were irradiated with 2 MeV Ti ions at RT and 75˚C, to doses up to 30 dpa. Irradiation at 75˚C led to the formation of ≈ 5 nm $Al_{50}Sb_{50}$ precipitates inside grains larger than 40 nm and of ≈ 9 nm precipitates along GBs, see Fig. 3. STEM-EDS and APT measurements show that the system reaches a unique steady-state microstructure, whether starting from the as-grown state or from an annealed state (2 hours at 150˚C) to introduce large AlSb precipitates at triple junctions (TJs). This "self-organized" state requires solute redistribution over lengths exceeding several grain diameters. Such global self-organized microstructures are intrinsically self-healing since features that deviate from the steady state, e.g., deviations from steady-state precipitate size and shape, continuously form and decay.

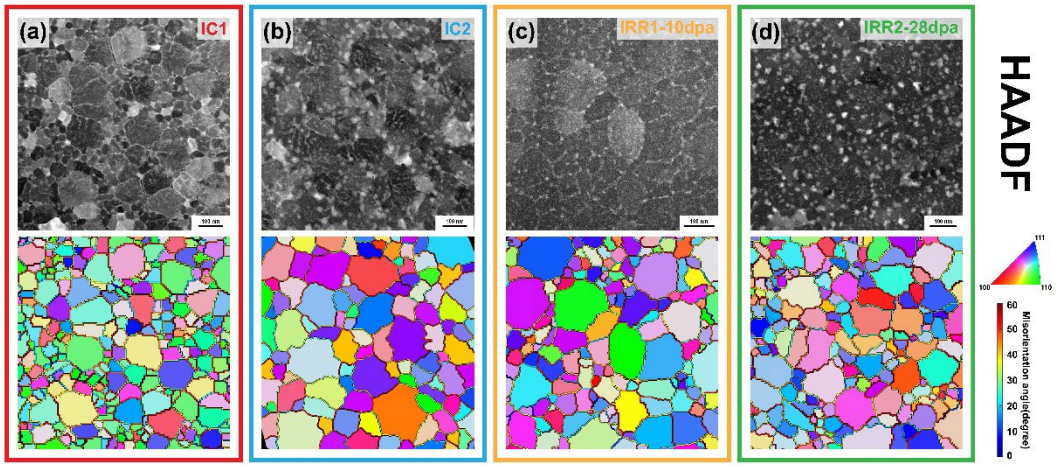

Figure 3: *HAADF micrographs of Al-$Sb_{1.5}$ alloys (a) as-grown (IC1), (b) reached after annealing for 2 hours at 150˚C (IC2), (c) after irradiation at 75˚C to 10 dpa starting from IC1 (IRR1), and (d) after irradiation at 75˚C*

to 28 dpa starting from IC2 (IRR2). IPF maps obtained from 4D-STEM are given below HAADF micrographs. The distribution of the misorientation angle of GB segments indicates all states have random texture.

2. Development of correlative microscopy for nanoscale characterization of irradiated alloys

We have developed a workflow to overlap phase information (precipitate versus matrix), segmented from STEM images, with crystallographic orientation collected using 4D-STEM over the same microstructural region. These multi-modal datasets enable analyses of the precipitates' size, location, and orientation relationships with their surrounding matrix, and thus they relate the topology of precipitates with the grain boundary and triple junction network in a statistical manner. One example of such analysis is presented in Fig. 2 for Ni-Ge, establishing the precipitation of Ni_3Ge at a GB. The same workflow was applied to Al-Sb to determine whether the self-organization of precipitates along GBs was affected by the GB character, see Fig. 3.

3. Modeling and simulations of bulk and GB self-organization irradiated alloys

Phase field modeling was employed to build the steady-state phase for a model system mimicking Al-Sb. As in the experiments, a unique steady state was found, and compositional patterning of precipitates was observed along GBs.

We performed parametric studies using PFM and kinetic Monte Carlo (KMC) simulations to determine whether RIS could (i) suppress precipitate coarsening by overriding capillary effects, as we reported from PFM [2], and (ii) whether accelerating diffusion along a structural defect where segregation takes place, e.g., dislocation line, could re-establish precipitate coarsening. For small ~~diffusion~~ acceleration of diffusion along the sink, segregation leads to the formation of a continuous tubular structure. When pipe diffusion is large, however, the continuous precipitate tube develops morphological instability and eventually breaks up into a single ellipsoidal precipitate.

Future Plans

Future experiments will consider the Ni-Zr system, since RIS may lead to the stabilization of interfacial amorphous precipitates. These precipitates are anticipated to suppress grain growth during elevated temperature irradiation. We will also investigate in Ni-Si and Ni-Zr whether irradiation accelerates solute diffusion along GBs. PFM will be developed in parallel, in collaboration with Dr. Remi Dingreville at SNL, to guide the design and analysis of these experiments. PFM modeling and KMC simulations will also be developed to investigate the stability of RIS and RIP patterns along linear sinks such as dislocation lines.

References

[1] G. F. B. Moladje, S. Das, A. Verma, Y. T. Chang, M. A. Charpagne, R. S. Averback, and P. Bellon, Grain Boundary Precipitation and Self-Organization in Two-Phase Alloys Under Irradiation: Phase Field Simulations and Experiments in Al-Sb JOM **76**, 2884 (2024).

[2] G. F. Bouobda Moladje, R. S. Averback, P. Bellon, and L. Thuinet, Convection-Induced Compositional Patterning at Grain Boundaries in Irradiated Alloys Phys Rev Lett **131**, 056201 (2023).

Publications

• S. E. Kim, N. Verma, S. Özerinç, S. Jana, S. Das, P. Bellon, and R. S. Averback, Materialia **26**, 101564 (2022).

• G. F. Bouobda Moladje, R. S. Averback, P. Bellon, L. Thuinet, Physical Review Letters **131**, 056201 (2023).

• G. F. Bouobda Moladje, S. Das, A. Verma, Y.-T. Chang, M.-A. Charpagne, R. S. Averback, P. Bellon, JOM **76**, pp 2884-2898 (2024).

• S. Das, A. Verma, G. F. Bouobda Moladje, Y.-T. Chang, M.-A. Charpagne, R. S. Averback, P. Bellon, "Global self-organization induced by ion irradiation in polycrystalline alloys" in preparation (2024).

• S. Das, G. Jawaharram, R. S. Averback, S. J. Dillon "Electron irradiation induced creep in amorphous alloys", in preparation (2024).

Role of Subgrain Heterogeneous Processes in Slip Localization in Polycrystalline Metals During Cyclic Plasticity

I. J. Beyerlein, T. M. Pollock, University of California at Santa Barbara

M. P. Miller, K. E. Nygren, Cornell University

Keywords: slip localization, lattice rotation, crystal plasticity, triple junction, irreversibility

Research Scope

The overarching goal of the proposed research is to establish a fundamental understanding of the formation and development of rare slip events that precede fatigue fracture of polycrystalline materials made for extreme environments. Fatigue of ductile polycrystalline metals is a microstructure-sensitive localization process, beginning with cyclic plasticity-driven production of substructural inhomogeneities and ending with the eventual development of cracks. While irreversible slip mechanisms under cyclic conditions have been studied extensively, *designing a material for extended fatigue life is rarely performed based on knowledge of how rare slip instabilities first form and grow below the scale of the grain*. While slip irreversibility has long been suggested as an important aspect of fatigue crack initiation, quantitative information on the localization processes over the large volumes of material, required to capture the relatively rare nucleation events, has been lacking. Thus, a key remaining challenge lies in identifying *when, where, why and how* cyclic loading leads to the formation and intensification of rare but terminal material instabilities. Such fundamental four-dimensional knowledge would be foundational for physics-based fatigue models and could guide microstructural design of more durable energy-relevant materials for future energy technologies.

Our *central hypothesis* is that a special combination of microstructural and deformation properties of the full 3D mesoscale grain neighborhood makes a rare few slip localizations accumulate irreversibly during cyclic loading. Research activities in all tasks will be driven to determine the 3D features of the crystalline nearest neighborhood of a grain that foster the formation and development of the most irreversible (or highest accumulating) slip localization and how does a concentrated irreversible slip localization transition into an incipient fatigue crack. To address these questions, the proposed project unites a suite of state-of-the-art experiments, High Energy X-ray Diffraction Microscopy (HEDM), Heaviside and High-Resolution Digital Image Correlation (H-DIC, HR-DIC), TriBeam tomography and 3D plasticity modeling techniques. With this union, we aim to achieve a four-dimensional understanding (spatial and temporal) of where, when, and how they occur to a degree that such materials can be processed and re-designed at the microstructure level to significantly extend lifetime. This proposal is for unclassified, fundamental research; as such, there should be no restrictions on the citizenship on those performing the work.

Recent Progress

With far-field (ff)-HEDM, we studied the evolution of the lattice rotations and strains within thousands of grains across a 3D volume of the FCC Ni alloy IN718. Significant progress was made in detecting signatures of rare deformation behavior, 2) quantitatively merging HEDM, TriBeam, and CP modeling results (Fig. 1), and 3) faster HEDM and TriBeam data acquisition.

We focused at the outset on identifying signatures of rare slip events from the textures of individual grains measured in *in-situ* ff-HEDM testing, which we refer to as Discrete Single Crystal Orientation Distributions (DSGODs). ff-HEDM is a non-destructive probe that reliably provides DSGODs and a grain-average elastic strain tensor for every grain in the polycrystal during *in-situ* monotonic or cyclic loading [1]. To know *where* to look in the polycrystalline 3D volumes, however, HR-DIC and Tribeam analyses of deformed material were used to first establish grains and grain neighborhoods vulnerable to localization formation. For these grain groups, we sought to identify a measurable signature in the X-ray signal. As one major outcome of this effort, we showed that higher statistical moments, such as the covariance, skewness, and kurtosis, of the DSGODs, can be used to indicate those few percent of grains exhibiting highly heterogeneous deformation [2]. With validation from post-mortem TriBeam analysis, we showed that high skewness and kurtosis are correlated with localized regions of high gradients of orientation within a grain. These extreme intragranular orientation gradients have been linked to vulnerable areas for fatigue crack initiation or areas adjacent to concentrated slip localizations [3]. We refer to this high-skewness/high-kurtosis signature as *grains exhibiting microscale localized-deformation inside* (gremlins).

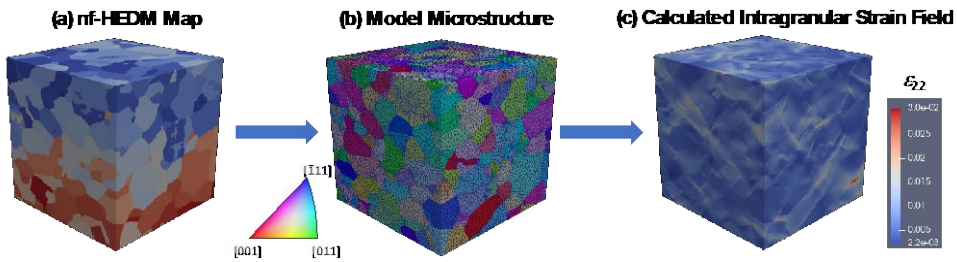

Figure 1. (a) nf-HEDM measured microstructure (b) 3D CP model instantiated by the nf-HEDM. (c) CP model spatial fields of intragranular strain.

To relate the DSGOD and strain evolution in every grain, the nf- and ff-HEDM data were paired with CP modeling. To quantify intragranular lattice rotations, we study the covariance (CoV) of the DSGOD, measured from ff-HEDM and predicted from CP (Fig. 1). The CoV metric indicates the dispersion in grain texture and with it, we grouped thousands of grains into distinct deformation behaviors both around a hysteresis loop and at the loop tips across many cycles of fatigue [4]. To ensure that the CP model correctly reflects the grain position and those of the grains in its 3D neighborhood, the model microstructure was built using a high-fidelity 3D morphology technique, called XtalMesh, from the nf-HEMD data [5]. Not only could the model replicate the true initial grain-average orientations and grain-average residual strain state from the HEDM data,

but also the details of the grain boundary surfaces and triple junction lines (*e.g.*, see the experimentally informed 3D model microstructure in Fig. 1). With this set up, CP-computed and HEDM-measured DSGODs and stress and strain tensors at equivalent cycles and positions around the hysteresis loop are *directly compared*. We first validated the model at all measurement steps of applied strain. With no adjustable parameters, the calculated grain-average elastic strains achieve excellent agreement with HEDM for thousands of grains (Fig. 2a,b).

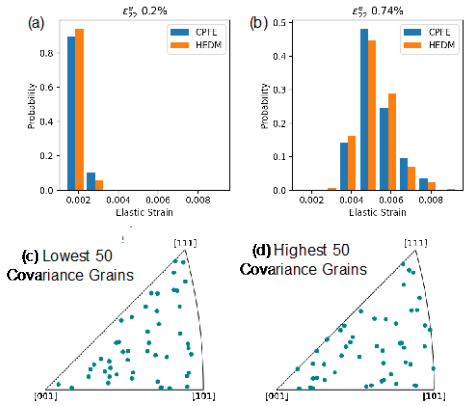

Figure 2. Comparison of the grain-average elastic strains from the HEDM and CP modeling at (a) low and (b) high applied strains. Agreement for >1000 grains is excellent. The 50 grains with the (c) lowest and (d) greatest dispersion in their texture are uncorrelated with their initial orientation.

Using the model, we examined the CoV in the DSGODs. Our CP model predicts the range in intragranular orientation dispersion seen in HEDM. At the greatest level of strain of 1.83%, we find that grains in the same polycrystal exhibited a wide range of CoV, with some becoming substantially heterogeneous (high CoV), while others nearly sustaining their initial uniform state (low CoV). This outcome would not be anticipated by conventional polycrystal plasticity models. Special groups of grains exhibiting either low or high CoV require further investigation as they may be signatures of irreversibilities. Analysis finds that these two extremes correlated neither with average grain stress nor grain orientation (Fig. 2c,d), defying the general expectation that individual grain properties dominate intragranular deformation behavior.

Most recently, we found that a multi-axial bending stress from small misalignments in the load frame and grip exaggerated the deformation evolution behavior and asymmetric response between loading in tension and compression (Fig. 3). Further analysis suggested that this altered initial stress state had a dominating influence on behavior over subsequent cycles. In our CP modeling, close attention is paid to replicating these complex loading and boundary conditions, considering the multiaxiality and asymmetry from bending in the applied loading of the *in-situ* HEDM experiment. To date, we have established agreement in the multi-axial stress and strain state in every grain, critical for next steps. At the same time, this study opened questions on the best way to discuss fatigue responses and loading histories where stress states across the polycrystalline are inherently *multi-axial*, especially considering that fatigue behavior is often grounded in the context of uniaxial tension (*e.g.,* stress ratios, stress amplitudes).

Future Plans

Our studies involving HR-DIC, *in-situ* LCF testing, and micromechanical modeling identified that special grain configurations, comprising large elastic compliance and inclined planar boundaries, result in exceptional, highly localized elastic strains at a triple junction, long before the material

globally reaches the elastic-plastic transition. Modeling further suggested these severe elastic concentrations were a consequence of the large elastic anisotropy of IN718. Here, we question whether premature slip triggered at the most extreme elastic stress or strain concentrations, arising from elastic anisotropy in the complex polycrystal network, can manifest later, with subsequent cycling, as the more intense, irreversible slip localizations. In the next year, we plan to identify the 3D microstructural configurations that lead extreme elastic concentrations and determine the propensity of the micro-plasticity that ensues to develop into the concentrated, irreversible slip localizations. Our activities will involve characterizing the elastic response of configurations known to produce a slip localization in LCF, simulating digital replicas of the reconstructed microstructures to predict the elastic stress and strain gradients, as well as the local onset of local slip and identifying signatures of elastic strain concentrations for subsequent *in-situ* HCF and VHCF HEDM experiments.

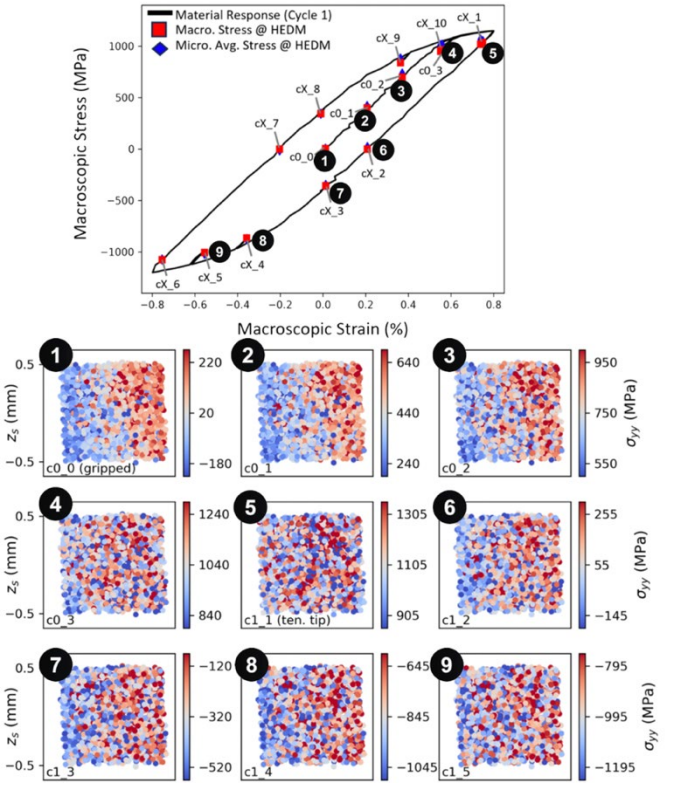

Figure 3. Stress in the loading direction plotted for each centroid of a grain across the gauge section of the sample for a few load steps along the first cycle in the hysteresis loop showing initial bending moment that is mostly absent after yielding the material

References

1. T.J.H. Long and M.P. Miller, *Statistical characterization of intragrain misorientations at large strains using high-energy x-ray diffraction: Application to hydrogen embrittlement*, Intrg. Mater. Manufact. Innov. **8**, 423 (2019)

2. D.J. Shadle, K.E. Nygren, J.C. Stinville, M.A. Charpagne, T.J.H. Long, M.P. Echlin, C.J. Budrow, A.T. Polonsky, T.M. Pollock, I.J. Beyerlein, and M.P. Miller, *Integrating in-situ multi-modal characterizations with signatures to investigate localized deformation*, Mater. Char. **205**, 113332 (2023)

3. J.C. Stinville, P.G. Callahan, M.A. Charpagne, M.P. Echlin, V. Valle, and T.M. Pollock, *Direct measurements of slip irreversibility in a nickel-based superalloy using high resolution digital image correlation*, Acta Mater. **186**, 172 (2020).

4. D.J. Shadle, M.P. Miller, and K.E. Nygren, *Using real-time data analysis to conduct next-generation synchrotron fatigue studies*, Int. J. Fatigue **164**, 107113 (2022).

5. J.M. Hestroffer, and I.J. Beyerlein, *Xtalmesh toolkit: High-fidelity mesh generation of polycrystals*, Intrg. Mater. Manufact. Innov. **11**, 109-120 (2022).

Publications

1. J. M. Hestroffer, J. C. Stinville, M.-A. Charpagne, M. P. Miller, T. M. Pollock, and I. J. Beyerlein, *Surface—subsurface grain structure relationships*, Acta Materialia **266**, 119660 (2024).
2. D.J. Shadle, Exploring Grain-scale Cyclic Deformation by Coupling High Energy X-ray Diffraction with Signatures. Ph.D. Dissertation, Cornell University, Dec. (2023).
3. J. M. Hestroffer, J. C. Stinville, M.-A. Charpagne, M. P. Miller, T. M. Pollock, and I. J. Beyerlein, *Slip localization behavior at triple junctions in nickel-base superalloys*, Acta Materialia **249**, 118801 (2023).
4. J.M. Hestroffer, M.I. Latypov, J.-C. Stinville, M.-A. Charpagne, V. Valle, M.P. Miller, T.M. Pollock, I.J. Beyerlein, *Development of grain-scale slip activity and lattice rotation fields in Inconel 718*, Acta Materialia **226**, 117627 (2022).
5. J. M. Hestroffer, M.-A. Charpagne, M. I. Latypov, and I. J. Beyerlein, *Graph neural networks for efficient learning of mechanical properties of polycrystals*, Computational Materials Science **217**, 111894 (2023).
6. J. C. Stinville, M.A. Charpagne, R. Maass, H. Proudhon, W. Ludwig, P.G. Callahan, F. Wang, I.J. Beyerlein, M.P. Echlin, and T.M. Pollock, *Insights into Plastic Localization by Crystallographic Slip from Emerging Experimental and Numerical Approaches*, Annual Review of Materials Research **53**, 275-317 (2023).
7. J. M. Hestroffer and I. J. Beyerlein, *XtalMesh Toolkit: High-Fidelity Mesh Generation of Polycrystals*, Integrating Materials and Manufacturing Innovation **11**, 109-120 (2022).
8. D.J. Shadle, K.E. Nygren, J.C. Stinville, M.A. Charpagne, T.J.H. Long, M.P. Echlin, C.J. Budrow, A.T. Polonsky, T.M. Pollock, I.J. Beyerlein, and M.P. Miller, *Integrating in-situ multi-modal characterizations with signatures to investigate localized deformation*, Mater. Char. **205**, 113332 (2023).
9. J.C. Stinville, J.M. Hestroffer, M.A. Charpagne, A.T. Polonsky, M.P. Echlin, C.J. Torbet, V. Valle, K.E. Nygren, M.P. Miller, O. Klaas, A. Loghin, I.J. Beyerlein and T.M. Pollock, *Multimodal Dataset of a Polycrystalline Metallic Material: 3D Microstructure Fields*, Scientific Data **9**, 460 (2022).
10. D.J. Shadle, M.P. Miller, and K.E. Nygren, *Using real-time data analysis to conduct next-generation synchrotron fatigue studies*, International Journal of Fatigue **164**, 107113 (2022).

Nanomechanics and Nanometallurgy of Boundaries

Brad L. Boyce[a], Rémi Dingreville[a], Douglas L. Medlin[a], Khalid Hattar[a,b]

[a] Sandia National Laboratories
[b] University of Tennessee

Keywords: nanostructured metals, grain boundaries, microstructure defects, mechanical properties, grain growth

Research Scope

Grain boundaries (GBs) are complex two-dimensional/pseudo-three-dimensional crystal defects that moderate many material properties including mechanical response. While it is well appreciated that elevated temperature stimulates GBs and thereby altering the stability of nanocrystalline materials via grain growth and changes in material properties, other stimuli and microstructure defects can also induce microstructural evolution. To understand how GBs affect the stability and nanomechanics of nanocrystalline metals, this program focuses on the evolutionary nature of GBs. Specifically, we consider GBs as "living" defects whose own internal configuration and defect state evolves with external stimuli. We examine the dynamic changes that occur in GBs by intentionally disrupting their state through mechanical and other stimuli and we manipulate that response through chemical and microstructural modifications. This effort ranges from fundamental characterization and theory of structural changes in GBs to the role of different GB defects and extended GB networks on various properties in NC metals such as fatigue and radiation tolerance. We emphasize nanocrystalline metals because of their particularly strong interplay between GBs, microstructural stability, and material properties, including mechanical behavior.

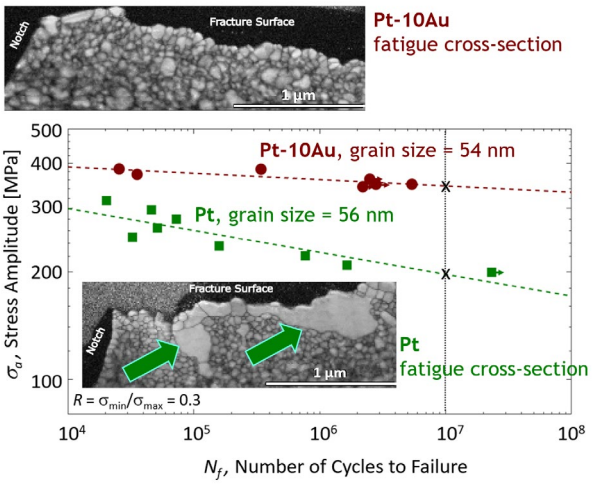

Figure 1. When alloyed with Au, nanocrystalline Pt exhibits a dramatic increase in fatigue resistance, including a 75% increase in the endurance limit. This is largely caused by grain boundary pinning, not a solute strengthening effect.

Recent Progress

Through our prior studies on thermal, mechanical, and irradiation-induced evolution, we have grown to appreciate that GB character is not static but evolves as defects and/or allying elements are introduced – a common theme that motivates our recent progress. This idea of a GB as a "living" defect guided our recent report that fatigue cracks in pure metals can undergo intrinsic self-healing [1]. Under tensile high-cycle fatigue in a transmission electron microscope (TEM),

we directly observed the early progression of nanoscale fatigue cracks in pure Pt. As expected, the cracks advance, deflect and arrest at local microstructural barriers. However, unexpectedly, cracks were also observed to heal by a process that can be described as crack flank cold welding induced by a combination of local stress state and GB migration. The dynamic changes occurring during GB/crack interactions are at the root of this healing process. Atomistic and continuum-level simulations showed and confirmed that inhomogeneous local stresses and progressive migration of a (defected) GB in the vicinity of the crack tip facilitated this counterintuitive healing behavior.

Fatigue crack healing has fundamental implications for understanding how damage progresses at the nanoscale, highlighting notably the role of microstructural inhomogenities near the GB/crack nexus alter GB migration and vice versa. In [2], we focused on this notion that a mechanical stimulus can indeed change the character of GB migration. We performed a detailed atomistic study to reveal the heterogeneous nature of mechanically accelerated grain growth in polycrystalline Pt nanowires. Using molecular dynamics simulations, we compared the grain-growth behavior of individual grains during tensile and shear cyclic loading. Pure thermal grain growth with no mechanical loading provided a baseline reference case. On average, grains that were already susceptible to thermal grain growth were stimulated to grow faster with mechanical loading, as expected. However, when analyzed on a grain-by-grain basis, the results were far more complex: grains that grew fastest under one mechanical stimulus (*i.e.* tensile *vs.* shear) were less accelerated under another mechanical stimulus. Even when the magnitude of mechanical loading changed, the relative growth of individual grains was distorted. We interpreted this complexity from the perspective of superimposed growth mechanisms and the presence of defects at GBs.

Understanding of GB behaviors like the two studies provided in [1] and [2] lead to several additional foundational questions on the role of impinging defects on GB response. In particular, we expect interfacial defect processes to be highly sensitive to alloying, whether through local segregation of solute atmospheres at the interfacial defect cores or through global changes to the alloy properties. For instance, in [3] and [4], we used large-scale atomistic simulations to elucidate the nature of defect-GBs interactions in the presence of segregating solutes. Starting with GB line defects, we investigated in [3] the impact of disconnections (*i.e.* a type of interfacial line defects that have both a dislocation and step character to it) on solute segregation at twin boundaries in a broad range of face-centered cubic (FCC)-based binary alloys. We showed that disconnections can induce discontinuities in segregation patterns between the terraces of twin boundaries under certain conditions. This discontinuity may cause a change from segregation to anti-segregation or vice versa, driven by the dislocation character of the disconnection and its associated influence on the local stress field. For more complex GB defects such as GB junction defects, we studied in [4] the impact of triple-junction segregation on the thermal stability of nanocrystalline Pt–Au alloys. We showed that doping the triple junctions with Au solutes renders them immobile, thereby effectively locking the GB network and hindering its evolution. In dilute alloys, we showed that

GBs and triple-junction segregation are not as effective at mitigating grain growth, as the solute content is not sufficient to dope and pin all GBs and triple junctions.

These studies suggest that controlling segregation across the GB network could be a crucial strategy for developing thermally stable nanocrystalline materials. In [5], we used these thermodynamic considerations and presented a novel approach to designing gradient nanostructured metals that combine the benefits of solute stabilization and gradient grain structures, offering a promising route for developing mechanically stable and ductile nanocrystalline metals. We developed a new method to fabricate gradient nanostructured metals by introducing a compositional gradient. Using Pt–Au as a model material system, we fabricated films with varying Au content across its thickness via physical vapor deposition, leading to a spatial microstructural gradient after annealing. The gradient resulted in nanocrystalline grains at the film's edges and larger grains in the middle. This approach provides enhanced thermal and mechanical stability without requiring severe mechanical deformation, which is typically used to create gradient structures. Additionally, our phase-field model corroborated the experimental results, providing insights into the competing mechanisms of Au diffusion and grain growth leading to these graded microstructures. Our findings showed that annealing the gradient films at different temperatures and times resulted in varying grain sizes, with Au-rich areas exhibiting slower grain growth due to solute stabilization. The compositional gradient and corresponding microstructural gradient were confirmed through various characterization techniques, including Dynamic Secondary-ion mass spectrometry (SIMS) and Scanning Transmission Electron Microscope (STEM), revealing the relationship between grain size, Au concentration, and hardness.

Future Plans

Moving forward, we are interested in stimuli that cause a more aggressive repetitive disruption to the GB, leading to high-energy states and accelerated evolution for deeper understanding of the evolutionary nature of GBs. Our future plans are organized around three themes:

GB defects interactions: Motivated by our recent findings on the role of disconnections and triple junctions on segregation, we are interested in how they interact with each other and with point defects and solutes already present in nanocrystalline structures. Our aim is to reveal the mechanisms governing these interactions, the influence of alloying on the stability of such defected interacting network, and the cumulative impact of defect accumulation on these GB defects. We will start with defect interactions at GB facet junctions (which join two singular, low-energy boundaries) and then extend our analysis to more complex triple-junction GB configurations. For instance, we previously discovered that the spatial distribution of junctions is closely linked to the distribution of disconnections required to accommodate interfacial coherency strains, suggesting both a strong interaction between these two types of defects and that strain accommodation is a competing factor limiting facet coarsening. But what controls the strength of this interaction? We hypothesize that there are two primary effects dominating such interactions: the elastic dislocation-

junction interactions, and reconfiguration of the junction core following absorption (or emission) of a disconnection. We will test this hypothesis by comparing detailed atomic resolution observations and atomistic and phase-field models of defected facet junctions and triple junctions. Our goal is to elaborate the structural details of the junction cores and their relationship to the energetic and kinetic properties of the junctions. Building on these preliminary discoveries, we will then extend our analyses to disconnection/triple junction interactions.

GB response to repeated disruptions under cyclic loading: As illustrated by our work and other research groups, solute stabilization strategies are known to be effective for thermal exposure but less clearly effective for mechanical stimuli. Indeed, our group and others have now shown astonishing abnormal grain growth induced by fatigue loading. This runaway boundary migration process results in a transformation of the initial nanocrystalline grain structure to nearly-single-crystal regions reminiscent of dynamic abnormal grain growth observed under high-temperature tension. While others have attributed grain growth to elastic anisotropy, our hypothesis is that cyclic loading serves to repeatedly perturb the GB configuration, allowing the GB to access less-stable elevated states. We will employ three complementary methods to study GB response to repeated disruptions under cyclic loading. First, we will employ our unqiue high-throughput fatigue testing using both ex-situ and in-situ SEM to explore overall fatigue response and sample a 'continuum' of microstructural configurations. Second, we will employ in-situ TEM high-cycle fatigue testing combined with atomistic and phase-field modeling to systematically study the role of elastic anisotropy, solute effects, and microstructural modifications, like nanovoids, in stabilizing GBs and impeding defect migration under cyclic loading. By comparing different FCC metals and alloy systems, our research aims to clarify the mechanisms driving fatigue-induced GB evolution and identify strategies to mitigate these effects.

Synergistic or antagonistic GB mechanisms under combined stimuli: Finally, building on our work on GB response to monotonic and cyclic loading, we will investigate the mechanisms by which defects control mechanically accelerated grain growth when superimposed with additional stimuli (elevated temperature, irradiation, and external chemical changes). We are motivated here by the observation from our own work that combinations of sequential or superimposed stimuli can act either synergistically or antagonistically. These observations raise the broader question of what controls the coupling between mechanisms in determining whether the response is augmented or diminished by the combined stimuli? Fundamentally, we expect that the nature of the defects generated and evolved by different stimuli are not equal, nor that they should necessarily act independently. We will investigate how these combined stimuli affect GB migration and defect evolution, using a combination of experimental in-situ TEM heating and straining, atomistic simulations, and phase-field simulations. Additionally, we aim to manipulate these antagonistic effects by adjusting stimulus intensity or modifying microstructure and chemistry, particularly focusing on Cu-based binary alloys, to control GB behavior under superimposed conditions.

Publications

1. C. M. Barr, T. Duong, D. C. Bufford, A. Molkeri, N. M. Heckman, D. P. Adams, A. Srivastava, K. Hattar, M. J. Demkowicz, and B. L. Boyce, *Autonomous healing of fatigue cracks via cold welding*, Nature **620**, 552–556 (2023).
2. E. Y. Chen, P. Hamilton, B. L. Boyce, and R. Dingreville, *The heterogeneous nature of mechanically-accelerated grain growth*, Journal of Materials Science **57**, 21743–21755 (2022).
3. C. Hu, S. Berbenni, S., D. L. Medlin, and R. Dingreville, *Discontinuous segregation patterning across disconnections*, Acta Materialia, **246**, 118724 (2023).
4. A. K. Barnett, O. Hussein, M. Alghalayini, A. Hinojos, J. E. Nathaniel II, D. L. Medlin, K. Hattar, B. L. Boyce, and F. Abdeljawad, *Triple junction segregation dominates the stability of nanocrystalline alloys*, Nano Letters **24**, 9627–9634 (2024).
5. A. Barrios, A., J. E. Nathaniel II, J. Monti, J., Z. Milne, D. P. Adams, K. Hattar, D. L. Medlin, R. Dingreville, and B. L. Boyce, *Gradient nanostructuring via compositional means*, Acta Materialia **247**, 118733 (2023).
6. R. Schoell, C. M. Barr, D. L. Medlin, D. P. Adams, Y. Mahmood, F. Abdeljawad, and K. Hattar, *The radiation instability of thermally stable nanocrystalline platinum gold*, Journal of Materials Science **59** 11497–11509 (2024).
7. [invited] C. Hu, R. Dingreville, and B. L. Boyce, *Computational modeling of grain boundary segregation: A review*, Computational Materials Science **232**, 112596 (2024).
8. D. M. Britton, A. Hinojos, M. Hummel, D. P. Adams, D. L. Medlin, *Application of the Polyhedral Template Matching Method for Characterization of 2D atomic resolution images*, Materials Characterization **213**, 114017 (2024).
9. A. Barrios, C. Kunka, J. Nogan, K. Hattar, and B. L. Boyce, *Automated High-Throughput Fatigue Testing of Freestanding Thin Films*, Small Methods **7**, 2201591 (2023).
10. E. J. Lang, N. M. Heckman, T. Clark, B. Derby, A. Barrios, A. Monterrosa, A., C. M. Barr, D. L. Buller, D. D. Stauffer, N. Li, and Boyce, B.L., *Development of an in situ ion irradiation scanning electron microscope*, Nuclear Instruments and Methods in Physics Research Section B: Beam Interactions with Materials and Atoms **537**, 29–37 (2023).

SNL is managed and operated by NTESS under DOE NNSA contract DE-NA0003525.

Effect of heterogeneous architectures on the mechanical behavior of metallic glasses

Paulo Branicio, University of Southern California

Keywords: metallic glasses, nanoglasses, mechanical behavior, molecular dynamics, machine learning

Research Scope

This research program investigates the intrinsic mechanical behavior mechanisms in heterogeneous metallic glasses (MGs) and nanoglasses (NGs) that lead to deformation and failure. The study centers on the design, generation, and characterization of the structure and mechanical properties of heterogeneous MGs using molecular dynamics (MD) simulations, visualization techniques, data analysis, and machine learning. By conducting large-scale MD simulations, the program aims to describe the structural and mechanical behavior of these materials, while data analysis is used to elucidate the mechanisms governing their mechanical response. The research focuses on copper-zirconium amorphous alloys, operating under the hypothesis that structural heterogeneity in MGs and NGs will affect their mechanical behavior, promoting deformation delocalization and restricting early failure, thereby enhancing strength. This could potentially lead to the development of structures with improved strength-to-ductility ratios beyond what is currently achievable in MGs and NGs. Recent accomplishments of the research program are summarized below.

Nanoindentation simulations on nanoglasses and gradient nanoglasses: Nanoindentation simulations were conducted to investigate the mechanical properties of NGs and gradient nanoglasses (GNGs) with varying grain sizes. Molecular dynamics simulations of nanoindentation were performed on $Cu_{64}Zr_{36}$ NGs with uniform grain sizes of 3 nm and 7 nm, as well as on GNGs with gradient grain sizes ranging from 3 to 7 nm. The results indicate that NGs with smaller grain sizes exhibit deformation mechanisms dominated by the activation and evolution of multiple shear transformation zones. Increasing grain size improves the elastic modulus and hardness yet reduces abrasion resistance. While the average grain size at the indentation surface significantly influences the deformation behavior in GNG models, strain localization and plastic deformation are also affected by

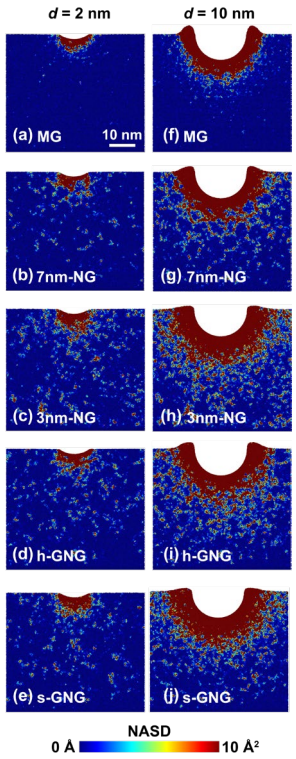

Fig. 1 Non-affine squared displacement (NASD) for CuZr MG, NG, and GNG models at different indentation depths, *d*.

grain sizes distant from the indenter. The simulation results suggest that GNGs display mechanical behavior distinct from that of NGs with uniform grain sizes, achieving superior mechanical properties through heterogeneous design. Further studies, including compression loading simulations, are underway to deepen the understanding of the observed mechanical synergy in GNGs. These findings underscore the potential of heterogeneous design in tuning the mechanical properties of MGs. These results were reported in a recent publication in Intermetallics (1).

Uncovering hidden vacancy-like motifs in MG with machine learning: In a programmatically related investigation, we employed MD simulations and machine learning to uncover a previously unidentified vacancy-like structural motif, named Q7, in MGs resembling vacancies in crystalline materials. The MG short-range order was described based on analysis of the atomic Voronoi statistics. The Q7 motif, characterized as an atomic Voronoi polyhedron with seven quadrangular faces, significantly influences short-range structural disorder in MGs, affecting properties such as atomic diffusivity and deformation processes. The presence of Q7 motifs, which show an Arrhenius-like relationship with temperature, is strongly correlated with the glass transition temperature and mechanical deformation behavior. The Q7 motif is further identified as a vacancy-like motif as it is linked to larger local entropy, atomic volume, and tension. This discovery enhances the understanding of local disorder and structural relaxation in MGs, offering predictive insights into their thermal and mechanical properties, and potentially advancing the design and manufacturing processes of MGs and other amorphous materials. In addition, these results bring fresh perspectives to the interpretation of unfavorable topological descriptors in MG atomic configurations and pave the way for constructing structure-property relationships and designing MGs with desired properties by tuning the population of favorable and unfavorable short-range order motifs. These results are reported in Materials and Design (2).

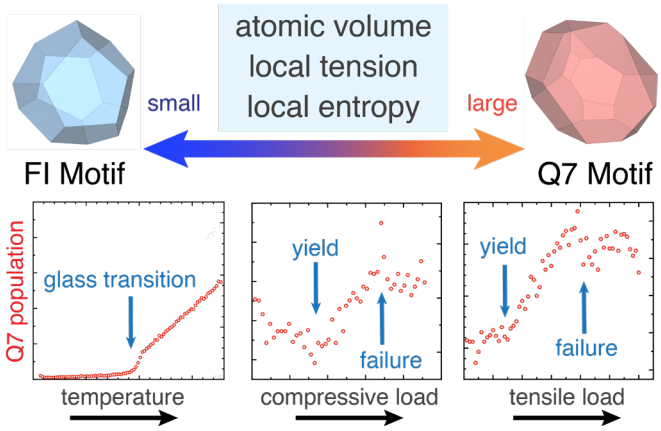

Fig. 2 Illustration of the influence of atomic volume, local tension, and local entropy on the deformation behavior of MGs under different conditions. Smaller atomic volumes correlate with lower local tension and entropy, affecting glass transition, yield, and failure under compressive and tensile loads. The Q7 population, a key vacancy-like motif, shows distinct responses during temperature increase, compressive and tensile loading.

Structural and thermodynamic characterization of deeply relaxed CuZr MG nanoparticles - insights from atomistic simulations: In this study, MD simulations were used to investigate the size-dependent properties of $Cu_{64}Zr_{36}$ MG nanoparticles (NPs) with sizes ranging from 1 to 20 nm. The NPs were generated by cooling molten systems at a relatively slow rate of 10^9 K/s. Results revealed that the NPs are coated with a Cu-rich layer, the thickness of which increases with NP

size. Various heating rates, from 10^{11} to 10^{13} K/s, were applied to determine the melting points of these NPs, showing a significant decrease in solidus temperature for NPs smaller than 10 nm. Additionally, as the NP size decreases, the fraction of Cu full icosahedra increases, indicating that smaller NPs are stronger and harder. These findings offer valuable insights into the design of heterogeneous metallic NG materials that exploit the size-dependent properties of MG NPs. These results were published in Physical Review Materials (3).

Harnessing Graph Convolutional Neural Networks for identification of aging states in metallic glasses: In this study, we harnessed Graph Convolutional Neural Networks (GCNNs) to analyze structural characteristics of CuZr MGs and identify their aging states. We used MD to simulate the quenching process of CuZr at cooling rates ranging from 10^{9} to 10^{15} K/s, producing six unique MG states. A dataset comprising 1,800 distinct samples was created for each state. We evaluated the effectiveness of various GCNNs, including Graph Attention Neural Network (GANN), Graph Sample and aggreGatE (GraphSAGE), Graph Isomorphism Network (GIN), and Relational Graph Convolutional Neural Network (RGCN). GANN and GraphSAGE demonstrated comparable performance, achieving an overall accuracy of 81% in classifying the MG states. The results underscored the potential of GCNNs to detect subtle structural variances in disordered materials and highlight the broader application of deep learning in analyzing MGs and other amorphous

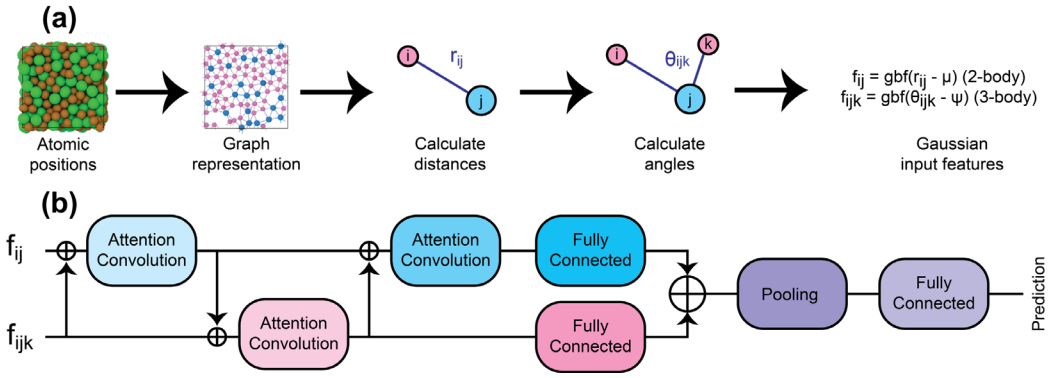

Fig. 3 Overview of Graph Neural Networks applied to atomic structures. (a) Method for transforming atomic coordinates into Gaussian basis function input features for neural networks. (b) Graph Attention Neural Network architecture showcasing the attention mechanism in convolution layers in addition to fully connected layers leading to the pooling and prediction stages.

materials. These results were published in Computational Materials Science (4).

Future Plans

The future goals of this research program focus on completing the development of GNGs models and advancing our understanding of their mechanical behavior. These goals are three-fold: i) Finalize the construction and characterization of seamless GNG models generated from glassy nanoparticles, with a focus on the GGI network and excess free volume; ii) Investigate the intrinsic properties of these GNG models, including their potential energy landscape, activation energies, and mass transport characteristics; iii) Evaluate the mechanical behavior of GNGs under various loading conditions, such as tensile and compressive simulations, to understand their Young's

modulus, yield strengths, and deformation mechanisms. The research is planned to follow four specific aims, each critical to deepening our understanding of GNGs: 1) Complete the construction and thorough characterization of realistic GNG models, ensuring accurate representation of microstructural features; 2) Study the potential energy landscape at GGIs and their influence on the mechanical behavior of GNGs, particularly in relation to grain size dependency; 3) Perform comprehensive MD simulations under different loading conditions to assess mechanical properties and deformation profiles; 4) Analyze the deformation behavior in GNGs and compare it with that of gradient nanostructured metals, gradient MGs, and theoretical predictions, aiming to identify key atomistic mechanisms that drive strength and ductility in these advanced materials. In addition to the planned tasks, we will continue to explore additional programmatically related topics as they arise, further expanding the knowledge base and ensuring comprehensive coverage of the

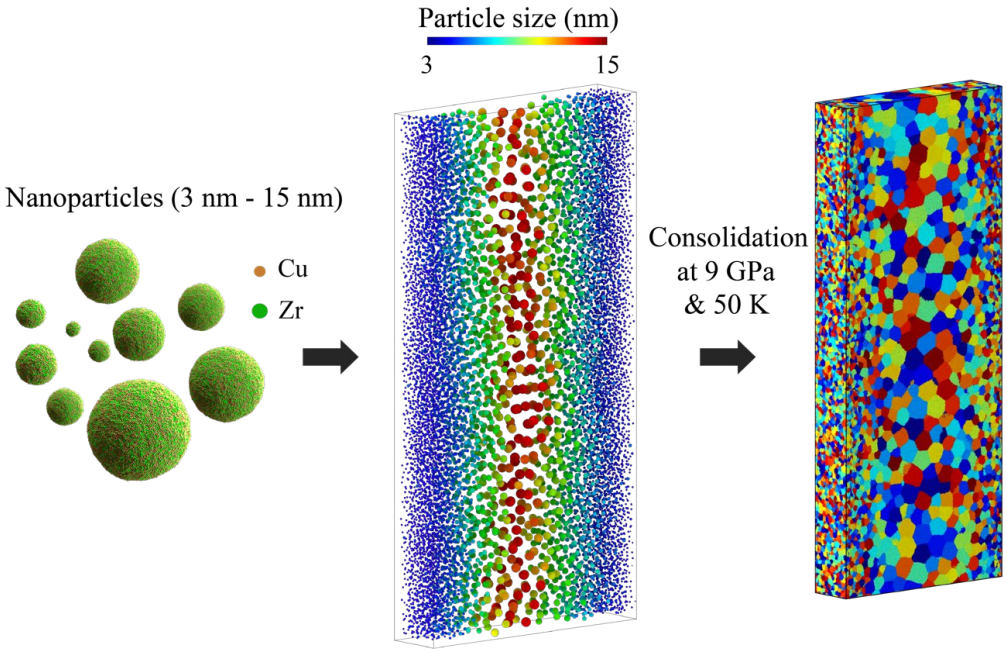

Fig. 4 Synthesis of a double gradient GNG using nanoparticles of sizes ranging from 3 nm to 15 nm, consolidated at 9 GPa and 50 K. Colors in the last figure indicate distinct glassy grains.

mechanical properties of GNGs.

References

1. Suyue Yuan, P. S. Branicio, *Atomistic simulations of nanoindentation on nanoglasses: Effects of grain size and gradient microstructure on the mechanical properties*, Intermetallics, **153**, 107782 (2023).
2. Suyue Yuan, Aoyan Liang, Chang Liu, Aiichiro Nakano, Ken-ichi Nomura, Paulo S. Branicio, *Uncovering metallic glasses hidden vacancy-like motifs using machine learning*, Materials & Design, **233**, 112185 (2023).
3. Xuezhen Ren, Suyue Yuan, Emily J. Gurniak, and Paulo S. Branicio, *Structural and thermodynamic characterization of CuZr metallic glass nanoparticles: Insights from atomistic simulations*, Physical Review Materials **8**, 046001 (2024).

4. Emily J. Gurniak, Suyue Yuan, Xuezhen Ren, Paulo S. Branicio, *Harnessing graph convolutional neural networks for identification of glassy states in metallic glasses*, Computational Materials Science **244**, 113257 (2024).

Publications

1. Suyue Yuan, P. S. Branicio, *Atomistic simulations of nanoindentation on nanoglasses: Effects of grain size and gradient microstructure on the mechanical properties*, Intermetallics, **153**, 107782 (2023).
2. Suyue Yuan, Aoyan Liang, Chang Liu, Aiichiro Nakano, Ken-ichi Nomura, Paulo S. Branicio, *Uncovering metallic glasses hidden vacancy-like motifs using machine learning*, Materials & Design, **233**, 112185 (2023).
3. Shan Li, Yue Yu, Paulo S. Branicio, Zhen-Dong Sha, *Effects of rejuvenation modes on the microstructures and mechanical properties of metallic glasses*, Materials Today Communications, **36**, 106493 (2023).
4. Hong Li, Jia-Cheng Zhang, Paulo S. Branicio, and Zhen-Dong Sha, *Composition-dependent fracture energy in metallic glasses*, Physical Review Materials, **7**, 035602 (2023).
5. Xuezhen Ren, Suyue Yuan, Emily J. Gurniak, and Paulo S. Branicio, *Structural and thermodynamic characterization of CuZr metallic glass nanoparticles: Insights from atomistic simulations*, Physical Review Materials **8**, 046001 (2024).
6. Emily J. Gurniak, Suyue Yuan, Xuezhen Ren, Paulo S. Branicio, *Harnessing graph convolutional neural networks for identification of glassy states in metallic glasses*, Computational Materials Science **244**, 113257 (2024).

Beyond Shear: Improving the Prediction of Plastic Deformation Activation in HCP Materials

Ashley Bucsek (University of Michigan), Huseyin Sehitoglu, (University of Illinois at Urbana-Champaign)

Keywords: plastic deformation, hcp materials, titanium, non-Schmid behavior, x-ray microscopy

Research Scope

The advancement of lightweight structural metals remains one of the greatest potential contributions of the materials community to a more energy-efficient future. Many lightweight metals with hexagonal close-packed (hcp) crystal structures require improvements to ductility and formability while maintaining strength. Tuning the critical activation energies associated with plastic deformation (i.e., slip versus twinning) is a forward-looking methodology for making these improvements, but there is a fundamental gap in our ability to predict the activation of plastic deformation in hcp materials. Our goal is to improve the prediction of the onset of plastic deformation in hcp materials by studying the sensitivities of slip and twin activation to the local, three-dimensional (3D) stress state.

Slip and twinning activation is predicted using a critical resolved shear stress (CRSS) criterion that states that a specific deformation mode will initiate when its unique CRSS value is exceeded: This is known as *Schmid's law*. Although Schmid's law was originally derived for face-centered cubic (fcc) materials, today, Schmid's law is applied across all crystallographic structures. For hcp materials, reports showing a breakdown of Schmid's law called *non-Schmid behavior* are prolific. In addition to microscale explanations for non-Schmid behavior (e.g., grain-grain interactions), research has shown that the 3D, anisotropic atomic configurations involved with slip in non-fcc materials can lead to sensitivities to the full 3D stress state (i.e., beyond the resolved shear stress). We hypothesize that accounting for these sensitivities can improve the prediction of plastic deformation in hcp materials. We present an integrated theoretical-experimental approach to understanding the energetics associated with plastic deformation activation in hcp materials by connecting the atomic-scale origins of non-Schmid behavior to microscale crystal plasticity.

Recent Progress

Toward these goals, we have made significant progress computationally investigating non-Schmid slip behavior in hcp titanium (Ti), and are more than halfway through an experimental validation portfolio that incorporates nanoscale to microscale characterization. This includes investigating the energy barriers and non-planar core structure of slip dislocations under the influence of non-Schmid stress components, ab-initio CRSS calculations for the basal, prismatic, and pyramidal slip planes in Ti and Ti-6.6Al at 0K and 300K, and experimental validation of the

CRSS calculations using in-situ transmission electron microscopy (TEM) under tension, micropillar picoindenter compression testing, and in-situ point-focused high-energy diffraction microscopy (pf-HEDM) experiments at the Advanced Photon Source (APS) and the European Synchrotron Radiation Facility (ESRF). Thus far, the CRSS calculations—which do not require any fitting or calibration parameters—have shown remarkable agreement with both literature and new experimental validations.

Room temperature CRSS values for the basal, prismatic, and pyramidal slip planes were calculated using density functional theory (DFT), molecular dynamics (MD), and anisotropic elasticity. The inputs required for these calculations are generalized stacking fault energy (GSFE) curves for all the slip systems (obtained using DFT), temperature effects (obtained using ab-initio MD), and elastic constants. Distinctively, this theory considers a Wigner-Seitz based cell for calculations of core energies, which deviates from previous treatments in the Peierls-Nabarro (PN) formalism that assume a simple-cubic cell. This approach was used to quantify the CRSS values, including tension-compression asymmetry (see **Table 1** for predictions at 0K and comparisons [1,2]), as well as the errors associated with the simple-cubic approximation. The dislocation core structures—which are *distorted* in hcp materials—can be obtained directly from the symmetry (or, in the case of hcp materials, the *asymmetry*) of the GSFE curves. The dislocation core structures are obtained for each slip plane, showing significant distortion of the disregistry profile. Without accounting for this distortion, the CRSS calculations have errors up to ~40%. This distortion is also responsible for the significant tension-compression asymmetry in slip resistance for certain slip systems (i.e., the ones with asymmetric restoring force profiles). The results explain why certain slip systems are favored over others.

Critically, the above calculations do not require any empirical constants, and so the experimental validation summarized in **Table 1** and **Fig. 1** and discussed below was completely independent. We find that experimental CRSS values show good agreement with the calculated

Table 1. Predicted CRSS levels from the present theory and comparison against the original PN model, experimental measurements of CRSS in this study and comparison with the literature [1−3]. (CRSS units: MPa)

	Basal $\langle a \rangle$	Prism $\langle a \rangle$	Pyr $\langle a \rangle$	Pyr $\langle c+a \rangle$
0K (Theory – This study)	942	161	539	1,274
0K (Theory – PN model)	544	2,115	35,900	9,260
Compression-to-tension ratio (Theory – This study)	1.0	1.0	1.8	1.1
300K (Theory – This study)	75	37	188	331
300K (Expt. – Literature*)	82	30−40	160	474
300K (Expt. – This study)	72^{+}, 75^{++}	46^{+}, 43**	--⌘	--⌘

*Refs. (See [1,2] for full reference list.)
**In-situ TEM measurement in this study [3].
$^{+}$Microscale (intragranular) pf-HEDM measurement in this study [3,4].
$^{++}$Microscale (grain-averaged) ff-HEDM measurement in this study [4].

⌘Will be included in the next annual reporting period.

values. Note that the experimental data at different temperatures includes both literature and new UM/UIUC measurements [2−4].

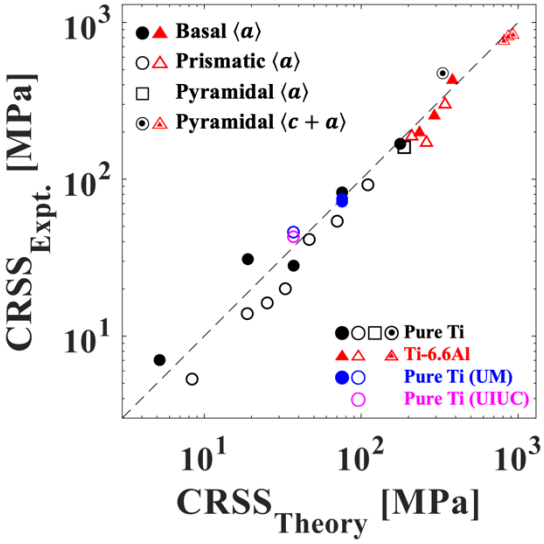

Fig. 1. Comparison of theory and experiment (from this work and literature) for Ti and Ti-6.6Al over a wide temperature range [2].

On the nanoscale, we are using in-situ TEM tension testing (**Fig. 2**) and in-situ micropillar compression testing (ongoing). In-situ TEM experiments on Ti single crystals resulted in a prismatic CRSS of 43 MPa (our theory predicted 37 MPa) [3]. On the microscale, we are using both *grain-averaged* stress evolution measurements and *intragranular* measurements. For grain-averaged CRSS validation, we performed in-situ far-field high-energy diffraction microscopy (ff-HEDM) tension testing (compression currently underway) and measured CRSS using the maximum and subsequent saturation RSS values for each slip system. In-situ ff-HEDM experiments on polycrystalline Ti resulted in a basal CRSS of 75 MPa (our theory predicted 75 MPa) [3]. For intragranular CRSS validation, we are continuing the development of the pf-HEDM technique (**Fig. 3**). These efforts are discussed more in the next paragraph. In-situ pf-HEDM experiments on polycrystalline Ti resulted in a basal CRSS of 77 MPa and a prismatic CRSS of 46 MPa (our theory predicted 75 MPa and 37 MPa, respectively) [4].

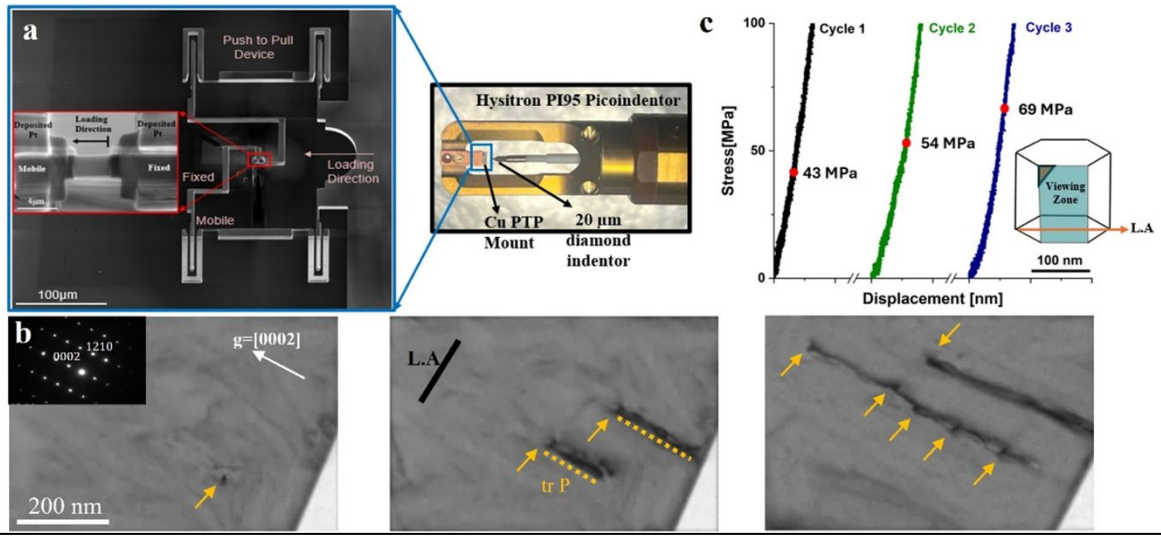

Fig. 2. In-situ TEM: (a) A push-to-pull (PTP) device to apply tension during picoindentation testing. (b) Snapshots before and after prismatic glide. Yellow arrows point to dislocations, and yellow dots show prismatic trace. (c) Stress-displacement curves for three cycles. The prismatic glide starts around 43 MPa, and the glide stress increases to 54 MPa and 69 MPa for cycles 2 and 3, respectively [3].

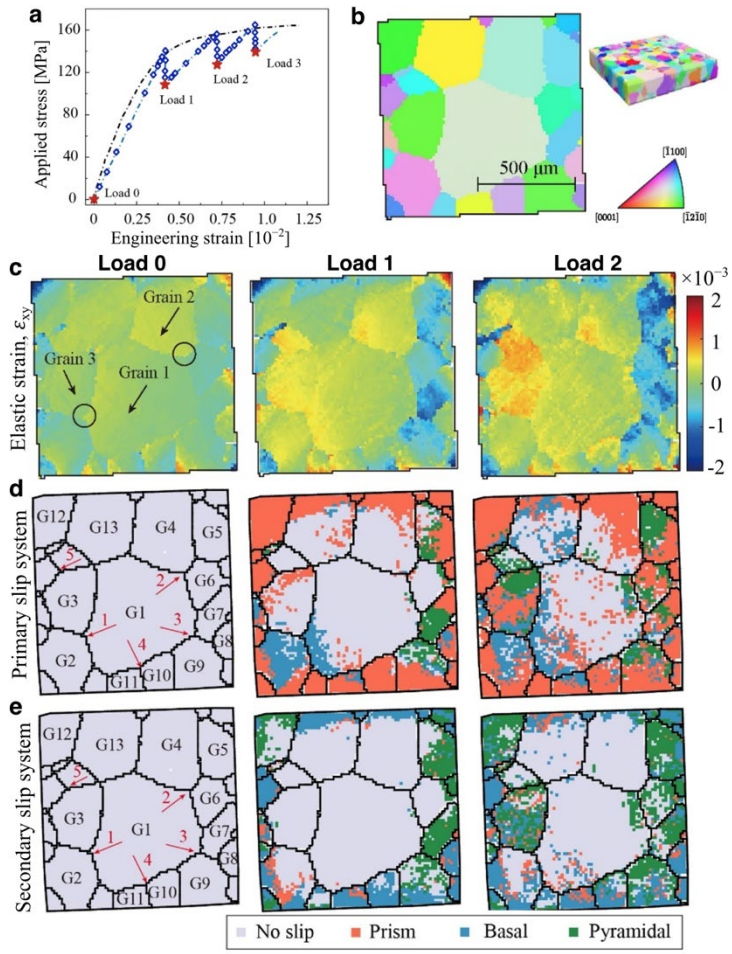

Fig. 3. In-situ pf-HEDM: (a) Macroscopic stress-strain curve; (b) Orientation map of the measured region; (c) Evolution of the elastic strain tensor (the ε_{xy} component is shown here), used to measure the intragranular CRSS of each slip system and the activation of the (d) primary and (e) secondary slip systems [4].

The development of the pf-HEDM technique has potential broad impact on a diversity of materials science and mechanics communities. During the first reporting period, we conducted the first-ever pf-HEDM experiments at the APS. These (ex-situ) measurements, conducted on plastically-deformed Ti with 15 μm spatial resolution, demonstrated the effectiveness of pf-HEDM for measurements on even severely plastically-deformed materials and were used to develop pf-HEDM analysis procedures [5]. During the second reporting period, we conducted the first in-situ pf-HEDM experiment at the APS on Ti under tension (**Fig. 3**) [4]. The evolution of the local elastic strain tensor and orientation are mapped with subgrain spatial resolution. Like with ff-HEDM, the CRSS values are measured using the maximum and subsequent saturation RSS values for each slip system—but this time on an *intragranular* basis vs. grain-averaged. The intragranular CRSS values (**Table 1**, **Fig. 1**) were subsequently used to map slip activities (**Fig. 3d**,**e**) and plastic shear strain using a crystal kinematics model [4].

Future Plans

Extending our efforts to Ti-6.6Al, which requires a consideration of the short-range order (SRO), we will study the tension-compression asymmetry and the temperature dependence of CRSS with theory and experiments. We will conduct in-situ TEM experiments and micropillar compression testing to pinpoint the activation of slip to validate the theory. Electron diffraction will be used to investigate if the predicted changes in SRO agree with the experiments. Finally, we will also be extending our model and experimental procedures to the case of deformation twinning and cross-slip. Regarding pf-HEDM, we will continue to use this unique tool to validate the theory at the microscale and, more generally, push the capabilities of pf-HEDM itself. This includes new

in-situ pf-HEDM experiments performed on the European Synchrotron Radiation Facility (ESRF) with 250 nm spatial resolution and the development of the new 20-ID HEXM beamline at the APS, which will also have 100−200 nm spatial resolution capabilities.

References/Publications

[1] O.K. Celebi, G. Gengor, D. You, A.S.K. Mohammed, A. Bucsek, H. Sehitoglu, Distorted dislocation cores and asymmetric glide resistances in titanium, Acta Materialia 274 (2024) 119967.

[2] D. You, O. Celebi, A. Mohammed, A. Bucsek, H. Sehitoglu, The Derivation of CRSS in pure Ti and Ti-Al Alloys, International Journal of Plasticity (submitted).

[3] T. Celebi, O. Celebi, A. Mohammed, A. Bucsek, H. Sehitoglu, Exploring Glide and Cross-slip Stresses in Titanium: Theory and Experiments, (in prep.).

[4] W. Li, H. Sharma, P. Kenesei, J.S. Park, S. Ravi, O. Celebi, D. You, T. Celebi, H. Sehitoglu, A. Bucsek, Intragranular measurement of slip system strength and activity in polycrystalline titanium using point-focused high-energy diffraction microscopy, (in prep.).

[5] W. Li, H. Sharma, P. Kenesei, S. Ravi, H. Sehitoglu, A. Bucsek, Resolving intragranular stress fields in plastically deformed titanium using point-focused high-energy diffraction microscopy, Journal of Materials Research (2023) 1–14.

Elucidating the influence of bulk slip morphology on hydrogen environment-assisted cracking behavior in precipitation-hardened alloys

James T. Burns, University of Virginia

Keywords: Environmental cracking, nickel, dislocation, H-embrittlement, crack tip

Research Scope

The overarching objective of the proposed research is to elucidate the mechanistic influence of bulk slip morphology on the HEAC behavior of a model precipitation-hardened alloy by coupling high-fidelity fracture mechanics testing methods with a state-of-the-art multiscale characterization strategy. The following specific research questions will be addressed. First, for a constant global mechanical driving force (*e.g.,* stress intensity factor), grain size, grain orientation, and hydrogen uptake behavior, do differences in bulk slip morphology result in quantitatively different (both spatially and in intensity) near-crack plastic deformation distributions during HEAC? Addressing this question will rigorously establish the causal role of bulk slip morphology on HEAC susceptibility by controlling possible obfuscating factors. Second, how does the observed deformation distributions proximate to the crack at a constant stress intensity factor vary as a function of grain orientation and environmental severity (*e.g.*, hydrogen uptake behavior) for a given bulk slip morphology? Addressing this question will establish the sensitivity of observed deformation distributions for a given bulk slip morphology to two expected modifying influences. This will provide insights into (1) the mechanistic contribution of H content on crack propagation and (2) the impact of grain orientation on the deformation responsible for crack propagation. Third, differences in bulk slip morphology impact the deformation distribution *in front* of the crack tip for a constant applied stress intensity factor and hydrogen uptake behavior? Any observed variations in deformation distribution and grain boundary-deformation interactions proximate to the crack tip can provide a mechanistic pathway to understand *how* bulk slip morphology may induce differences in HEAC propagation metrics for a constant stress intensity factor and H uptake behavior.

During the last reporting period efforts have focused on the following. First, identifying targeted heat-treatment protocols for a model Ni-Cu system to achieve a grain size of 75-100 μm and non-aged, under-aged, peak-aged, over-aged (at the same strength level as under-aged), and highly over-aged. Second, to characterize the precipitate size/distribution and bulk slip morphology associated with each thermal treatment. Third, to complete fracture mechanics specimen design and initiate the linear elastic fracture mechanics (LEFM) environment assisted cracking testing. Fourth, to optimize the sample preparation process for the multi-scale characterization process.

Recent Progress

Obtaining a consistent and moderate grain size of 75-100 μm is desired to assist in the clarity of the characterization results. Based on literature findings and a sensitivity study over the past year, a 1323K thermal treatment was performed for 12 h to achieve this goal. The results of effect of annealing duration on the grain size and an example CBS image is shown in Figure 1. Additionally, an aging study (first using hardness then tensile testing) was conducted at 923K to

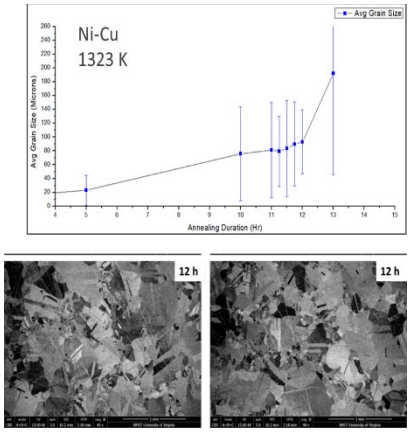

Figure 1: Grain size versus annealing time at 1323K for Ni-Cu and CBS images of the grain structure at 12 h.

identify targeted aging times then to achieve the desired strengths, thus precipitate morphologies that will lead to the various slip morphologies. The results in Table 1 illustrate the selected aging treatments to achieve the desired strength levels. Then 3mm disks were punched from the necked region of the gauge section (after global deformation to 2% plastic strain) to enable TEM analysis of the precipitate character and the bulk slip morphology. The quantitative results of the precipitate analysis are shown in Table 2, where the mean precipitate size and overall area fraction increased with increasing aging time. The results of the TEM analysis of the bulk slip morphology are also summarized in Table 2; these results indicate the expected behavior for under-aged and over-aged conditions. This is illustrated in Figure 2, where TEM images of the under-aged (taken along the [001] zone axis) demonstrate clear pile-up features that are indicative of planar slip whereas the over-aged conditions (taken along the [110] zone axis) shows clear signs of dislocation bowing that are indicative of a homogenized/wavy slip morphology.

Table 1: The selected aging protocols and corresponding yield strength values.

Measured Mechanical Properties

Specimen ID	Aging Time	Elastic limit (Mpa)	E (GPa)	Yeild Strength (MPa)
NA	0	138	157.4	181
UA	8	394	186.1	481
PA	17	469	188	540
OA	37	409	181.3	495
HOA	66	398	180.4	465

The sample design and machining of the EAC LEFM fracture samples has been completed for each of the aging conditions. The initial testing has focused on (1) establishing the plasticity induced resolution limit for each of the samples using inert dry nitrogen testing, (2) performing rising K (dK/dt) testing in 0.6 M NaCl at electrochemical potentials of -900 and -1000 mVsce to establish the baseline crack growth kinetics and sensitivities of the materials and enable initial comparative characterization to begin. LEFM testing begun on 12 July 2024 and 10 tests are complete or underway. A representative result is shown in Figure 3 for the peak-aged condition tested in 0.6M NaCl at -900 mVsce polarization at 0.33 MPa$\sqrt{m}$/hr loading rate. These results are

Table 2: Results of TEM precipitate analysis of size/distribution and slip morphology analysis.

Aging Condition	**Average Precipitate Radius (nm)**	**Radius Std. Dev. (nm)**	Average Precipitate Area (nm^2)	Precipitate Area Fraction (%)	**Dislocation Morphology**
Non-Aged	-	-	-	-	**Planar & Wavy**
Under-Aged	**6.25**	**2.76**	122.67	0.07	**Planar**
Peak-Aged	**7.18**	**3.72**	128.00	0.089	**Planar**
Over-Aged	**10.08**	**4.58**	319.57	0.18	**Wavy**
Highly Over-Aged	**12.43**	**4.88**	486.06	0.36	**Wavy**

aligned with prior results from similar materials and environments (Monel K-500), which provides confidence in the current design and experimental set-up.

Significant efforts were completed during this reporting effort on optimizing the sample preparation procedure on a related alloy for the crack wake analysis portion of the characterization. Ar-based ion milling of the samples were used to section the samples through the mid-thickness of the fracture surface. Subsequently fractography and registration of the dcPD data to identify the crack length regions correlated to a given K value. EBSD of the cross-sections then enabled identification of the grain orientation so that to enable isolation of this variable. These EBSD scans then enabled KAM mapping to get a first order description of the level of local plasticity and also serve as the basis for an OpenXY analysis to calculate the geometrically necessary dislocation density. At each of these cases the FIB extraction protocol has been established and TEM analysis is ongoing for a higher fidelity local analysis. This work was completed on two different commercially available lots of Monel K-500 and demonstrated that different measured LEFM based growth rates correspond to clear differences in the local plastic damage behavior characterized by the GND maps. Critically, this analysis demonstrates that an optimized sample preparation protocol has been established and is enable to evaluate the hypotheses put forth in the current program.

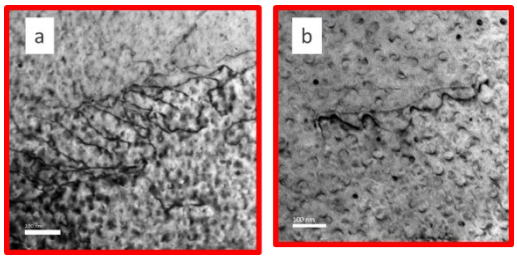

Figure 2: TEM images of the under-aged (a) and over-aged (b) Ni-Cu alloy demonstrating the expected differences in slip morphology.

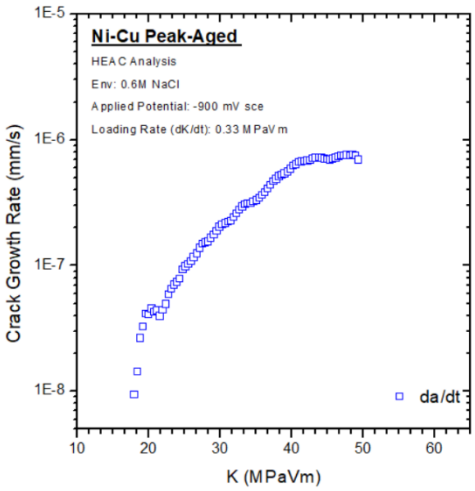

Figure 3: Crack growth rate versus K relationships for the peak-aged condition.

Future Plans

The plan for the next year of the program is to focus on generation of the LEFM based growth rate data with a focus on a sub-set of testing for each aging condition and two environments (-900 and -1000 mV sce). Once complete the characterization protocol will be implemented in a staged manner, beginning with examining the constant yield strength under-aged and over-aged conditions.

Publications

1. Z.D. Harris, A.W. Thompson, J. Smith, R. Jayamohan, J.T. Burns, *Influence of grain boundary sulfur, local hydrostatic stress, and precipitate character on heat-to-heat variations in hydrogen environment-assisted cracking of Monel K-500*, Corrosion Journal, **In-review**.

The Role of Local Chemical Order on Defect Kinetics in Alloys under Irradiation

Penghui Cao, University of California, Irvine

Keywords: Defect kinetics; Vacancy; Dislocation; Diffusion; Irradiation effect

Research Scope

High-energy particle irradiation often has detrimental effects on materials, but in certain cases, it can be beneficial. For example, it orients high-density magnetic alloys by promoting chemical order. The phenomenon of radiation-induced ordering first postulated and demonstrated by Averbach over half a century ago (1), has been frequently observed in binary alloys (2). Multi-principal element alloys (MPEAs), which include medium- and high-entropy alloys with multiple principal elements in high concentration, are typically presumed to be random solid solutions that maximize configurational entropy. However, ideal random mixing in MPEAs may only be achievable at elevated temperatures. As temperatures decrease, the enthalpic contribution to the total free energy may dominate, leading to local chemical ordering. The emergence of chemical short-range order, whether due to material processing or irradiation, can play a vital role in radiation defect kinetics and material radiation tolerance.

This research project aims to understand the role of local chemical order on the kinetics of defects in MPEAs and to evaluate the mechanistic strategy for controlling radiation defects migration and evolution through tailoring local ordering at the nanoscale. The research focuses on single-phase MPEAs and addresses the questions regarding local ordering: (i) how does the local chemical order influence defect migration, coalescence, and growth; (ii) what are the new atomistic mechanisms and processes enabled by local order that could lead to radiation damage reduction; and (iii) is tuning the degree of local ordering able to promote defect recombination and to alleviate radiation-induced damage accumulation?

Specifically, research activities are driven by three mechanistic hypotheses pertaining to the role of local ordering on point defects, defect cluster, and interface: (1) the presence of local chemical order raises migration energy barriers of point defects and localizes their diffusion; a localized diffusion can promote defects recombination and mitigate defect cluster growth; (2) local chemical order roughens the potential energy landscape, which can locally pin a dislocation loop and reduce its diffusivity; and (3) the introduced local ordering in the grain matrix increases grain boundary migration energy and lowers its mobility. These hypotheses will be evaluated by integrated theoretical and computational techniques, including molecular dynamics, kinetic Monte Carlo, accelerated molecular dynamics, climbing image nudged elastic band method, and machine learning models. The modeling and theoretical predictions will be validated by targeted experiments, including energy-dispersive x-ray spectroscopy characterization and in-situ ion irradiation. Evaluation of these hypotheses will advance the fundamental understanding of atomistic mechanisms underlying the extraordinary properties of MPEAs, facilitate material

design strategies to manipulate defect behaviors via tailoring nanoscale features and result in tunable material properties.

Recent Progress

The major progresses of the project in the past two years pertain to evaluating hypotheses 1 and 2, and advancing the fundamental understanding of vacancy and dislocation kinetics behaviors in concentrated solid solutions and the role of local chemical order.

<u>Progress 1: Revealed the crucial role of vacancy diffusion correlation and diffusion barrier spectrum in concentrated alloys</u>

This study focuses on the essential question about how chemical complexity affects vacancy diffusion and what unique characteristics, if any, set concentrated alloys apart from traditional metals. By studying vacancy diffusion in NbMoTa alloy across a broad temperature range from 2600 to 800 K, we reveal that, unlike pure metals, the two key diffusion parameters (diffusion correlation factor and activation energy) are not constant in alloys, but instead substantially decrease with decreasing temperature. This temperature dependence arises from a reduced number of active jump pathways at lower temperatures, leading to more correlated vacancy jumps (*Figure 1*). Compared to traditional metals, the diffusion correlation factor can be two orders of magnitude lower, which is believed to be the primary reason for the observed slow vacancy diffusion in concentrated alloys. Finally, we find that the vacancy diffusion

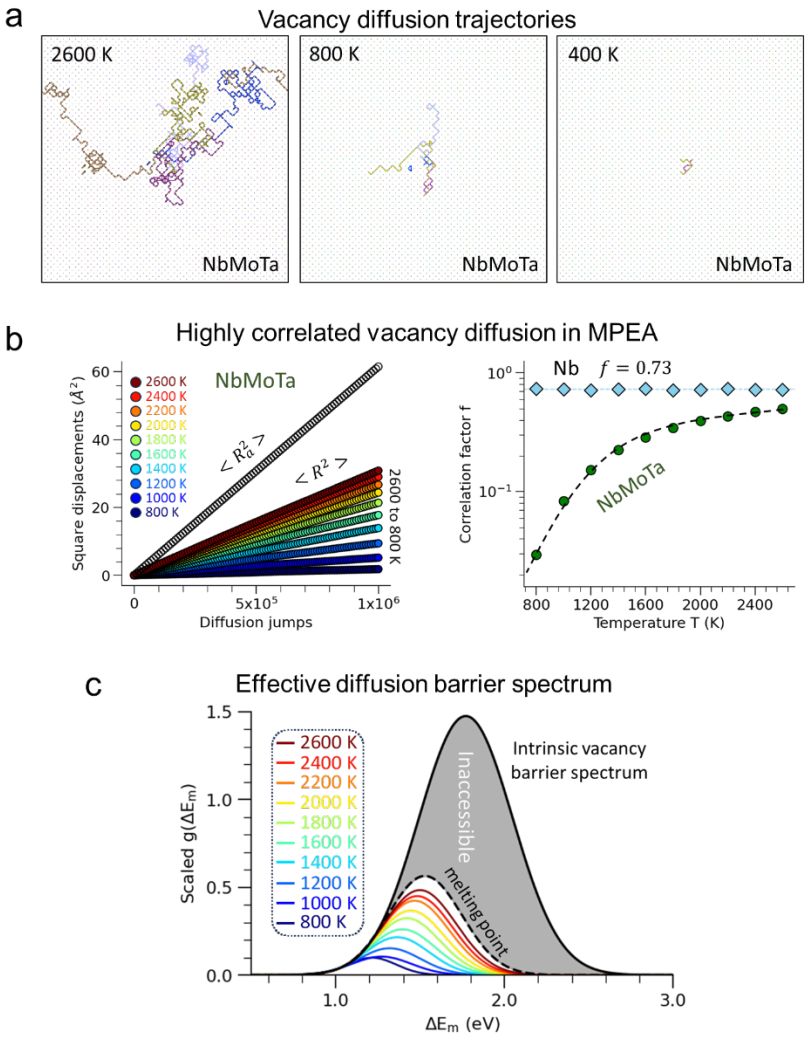

Figure 1. Vacancy diffusion barrier spectrum and diffusion correlation in multicomponent alloys. (a) The recorded diffusion trajectories of five individual vacancies at 2600, 800, and 400 K after 400 atom jumps. (b) Vacancy diffusion correlation factor in Nb and NbMoTa. (c) The effective diffusion barrier spectrum at different temperatures.

rate drops noticeably in the presence of local chemical order in the NbMoTa system, particularly for MoTa alloys with long-range B2 order.

Progress 2: The ubiquitous chemical short-range order in MPEAs enabled by swift ion diffusion during solidification

Extensive research has been directed towards tailoring SRO through thermal processing and ageing to modify material properties. However, recent experiments show that quenched and aged materials exhibit nearly identical strength, leading to an ongoing debate about the role of SRO. Our atomistic simulations have uncovered that a prevalent degree of SRO forms during solidification at the liquid-solid interface, even at extremely fast cooling rates. This phenomenon stems from the rapid atomic diffusion in the supercooled liquid, which matches or even surpasses the rate of solidification. Consequently, SRO is an inherent characteristic of most face-centered-cubic (fcc) MPEAs, insensitive to variations in cooling rates and even annealing treatments. *Figure 2* illustrates the kinetics of SRO formation at the solidification front. Unlike in dilute alloys where local ordering or precipitation necessitates long-range diffusion, local diffusion in concentrated solid solutions in MPEAs is sufficient to build a large degree of SRO.

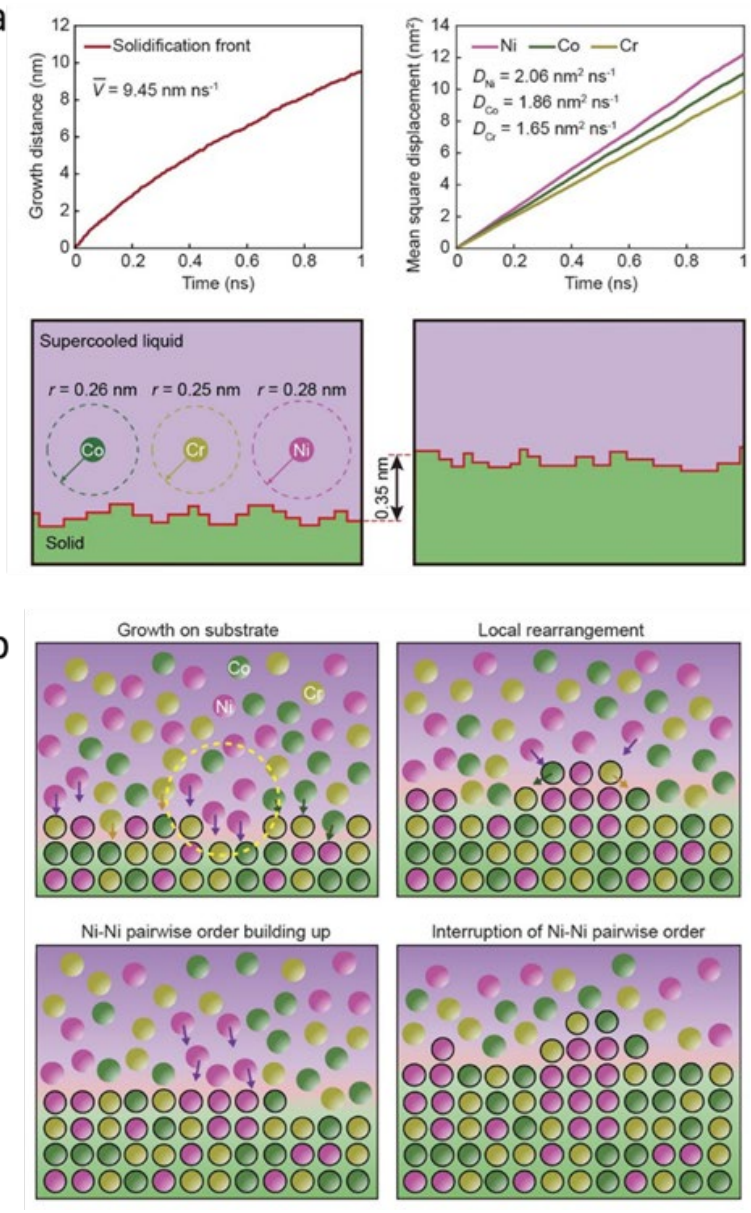

Figure 2. Rapid formation mechanism of SRO at the solid-liquid interface. (a) Ion diffusion in the supercooled liquid matches or even surpasses the rate of solidification. (b) SRO formation mechanism and the suppression of long-range chemical order during solidification.

Progress 3: Understood the dislocation barrier spectrum and its influence on dislocation motion mechanism

We introduced a neural network model that captures the chemistry and structure of screw dislocations, enabling accurate and efficient prediction of the Peierls barriers in multi-component space. Using this neural network, we construct a barrier diagram across the entire ternary space of refractory Nb-Mo-Ta alloys, from which the compositions with high or low barriers can be quickly identified. Different from the traditional understanding, we discover that the NbMo binary alloy can have a higher barrier than NbMoTa ternary system, suggesting chemical complexity is not the predominant factor governing dislocation barrier. Atomistic simulations reveal that a higher mean barrier slows down dislocation mobility, while a broader distribution of barriers facilitates kink pair nucleation, altering the rate-limiting process from kink pair nucleation to kink glide and cross kinking.

Future Plans

As we move forward, our focus will be on evaluating the remaining aspects of Hypotheses. Our primary objective in the near future is to demonstrate the mechanisms of chemical trapping of vacancy and the suppression of void growth under irradiation.

Trapping vacancy and suppressing void formation in irradiated alloys: Vacancy diffusion is a critical factor in the growth of defect clusters and void formation in materials subjected to irradiation. Our goal is to show that the control and trapping of vacancies can be achieved through the tailoring chemical composition. In contrast to pure metals, where vacancies move through random lattice walks, vacancy diffusion in concentrated alloys is highly correlated. This correlation, driven by a reduced number of active jump pathways, leads to lower diffusivity and results in chemical trapping within a confined volume. By irradiating W-alloys, we aim to demonstrate that the growth of vacancy clusters can be effectively suppressed by chemical trapping effect.

References

1. C. R. Houska, B. L. Averbach, *Neutron Irradiation Effects in a Copper-Aluminum Alloy*. *J Appl Phys* **30**, 1525–1531 (1959).
2. N. P. Filippova, V. A. Shabashov, A. L. Nikolaev, *Mössbauer study of irradiation-accelerated short-range ordering in binary Fe-Cr alloys*. *Physics of Metals and Metallography* **90**, 145–152 (2000).

Publications

1. B. Xing, W. Zou, T.J. Rupert, P. Cao, *Vacancy diffusion barrier spectrum and diffusion correlation in multicomponent alloys*, Acta Materialia, **266**, 119653 (2024).
2. Y. Han, H. Chen, Y. Sun, J. Liu, S, Wei, B. Xie, M. Li, J. Yang, W. Chen, P. Cao, Y. Yang. *Ubiquitous short-range order in multi-principal element alloys*. Nature Communications, **15**, 6486 (2024)

3. X. Wang, L. Valdevit, P. Cao. *Neural network for predicting Peierls barrier spectrum and its influence on dislocation motion*. Acta Materialia **267**, 119696 (2024).
4. A. Abu-Odeh, B. Xing, P. Cao, B. P. Uberuaga, M. Asta. *A simple model for short-range ordering kinetics in multi-principal element alloys*, Scripta Materialia **252**, 116224 (2024).
5. D. Aksoy, P. Cao, J.R. Trelewicz, J.P. Wharry, T.J. Rupert, *Enhanced radiation damage tolerance of amorphous interphase and grain boundary complexions in Cu-Ta*. JOM **76**, 2870–2883 (2024).
6. I.J. Beyerlein, P. Cao, T.M. Pollock, *Complex concentrated alloys and chemical short-range ordering*, MRS Bulletin **48**, 746–752 (2023).
7. X. Zhou, X. Wang, L. Fey, S. He, I.J. Beyerlein, P. Cao, J. Marian, *Models of dislocation glide and strengthening mechanisms in bcc complex concentrated alloys*, MRS Bulletin **48**, 777–789 (2023).
8. P. Cao, *Maximum strength and dislocation patterning in multi–principal element alloys*, Science Advances **8**, eabq7433 (2022).
9. Z. Fan, B. Xing, P. Cao, *Predicting path-dependent diffusion barrier spectra in vast compositional space of multi-principal element alloys via convolutional neural network*s, Acta Materialia **237**, 118159 (2022).
10. X. Wang, F. Marescac, P. Cao, *The hierarchical potential energy landscape of screw dislocation motion in refractory high-entropy alloys*, Acta Materialia **234**, 118022 (2022).

Deformation Twinning Networks in Metals with Hexagonal Close-Packed Crystal Symmetry

PI: Laurent Capolungo
Materials Science and Technology Division, Los Alamos National Laboratory

Keywords: Deformation twinning, twin networks, plasticity, hexagonal close-packed

Research Scope

Deformation twins play a key role in accommodating strain during plastic deformation in hexagonal close-packed (hcp) metals and their alloys. The typical deformed microstructure in hcp polycrystals corresponds to a relatively complex and interconnected 3D twin network. The nature of the twin network and its potential role on plastic flow remains unclear. This epistemic gap is critical as twinning plays a dual role on plasticity. On the one hand, it provides a path for plastic flow to proceed; thereby potentially improving strength and ductility. On the other hand, the formation, growth, and interactions of 3D twin domains (leading to the formation of twin networks) can lead to a significant buildup of internal strain energy and incompatibilities in the system, potentially facilitating materials failure. Unraveling the interplay between these simultaneous and competing effects has strong implications for optimizing the performance of these materials under service conditions. To this end, we study the full 3D character of deformation twins and their associated networks, using a combination of experiments, models, and theory.

Recent Progress

To study the morphology of twin networks, we have introduced a 3D-electron backscatter diffraction (3D-EBSD) characterization approach combined with a graph theory-based code to reconstruct and analyze twin networks in 3D. Briefly, serial 2D-EBSD maps are first collected following serial sectioning using a plasma focused ion beam. The 2D-EBSD layers are then aligned via cross correlation of the collective 2D parent grain

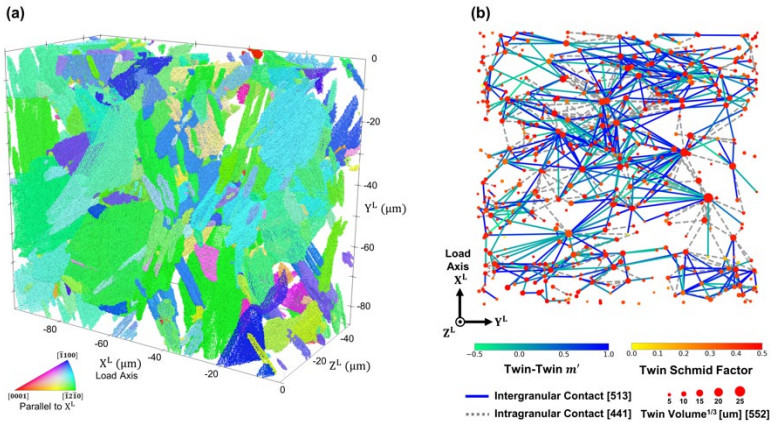

Figure 1. (a) Reconstructed 3D deformation twin network in high-purity Ti following cryogenic compression to 2.6% strain. The twins (552 total) are colored with respect to their crystal lattice direction parallel to the loading axis (X^L). (b) Graphical abstraction of twin network projected onto the $X^L - Y^L$ plane. Nodes are located at the twin centroids, with node size corresponding to twin volume and node color corresponding to twin nominal Schmid factor. Dashed edges represent intragranular twin contacts (441), and solid edges represent intergranular twin contacts (513) color mapped by the geometric compatibility (m') of the adjoining twins.

boundary traces from each layer, and the 3D microstructure is reconstructed using the Microstructural Evaluation Tool for Interface Statistics (METIS3D) framework [1]. Figure 1a shows a reconstructed 3D deformation twin network in high-purity Ti following cryogenic compression to 2.6% strain. The twins (552 total) are colored with respect to their crystal lattice direction parallel to the loading axis (X^L). A graphical abstraction of the twin network projected onto the X^L-Y^L plane is shown in Fig. 1b. The network displays a complex morphology with large 'hub' (comprising a high number of intergranular and intragranular connections) twins bridging between different highly interconnected twin regions throughout the microstructure. Overall, adjoining intergranular twin pairs, high order twin intersections (e.g. triple junctions of twins), and twin network hubs with over 15 separate intergranular and intragranular contacts are found to be salient morphological features of these networks. We note that these features of the twin network could not be unraveled with surface characterization methods.

The interfacial incompatibilities resulting from twin intersections at grain boundaries are subsequently analyzed through the lens of the geometrically necessary surface dislocation content necessary to accommodate the jump in the plastic distortion across contact zones [2]. Summarizing, it is observed that the induced incompatibility varies for different configurations of twins: (i) adjoining twin pairs, corresponding to twin transmission events, on average result in less incompatibility than individual non-transmitting twins, and (ii) twin branches and twin triple junctions, comprising three co-located twin contacts, generally display higher incompatibility than either twin pairs or individual twins. This suggests that, in the absence of elastic/plastic accommodation at the interface and/or in the surrounding grains, these zones could lead to localization of shear at the onset of necking or lead to initiation of intergranular damage during continued deformation. Critically, we reveal that the highest incompatibilities are expected to be found when two separate twin chains collide; such event had not been characterized thus far. Necessarily modeling efforts are necessary to assess how plasticity could accommodate these geometric incompatibilities. To this end, one needs to characterize and simulate micromechanical fields in twin networks.

As a first step, we investigated the energetic landscape associated with propagating twin tips using a novel combination of in-situ straining/strain mapping and phase field modeling. First, the short- and long-ranged mechanical fields around a $(0\bar{1}12)$ twin tip held under load were measured with high accuracy/resolution using patterned-probed four-dimensional scanning transmission electron microscopy. These fields were subsequently corroborated against the fields predicted via phase field modeling. This comparison demonstrated good agreement between the experimental and the modeling results, particularly in the context of the key characteristics of the mechanical fields, such as stress concentrations at facet junctions and the polarization of the twin resolved shear stress (TRSS) at the twin tip. Further scrutiny of the lattice rotation fields revealed that certain defect configurations (i.e., disclinations) at twin facet junctions can shield a significant portion of the distortion induced by the twin transformation, ultimately resulting in considerably smaller magnitudes of internal strain energy buildup than previously predicted. This elastic

shielding mechanism introduces a new paradigm and shifts our current understanding of the actual contribution of the local fields to twin propagation, interactions, and transmission. Among others, it shows that internal stresses and incompatibilities resulting from twinning can themselves be shielded by the twin interface itself.

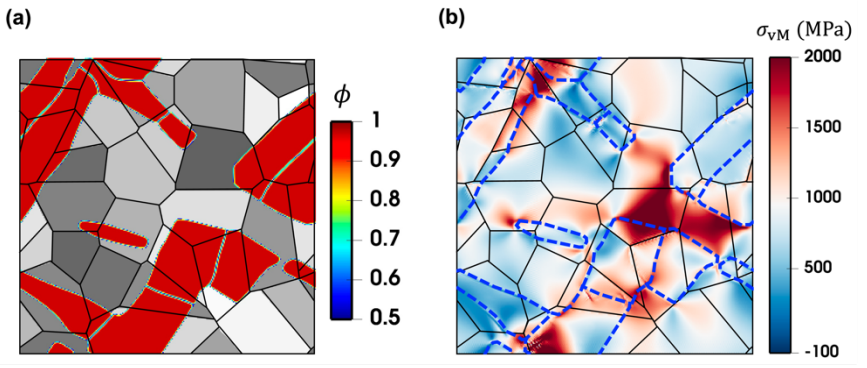

Figure 2. (a) Snapshot showing the deformation twin microstructure predicted by the multi-phase field-crystal plasticity framework at 190 ps. (b) Equivalent (von Mises) stress field map for the twin microstructure shown in (a). High magnitude stress zones are primarily observed in grains with interacting/terminating twins and around facet junctions. The positions of the twins are indicated via the dashed blue outlines.

To study the evolution of the twin network and rationalize the impact of plastic deformation on twinning, we have developed a multi-phase field-crystal plasticity (MPF-CP) framework to simulate the concomitant evolution of 3D twin domains (and consequently, twin microstructures/networks) and slip in polycrystalline representative volume elements with high numerical efficiency. Further, a model for the incorporation/transfer of dislocation densities between different phases (i.e., twin/matrix and twin/twin) is implemented, allowing the effects of slip-twin interactions to be captured effectively. A parametric investigation of twinning behaviors in Mg single crystals and polycrystals reveals that the interplay between plasticity and anisotropy in facet behaviors has a significant influence on the stress relaxation response, twin propagation/thickening kinetics, twin volume fraction evolution, and consequently, the overall morphology of the twin network. This is primarily attributed to the 3D twin domains evolving to conform to the intra-/inter-granular micromechanical fields, which are conditioned by plasticity and other twins. Further, incorporation of matrix dislocations is seen to have a negligible influence over twin evolution in the cases investigated here. Figure 2a shows a snapshot of the microstructure predicted in a twinned Mg polycrystal undergoing stress relaxation following loading. The twins are observed to be highly irregular, and the microstructure consists of multiple twins crossing grain boundaries and multiple contacts between active twins; this is consistent with 3D characterization of the network. Figure 2b shows the corresponding equivalent (von Mises) stress field, which is observed to be rather heterogeneous. Several zones or regions of high magnitude stresses (i.e., stress hotspots) are observed primarily in the vicinity of facet junctions. This indicates the important role these facet junctions are expected to play in modulating the local micromechanical landscape in twinned grains.

Future Plans

The analysis of twin networks following experimental characterization reveals that twins rapidly form a very dense network akin to a truss-like structure, inviting us to rethink cooperative evolution of the network. Accordingly, our future efforts will be focused on investigating how key attributes of twin networks (adjoining twin pairs, twin triple junctions, branches resulting from intersection between twin chains), and the intrinsic plastic responses of the parent grains/twins contribute to the buildup of incompatibilities and initiation of high shear localization.

To this end, we will be employing a combination of in-situ experiments and modeling. Specifically, in-situ mechanical testing, in conjunction with characterization techniques (high resolution digital image correlation, high energy diffraction microscopy, four-dimensional scanning transmission electron microscopy), will be used to understand the mechanical response of the different pre-deformed/annealed microstructures, assess the processes leading to shear localization (i.e., how plastic flow propagates through distinct twin networks), and identify features of interests in which localization is likely to begin. Following this, virtual experiments will be performed using the MPF-CP framework instantiated with microstructural configurations extracted from experiments. To rationalize the role of twin nucleation rates on shear localization, the MPF-CP will be extended to include nucleation events. The idea is to use atomistic simulations to derive temperature, stress, and composition specific heterogeneous nucleation laws for twins. The model will then be used to study how twin nucleation rates, twin expansion/growth rates, slip activity inside parent grains/twins, and compatibility of configurations collectively influence the efficiency of deformation twins in hexagonal close-packed materials, vis-à-vis the balance between dissipation and the build-up of internal strain energy/incompatibilities, over the entirety of the stress-strain response.

References

1. C. Pradalier, P.-A. Juan, R.J. McCabe, L. Capolungo, *A Graph Theory-Based Automated Twin Recognition Technique for Electron Backscatter Diffraction Analysis*, Integrating Materials and Manufacturing Innovation **7(1)**, 12-27 (2018).
2. C. Fressengeas, V. Taupin, M. Upadhyay, L. Capolungo, *Tangential continuity of elastic/plastic curvature and strain at interfaces*, International Journal of Solids and Structures **49(18)**, 2660-2667 (2012).

Publications

1. **H. T. Vo**, **D. Bamney**, **R. J. McCabe**, M. M. Schneider, **K. Dang**, M. Pettes, **C. N. Tomé**, and **L. Capolungo**, *Elastic shielding mediated by deformation twin facets in hexagonal close-packed metals*, Applied Materials Today **39**, 102265 (2024).
2. **M. A. Kumar**, T. Yu, Y. Wang, Z. Jianzhong, **R. J. McCabe**, **C. N. Tomé**, and **L. Capolungo**, *Effect of dislocation slip and deformation twinning on the high-pressure phase transformation in Zirconium*, Scripta Materialia **242**, 115941 (2024).
3. **D. Bamney** and **L. Capolungo**, *On the co-nucleation of adjoining twin pairs at grain boundaries in hexagonal close-packed materials*, Scripta Materialia **241**, 115882 (2024).

4. **H. T. Vo**, **P. Pinney**, M. M. Schneider, **M. A. Kumar**, **R. J. McCabe**, **C. N. Tomé**, and **L. Capolungo**, *Automated characterization and classification of 3D microstructures: an application to 3D deformation twin networks in titanium*, Materials Today Advances **20**, 100425 (2023).
5. **D. Bamney** and **L. Capolungo**, *Assessing the predictive capabilities of precipitation strengthening models for deformation twinning in Mg alloys using phase-field simulations*, Journal of Magnesium and Alloys **no. 12**, 4525-4541 (2023).
6. Y. Peng, J. Rigelesaiyin, T. Phan, **L. Capolungo**, V. I. Levitas, and L. Xiong, *Effect of a micro-scale dislocation pileup on the atomic-scale multi-variant phase transformation and twinning*, Computational Materials Science **230**, 112508 (2023).
7. **K. Dang**, **C. N. Tomé**, and **L. Capolungo**, *The role of deviatoric stress and dislocations on the α to ω phase transformation in Ti*, Acta Materialia **244**, 118510 (2023).
8. **M. A. Kumar** and I. J. Beyerlein, *Embryo-to-lamella transition of grain boundary twins in magnesium*, Journal of Magnesium and Alloys **no. 12**, 4485-4497 (2023).
9. J. Wang, **M. A. Kumar**, and I. J. Beyerlein, *Investigation of crossed-twin structure formation in magnesium and magnesium alloys*, Journal of Alloys and Compounds **935**, 168094 (2023).
10. B. Ahmadikia, L. Wang, **M. A. Kumar**, and I. J. Beyerlein, *Grain boundary slip–twin transmission in titanium*, Acta Materialia **244**, 118556 (2023).

Role of nanoscale heterogeneities on charged species transport in oxide

Adrien Couet[1,2], Jennifer Choy[3], Yongfeng Zhang[1,2]
[1]Nuclear Engineering and Engineering Physics Department, 1500 Engineering Dr, Madison, WI 53711, USA
[2]Materials Science and Engineering Department, 1509 University Ave, Madison, WI 53706, USA
[3]Electrical & Computer Engineering Department, 1415 Engineering Dr, Madison, WI 53706, USA
Keywords: Corrosion, Local Ordering, Interface, Space Charge, Oxides

Research Scope: A careful literature survey has identified a clear knowledge gap on how the transport of charged species (i.e., mass and charge transports) is affected by embedded nanoscale heterogeneities in the oxide and their associated interfaces. Elucidating the effect of nanoscale heterogeneities requires understanding beyond the current theories for homogeneous oxides, either pure or with parallel surface space charges[1]. Filling in this gap is urgently needed for predicting and mitigating high-temperature corrosion. Furthermore, the growth of oxide film depends on both the charge and mass transport across the oxide and the processes that occur at the Oxide/Metal (O/M) interface, including electrochemical reaction, mechanical deformation, and interface motion. Quantitative prediction of corrosion kinetics requires precise determination of transport through the oxide containing nanoscale heterogeneities, and across interfaces, such as the O/M interface. However, this is currently not achievable because the experimental and modeling capabilities for quantifying ionic and electronic transport at the nanoscale are yet to be established.

This project brings in such capabilities and thereby represents a breakthrough in quantifying corrosion kinetics in extreme environments. In addition to impacting the overall oxidation kinetics, nanoscale heterogeneities may also induce heterogeneous ion flux arriving at the O/M interface and possibly contribute to the evolution of O/M interface morphology. The observed O/M interfaces resulting from oxidation are often non-planar, contradicting the flat interface assumption made in most classical theories. In the past, extensive research efforts have been made to understand the O/M interface morphological stability. Theoretically, flat O/M interfaces are expected from the minimization of interfacial energy and the negative correlation between oxide thickness and growth rate (*e.g.*, oxide troughs have slower growth due to the longer diffusion length than peaks). However, the role of nanoscale heterogeneous charge and mass fluxes should not be ignored and may possibly dominate O/M interface instability under certain conditions. This project equips us with the necessary understanding and techniques for investigating how heterogeneous mass and charge transports resulting from nanoscale heterogeneities in the oxide affect O/M interface morphological instability.

We hypothesize that nanoscale heterogeneities embedded in high-temperature oxides can induce heterogeneous flux of charged species via nanoscale interfaces. Using ZrO_2 as the model system with Nanoscale Metal Inclusions (NMIs) as the nanoscale heterogeneities in oxide, this hypothesis will be investigated by accomplishing the following three research Tasks.

I) Quantifying the atomic structure and charge distribution of a flat O/M interface,

II) Quantifying the microstructure and microchemistry and the resulting local charge distribution at the oxide/NMI interface considering the NMI size and shape,

III) Quantifying the nanoscale ion and electron/hole fluxes in oxide with nanoscale heterogeneities considering the size and distribution of NMIs.

These Tasks are achieved by tightly coupling a list of atomic scale to mesoscale modeling and experimental techniques. The results help answer the Science Questions (SQs) raised below:

SQ1) *How the atomic structure of a flat O/M interface affects charge distribution*. Answering **SQ1** centers on characterizing the atomic structure, valence state, and charge distribution across a flat O/M interface. Bridging with the existing theories in the semiconductor field, this will advance the atomic scale understanding of the effect of interface structure on charge distribution and pave the road for studying NMIs embedded in oxide. It has been well known in the semiconductor field that electronic charge transfer and redistribution take place at a M/S interface due to the alignment of Fermi levels, resulting in the formation of a Schottky barrier along with charge enriched/depleted zones. The barrier height and the size and shape of the charge enriched/depleted zones have been theoretically formulated for homogeneous interfaces. Combining existing semiconductor theories, DFT calculations, phase field modeling, 4D-STEM center of mass imaging[2], and synchrotron μ-XANES characterization, the dependence of charged particles distributions on the nature, size and interfacial characteristics of specific O/M flat interfaces will be established.

SQ2) *How the microstructure and microchemistry of nanoscale heterogeneity affects charge distribution in the oxide*. Extending the understanding and adopting the same techniques from **SQ1**, the atomic structure, composition, valence state, and charge density across the interface between ZrO_2 and embedded NMIs will be quantified. Here we focus on relatively noble NMIs in ZrO_2 to investigate the effects of size and shape of NMIs in controlling the Schottky barrier and the local charge distribution. Answering **SQ2** will provide us nanoscale understanding of how the NMI size and interfacial microstructure and microchemistry affect charge distribution. It also prepares us with the necessary understanding and techniques for investigating **SQ3**.

SQ3) *How the size and distribution of nanoscale heterogeneities (NMIs) affect charged species flux distribution, and mass transport, at the steady state*. Answering **SQ3** provides a mesoscale understanding on the correlation between ion and electron/hole fluxes and the size and distribution of NMIs. Novel and advanced experimental techniques such as isotopic oxidation followed by correlative TEM and APT characterizations, and quantum magnetometry using nitrogen-vacancy (NV) centers in diamond are utilized to quantify the local oxygen vacancies and electron/hole distributions with nanoscale resolution[3,4]. These experiments will be complemented by phase field modeling to investigate how NMIs with well-controlled chemistry, size, and shape alter the fluxes.

Recent Progress: The current efforts have synergistically focused on the three SQs. Firstly, the **SQ1** has been tackled by Dr. Alex Kvidt and Dr. Junliang Liu in Prof. Couet's group for ZrO_2 oxide growth on Si and Zr single crystal substrates. A PVD approach was used at multiple

temperatures up to 700°C to increase oxide grain size to allow for 4DSTEM analysis of TEM samples. To increase the oxide growth rate, a reactive O_2 gas was added to the cover gas. Oxides about 100 nm thick, with grain sized up to 40nm, were obtained and characterized by STEM and showed no observable defects. Au was then sputtered on top of the PVD ZrO_2. These ZrO_2 grain sizes allow for future 4DSTEM analysis across ZrO_2/Au flat interfaces. To prevent atomic scale damage and chemical artefacts in the oxide induced by FIB during TEM sample preparation, which would prevent 4DSTEM data analysis, it was decided to perform TEM sample preparation using micro-cleavage method. Micro-cleavage was attempted on multiple PVD samples, and no visible defects or contamination of the sample were observed. At the same time, 4DSTEM data acquisition and analysis was performed on a model MBE frown GaN(0001) / ZrN(111) system to advance on SQ1. GaN acts as a semi-conductor and ZrN as a metal, such that this system should present space charges at the interface relevant to **SQ1**. A micro-cleaved sample was studied by 4D-STEM, as shown in Fig.1 and the Center of Mass shift was computed. It is clear that the CoM is significantly shifted at the interface and considering the low lattice misfit (<1%) of this interface, it is likely resulting from space charge. DFT modeling of this interface is also being computed by Dr. Ximeng Wang in Prof. Zhang's group with 3D charge density, Bader charge, and density of states analysis to validate the experimental observations.

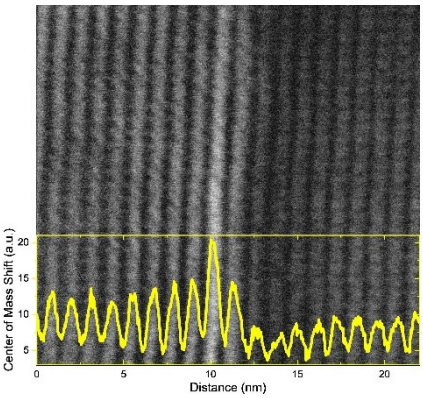

Fig. 1 4DSTEM of GaN(0001) / ZrN(111) and 1D CoM shift analysis

To start answering **SQ2**, Andrew Tong and Dr. Maryam Zahedian in Prof. Choy's group have developed methods for depositing monodispersed metallic nanoparticles with large-area coverage and uniform density on ZrO_2. These nanoparticles serve as NMIs after an additional ZrO_2 is grown over them by PVD. Our recipe consists of a multi-step spin-coating of solutions with Au nanoparticles on clean ZrO_2 substrates, in which the spin speed and number of spin-coating runs can be used to control the density of nanoparticles on the surface. We have demonstrated a surface coverage of 1% to 10% for 50-nm-diameter Au nanoparticles (Fig.2), an area coverage that is consistent with observed NMI density in thermally grown oxides. ZrO_2 was further deposited on these samples by Dr. Liu, such that we now have samples with NMI embedded in ZrO_2. Finally, to define procedures to acquire and analyze Au/ZrO_2 interfaces of various orientations, stress-free ZrO_2 nanocrystals with sputtered Au nanoparticles were prepared by Dr. Kvit. After care was taken to stabilize them under the electron TEM beam by "sandwiching" the nanocrystals with C deposits, 4DSTEM analysis was performed and results are being analyzed. To better characterize the energy levels of the NMIs in the oxide, Dr. Riccardo Vidrio in Prof. Choy's group and Dr. Liu also investigated

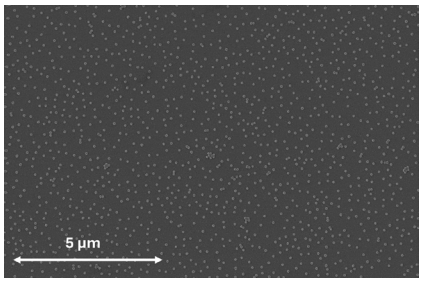

Fig. 2 50nm Au NP deposited on ZrO_2 by spin coating

the characteristics of electron emission from cross sections of thermally grown ZrO_2 on ZrFeCr substrate through SEM-CL. Indeed, SEM-CL provides insight on the bandgap energies of different regions on the sample. We developed a platform for correlating SEM-CL measurements with the chemical composition (through EPMA) and microstructure (through nano-EBSD and TKD) of the oxide. We have completed data collection and are now focusing on analysis and correlation of data taken across the different characterization techniques. To support **SQ1** and **SQ2**, Dr. Ximeng Wang also studied the charge redistribution and charge transfer at the Au/ZrO_2 flat interface using DFT calculations. The interface is constructed between the closest packed planes of Au ({111}) and ZrO_2 ((110) for tetragonal and (-111) plane for monoclinic). The orientation relationship is determined by minimizing the mismatch strain while considering the computation cost of DFT. Bulk ZrO_2 is found to have a lower Fermi level than Au. After forming an interface, charge transfer occurs from the ZrO_2 side towards Au. The charge transferred is found to be about 0.212 e/nm^2 and 0.214 e/nm^2 for t- and m-ZrO_2.

To tackle SQ3, a combination of TEM and APT to analyze the distribution of oxygen in the oxide layer of ^{18}O-spiked ZrO_2 samples was performed. The APT experiments was performed at the University of Michigan by Dr. Liu, thanks to the support of Dr. Fei Xue and Prof. Emmanuelle Marquis. Our data analysis and results revealed that ^{18}O was segregated at ZrO_2 grain boundaries (Fig. 3). This promising approach enables us to locate ^{18}O in future spiked NMI/ZrO_2 system and infer charged species transport.

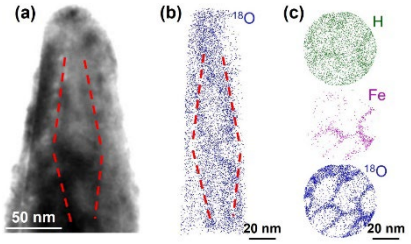

Fig. 3 TEM/APT analysis of 18O spiked ZrO2 showing 18O along oxide grain boundaries

Future Plans: For **SQ1,** we are finalizing the planar interfacial space charge study on GaN/ZrN model system by validating the experimental results using DFT. In addition, we will convert the 4DSTEM CoM imaging to space charge density. We will finalize the deposition of ZrO_2 on Zr single crystal substrate with sufficiently large oxide grain size. We will perform the planar interfacial space charge study of the Au/ZrO_2 system. For **SQ2**, we will finalize the study on photo-luminescence correlation to microstructure. We will start analyzing the spherical Au NMIs embedded in ZrO_2 in terms of microstructure using TEM and DFT. A framework for 4DSTEM CoM analysis of multiple Au/ZrO_2 interfaces will be established. Spin coating recipes to obtain repeatable density of Au NP in ZrO2 films will be developed. Finally, a modeling scoping study will be performed to study other elements for NMIs beyond Au including Ag, Ni, and Al. To prepare for **SQ3** and spatially resolved electron transport measurements of oxide cross sections, we will demonstrate vector magnetometry and electron density measurements using quantum sensors based on nitrogen-vacancy centers in diamond. The confocal microscope and microwave electronics needed for the measurements have already been constructed, so our work will focus on the fabrication of diamond quantum sensors and demonstration of the technique on test circuits and samples. We will also finalize the study on the ^{18}O detection and distribution in ^{18}O spiked ZrO_2.

References

1. Macdonald, D. D. *The history of the Point Defect Model for the passive state: A brief review of film growth aspects*. Electrochim. Acta **56**, 1761 – 1772 (2011).
2. Q. Jia, A. Gloter, *Real-Space Observation of Potential Reconstruction at Metallic/Insulating Oxide Interface*. Adv. Mater. Interfaces **10**, 2202165 (2023).
3. Balasubramanian, G. et al. *Nanoscale imaging magnetometry with diamond spins under ambient conditions*. Nature **455**, 648 – 651 (2008).
4. Chang, K., Eichler, A., Rhensius, J., Lorenzelli, L. & Degen, C. L. *Nanoscale Imaging of Current Density with a Single-Spin Magnetometer*. Nano Lett. **17**, 2367 – 2373 (2017).

Understanding the effect of stress on complexion transitions and the interplay with creep in thermally stabilized nanocrystalline materials

[1]Maarten de Boer, [2]Elizabeth Dickey, [2]Greg Rohrer
[1]Mechanical Engineering, [2]Materials Science and Engineering, Carnegie Mellon University

Keywords: complexions, nanomechanical test platform, oxidation, dewetting

Research Scope

The phase of a bulk material depends on thermodynamic variables such as temperature, composition, and pressure. Most metals are polycrystalline and the crystals are separated by grain boundaries (GBs). Grain boundary phases, known as complexions, influence mechanical properties such as strength and toughness. Such complexions have been studied to date as a function of temperature and composition. Here, we examine whether mechanical stress can effect complexion transitions, **Fig. 1** [1].

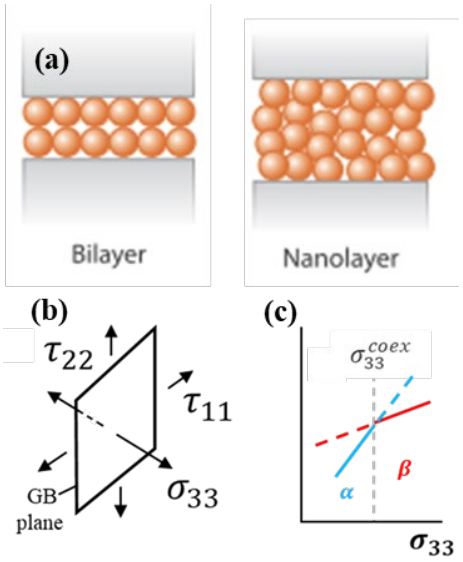

Fig. 1 (a) conceptual schematic of a bilayer to multilayer complexion transition. (b) associated stress state at a grain boundary plane. (c) associated phase diagram.

Recent Progress

A versatile nanomechanical platform that can apply a controlled stress over a wide range of temperature to a freestanding nanocrystalline metal in thin film form is being fabricated. High resolution transmission electron microscopy is being used to determine the structure and composition of boundaries equilibrated at different stresses. Over time at elevated temperature, the material is likely to creep, which will be associated with a slow stress relaxation. If complexions transform from an amorphous to an ordered state, they will become denser, which will reduce diffusion and hence a change in creep rate should be observable. Creep rates will be monitored to search for these transitions.

We will discuss how we have surmounted several issues regarding manufacturability of the test platform. We are also characterizing the platform's actuation capabilities [2]. The materials system of interest has been nanocrystalline Cu-Zr, which has been reported to form complexions up to ~7 nm in thickness while maintaining a grain size of less than 100 nm. Given the high susceptibility of Zr to oxidation, we are evaluating conditions under which oxide-free nanocrystalline grain boundaries can be established. As freestanding thin films are annealed at high temperatures, we observe dewetting and agglomeration. We have developed an understanding of the associated kinetic mechanism.

Future Plans

The goal of our research is to extend the understanding of thermally stabilized nanocrystalline metals by assessing how nanocrystalline metals perform mechanistically in their intended application – high temperature *and* high stress.

We are evaluating the optimum concentration of Zr to minimize the oxidation and dewetting issues. We are considering other materials systems to determine if there is a better candidate to test our hypotheses.

References

[1] P. R. Cantwell, T. Frolov, T. J. Rupert, A. R. Krause, C. J. Marvel, G. S. Rohrer, J. M. Rickman, and M. P. Harmer, "*Grain boundary complexion transitions*," Annual Review of Materials Research, **50**, pp. 465-492, 2020.

Publications

[2] R. M. Pocratsky, M. S. Islam, L. Ni, E. J. Fox, and M. P. de Boer, "*Oxygen diffusion in freestanding body centered cubic tantalum structural thin films in air and in high vacuum*," Thin Solid Films, **800**, p. 140392, 2024.

The effect of curvature on the radiation response of heterophase interfaces

Michael J. Demkowicz, Kelvin Y. Xie (Texas A&M University)

Keywords: interfaces, radiation, curvature

Research Scope

The goal of this project is to discover the effects of curvature on the radiation response of solid-state interfaces and to explore strategies for elevating the radiation resistance of composite materials via control of interface curvature. At this meeting, I will highlight progress on two (out of three) hypotheses that motive our work, namely

Hypothesis A: curved interfaces absorb radiation-induced point defects more efficiently than flat ones because curvature imparts additional, atomic-level sites that absorb defects.

Hypothesis B: damage accumulates faster on the concave side of curved interfaces because positive curvature reduces the energy barrier to nucleate defect clusters.

Our research relies on model materials specially synthesized using physical vapor deposition (PVD) and vacuum annealing. These materials are two-element, three-layer composites, such as the Nb-Cu-Nb composite shown in Fig. 1.a). The heterophase interfaces between the layers are flat upon deposition, but acquire significant curvature after annealing at 800C. We use focused ion beam (FIB) milling to extract a ~100nm-thick lamella, which is then irradiated with 200keV He^+ ions at 450C. The energy of the incident ions is high enough so that they pass through the lamella, creating displacement damage but not becoming implanted. Deposition, annealing, and irradiation are conducted at Los Alamos National Laboratory. These samples are then characterized using transmission electron microscopy (TEM) at Texas A&M University.

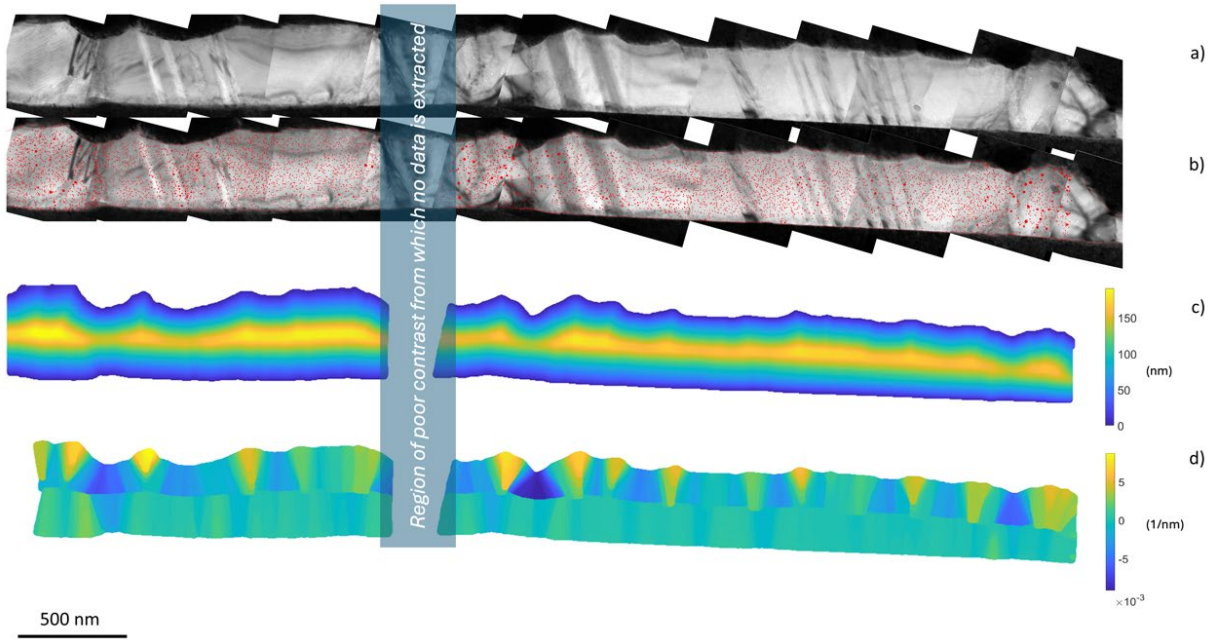

Fig. 1: a) PVD Nb-Cu-Nb composite after annealing at 800C and irradiation with 200keV He+ ions at 450C. b) Red dots indicate radiation-induced voids in the Cu layer. c) Locations in the Cu layer are color-coded according to their

distance to the nearest Cu-Nb interface. d) Locations in the Cu layer are color-coded according to the curvature of the nearest Cu-Nb interface

Recent Progress

We used quantitative image processing to assess the effect of interface curvature on radiation-induced damage in the Nb/Cu/Nb composites shown in Fig. 1. We collected the locations and sizes of all radiation-induced cavities in the Cu layer (Fig. 1.b) as well as the curvatures of the nearest interface segments (Fig. 1.c and 1.d). Based on this data, we constructed distributions of void densities as a function of distance from interfaces of different curvatures.

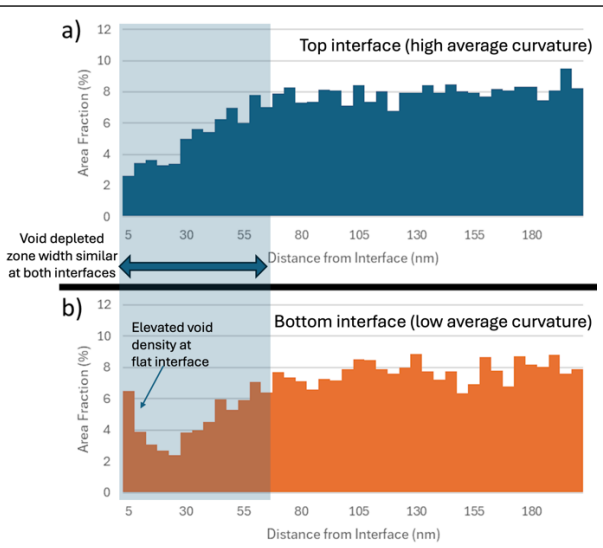

Fig. 2: Void density as a function of distance from the a) top interface (which is highly curved) and b) bottom interface (which is nearly flat). There is a clear reduction of bubble density at the highly curved interface, compared to the flat one. The void depleted zone width for both interfaces is comparable.

By way of example, Fig. 2 shows void density distributions near all the high curvature interfaces along the upper Cu-Nb interface shown in Fig. 1 (Fig. 2.a) and along the comparatively flat lower Cu-Nb interface in Fig. 1 (Fig. 2.b). The distributions suggest that the main effect of curvature is on the degree of damage accumulated at the interfaces, with curved interfaces containing fewer radiation-induced voids than flat ones. This outcome is consistent with curved interfaces containing a greater density of defect trapping sites, as hypothesized, and therefore being less prone to damage.

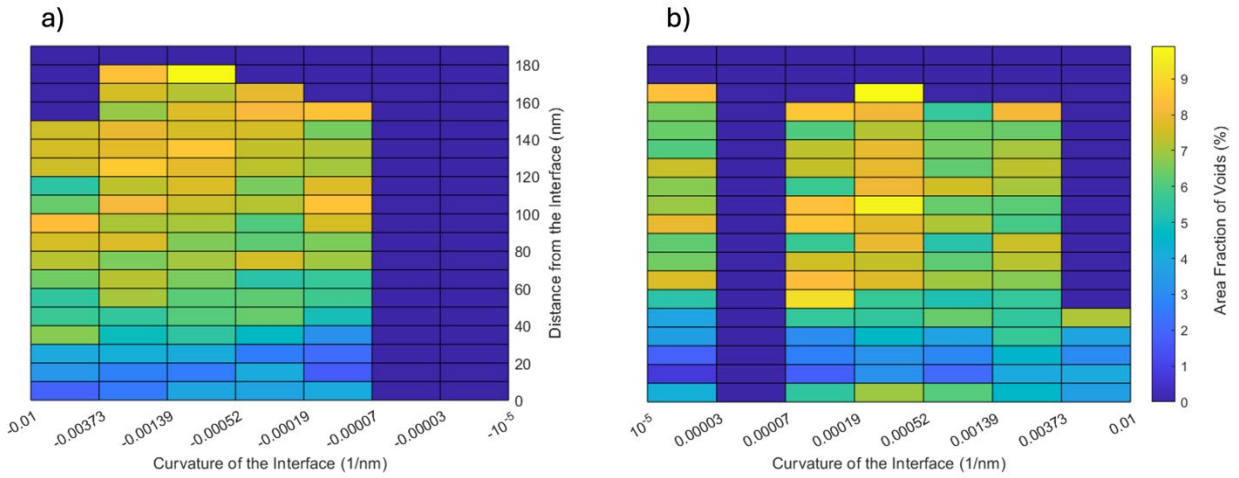

Fig. 3: Distribution of void density as a function of distance from interfaces with different curvatures: a) negative curvature (concave) and b) positive curvature (convex).

As shown in Fig. 3, we are also analyzing the widths of void-depleted zones to ascertain the effect of curvature on interface sink efficiency and on the range interface interactions with radiation-

induced point defects. To this end, we partition our data into sets distinguished by the curvature of the Cu-Nb interface nearest to each radiation-induced void. Analysis of the resulting distribution shown in Fig. 3 suggests that the range of interface-defect interactions and interface sink efficiency are both relatively insensitive to curvature. However, concave (positive curvature) interfaces have a greater propensity for accumulating damage in the form of radiation-induced voids, compared to convex (negative curvature) interfaces. We have carried out extensive statistical analysis to ensure that the observed interface curvature effects are not due to imaging or geometrical artifacts.

In addition to the work described above, we have also

- Falsified the 3rd (and final) hypothesis motivating out project, namely "*Hypothesis C:* radiation damage decreases the mobility of curved interfaces by reducing the diffusivity of interfacial defects, enhancing thermal stability of composites with curved interfaces." We investigated the effect of temperature on coarsening during high energy helium (He) implantation of physical vapor co-deposited nanocomposites of copper (Cu) and molybdenum (Mo). These composites containing a large area per unit volume of highly curved interfaces. Higher temperature leads to greater coarsening of Cu and Mo domains. However, the coarsening rate is the same in He-implanted and He-free regions, suggesting that radiation damage does not have a pronounced effect on the coarsening rate of composites with curved interfaces. This finding leads us to conclude that curvature does not appreciably affect (reduce or enhance) the diffusivity of interfacial defects.
- Inferred the Cahn-Hilliard mobility of Cu and Nb from experiments showing the breakup of a terminated Cu layer in a Nb matrix upon annealing at 800C. Our findings are consistent with mass transport in the Cu-Nb system being dominated by interfaces.
- Discovered that refractory impurities, including Nb and V, undergo short circuit diffusion through certain grain boundaries in Cu upon annealing at 800C. This finding is surprising in light of the negligible solid solubility of these impurities in single-crystal Cu. Atomistic modeling revealed that this effect is due to an elevated solubility of these impurities at grain boundaries with high free volume.
- Showed that, in Cu-W nanocomposites, He impurities undergo short-circuit diffusion along both Cu-W interfaces as well as grain boundaries in Cu and W.
- Contributed to an investigation of the role of slip in hydrogen-induced crack initiation in Ni-based alloy 725. This investigation revealed no tendency for hydrogen to enhance localized slip and no necessity of slip for crack initiation. These findings suggest that hydrogen enhanced localized plasticity (HELP) is not responsible for hydrogen-induced crack initiation in alloy 725.

Future Plans

Our next step is to repeat the analysis described above on irradiated Mo-Cu-Mo, V-Cu-V, Ag-Cu-Ag, and Ir-Cu-Ir composites. This work will examine how the level of lattice misfit affects the influence of curvature on interface radiation response. All the required samples have already been deposited, annealed, and irradiated. They are currently undergoing TEM characterization.

Moreover, we will conduct theoretical and modeling investigations to elucidate the physical mechanisms underlying the interface curvature effects discovered through our experiments. The focus of this work will be to characterize the influence of interface curvature on the density and types of defects formed at heterophase interfaces, the interactions of these defects with radiation-

induced vacancies and interstitials in grain interiors, and processes of radiation-induced damage nucleation and evolution at heterophase interfaces. Our findings will form the basis for predicting the performance of advanced composite materials containing curved interface under irradiation.

Publications

1. D. Yadav, P. Chen, S. Xiang, Y. Q. Wang, J. K. Baldwin, P. Evans, N. Williams, M. J. Demkowicz, K. Y. Xie, *Outgassing of implanted He via short circuit transport along phase and grain boundaries in vapor co-deposited Cu-W nanocomposites*, Acta Materialia **240**, 118306 (2022).
2. E. Sheu, Y. F. Zhang, H. Kim, D. J. Williams, J. K. Baldwin, M. J. Demkowicz, *Fragmentation of the edge of a terminated Cu nanolayer within a Nb matrix upon annealing*, Scripta Materialia **225**, 15168 (2023).
3. E. Sheu, T. Y. Liu, D. J. Williams, J. K. Baldwin, M. J. Demkowicz, *Permeation of niobium through grain boundaries in copper*, Acta Materialia **274**, 120002 (2024).
4. M. Y. Liu, L. Jiang, M. J. Demkowicz, *Role of slip in hydrogen-assisted crack initiation in Ni-base alloy 725*, Science Advances **10**, eado2118 (2024).
5. T. Y. Liu, E. Sheu, D. J. Williams, J. K. Baldwin, M. J. Demkowicz, *Reduction of vanadium mobility within copper grain boundaries due to enhanced binding and free volume exhaustion*, Scripta Materialia (2024).

Coupled effects of stress and hydrogen on stress corrosion cracking of Fe-based alloys

Arun Devaraj, Pacific Northwest National Laboratory

Keywords: Stress corrosion cracking, steel, hydrogen, deformation, correlative microscopy

Research Scope

The overarching goal of this project is to develop predictive, mechanistic understanding of the coupled influence of applied stress, H concentration and distribution, and intergranular oxidation on propagation of stress corrosion cracking (SCC) in Fe-based alloys in high-temperature water environments. When steels are subjected simultaneously to an applied tensile stress and high-temperature water environment, it is hypothesized that a combination of H-assisted mechanisms and intergranular oxidation leads to intergranular stress corrosion cracking (SCC), which can cause catastrophic failures. Although SCC mechanisms of steels has been studied for decades, crucial knowledge gaps still exist, especially due to the complexity of the coupled mechanisms. This project correlates results from unique, state-of-the-art microscopy and spectroscopy capabilities housed at Pacific Northwest National Laboratory and at synchrotron light source user facilities to quantitatively analyze the influence of hydrogen, oxidation, and local deformation in Fe-based alloys from the atomic scale to the mesoscale. Additionally, judiciously selected in situ and in operando methods and computational simulations are used to unravel the coupling between H and the chemical and mechanical factors that influence SCC mechanisms. This project also investigates the SCC mechanisms operating at defected grain boundaries, revealing the influence of high defect density, modified grain boundary structure, and solute segregation to facilitate predictive control of H-assisted and oxidation-based SCC mechanisms of Fe-based alloys.

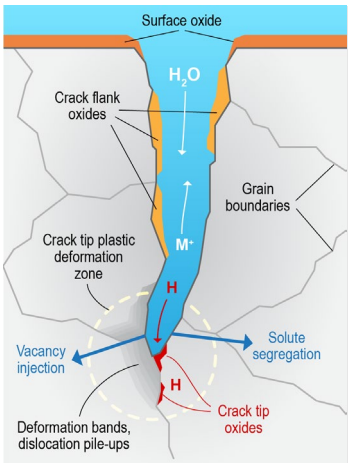

Figure 1. The crack tip phenomenon during SCC of Fe-based alloys in high-temperature water is a complex, multiscale problem. This proposed work will develop a predictive, mechanistic understanding of the coupled influence of applied stress, H, and intergranular oxidation on propagation of SCC in Fe-based alloys in high-temperature water environments.

Recent Progress

Influence of alloy composition and Hydrogen on deformation mechanisms: Understanding the composition dependent change in deformation mechanisms of austenite in stainless steels is crucial to develop accurate predictive models both for stress induced failures and stress corrosion cracking. Specifically, the understanding of the interplay between the composition dependence on the stacking fault energy (SFE) and the compositional short-range ordering (SRO) and thereby the deformation mechanisms of austenitic stainless steels is still at its infancy. We investigated this interplay between SFE and SRO on modifying the deformation mechanism of Fe-Cr-Ni alloys as a function of Ni concentration by coupling computational simulations with experimental in situ

synchrotron XRD tensile testing and post-mortem electron microscopy. The thermodynamic linear-response theory as implemented within DFT framework, that addresses compositional fluctuations, was used to calculate Warren-Cowley SRO parameters which revealed low SFE and low SRO in Fe18Cr10Ni (wt%) alloy (Fig. 1(a)). This was observed to lead to formation of HCP ε martensite after 40% tensile plastic strain in the Fe18Cr10Ni alloy, as highlighted in the center of symmetry (COS) map of high angle annual dark field scanning transmission electron microscopy (HAADF-STEM) image (Fig. 1 (b)). The computational simulation predicted a higher SFE and higher SRO for the Fe18Cr14Ni (wt%) alloy as evidenced by the higher Ni-Cr SRO parameter. This led to enhanced twinning as shown in the COS map of Fe18Cr14Ni alloy (Fig. 1(d)). Synchrotron X-ray diffraction during in situ tensile testing of both model alloys revealed a faster increase in dislocation density with increasing strain in Fe18Cr14Ni alloy (Fig 1(e)), while stacking fault probability increased faster with strain for Fe18Cr10Ni alloy (Fig. 1(f)). In addition, synchrotron XRD during tensile testing of hydrogen charged Fe18Cr14Ni alloy demonstrated an enhancement of its stacking fault probability and enhanced occurrence of deformation twinning. These observations highlighted the need to better understand not just the role of SFE but also SRO and hydrogen on the deformation mechanisms of austenitic stainless steels which we believe will be important for understanding the coupling between deformation mechanisms and stress corrosion cracking in high temperature pressurized water environments.

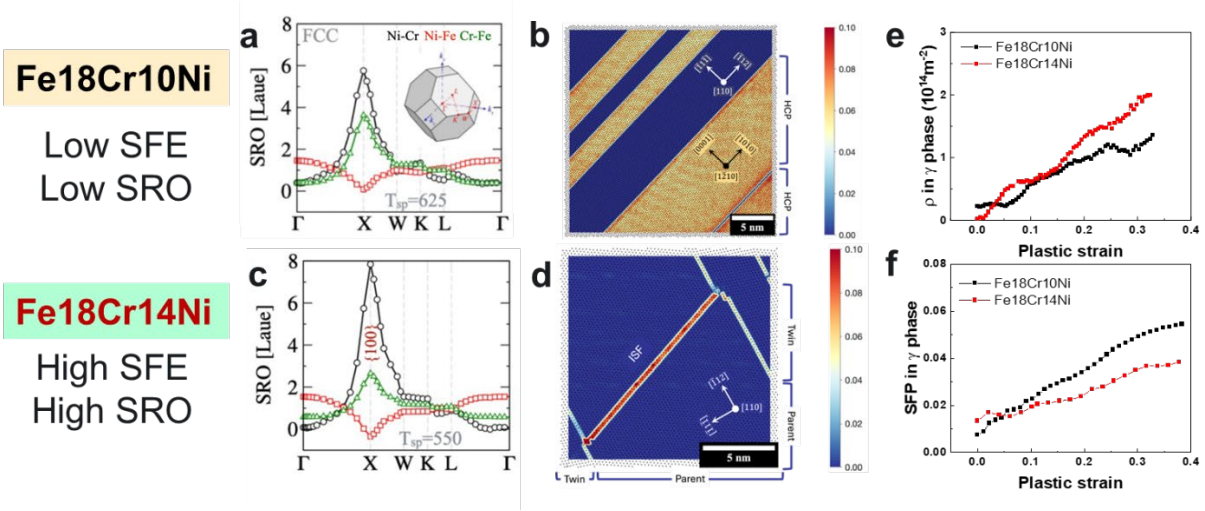

Fig. 2: (a) computational simulations predicted low SFE and low SRO in Fe18Cr10Ni alloy which led to (b) formation of hexagonal close packed (HCP) ε martensite highlighted in the warmer colors in between the austenite matrix (shown in blue) in the center of symmetry (COS) map of high angle annual dark field scanning transmission electron microscopy (HAADF-STEM) image after 40% tensile strain. (c) Fe18Cr14Ni alloy was predicted to have higher SFE and higher SRO, as evidenced by the higher Ni-Cr SRO value. (d) the COS map revealed formation of twins. From synchrotron XRD during in situ tensile testing, the (e) dislocation density was observed to increase more rapidly with strain in Fe18Cr14Ni alloy but (f) the stacking fault probability increased faster for Fe18Cr10Ni alloy.

Quantitative mapping of hydrogen segregation in austenite: We established new capabilities in the PNNL Energy Science Center including a cryogenic nitrogen glove box that houses an electrochemical hydrogen charging station along with a dedicated cryogenic-ultrahigh vacuum transfer shuttle, a 360-degree rotation cryogenic stage for the Thermo Fisher scientific Hydra plasma-focused ion beam (PFIB) and a state-of-the-art CAMECA LEAP 6000XR atom probe tomography (APT) [1]. These capabilities aided in achieving a complete ultrahigh vacuum cryotransfer of hydrogen-charged model Fe18Cr14Ni alloy samples from the glove box to PFIB to APT. Using this capability, the influence of hydrogen on modifying the deformation-induced defects and on enhancing hydrogen trapping in the austenitic model Fe18Cr14Ni alloy was analyzed.

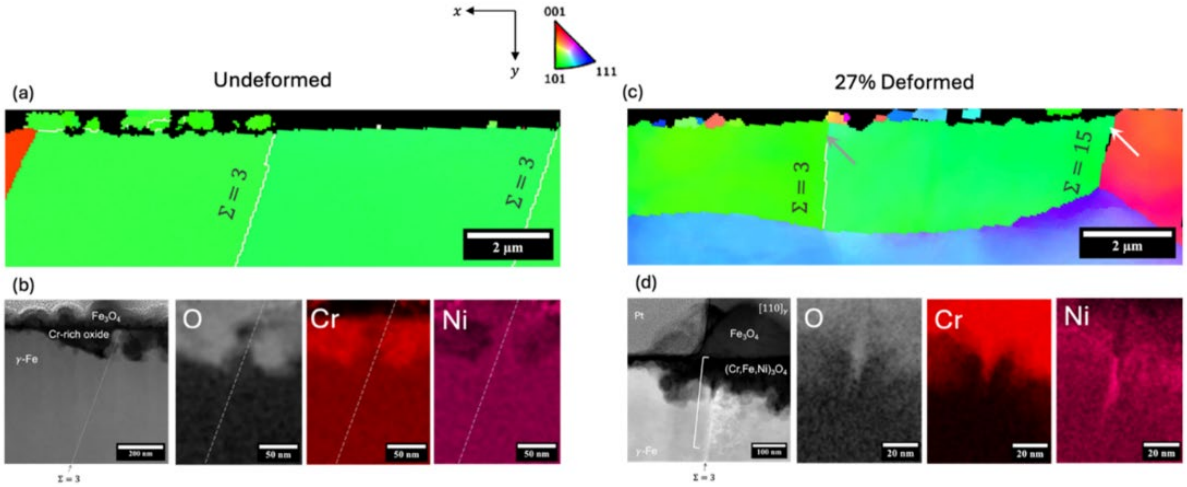

Figure 3: Transmission Kikuchi diffraction (TKD) (a, c) and Scanning Transmission Electron Microscopy-Energy Dispersive X-ray Spectroscopy (STEM-EDS) (b, d) results obtained from Σ=3 GBs in oxidized undeformed and deformed Fe18Cr14Ni austenite alloy showing higher misorientation (than the Brandon criteria), dislocation content, and penetrative oxidation in the deformed sample. The arrows in (c) indicate regions of significantly higher misorientation. This region of higher misorientation is also shown in the BF-STEM micrograph in (d) with a white bracket where penetrative intergranular oxidation is evident.

Influence of deformation induced defects on intergranular corrosion mechanisms: Extensive intergranular SCC is often preceded by penetrative oxidation along grain boundaries (GBs). GB oxidation follows diffusion-induced grain boundary migration (DIGM), which enables short-circuit pathways for necessary transport phenomena [2]. We hypothesized that prior deformation induced defects may introduce structural change at the austenite grain boundaries (GB) in Fe18Cr14Ni alloy, which could then alter the mechanism of penetrative oxidation at such boundaries when exposed to high temperature pressurized water environments. To test this hypothesis, we first selected coherent annealing twin boundaries (ATB), which are typically reported to be inert to IGSCC and oxidation [3]. Structurally, ATBs are coherent {111} ∑3 boundaries. Reports of their inertness and enhanced resistance to oxidative attack are generally attributed to their low-energy and coherent structure. However, there is growing evidence

indicating that deformation can restructure these GBs. Further, minor deviations from the ideal ∑3 structure may be expected to significantly increase GB energy which in turn could influence the mechanism of penetrative oxidative attack.

To test our hypothesis, the undeformed and 27% tensile strained Fe18Cr14Ni alloy samples were subjected to simulated pressurized water reactor (PWR) conditions at 300 ° C for 300 hours and the resultant oxidation on the alloy surface and grain boundaries was characterized with cross-sectional TKD and STEM-EDS, revealing penetrative oxidation at Σ=3 ATBs in the deformed sample (fig 3). This finding is particularly significant because Fe18Cr14Ni alloys also exhibit extensive deformation twinning with higher hydrogen, which may also encourage penetrative GB oxidation and failure at those twins during PWR conditions.

Future Plans

Using the cryogenic transfer capabilities established in PNNL, we will quantify the hydrogen segregation at grain boundaries within FeCrNi alloys both before and after tensile deformation utilizing the cryogenic transfer APT capability. This will help quantify the H concentration and H cluster size at grain boundaries near crack tips. In addition, we also aim to reveal the atomic scale mechanism by which hydrogen enhances twinning and grain boundary decohesion in austenitic FeCrNi alloys. We will also reveal the hydrogen distribution near oxidized grain boundaries in the FeCrNi alloys exposed to high-temperature pressurized water. This would aid in verifying if diffusion-induced grain boundary migrated zones beneath intergranular oxidation zones act as hydrogen traps. Finally, we will also test the influence of modified grain boundary structure and composition of FeCrNi alloys achieved by friction stir processing for altering the high-temperature pressurized water corrosion, hydrogen embrittlement, and stress corrosion cracking mechanisms. We will also collaborate with computational modeling researchers in PNNL and external institutions, to leverage the experimental results to develop predictive models for describing oxidation mechanisms and diffusion-induced grain boundary modification in alloys when undergoing SCC.

References

1. D. J Barton, D-T. Nguyen, D. E Perea, K. A. Stoerzinger, R. M. Lumagui, S. V. Lambeets, M. G. Wirth & A. Devaraj, Towards quantitative analysis of deuterium absorption in ferrite and austenite during electrochemical charging by comparing cyclic voltammetry and cryogenic transfer atom probe tomography, International Journal of Hydrogen Energy **50 (A)**, 30-40 (2024).
2. Z. Shen, K. Arioka, & S. Lozano-Perez, A study on the diffusion-induced grain boundary migration ahead of stress corrosion cracking crack tips through advanced characterization. *Corrosion Science* **183**, 109328 (2021).
3. E. M. Lehockey, A. M. Brennenstuhl, & I. Thompson, On the relationship between grain boundary connectivity, coincident site lattice boundaries, and intergranular stress corrosion cracking. *Corrosion Science* **46**, 2383–2404 (2004).

Publications

1. D. J. Barton, D-T. Nguyen, D. E. Perea, K. A. Stoerzinger, R. M. Lumagui, S. V. Lambeets, M. G. Wirth, A. Devaraj, *Towards Quantitative Analysis of Deuterium Pick Up in Ferrite and Austenite during Electrochemical Charging by Comparing Cyclic Voltammetry and Cryogenic Transfer Atom Probe Tomography*. International Journal of Hydrogen Energy, **50**, 30-40 (2024). doi:10.1016/j.ijhydene.2023.06.256

2. A. Devaraj, D. J. Barton, M. G. Wirth, D. E. Perea, *Nanoscale Mapping of Hydrogen Distribution in Nuclear Structural Materials Using Cryogenic Transfer Atom Probe Tomography*, Microscopy and Microanalysis, **29, S1**, 1553–1554 (2023). doi:10.1093/micmic/ozad067.799

3. B. Gwalani, A. Martin, E. J. Kautz, B. Guo, S. V. Lambeets, M. Olszta, A. K. Battu, A. Malakar, F. Yang, J. Guo, S. Thevuthasan, R. Li, A. Amassian, M. Thuo, A. Devaraj, *Mechanistic Understanding of Speciated Oxide Growth in High Entropy Alloys*, Nature Communications, **15**(1), 5026 (2024). doi:10.1038/s41467-024-49243-8

4. D. H Cook, P. Kumar, M. I. Payne, C. H. Belcher, P. Borges, W. Wang, F. Walsh, Z. Li, A. Devaraj, M. Zhang, M. Asta, A. M. Minor, E. J. Lavernia, D. Apelian, R. O. Ritchie, *Kink bands promote exceptional fracture resistance in a NbTaTiHf refractory medium-entropy alloy*, Science, **384**, 6692, 178-184 (2024). doi: 10.1126/science.adn2428

5. G. Sahragard-Monfared, C. H. Belcher, S. Bajpai, M. Wirth, A. Devaraj, D. Apelian, E. J. Lavernia, R. O. Ritchie, A. M Minor, J. C. Gibeling, C. Zhang, M. Zhang, *Tensile creep behavior of the Nb45Ta25Ti15Hf15 refractory high entropy alloy*, Acta Materialia, 271, 119940 (2024). doi:10.1016/j.actamat.2024.119940

6. J. Ballor, J. D. Poplawsky, A. Devaraj, S. Misture, C. J. Boehlert*, Lattice Parameter Evolution during the β-to-α and β-to-ω Transformations of Iron-and Aluminum-Modified Ti-11Cr (at.%)*, Crystals, **14**(2), 145 (2024). doi: 10.3390/cryst14020145

7. T. Liu, C-H. Li, M. Olszta, J. Tao, A. Devaraj, *Directly monitoring the shift in corrosion mechanisms of a model FeCrNi alloy driven by electric potential*, 2023, npj Materials Degradation, **7**(1), 42, (2023). DOI: 10.1038/s41529-023-00357-2

8. Y-S. Chen, P-Y. Liu, R. Niu, A. Devaraj, H-W. Yen, R. K. W. Marceau, J. M. Cairney, *Atom Probe Tomography for the Observation of Hydrogen in Materials: A Review*, Microscopy and Microanalysis, **29**, 1, 1–15 (2023). doi:10.1093/micmic/ozac005

9. Z. Yu, E. J. Kautz, H. Zhang, A. Schneider, T. Kim, Y. Zhang, S. Lambeets, A. Devaraj, A. Couet, *Irradiation Damage Reduces Alloy Corrosion Rate via Oxide Space Charge Compensation Effects*, Acta Materialia, **253**, 118956 (2023). doi:10.1016/j.actamat.2023.118956

Understanding the Mechanics of Reverse Phase Transformation and Detwinning in BCC Metal Microstructures

Avinash M. Dongare, University of Connecticut

Keywords: Molecular dynamics, BCC metals, twins, phase transformation, anti-twinning, diffraction

Research Scope

BCC metal microstructures can exhibit contributions from twinning-induced plasticity (TWIP) and transformation-induced plasticity (TRIP). The high SFE values for BCC metals render a poor ability to twin compared to FCC metals, and dislocation slip typically dominates the contribution to plasticity. In addition, owing to the non-planar dislocation core, the stress for the motion of dislocations in a direction differs from the motion in the opposite direction. This asymmetry results in the shear stresses for twinning shear in one direction being lower than the twinning shear in the opposite direction (anti-twinning). Thus, Schmid effects (loading orientation) and non-Schmid effects (asymmetry in twinning and anti-twinning) can influence the twinnability of the BCC metal microstructures and, hence, the slip vs twin contributions to the plastic deformation. The current experimental strategies to understand these mechanisms and their contributions to the stress-strain response are based on loading the specimens to different strain levels and then unloading them to characterize the unloaded microstructures using electron backscattered diffraction (EBSD). However, the high energy of the twin boundaries in BCC metals can result in detwinning behavior during unloading, making it challenging to understand orientation and non-Schmid effects on the interplay between dislocation slip and deformation twinning. In addition, Fe-based microstructures demonstrate a BCC (α) $\rightarrow$ HCP (ε) phase transformation when deformed above a threshold pressure, and unloading can render in a distribution of twins in the bcc microstructure. The distribution of these twins, referred to as transformation twins, is attributed to the ε phase variant selections during the $\alpha \rightarrow \varepsilon$ transformation and their reverse transformation during unloading. Thus, while loading orientations influence the variant selections, the factors that influence the stability of transformation twins are not understood. This proposed program uses model BCC metal microstructures (Fe, Ta, Mo, and Nb) and a novel computational framework to understand the factors (Schmid and non-Schmid effects) that influence (a) twinnability, the contributions of twins to plasticity during deformation, and detwinning behavior during unloading, and (b) variant selections phase transformation and twinnability during reverse transformation. The program will use a novel combination of (a) large-scale molecular dynamics (MD) simulations to model the behavior at the atomic/nanoscales, (b) quasi-coarse-grained dynamics (QCGD) simulations to model the behavior at the mesoscales, (c) a virtual texture analysis (VirTex) tool [1] that creates EBSD maps of the simulated microstructures to compare with experimental EBSD maps, and (d) virtual x-ray diffraction (XRD) and selected area diffraction (SAED) to characterize and quantify the Schmid and non-Schmid effects on the contributions to plasticity.

Recent Progress

Twinnability of grains in polycrystalline microstructures:

MD simulations are carried out to investigate the role of grain orientation on the twinning and detwinning behavior using a nanocrystalline (nc) Fe microstructure as a model BCC system. The deformed microstructure snapshots are characterized using VirTex to understand orientation effects on the twinnability of individual grains. Example snapshots showing deformed microstructures at different strains are shown in Figure 1(a) and (b) for loading under uniaxial stress compression and tension, respectively. It can be seen that some grains twin under compression and tension, some grains twin only under compression, and some grains do not twin. Thus, characterization and visualization based on orientation and rotation vectors using VirTex provides new insights into the deformation twinning behavior of individual grains in polycrystalline microstructures. The nc-system is also deformed along other loading directions to understand the effect of orientation and the Schmid Factor difference (SF_{diff}) calculated as the difference between the Schmid factor values for the slip system (SF_{slip}) and the twin system (SF_{twin}) using the initial orientations in the undeformed microstructure as: $SF_{diff} = SF_{twin} - SF_{slip}$. The grain is expected to deform by twinning if the difference is positive and dislocation slip if the difference is negative. The plot of the difference between the Schmid Factor for different grains in all the simulations is shown in Figure 11 (c) tension and Figure 11 (d) compression. The grains that do not twin are shown in red and the grains which have twinned are shown in green. These results demonstrate that the twinnability of individual grains in polycrystalline microstructures needs further investigation of non-Schmid effects along with effects due to misorientations with neighboring grains. A manuscript is currently under review.

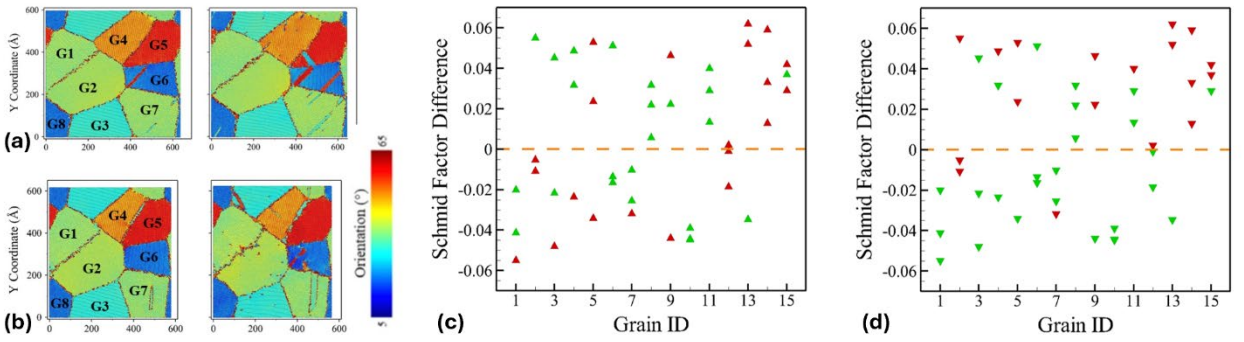

Figure 1: Deformed nc-Fe microstructure showing distribution of twins under loading conditions of uniaxial stress (a) compression and (b) tension. The propensity of a grain to twin based on Schmid factor difference for uniaxial stress (c) tension and (d) compression.

Characterization of Twinning and Anti-twinning Asymmetry:

The current efforts, therefore, investigate the twinning and anti-twinning asymmetry in BCC using model single-crystal nanowires of Fe, Ta, Nb, and W for several loading orientations. A new approach is being developed to characterize twins and anti-twins in deformed microstructures without any prior information on loading orientation and direction. This approach uses VirTex to characterize twins in deformed microstructures. Figure 2(a) shows a relatively large twin (orange) in a deformed Fe nanowire along the [110] loading direction that spans the length of the nanowire under compression. Figure 2(b) shows smaller twins (orange, blue) in the nanowire after deformation in tension, i.e., in the anti-twinning direction. Since VirTex cannot distinguish the twins and anti-twins, virtual SAED is used to generate patterns, as shown in Figures 2 (c) and (d), under compression and tension. SAED from the individual twins characterized using VirTex enables the identification of the spots from twins in the SAED patterns, as outlined by red dashed circles. The peak positions and peak shifts relative to the matrix spots are then used to identify anti-twins and twins. A manuscript on this approach is currently being prepared for submission.

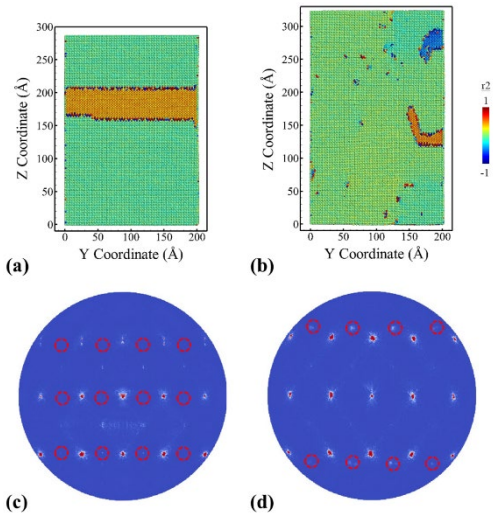

Figure 2: Deformed microstructures of Fe nanowires deformed along the [110] direction in (a) compression and (b) tension. The corresponding virtual SAED patterns are shown in (c) compression and (d) tension, where dashed red circles indicate contributions from twins.

Future Plans

Non-Schmid effects on the stability of transformation twins:

The current efforts have provided critical insights into the role of orientations (Schmid factor) and asymmetry (non-Schmid effects) on the twinnability of BCC single-crystal systems and nanocrystalline systems. Future efforts aim to investigate the role of this asymmetry on the variant selections during phase transformation that influences the stability of transformation twins in unloaded microstructures. MD simulations will be carried out to understand the stability of transformation twins in Fe single crystal systems following the $\alpha \rightarrow \varepsilon \rightarrow \alpha$ transformation under

conditions of uniaxial strain compression. The response will be compared with that for single crystal systems of Ta, Nb, and W systems for the same loading orientations and conditions wherein twins and anti-twins will be predicted. The hypothesis here is that the asymmetry between twinning and anti-twinning influences the stability of transformation twins. An example comparison shows the reverse-transformed single-crystal Fe microstructures loaded along the [110] orientation that shows twins in Figure 3(a), and along the [100] orientations showing no twins in Figure 3(c). A comparison with the deformed Ta single-crystal systems under the same orientations suggests that compression along the [110] orientation is along the twinning direction and shows longer twins in Figure 3(b). Similarly, compression along the [100] orientation is along the anti-twinning direction, showing smaller twins in Figure 3(d). These preliminary results suggest that a reverse transformed microstructure will render transformation twins if the loading orientation and direction are along that of a twinning shear. Similarly, a reverse-transformed microstructure will show no transformation twins if the loading orientation and direction are along the anti-twinning direction. These non-Schmid effects, if applicable, will also influence the variant selections during the $\alpha \rightarrow \varepsilon \rightarrow \alpha$ phase transformation in Fe microstructures and will be influenced by microstructure. These non-Schmid effects on the stability of transformation twins will be investigated to test the hypothesis.

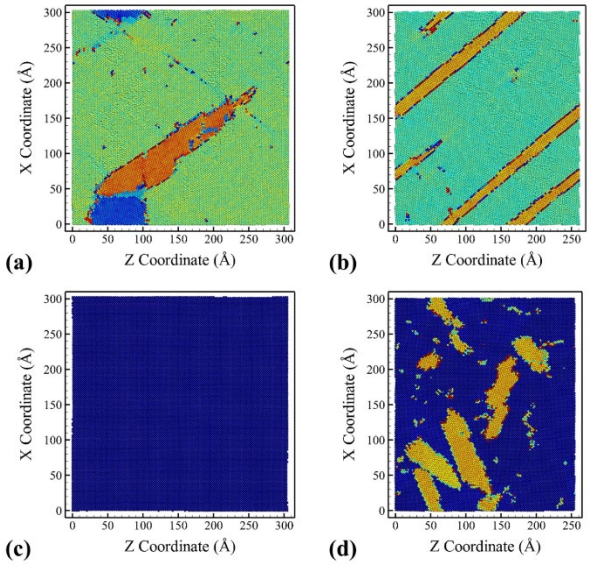

Figure 3: Microstructures of (a, c) unloaded Fe and (b, d) compressed Ta characterized using VirTex. Systems were loaded/unloaded along the (a, b) [110] twinning direction and (c, d) [001] anti-twinning direction.

References

1. A. Mishra, K. Ma, and A.M. Dongare, *Virtual diffraction simulations using the quasi-coarse-grained dynamics method to understand and interpret plasticity contributions during in situ shock experiments*, J. Mater. Sci., **57**, 12782 (2022).

Publications

1. A. Kannan, P. Tsurkan, and A. M. Dongare, Virtual texture analysis to understand microstructure effects on twinning and de-twinning behavior in polycrystalline Iron, Scientific Reports (submitted, in review)

Advancing clean energy through fundamental insights into defect generation and transport phenomena at grain boundaries in nuclear energy materials

S. Dillon[1], W. Neilson[2], J. White[2], M. Cooper[2], D. Andersson[2], S. Finkeldei[3]

[1]University of California, Irvine, Department of Materials Science and Engineering; [2]Los Alamos National Laboratory, Materials Science and Technology Division; [3]University of California, Irvine, Department of Chemistry;

Keywords: grain boundaries, defect generation, transport, bicrystal creep experiments

Research Scope

The transport kinetics at grain boundaries (GBs) affect numerous microstructure processes of considerable importance to nuclear fuel processing, lifetime, and safety. Moreover, all GB phenomena are coupled: a synergistic understanding of transport processes, irradiation, the impact of dopants, as well as the space charge effect will deliver new insight into our understanding of grain boundaries in materials. Recent efforts derived a new model for nucleation rate limited kinetics capturing existing creep data well. Experimental bicrystal creep efforts are combined with molecular dynamic efforts

Recent Progress

Self-diffusion due to vacancies and interstitials in UO_2 GBs has been examined using MD simulations. These results have been compared to UCI measurements revealing good agreement, with the difference being well-within one order of magnitude, see Fig. 1. This atomic scale data has been used to parameterize a cluster dynamics model to evolve GB defect concentrations under irradiation, as well as predict irradiation-enhanced self-diffusion and Coble creep rates. The model accurately reproduces creep rates for in-reactor irradiation conditions (see Fig. 2). Thus, a new mechanism of irradiation-induced creep through enhanced interstitial concentrations within the GBs is proposed.

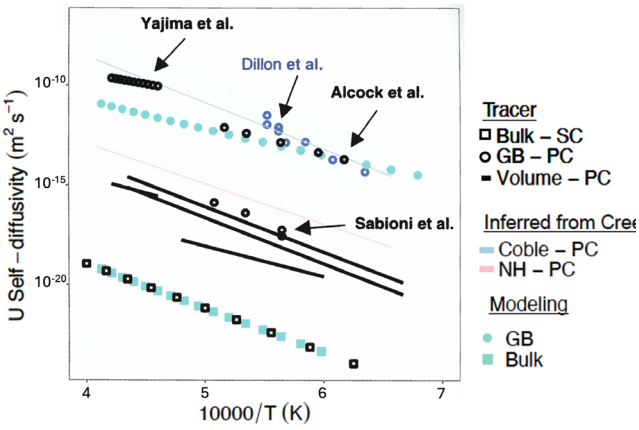

Figure 1. Comparison of atomic scale predictions and experiments of self-diffusivity at GBs and in the bulk UO_2 lattice. The results of this project can be seen by teal solid circles (modeling) and blue open circles (experiment by Dillon et al.).

This mechanism involves several inter-dependent processes. We were able to demonstrate that GB defect processes are tightly coupled to bulk defect processes: the bulk material acts as a source of

defects arriving at the GB under irradiation. This source is balanced at steady-state by loss of defects, either by defect-defect recombination, or annihilation at sinks. We show how defect incorporation at GB fission gas bubbles results in their pressurization, and how defect mobilities, which are GB structure-dependent, controls whether loss of defects to sinks or defect-defect recombination is favored. This fundamental behavior not only impacts creep, but other important mechanisms such as grain growth, sintering and fission gas behavior. Key to facilitating this is the high segregation energy of defects in ceramics; this results in higher defect concentrations at the GB compared to the bulk and promotes fast GB transport and Coble creep.

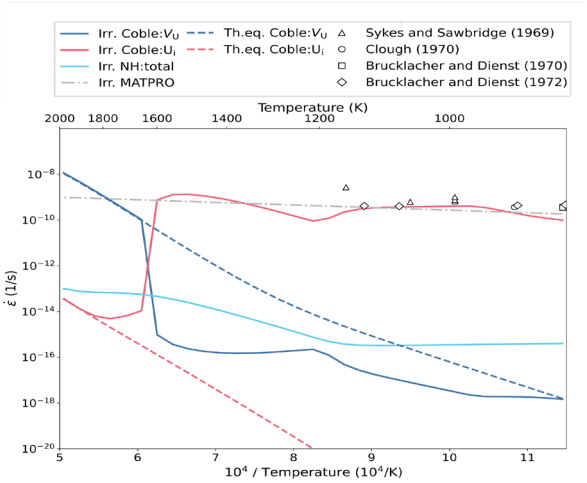

Figure 2. Predictions of Coble (GB diffusional) creep rate as a function of inverse temperature due to vacancies (blue lines) and interstitials (red lines). Dashed lines show the thermal equilibrium creep and the solid lines show the irradiation-creep for typical in-reactor conditions. Comparison is made to experiments carried out in-reactor (open symbols).

Non-Newtonian grain boundary creep

Bicrystal creep was performed as a function of temperature in UO_2. Fig. 3a shows an example of the profile of a bicrystal during tensile creep as a function of time and Fig. 3b provides the calculated stress along the length of the test specimen. The magnitude of the stress is on the order of 100 MPa. We fit the displacement rate, $\dot{z}_{nuc}$, as a function of radius, R; $\dot{z}_{nuc} = 2\pi R\dot{\eta}_o \exp\left(\frac{-H^* + S^*T - v^*\sigma}{k_B T}\right)$, where $\dot{\eta}_o$ is the attempt frequency, H^*, S^*, and v^* are the activation enthalpy, entropy and volume respectively, σ is the stress, k_B is Boltzmann's constant, and T is temperature. We compare the results with a polycrystalline creep model we developed in Ref. 1. The polycrystalline model defines the strain rate as $\dot{\varepsilon}^{nuc} = B\frac{v^*}{d^3}\dot{\eta}_o \exp\left(-\frac{H^* - S^*T - \sum_{i=1}^{i=n}(\Phi\sigma)_i v^*}{kT}\right)$, where B is a geometric factor approximately equal to unity. The key component of the model is a grain size dependent stress concentration factor, $\Phi \approx 0.5\sqrt{\left(a/l\right)}$ where a is the edge length of a grain, assumed to be half the grain diameter, and l is the distance of concern from the triple junction. Fig 3c shows a fit of the model to literature data for UO_2, note the model fit also transitions to Coble's model for diffusive creep. The activation volume is extracted from this model and is compared with the bicrystal creep result in Fig. 3d. The two models produce reasonable agreement supporting the validity of both. The nucleation rate limited kinetic model implies that the concentration of climb mediating GB disconnections are low at low stresses and that high local stresses are required to nucleate them. This result is counter to the common understanding of GB disconnections, which have been assumed to be abundant and/or able to nucleate at low stresses.

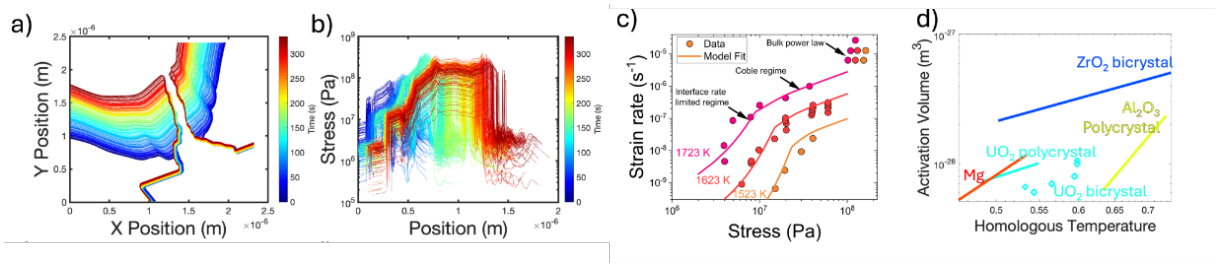

Figure 3.a) time dependent surface profile of a urania bicrystal deforming under tensile creep along with b) the calculated stress along the length of the sample. c) Provides a fit of our polycrystalline creep model to urania creep data from the literature. d) shows the activation volumes fit to our bicrystal experiments and polycrystalline data from the literature. The plot shows both urania data sets, which agree well within experimental uncertainty and uncertainty regarding differences in nominal sample chemistry.

One anticipates that the nucleation of high energy non-equilibrium GB dislocations should impact the physical properties of the boundaries. We tested this hypothesis by performing tensile fracture strength measurements at high temperatures as a function of loading rate, where fracture could be measured before and after yield. The onset of GB yield, and the associated nucleation of non-equilibrium GB dislocations, reduces the fracture strength of the boundary significantly; see Fig. 4. This observation was supported by complementary MD simulations that produced a similar trend. The results provide insights into how processing conditions can potentially influence the distribution of interfacial properties within polycrystals.

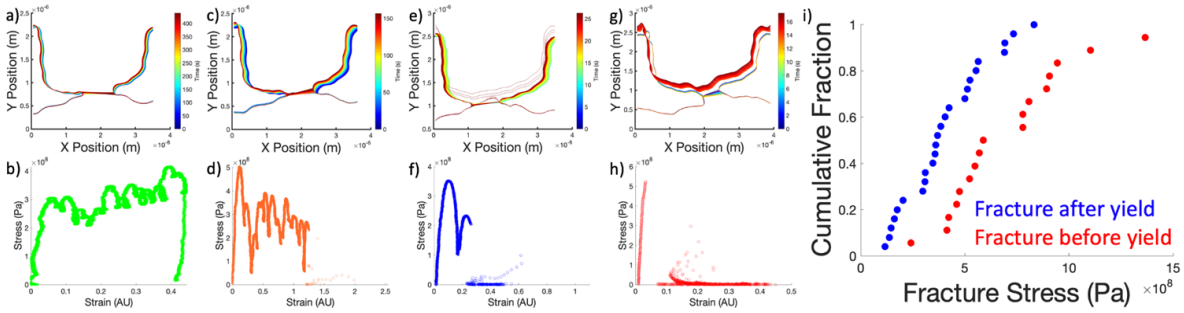

Figure 4. Time dependent surface profiles during tensile loading of zirconia along with the stress-strain response shown for increasing displacement rates. It is observed that the onset of yield reduces the subsequent fracture strength relative to brittle fracture prior to yield. The result suggests that the nucleation of non-equilibrium GB dislocations reduces the GB fracture strength.

Future Plans

The immediate future work will couple our new understanding of transport processes under irradiation (as described in recent progress) to the effects of GB electrical and dopant properties. Electrochemical impedance spectroscopy (EIS) is a technique capable of providing meaningful data on charge carriers mobility and transport in metal oxides, e.g. UO_2 and surrogates. Provided a change in the resistive/capacitive properties of a metal oxide resulting from irradiation events either using TRIGA reactor or ion beam implantation, this technique could potentially distinguish different mass transport processes. First EIS measurements are underway on a more simplistic

single crystal system in order to obtain understanding regarding the effects of irradiation on a system devoid of the complexities introduced by GBs, possibly unraveling radiation-enhanced transport mechanisms related to the bulk. Later EIS investigation will focus on GB effects using bi- or poly-crystalline oxide samples. GBs, in their role as defect sinks, present far more substantial capacitive properties (compared to the bulk), similar to an electrochemical double layer (charge separation). Exploring the specific nature of this double layer capacitance (Helmholtz, Gouy-Chapman-based models etc.) will enable detailed insights into radiation-derived transport in GBs. This experimental insight will be supported by a new model capable of predicting defect concentrations in the GB space charge layer, thus delivering mechanistic insight to our experimental predictions. The space-charge potential, derived from predicted point defect concentrations in the space charge layer, can be compared to electrical properties gathered via EIS measurements. Complementary experimental and theoretical predictions of the properties and impact of GBs is expected to prove particularly useful when studying the impact of dopants on GB properties.

Also using atomic scale modeling, we have set out to make a prediction of how dopants are accommodated within UO_2 grain boundaries. We hope to unlock fundamental understanding of how dopants control grain boundary transport and properties; this may unlock a pathway to exploiting the phenomenon. To do so, we have constructed a new DFT methodology based on higher fidelity physics, larger supercells and a more accurate description thermochemistry that highly accurately reproduces the known thermodynamics of UO_2. This is essential in this complicated ceramic system where temperature and oxygen partial pressure dictate the stoichiometry - and by extension, properties - of the material. This approach will form the basis of investigating the mechanism of Cr accommodation in the bulk and in grain boundaries, which, in turn, will allow the impact of doping on grain boundary to properties to be investigated. For example, if dopants change the charge compensation mechanism in the grain boundary they can alter the concentration and nature of defects that mediate creep.

Publications

1. Shen J. Dillon, Eric Lang, Sarah C. Finkeldei, Jia-hu Ouyang, Khalid Hattar, "A nucleation rate limited model for grain boundary creep" Acta Materialia, **246**, 118718 (2024).
2. Shen J. Dillon, Sarah C. Finkeldei, Eric Lang, Khalid Hattar, Andrew T. Nelson, *Using in situ UO_2 Bicrystal Sintering to Understand Grain Boundary Dislocation Nucleation Kinetics and Creep*, J. Am. Ceram. Soc. **107**, 6701-6714 (2024).
3. Isaac Martinez, Conor O.T. Galvin, Ryan M. Schoell, Michael W.D. Cooper, David A. Andersson, Khalid Hattar, Shen J. Dillon, *The effect of grain boundary yield and disconnections on grain boundary fracture strength*, Scripta Materialia, under revision.
4. Shen J. Dillon, Ryan M. Schoell, Andrew Wright, Jian Luo, Eugen Rabkin, Khalid Hattar, *Creep and failure at metal-oxide interfaces*, Acta Materialia, under revision.
5. Conor O.T. Galvin, David A. Andersson, Ryan T. Sweet, Laurent Capolungo, Michael W.D. Cooper, *Diffusional creep model in UO_2 informed by lower-length scale simulations,* Journal of Nuclear Materials, under review.
6. William D. Neilson, Conor O.T. Galvin, Shen J. Dillon, Michael W.D. Cooper, David A. Andersson, *Irradiation-induced creep in UO_2: the role of grain boundaries*, Phys Rev Materials, under review.
7. William D. Neilson, Jason Rizk, Michael W.D. Cooper, David A. Andersson, *Oxygen potential, uranium diffusion, and defect chemistry in $UO_{2\pm x}$: a density functional theory study*, Inorg. Chem., under review.

Stability of the B2 phase in refractory "high entropy" alloys

Maryam Ghazisaeidi (PI) and Michael Mills (Co-PI), The Ohio State University

Keywords: High entropy alloys, B2 ordering, phase stability

Research Scope

Improving energy efficiency requires the development of new materials capable of performing at high temperatures. Refractory multicomponent alloys with a BCC/B2 microstructure show potential as viable alternatives to the current leading Ni-based superalloys for use in elevated temperature environments. The overarching goal of this program is to provide a fundamental understanding of deformation mechanisms in a new class of two-phase multicomponent concentrated alloys, where disordered BCC and ordered B2-type phases coexist as either matrix or precipitates. Given the vast compositional space of these alloys, the fundamental question is whether the B2 phase can form among refractory metals. Here, we present our integrated computational/experimental approach to identify potential B2 formers among only refractory metals, explain the trends based on bonding nature, provide guidelines for identifying simplified compositions that can form the desired microstructure and validate the theory by making selected alloys and using multimodal characterization to confirm the presence of the B2 phase. These alloys will be used as testbeds to study slip transfer between a BCC matrix and B2 precipitates.

Recent Progress

Computational effort

There are no reports of binary B2 compounds formed by traditional refractory metals from group IV–VI elements. To encourage the formation of ordered phases, aluminum is often introduced into refractory high-entropy alloys (RHEAs). In some cases, this has led to the observation of a BCC/B2 structure. [1-3]. However, recent studies, including our own groups' investigation [P2], indicate that the Al- containing B2 phases in these alloys, are unstable and tend to transform into omega phases upon annealing [4]. Featuring our Multi-Cell Monte Carlo, $(MC)^2$ method, we searched the compositional space of refractory metals and identified promising combinations for more detailed analysis. We found that the B2 phase forms exclusively with the inclusion of elements from groups VII and VIII, such as Re, Ru, and Os. Further analysis of the electronic structure and bonding characteristics of these B2 systems revealed a pseudogap in the electronic density of states at the Fermi level. This pseudogap is attributed to the hybridization of *d* orbitals, leading to the formation of strong covalent bonds in the most stable compounds. This finding explains why B2 formation is restricted to elements from groups IV-VIII and V-VII refractory metals.

The procedure is summarized in Fig. 1 below. Our prediction of the formation of stable B2 phases between group IV elements and Ru aligns with experimental observations in refractory HEAs containing Ru in the literature. Notably, while Re has been used as an alloying element in refractory alloys, to the best of our knowledge, it has not been used to promote the formation of the B2 phase. In fact, no B2 phase is reported in the experimental phase diagram for the binary Ta-Re system. Therefore, this binary system has been

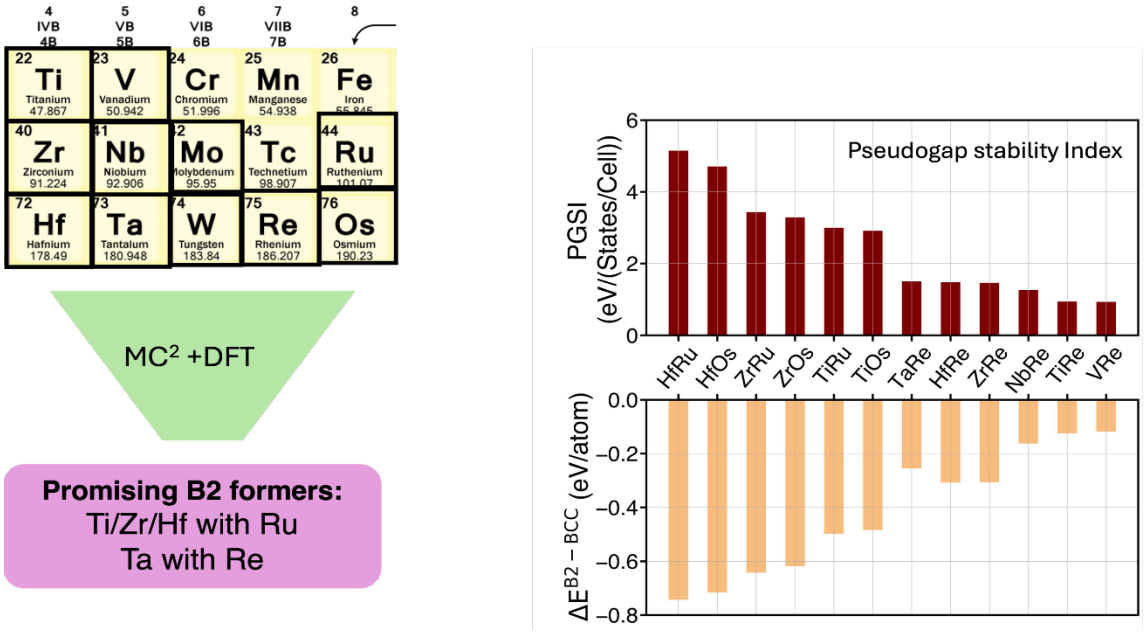

selected for further experimental investigation, with the primary objective of determining whether the B2 phase can indeed form in this alloy.

Fig.1 Summary of the computational procedure for identifying stable B2 phases among refractory metals.

Experimental effort

Alloy preparation:

The $Ta_{65}Re_{35}$ alloy was prepared by our collaborator Dr. Jean-Philippe Couzinié (ICMPE, France) into a 10 g button from raw metals in the form of slugs with a purity exceeding 99.9 wt%. The button was synthetized by arc melting on a water-cooled copper plate and subjected to 3 remelting to ensure chemical homogeneity. The alloy was then annealed at 1550 °C for 1 week in a furnace under dynamic Ar-atmosphere and then air-quenched. The alloy composition - measured by electron probe micro-analysis (EPMA) at 15 kV - was $Ta_{65.6}Re_{34.4}$.

Characterization:

Fig.2 shows the summary of the S/TEM characterization of the $Ta_{65}Re_{35}$ sample. A detailed microstructural characterization was performed on the annealed specimen using high-angle annular dark-field scanning transmission electron microscopy (HAADF STEM) and energy-dispersive X-ray spectroscopy (STEM EDS). The HAADF STEM micrograph taken along the [001] zone axis (ZA) reveals a body-centered cubic (BCC) matrix with cuboidal precipitates that display a higher atomic number (Z) contrast. The corresponding STEM EDS maps indicate significant rhenium (Re) enrichment within these precipitates. An integrated line scan across the matrix and precipitate shows a compositional transition from the $Ta_{65}Re_{35}$ matrix to a roughly equiatomic TaRe composition within the precipitates, which is expected if the precipitate adopts a B2 structure.

Further high-resolution STEM (HRSTEM) imaging provide additional insights. The matrix exhibits uniform atomic column intensity consistent with the expected BCC solid solution structure along the [001] ZA. Similarly, the precipitate displays a uniform atomic column intensity with no observed alternating intensity along the <110> direction, and the absence of {100} superlattice reflections in the FFT does not indicate the existence of the B2 structure. However, simulations of TaRe B2 diffraction pattern revealed that indeed it may not be able to distinguish the B2 superlattice reflections due to very similar atomic numbers of Ta and Re.

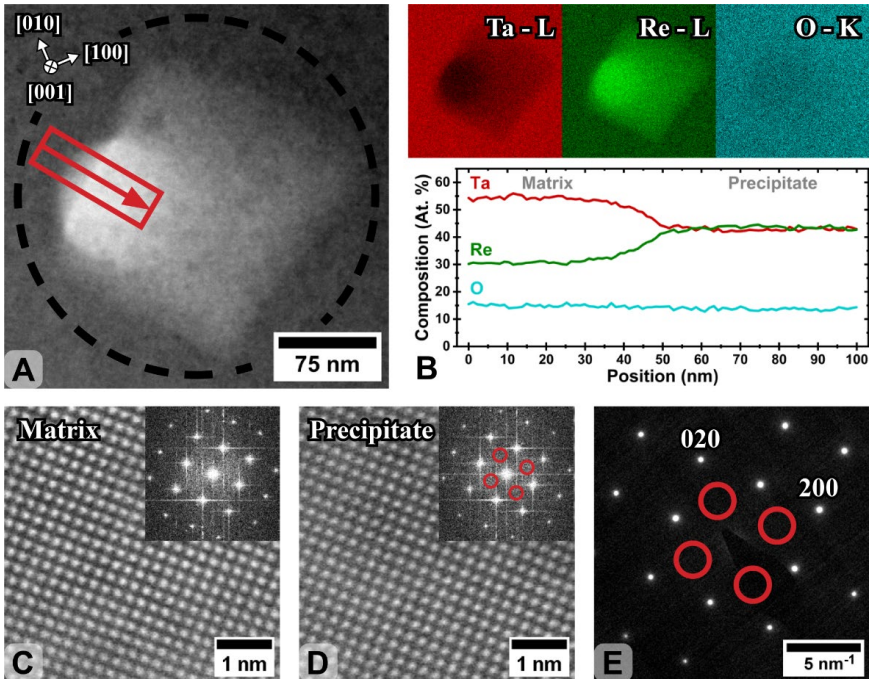

Fig. 2: Characterizing Microstructure of $Ta_{65}Re_{35}$ annealed specimen (a) [001] ZA HAADF STEM micrograph showing BCC matrix and cuboidal higher Z precipitate. (b) STEM EDS maps exhibit Re enrichment in the precipitate with integrated line scan from (a) showing transition from $Ta_{65}Re_{35}$ composition in the matrix to roughly equiatomic $TaRe$ in the precipitate. HRSTEM micrographs and FFTs show the (c) matrix exhibits uniform atomic column intensity and the [001] ZA FFT expected for a BCC solid solution. This is also observed for the (d) precipitate with no alternating atomic column intensity along <110> and no {100} superlattice reflections (circled in red) which would be expected for the B2 structure. (e) A DP was collected corresponding to the black dotted circle in (a) also show no signs of B2 {100} superlattice reflections (circled in red).

Next, Neutron diffraction was used to observe superlattice peaks, particularly useful for elements with similar atomic numbers (Z). Upon submission of a rapid response proposal, the measurements were conducted in collaboration with Dr. Si Athena Chen who is a Neutron Diffraction Instrument Scientist at ORNL. The diffraction spectra confirmed the presence of the B2 phase, with notable shouldering of the fundamental peaks suggesting the existence of a second cubic phase. The detection of {100} and {210} B2 superlattice peaks further validated the B2 structure. Through refinement, the B2 phase was estimated to constitute 28.53% of the volume, with a calculated lattice mismatch (δδ) of -0.59%. Fig.3 summarizes these results.

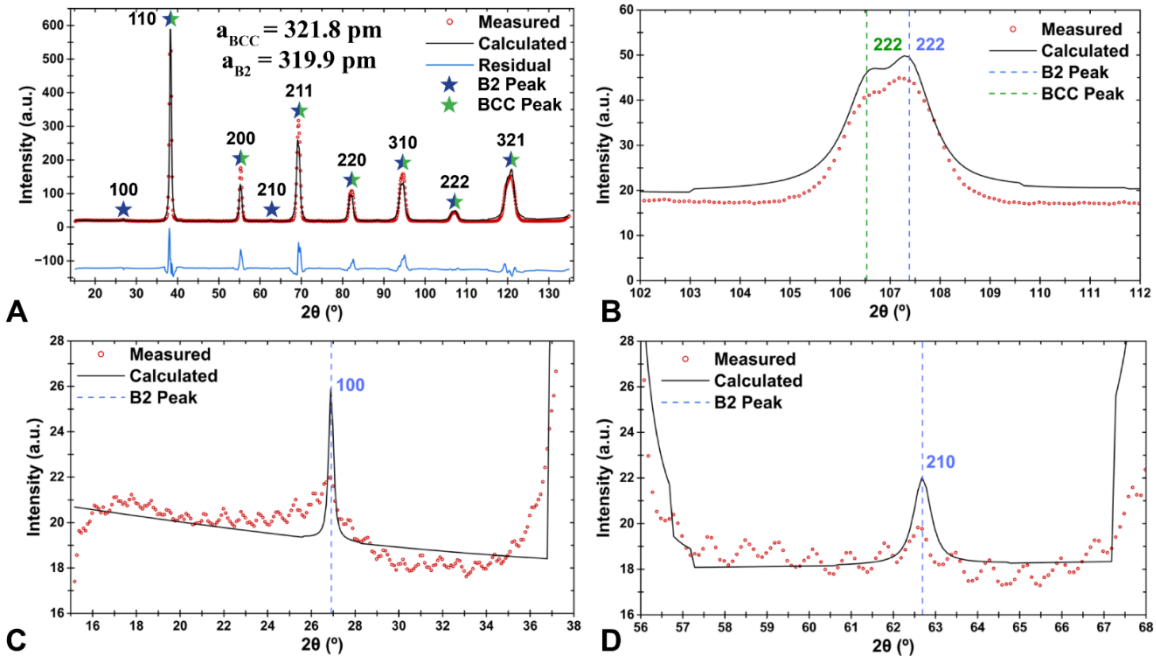

Fig. 3: For the $Ta_{65}Re_{35}$ annealed specimen (a) full Rietveld refined neutron diffraction spectra with a clear match for BCC fundamental peaks. The shouldering of fundamental peaks was exhibited at higher 2θ angles such as (b) the 222 plane indicating the presence of. Faint B2 superlattice peaks were also observed at (d) the 100 plane and (e) the 210 plane matching the lattice parameter of the second cubic structure.

Future Plans:

Experimentally, we are working on 4D STEM investigation of the B2 phase to complete the characterization. Next step involves mechanical deformation and studying the deformation behavior. Computationally, we will develop a machine learning interatomic potential to study dislocation behavior and slip transfer between the BCC and B2 phases of the binary Ta-Re model system via atomistic simulations.

References:

[1] D. B. Miracle et al., Refractory high entropy superalloys (RSAs), Scripta Materialia 187 (2020) 445–452.

[2] W. Xiong et al., Refractory high-entropy alloys: A focused review of preparation methods and properties, Journal of Materials Science & Technology 142 (2023) 196–215.

[3] Z. T. Kloenne et al., On the bcc/B2 interface structure in a refractory high entropy alloy, Scripta Materialia 223 (2023) 115071.

[4] Sharma, A. et al. B2 to ordered omega transformation during isothermal annealing of refractory high entropy alloys: Implications for high temperature phase stability. Journal of Alloys and Compounds 953,

Publications:

1. Junxin Wang; Ali Barooni; Maryam Ghazisaeidi, “Stability of the B2 phase among refractory metals", *Acta Materialia*, 279, 120323 (2024).
2. Julian Brodie; Junxin Wang; Jean-Philippe Couzinie; Milan Heczko; Veronika Mazanova; Michael J Mills; Maryam Ghazisaeidi, “Stability of the B2 phase in refractory high entropy alloys containing aluminum", *Acta Materialia* 268, 119745 (2024).
3. O.N. Senkov, B. Crossman, S.I. Rao, J.P. Couzinie, D.B. Miracle, T.M. Butler, R. Banerjee, M. Mills, “Mechanical properties of an $Al_{10}Nb_{20}Ta_{15}Ti_{30}V_5Zr_{20}$ A2/B2 refractory superalloy and its constituent phases”, *Acta Materialia*, 254, 119017 (2023)
4. J.P. Couzinie, M. Heczko, V. Mazanova, O.N. Senkov, M. Ghazisaeidi, R. Banerjee, M. J Mills, “High-temperature deformation mechanisms in a BCC+ B2 refractory complex concentrated alloy", *Acta Materialia,* 233, 117995 (2022)

Nanostructured Metallic Glasses through Ultra-Fast Joule Heating

Wendy Gu

Keywords: amorphous, nanocrystal, iron, ductility, magnetic

Research Scope

Metallic glasses are known to have low ductility, which limits their applications as structural materials. Iron-based metallic glasses are also gaining attention as high performance soft magnetic materials for use in electric machines such as electric motors, transformers and turbines[1]. Understanding the fundamental deformation mechanisms in these metallic glasses is imperative to achieve sufficient strength, ductility and toughness in industrial applications. One strategy to increase ductility and toughness is to introduce crystalline domains at length scales that limit shear banding, and introduce additional plasticity mechanisms. The introduction of nanocrystals into metallic glasses has been observed by our group and others to increase ductility[2].

Current methods of obtaining nanocrystals within iron-based metallic glasses utilize rare earth metals, such as niobium, to have better control of the crystallization time scale, or copper to increase the number of nucleation sites[3,4]. Here, we explore the use of ultra-fast Joule heating to achieve nanocrystals within iron-based metallic glasses (FeSiB) without these alloying elements. In this way, we will control the crystallization kinetics while maintaining a simple chemical composition, which is beneficial for understanding atomistic bonding and mechanical behavior. We will determine the crystallite size and density that is optimal for strength and ductility, and their influence on nanoindentation, tension and bending deformation mechanisms.

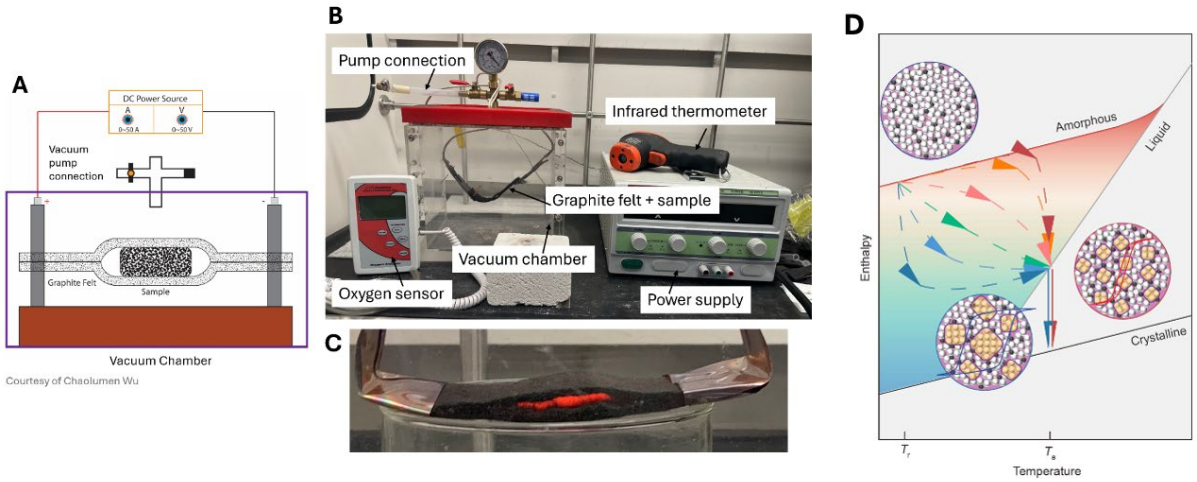

Figure 1. A) Schematic and B-C) photos of ultra-fast Joule heating setup in the Gu lab. C) Schematic of metallic glass crystallization kinetics[5].

Ultra-fast Joule heating has recently emerged as a method for the rapid processing of ceramics, magnetic materials, and cermets, which has been used to make metallic glasses in the past. A setup has been built in our lab (Figure 1). We hypothesize that fast heating to temperatures above the glass transition temperature, and short hold times will lead to the nucleation of a high density of nanocrystals but limited crystal growth. This rapid annealing has been demonstrated in iron-based metallic glasses using pre-heated Cu blocks[3,4], and a calorimetry setup[5], but has not yet been achieved using ultra-fast Joule heating, which is a scalable method with programmable heating and holding steps.

Initial experiments on FeSiB show that high heating rates of ~15 W/s and short hold times generally lead to amorphous/nanocrystalline XRD curves with one broad scattering peak although some samples crystallize fully (Figure 2). The heating rate and hold times are set to correspond to the two crystallization peaks of FeSiB.

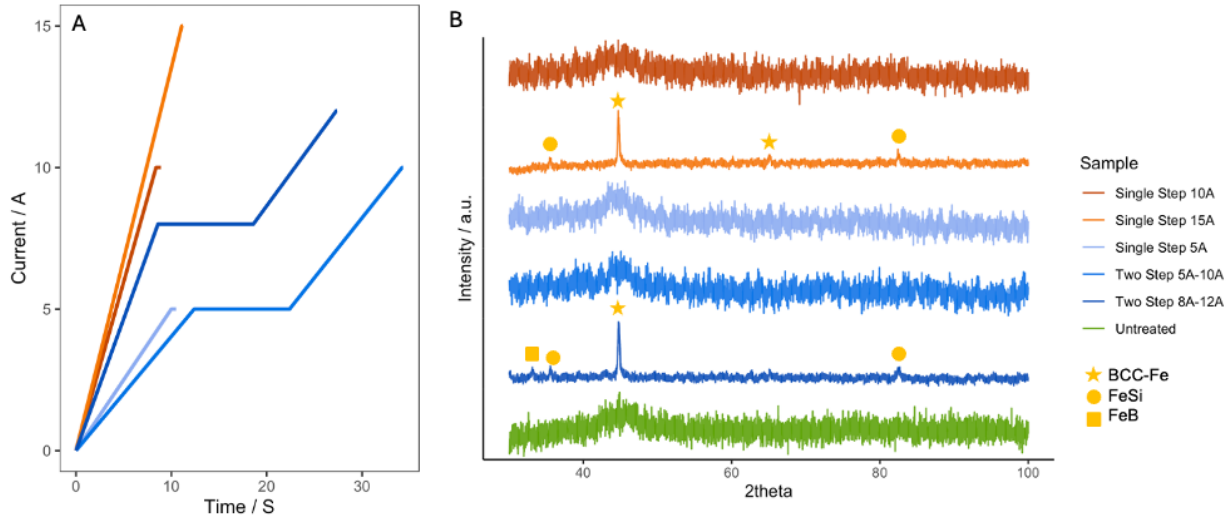

Figure 2. Preliminary results. A) Example ultra-fast heating curves. B) Example XRD curves after ultra-fast heating.

Magnetic measurements (B-H curves) were used as a rapid method to detect structural changes within the samples with amorphous/nanocrystalline XRD curves. Samples treated with the two-step annealing protocol present a superior magnetic saturation compared to the untreated sample (Figure 3). These samples also present coercivities comparable to the untreated sample, indicating that the nucleated crystals are below the superparamagnetic threshold. We anticipate that these samples will contain a large volume of crystallites smaller than 25 nm, which will be confirmed using scanning and transmission electron microscopy.

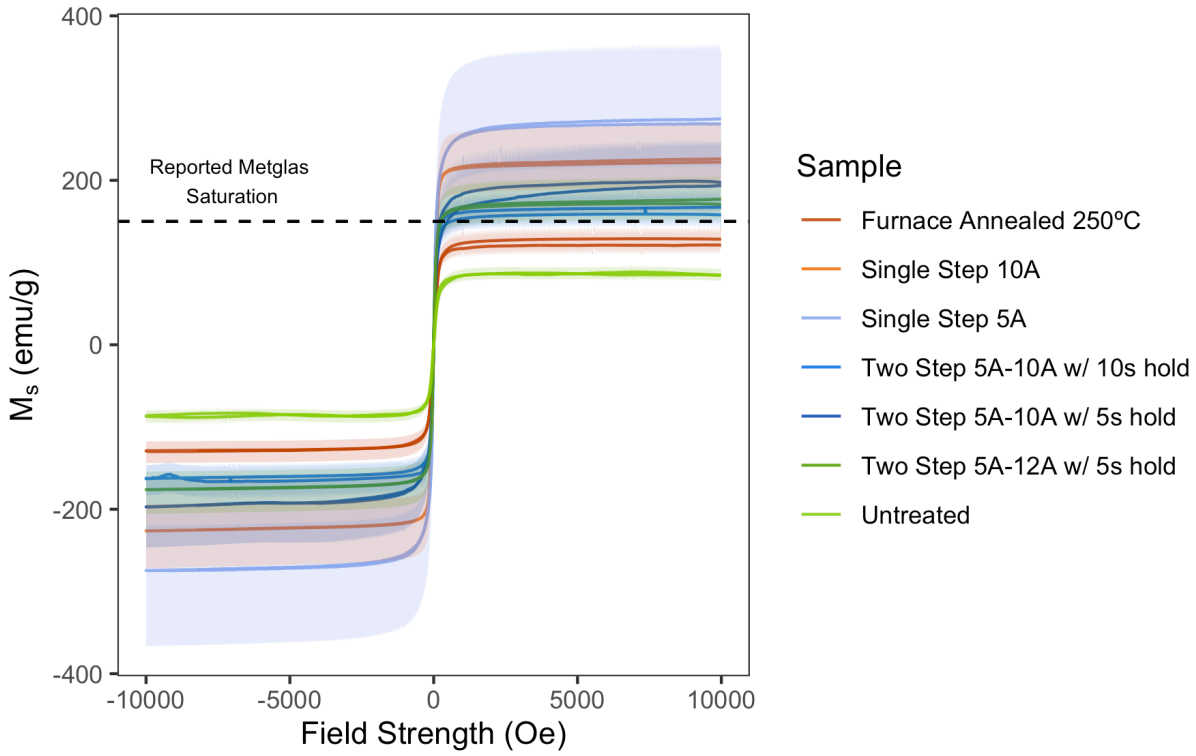

Figure 3. Example B-H loop measurements of treated samples.

Recent Progress

The current research builds on our recent progress on the synthesis and mechanical characterization of nanostructured metallic glasses. This includes the colloidal synthesis of ductile nickel boride metallic glass nanoparticles (Kiani et al., Nano Letters (2020)), and crystalline nanoparticles with amorphous metal shells (Kiani et al., RSC Advances (2023)). Using these synthetic techniques, we synthesized iron-based metallic glass nanoparticles at scale, which were sintered into bulk nanostructured metallic glasses with amorphous grain boundaries (Wang et al., JMST (2023)). Fracture occurred along the amorphous grain boundaries. Ductility was correlated with the formation of nanocrystals within the nanostructured metallic glass.

The metallic glass nanoparticles were found to be highly stable at GPa-level pressures (Parakh et al., J. Non. Crys. Solids (2022)), which led us to explore additional nanostructured metals at high pressure. We obtained nanotwinned alloys from Prof. Andrea Hodge at USC, which were compressed in a diamond anvil cell. We found that nanotwinned $Cu_{89.3}Ni_{10.7}$ experienced grain growth and detwinning at high pressure (Wang et al., In preparation; Figure 4). In collaboration with the group of Prof. Huajian Gao, molecular dynamics simulations revealed that hydrostatic pressure causes elevated local shear stress at grain boundaries, which leads to atomic rearrangements. A superposition of hydrostatic and deviatoric pressures lead to partial dislocation mediated twin boundary migration. The manuscript on this project has been completed, and will be submitted to *Acta Materialia* in the next week.

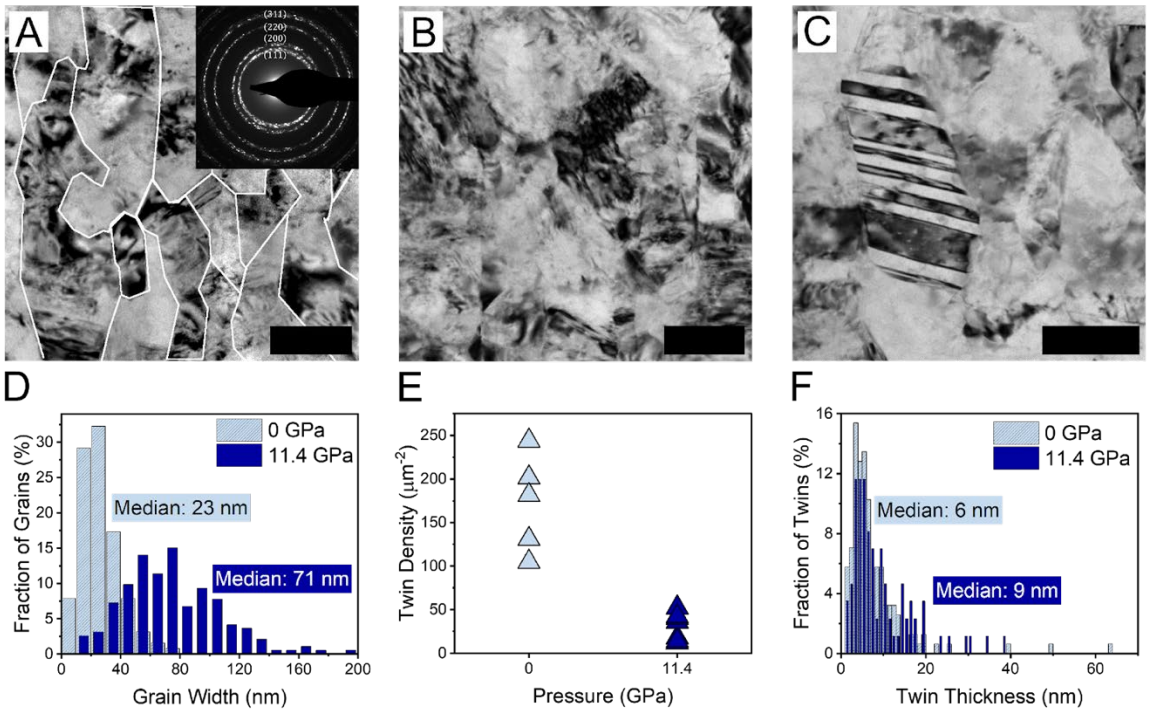

Figure 4. Microstructural changes after high pressure compression of $Cu_{89.3}Ni_{10.7}$ sample. A) Bright field image of the as-synthesized $Cu_{89.3}Ni_{10.7}$ sample with grain boundaries outlined in white. The inset shows no obvious preferred orientation. Bright field images of the post-compressed $Cu_{89.3}Ni_{10.7}$ sample showing B) unidentifiable twin boundaries and C) stable twin boundaries. The scale bars for the TEM images are 100 nm. Comparison of D) grain width, E) twin density, and F) twin thickness in the as-synthesized and post-compressed $Cu_{89.3}Ni_{10.7}$ sample.

Future Plans

In the next year, we plan to complete the structural, mechanical and magnetic characterization of iron-based metallic glasses subjected to ultra-fast Joule heating. Differential scanning calorimetry will be used to understand the crystallization process. Scanning and transmission electron microscopy will be used to directly image the formation (or absence) of nanocrystals, and their spatial distribution. Nanoindentation will be used to characterize elastic modulus and hardness, and an initial estimate of ductility by observing whether cracks form at the corners of the indentation. If nanoindentation results are promising, samples in the shape of ribbons will be tested in tension and bending to obtain stress-strain curves, and measure yield strength and ductility. This mechanical behavior will be correlated to signs of shear banding and/or plasticity at the nanocrystals. Initial experiments will be performed on an FeSiB metallic glass (MetGlas), after which other metallic glasses will be investigated to explore the connection between composition, crystallization kinetics and mechanical behavior.

References

1. H.X. Li, Z.C. Lu, S.L. Wang, Y. Wu, Z.P. Lu. "Fe-based bulk metallic glasses: Glass formation, fabrication, properties and applications." *Progress in Materials Scienc*e, 103 (2019).

2. **M.W. Wang, M.T. Kiani, A. Parakh**, Yue Jiang, X.W. Gu, "Effect of Grain Size on Iron-Boride Nanoglasses". *Journal of Materials Science and Technology. 141, 116-123, (2023).*

3. K.G. Pradeep, G. Herzer, D. Raabe, "Atomic scale study of CU clustering and pseudo-homogeneous Fe–Si nanocrystallization in soft magnetic FeSiNbB(CU) alloys." *Ultramicroscopy,* 159 (2015).

4. K.G. Pradeep, G. Herzer, P. Choi, D. Raabe, "Atom probe tomography study of ultrahigh nanocrystallization rates in FeSiNbBCu soft magnetic amorphous alloys on rapid annealing." *Acta Materialia*, 68 (2014).

5. B. Zang, L. Song, R. Parsons, J. Shen, M. Gao, Y. Zhang, J. Huo, Y. Sun, F. Li, K. Suzuki, J.Q. Wang, W. Wang "Influence of thermal history on the crystallization behavior of high-Bs Fe-based amorphous alloys." *Science China, Physics, Mechanics and Astronomy*, 66 (2023).

Publications

1. **M.M. Wang,** R. Dang, **A. Parakh, A.C. Lee**, Z. Li, S. Chariton, V.B. Prakapenka, *J. Kang,* Y.W. Zhang, A. Hodge, H. Gao, X.W. Gu, "Nanotwinned Alloys Under High Pressure." *In preparation.*

2. **M.T. Kiani, A. Parakh**, E. Lindgren, **A. Colmena, A.C. Lee**, Y. Suzuki, X.W. Gu, "Synthesis of Multifunctional Amorphous Metal Shell on Crystalline Metallic Nanoparticles". *RSC Advances. 13, 20491-20498 (2023).*

3. **M.W. Wang, M.T. Kiani, A. Parakh**, Yue Jiang, X.W. Gu, "Effect of Grain Size on Iron-Boride Nanoglasses". *Journal of Materials Science and Technology. 141, 116-123, (2023).*

4. **A. Parakh**, **M.T. Kiani, A.A. Colmenares**, **A.C. Lee**, G. Shen, S. Chariton, V.B. Prakapenka, X.W. Gu, "High Pressure Deformation of Metallic Glass Nanoparticles". *Journal of Non-Crystalline Solids. 597, 121923 (2022).*

5. **A. Parakh, A.C. Lee,** S. Chariton, **M.M. Wang, M.T. Kiani,** V. Prakapenka, X.W. Gu, "High Pressure Induced Precipitation in Al-Zn-Mg-Cu alloy (Al7075)," *Materials Science and Engineering A. 853, 143765 (2022).*

6. **M.T. Kiani,** Z. H. Aitken, **A. Parakh,** Y.W. Zhang, X.W. Gu, "Extraordinary Strain Hardening from Dislocation Loops in Defect-Free Al Nanocubes," *Nano Letters. 22, 10, 4036-4041 (2022).*

Computational and Experimental Investigation of Cryogenic Grain Boundary Motion for Enhanced Mechanical Properties

PI: Eric R. Homer, Brigham Young University, Provo, UT, USA.
Co-PI: Gregory. B Thompson, University of Alabama, Tuscaloosa, AL, USA.
Co-PI: Oliver K. Johnson, Brigham Young University, Provo, UT, USA.

Keywords: Grain Boundaries, grain boundary migration, cryogenic temperatures

Research Scope

The major goal of the project is to determine the feasibility of cryogenic processing to obtain enhanced mechanical properties by influencing the microstructural network of grain boundaries (GBs). GBs have a significant influence on numerous material properties, including strength and ductility. Conventionally, high temperature processing enables all GBs to migrate whereas cryogenic processing could allow select GBs to migrate (Zhang, 2005; Brons 2014). This presents a transformational opportunity to create different microstructural networks at cryogenic temperatures that have enhanced strength and ductility.

In past periods of this project, we have shown how ordered atomic migration mechanisms appear to be the source of this cryogenic mobility and the non-thermally activated nature of the migration. Key work during the past period demonstrated that a classical model for GB migration reconciles all the non-Arrhenius behaviors with a thermally activated model, which is consistent with traditional models for boundary migration (Homer, 2022). Currently, we are examining how to use the classical model to predict and control the conditions for non-Arrhenius migration.

Recent Progress

To understand how we have been using the classical model to predict and control the conditions for non-Arrhenius migration, we briefly review the classical model here. This classical model, which is arguably a forgotten model of migration, does not make particular assumptions common to the traditional model used by most researchers. This classical model is based on a simple two-state system for atoms jumping between two grains where an energetic barrier, Q, separates the two states (Homer, 2022). Here, migration is biased in one direction by a driving force p. A combination of forward and backwards jumps results in the following velocity model

$$v = v_o \exp\left(\frac{-Q}{k_B T}\right) 2\sinh\left(\frac{-p}{2k_B T}\right) \quad (1)$$

where v is the velocity, v_o is a reference velocity, k_B is Boltzmann's constant and T is temperature. Equation 1 simplifies to the traditional form of $v = Mp$ when $p \ll k_B T$, where M is the mobility.

But, this assumption is not always valid, as in the case of cryogenic conditions. In such conditions, the full equation leads to interesting insights.

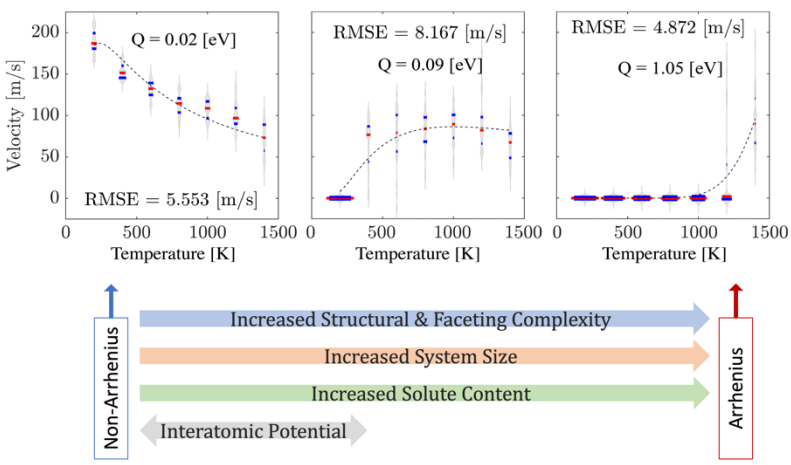

Figure 1. (top) Plot of velocity for 3 different metastable GBs. (bottom) Illustration of how factors change migration behaviors.

At high values of Q, one gets Arrhenius behavior at all temperatures, while at low values of Q, the result is Arrhenius behavior at low temperatures and non-Arrhenius behavior at higher temperatures (c.f. Figure 1). The non-Arrhenius behavior results from the increased frequency of "backwards" jumps that inhibit forward migration of the boundary at higher temperatures when the intrinsic barrier, Q, is sufficiently small. This classical model fits with the observations that the ordered atomic motions are increasingly frustrated at higher temperatures, leading to the non-Arrhenius response (Homer, 2022). With this new understanding, it is now clear that this 'forgotten' classical model of GB migration accounts for the non-Arrhenius behaviors and cryogenic coarsening observed in the past two decades (Zhang, 2005; Brons 2014). Finally, the classical model reconciles other observations in the literature that are not reviewed here for brevity. Thus, one may use this classical model to predict the conditions under which non-Arrhenius boundary migration might occur and how it can be controlled.

One of the first efforts by us following the publication of the classical model was to determine how a variety of different factors impact non-Arrhenius migration (Verma, 2023). The three velocity plots in Figure 1 are for different (metastable) atomic configurations for a GB with the same crystallographic character. Since these are the "same" GBs, it is clear that GB structure plays a critical role on the migration behaviors exhibited by a given GB. Specifically, we found that increased structural complexity, or boundaries with increasingly complex faceting, exhibited slower boundary migration with higher Q values. System size of the simulations also played an important role and we found that the same boundaries in large simulation cells migrated more slowly. Finally, a comparison of six different nickel interatomic potentials revealed that while there is some variability in the response of the different potentials, the behaviors were remarkably similar. In a different publication, it was also shown that non-Arrhenius migration can be induced with mechanical loading (Dora, 2024).

In investigating the effect of solute content on non-Arrhenius migration (Verma, 2024), we were unsurprised to see that increased solute content led to Arrhenius migration. However, we were surprised to find that the nature for this transition was highly dependent on the amount of solute and driving force. At high driving forces, the boundary migrated in a non-Arrhenius manner

up to 10 at.% Cu solute in Ni. But, at low driving forces, the boundary began to exhibit stick-slip behavior around 2-4 at.% Cu solute and had characteristics of both non-Arrhenius and Arrhenius migration. Overall, the results were consistent with the Cahn-Lücke-Stüwe (CLS) model except that no solute drag was observed; rather, the solute effects were likely the result of solute pinning. This suggests that the non-Arrhenius migration can be controlled by both driving force and solute content.

Experimental verification of these findings first involved ex situ indentation (Robinson, 2023a). In this work, a series of copper nanotwinned columnar grains were solid solution alloyed with aluminum and subject to ambient and cryogenic (−196 °C) environments during mechanical indentation. Post-mortem characterization by transmission electron microscopy (TEM) provided insight into the microstructural evolution and the influence of alloying on the detwinning that occurred. Under indentation, at a lower aluminum solute content (2 at.%), the columnar grains bent corresponding to a loss of twins. At a higher aluminum solute content (8 at.%), the grains shear and retained the nanotwins. Atomistic-scale simulations revealed an increase in the incoherent twin boundary velocity with decreasing temperature (consistent with the classical model), but this boundary velocity was also reduced with increasing alloy solute content. The coupling of solid solution strengthening and nanotwin stabilization was then used to explain the microstructural stability as a function of indentation at different temperatures and solute content, as summarized in Figure 2.

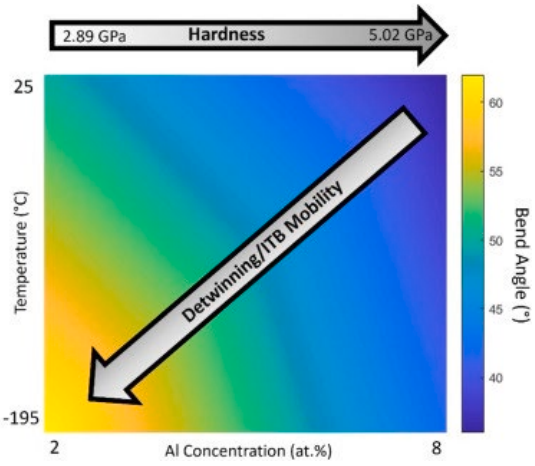

Figure 2. Summary plot of the relationships of solute content, hardness, and microstructural evolution characteristics.

Subsequent in situ cryogenic indentation has been developed and carried out in partnership with Bruker-Hysitron Micromechanical Systems, which resulted in their new product Pi89 Cryo indenter. The same columnar nano-twinned samples were prepared and indented parallel and tilted (~10° from parallel) to the surface of an indenter. The titled condition immediately facilitated a non-zero Schmid factor on the twin plane upon loading. These samples were prepared as a series of approximately 1 μm diameter pillars that were focus ion beam milled from the approximately 2.1 μm thick films (Robinson, 2024a). All alloys and twin conditions revealed a higher ultimate load as temperature decreased with the angled twin condition modestly reducing the measured ultimate load. Serrations in the load-displacement response were also observed as the temperature decreased. Interestingly, most samples under loading revealed a sinusoidal load-displacement response attributed to a macroscopic deflection of the pillar under the indenter. This modulation was facilitated by the deformation evolution being accommodated in upper portions of the pillar that was in contact with the indenter coupled with the retention of a high density of nanotwins throughout the remainder of the pillar. Where deflection was absent, notable barreling of the pillar

shape as well as detwinning within the pillar was observed indicting that the retention of twins strengthens the pillar resisting macroscopic deformation shape changes. Finally, shear banding was observed in the highest alloyed film at the lowest testing temperature revealing an important interaction between detwinning and dislocation pile-up at twin boundaries.

In order to better track in situ deformation, advanced TEM characterization in the form of digital image correlation (DIC) was pioneered by the group (Robinson, 2024b). DIC is routinely applied using optical and scanning electron microscopy methods to map local strains during deformation but has had limited applicability in TEM because of the complex contrast generation mechanisms. Nevertheless, the deformation mechanisms themselves contribute to this contrast and if one can track these changes, this can provide unique insights into boundary migration and local strain states. To achieve this end, we have recently published a variety of image analysis methodologies to enable the correlation of such features across a series of images. Through frame averaging, we were able to reconcile the average DIC strain with the far field strain values, providing increased confidence in its application while giving nanoscale insight to strain localization. Our results have now been applied in quantifying the effect of different deformation responses in a nanostructures, including dislocation propagation, cross-slip, Hall-Petch strengthening, and grain boundary strain accommodation that lend insights into inter- vs. intra-granular deformation.

Future Plans

Our in situ cryo-indentation setup will soon be used to track grain coarsening at several temperatures to compare experimental measurements with the predictions of the classical model (Eq. 1). By being in situ, these experiments will provide definitive observations of cryogenic migration. In these experiments we will also employ the use of DIC to capture the local strain environment that supports this migration. Furthermore, atomistic simulations are underway to verify the energetic Q values experienced by the migrating atoms with predictions obtained by fitting the velocity trends as in Figure 1. Other simulation work will examine the non-Arrhenius migration in the disconnection framework to understand how they correlate with overall GB migration and the classical model. Finally, migration will be sampled across the 5D space of crystallographic character in atomistic simulations, to understand the extent to which non-Arrhenius migration can be expected.

References

1. K. Zhang, J.R. Weertman, and J.A. Eastman, *Rapid stress-driven grain coarsening in nanocrystalline Cu at ambient and cryogenic temperatures*. Applied Physics Letters **87**, 061921 (2005).
2. J.G. Brons, J.A. Hardwick, H.A. Padilla II, K. Hattar, G.B. Thompson, and B.L. Boyce, *The role of copper twin boundaries in cryogenic indentation-induced grain growth*. Materials Science & Engineering A **592**, 182 (2014).

3. E.R. Homer, O.K. Johnson, D. Britton, J.E. Patterson, E.T. Sevy, and G.B. Thompson, *A classical equation that accounts for observations of non-Arrhenius and cryogenic grain boundary migration*, npj Computational Materials **8**, 157 (2022).

Publications

1. J. Robinson, E.R. Homer, and G.B. Thompson, *Temperature Dependent Twin Stability in Nanocrystalline Cu(Al) Under in-situ Cryogenic Pillar Compression*, Acta Materialia, Under review (2024a).
2. A. Robinson, E.R. Homer, and G.B. Thompson, *Application of digital image correlation for in-situ deformation studies using transmission electron microscopy*, Scripta Materialia **252**, 116253 (2024b).
3. A. Verma, O.K. Johnson, G.B. Thompson, S. Ogata, and E.R. Homer, *Solute influence in transitions from non-Arrhenius to stick-slip Arrhenius grain boundary migration*, Acta Materialia **265**, 119605 (2024).
4. A. Verma, O.K. Johnson, G.B. Thompson, I. Chesser, S. Ogata, and E.R. Homer, *Insights into factors that affect non-Arrhenius migration of a simulated incoherent Σ3 grain boundary*, Acta Materialia **258**, 119210 (2023).
5. J. Robinson, A. Verma, E.R. Homer, and G.B. Thompson, *Nanotwin stability in alloyed copper under ambient and cryo-temperature dependent deformation states*, *M*aterials Science and Engineering: A **871**, 144866 (2023a).
6. T. Dora, S.K. Singh, R.R. Mishra, E.R. Homer, S. Ogata, and A. Verma, *Deformation and boundary motion analysis of a faceted twin grain boundary*, International Journal of Mechanical Sciences **269**, 109044 (2024).
7. J. Robinson, E.D. Hintsala, D.D. Stauffer, S. Bhowmick, E.R. Homer, and G.B. Thompson, *Pearlite Size Effects on Ductility at Cryogenic Temperature via In-Situ Cantilever Loading*, Microscopy and Microanalysis **29**(Supplement_1), 1521 (2023b).
8. J. Robinson, E.D. Hintsala, E.R. Homer, and G.B. Thompson, *Stability of Nanotwins under in-situ Cryogenic Micro-Pillar Compression*, Microscopy and Microanalysis **29**(Supplement_1), 1500 (2023c).
9. R. Li, E.R. Homer, Y. Zhang, and D.J. Jensen, *Σ3 grain boundary dynamics studied by atomistic spherical bicrystal modeling*, Journal of Physics: Conference Series **2635**(1), 012025 (2023).

Understanding the Role of Surface Energy in the Deformation of Metal Nanoparticles

Tevis D.B. Jacobs (University of Pittsburgh) & Ashlie Martini (University of California, Merced)

Keywords: Nanoparticles, Deformation mechanisms, Dislocations, Surface diffusion,

1. Research Scope

Surfaces play a critical role in nanoscale deformation both due to surface-dislocation nucleation and surface diffusion; however, fundamental understanding of these mechanisms and their competitive or cooperative role in the mechanical behavior of nanoparticles is lacking. The long-term goal of this research program is to achieve fundamental understanding of how surface energy modifies (and is modified by) "bulk" deformation in nanoparticles. In service of that long-term goal, the current objective of this research is to understand how surface faceting and surface energy affect the deformation of small metal nanoparticles under compression. This research is carried out through a combination of *in situ* compression testing of nanoparticles inside of a transmission electron microscope with complementary atomistic simulations using molecular dynamics.

2. Recent Progress

2.1. Methods: Combining *in situ* TEM experimentation and atomistic simulation.[1]

In *in situ* experiments, platinum nanoparticles deposited directly on the substrate of an *in situ* nanomanipulator and are then compressed inside of a transmission electron microscope. The high-resolution video during compression enables characterization of the shape and size of the experimental nanoparticles,[2] as well as the calculation of the true strain and the visualization of the deformation mechanisms.[1] Real-time force measurement enables calculation of the true stress. Molecular dynamics simulations are designed to complement the experiments. We developed and validated a modeling protocol and a set of force fields that were optimized for platinum nanostructures, as described in Ref. 3. We created model nanoparticles of different sizes, shapes, and crystallographic orientations. The particles are equilibrated at the temperature of interest and then compressed between two parallel virtual walls. The stress and strain are calculated in various ways, including to match those of the experiments. These techniques complement each other (Fig. 1): for example, the simulations yield atomic-level detail about atom rearrangement that cannot be seen experimentally, while the experiments enable direct measurement of the force of atomic interactions, which is prescribed (as opposed to measured) in the simulations.

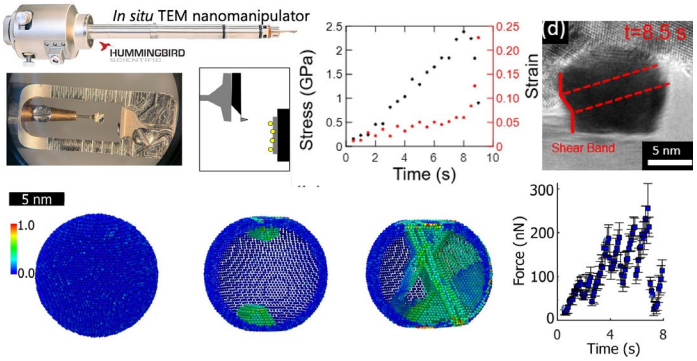

Fig. 1. *In situ* compression of metal nanoparticles (top) is combined with atomistic simulations (bottom).

2.2. Uncovering the size-dependence of nanoparticle deformation mechanisms.[4] The mechanical behavior of nanostructures is known to transition from a Hall-Petch-like "smaller-is-stronger" trend, explained by dislocation starvation, to an inverse Hall-Petch "smaller-is-weaker" trend, typically attributed to the effect of surface diffusion. Here, we used *in situ* nanomechanical testing inside of a transmission electron microscope (Fig. 2) to study the strength and deformation mechanisms of platinum nanoparticles, revealing the prominent and size-dependent role of surfaces.

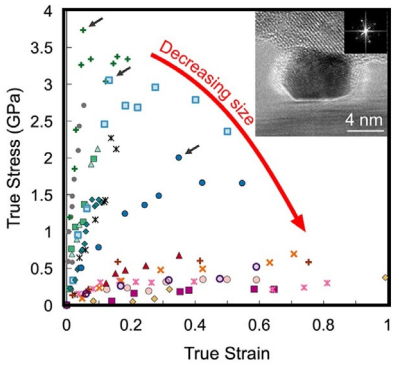

Fig. 2: Strength reduces dramatically in Pt nanoparticles below 40 nm.

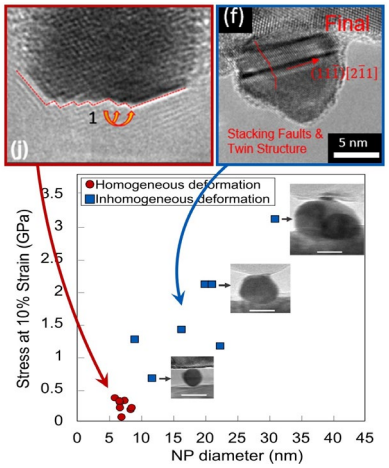

Fig. 3: Size-dependent weakening occurs when failure is controlled by surface-nucleated dislocations; ultra-small particles fail homogeneously by atom migration.

For larger-size particles (diameters of 41 nm down to 9 nm), deformation was predominantly displacive, yet still showed the smaller-is-weaker trend, suggesting a key role of surface curvature on dislocation nucleation. For particles below 9 nm, the weakening saturated to a constant value, and particles deformed homogeneously, with shape recovery after load removal. Our high-resolution TEM videos revealed the role of surface atom migration in shape change, during and after loading. During compression, the deformation was accommodated by atomic motion from lower-energy facets to higher-energy facets, which may indicate that it was governed by a confined-geometry equilibration; when the compression was removed, atom migration was reversed, and the original, stress-free-equilibrium shape was recovered.

2.3. Effect of dislocation entanglement on delaying nanoparticle failure. In the regime where nanoparticle failure is controlled by the nucleation of dislocations, the dislocations typically propagate across the particle causing irreversible deformation. However, the entanglement of partial dislocations can, in some cases, cause a metastable dislocation network, which exhibits recovery upon removal of the load. We studied the form, interaction, and eventual failure of these structures

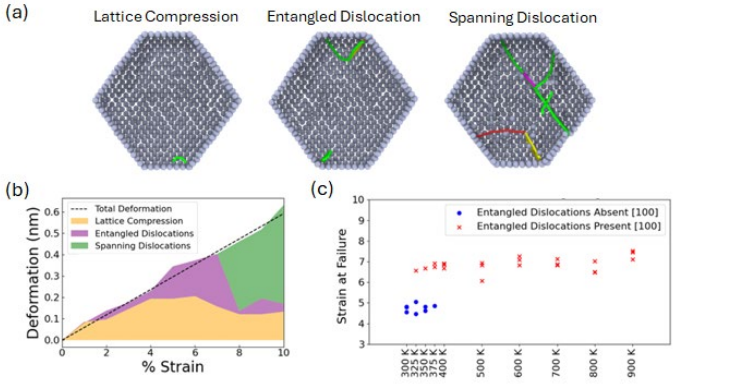

Fig. 4. Contributions to deformation (a) are quantified (b). Failure strain was doubled in cases of entangled dislocations (c).

in platinum nanoparticles, using classical molecular dynamics simulations. Force-strain data was calculated and mechanisms of reversible and irreversible deformation were isolated and quantified. Particularly, contributions to deformation (Fig. 4) were quantified from lattice compression as well as reversible (entangled) and irreversible (system-spanning) dislocations. Simulation temperature was varied to facilitate or suppress different mechanisms. Results showed that reversible deformation due to entangled dislocations was more likely at higher temperatures and for loading along the [100] direction. Dislocation-based reversible deformation increased the failure strain of the particles. Detailed analysis of *in situ* TEM images during and after compression corroborated the findings, showing characteristic sessile defects remaining in certain particles.

2.4. Distinguishing the effect of geometric and diffusive contributions. The failure nanoparticles with sizes in the range of 10-50 nm occurs by the surface nucleation of dislocations, which is a thermally activated process. Two different contributions have been suggested to cause the weakening of smaller particles: first, geometric effects such as increased surface curvature reduces the barrier for dislocation nucleation; second, surface diffusion happens faster on smaller particles, thus accelerating the formation of surface kinks which nucleate dislocations. These two factors are difficult to disentangle. Here we use the *in situ* compression testing inside a transmission electron microscope to measure the strength and deformation behavior of platinum particles in three groups: 12-nm bare particles; 16-nm bare particles; and 12-nm silica-coated particles (Fig. 5).

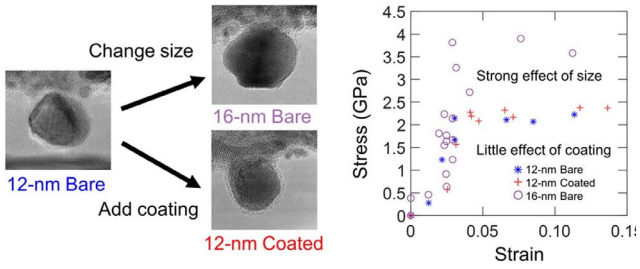

Fig. 5: Three groups of platinum nanoparticles were tested: a 12-nm bare particle (control); a 16-nm bare particle; and a 12-nm particle SiO_x-coated particle.

Thermodynamics calculations show that, if surface diffusion were the dominant factor, the two latter groups would show equal strengthening. Experimental results refute this (Fig. 6), instead demonstrating a 100% increase in mean yield strength with increased particle size and no statistically significant increase in strength due to the addition of a coating. A separate analysis of stable plastic flow corroborates the findings, showing an order-of-magnitude increase in the rate of dislocation nucleation with a change in particle size, and no change with coating. Taken together these results demonstrate that surface diffusion plays a far smaller role in the failure of nanoparticles by dislocations as compared to geometric factors that reduce the energy barrier for dislocation nucleation.

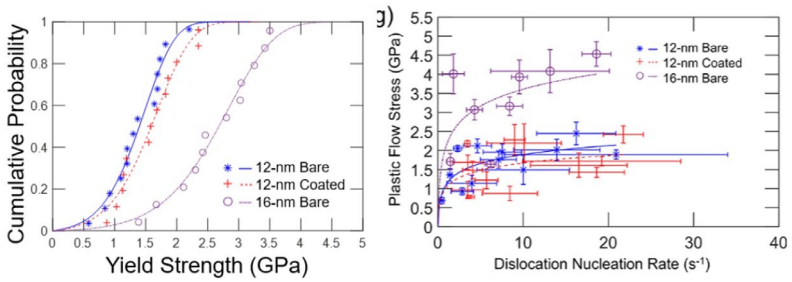

Fig. 6. Size effects dwarfed coating effects in both yield strength (left) and dislocation nucleation rate (right).

3. Future Plans and Ongoing Work

3.1. Determining the contribution of particle shape, and stress concentrations, on size-dependent failure. Some of the proposed mechanisms underlying the size-dependence of nanoparticle strength will be dependent on the shape of the particle. Particularly, the nucleation of dislocations is affected by stress concentrations which are, in turn, affected by shape-dependent parameters such as the angle of corners and the size of different facets. The MD simulations will be used to explore this shape dependence for shapes that are typical of metal nanoparticles (guided by TEM images) in the size range of a few to tens of nanometers in diameter. We hypothesize that the effect of shape on strength will explain some of the variation in size-dependent strength measured experimentally in our work and others. Further, we anticipate that understanding shape dependance will lead to a more complete understanding of nanoparticle strength more generally.

3.2. Measure the relative contributions to different deformation mechanisms in nanoparticles from a wide variety of material systems to test predictions about the effects of elastic modulus and surface energy. Prior results have yielded new insights into platinum, and the regimes over which different deformation mechanisms dominate. However, variations in materials system are required to test predictions about how material properties affect deformation. Specifically, we are now expanding to similar tests on nanoparticles of gold, silver, palladium, and copper, in order to achieve of range of moduli and a range of surface energies. A varying modulus changes the energetic penalty for elastic deformation; a range of surface energies varies the energetic penalty for changes in shape. The expected outcome of this work is the measurement of the relative amounts of deformation mechanisms for each of the five materials. These measurements will be used to confirm/disconfirm and refine hypothesized equations and material parameters governing deformation.

3.3. Refine the understanding of the thermodynamic driving forces by leveraging material anisotropy, to establish a regime map of deformation mechanisms. Further insight can be extracted from these same five materials systems by testing each one in two different crystallographic orientations. Previously, the loading direction was selected as along the [111] facet; in the present work, similar particles will be loaded along other loading directions. In addition to leveraging the differences in absolute values of modulus and surface energy (discussed earlier), the upcoming tests will leverage the naturally occurring variation that occurs within one material. Several particles are being tested and simulated for each system, selecting ones with the needed orientation and with the same approximate size as those used previously. The expected outcome of this work is measurements of flow stress and deformation behavior (relative fractions of elastic deformation and shape change), which will be used to create and refine regime maps describing how and where different deformation mechanisms contribute.

4. Publications in the last two years

1. I. M. Padilla Espinosa, S. Azadehranjbar, R. Ding, A. J. Baker, T. D. B. Jacobs, and A. Martini *Platinum Nanoparticle Compression: Combining In situ TEM and Atomistic Modeling*, Applied Physics Letters, **120**, 013101 (2022).
2. R. Ding, I. Padilla Espinosa, D. Loevlie, S. Azadehranjbar, A. J. Baker, G. Mpourmpakis, A. Martini, and T. D. B. Jacobs, *Size-dependent Shape Distributions of Platinum Nanoparticles*, Nanoscale Advances, **4**, 3978 (2022).
3. I. M. Padilla Espinosa, T. D. B. Jacobs, and A. Martini A, *Atomistic Simulations of the Elastic Compression of Platinum Nanoparticles*, Nanoscale Research Letters **17**, 96 (2022)
4. S. Azadehranjbar, R. Ding, I.M. Padilla Espinosa, A. Martini, and T. D. B. Jacobs, *Size-dependent Role of Surfaces in the Deformation of Platinum Nanoparticles*, ACS Nano, **17**, 8133 (2023).
5. R. Ding, S. Azadehranjbar, I.M. Padilla Espinosa, A. Martini, and T. D. B. Jacobs, *Separating Geometric and Diffusive Contributions to the Surface Nucleation of Dislocations in Nanoparticles*, ACS Nano, **18**, 4170 (2024).

Understanding the interplay between hydrogen and chemical short-range order in multiple principal element alloys

PI: Miaomiao (Mia) Jin, The Pennsylvania State University
Co-PI: Yang Yang, The Pennsylvania State University

Collaborators: Daniel Schreiber and Arun Devaraj, Pacific Northwest National Laboratory

Keywords: Hydrogen, chemical short-range order, multiple principal element alloy, dislocation, embrittlement.

Research Scope

Hydrogen embrittlement (HE) in metals and alloys can cause premature failure or catastrophic effects on materials [1,2], presenting a significant challenge in engineering systems where structural materials are exposed to hydrogen-rich environments, such as those containing water, hydrogen, acids, or a mixture thereof. Compounding this challenge is the fact that methods employed to improve the strength and ductility of materials often inadvertently diminish their resistance to HE. For instance, while introducing second-phase precipitates or interfaces can strengthen materials, these modifications may also promote hydrogen accumulation at interfaces, potentially facilitating interface decohesion or plastic softening [3]. Recently, it has been discovered that some multi-principal element alloys (MPEAs), like the CoNiV medium-entropy alloy (MEA) with a face-centered cubic (FCC) structure, exhibit both high resistance to HE and remarkable strength and ductility [3,4]. Several mechanisms have been proposed to explain this enhanced HE resistance [3,4]: (i) reduced hydrogen diffusivity, (ii) abundant deformation twinning that impedes crack propagation, and (iii) a robust surface oxide layer that minimizes hydrogen uptake. Meanwhile, the chemical short-range order (CSRO) in MPEAs, a unique structural characteristic, has recently attracted significant attention. There has been increasing studies that demonstrate non-uniform elemental distribution in MPEAs at the atomic scale, originating from the increasing significance of the enthalpy term in the Gibbs free energy as temperature decreases. The concept of tuning CSRO in MPEAs has garnered extensive interest for its potential as an innovative parameter to facilitate enhanced properties. This characteristic is believed to impact mechanical performance, radiation damage resistance, and corrosion resistance in these alloys [5]. However, how hydrogen interacts with the CSRO in MPEAs, and whether CSRO influences the HE resistance, remain unclear.

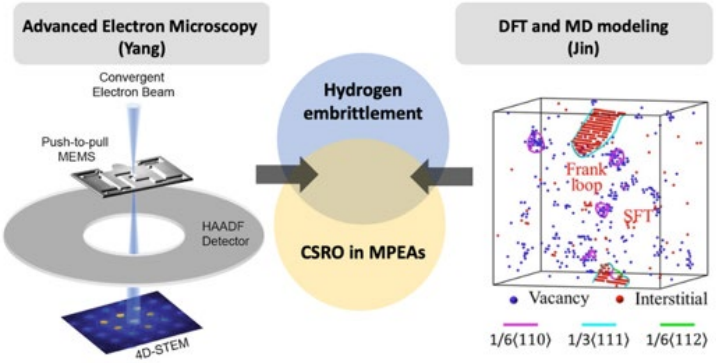

Figure 1. Schematic drawing showing the scope of the work and the major research methods.

In this project, we aim to bridge this knowledge gap by integrating advanced characterization experiments (Yang group) with atomistic computational modeling (Jin group) to understand the interplay between hydrogen and CSRO on the fundamental mechanical properties. A synergistic blend of advanced characterization and modeling techniques, including in-situ TEM, four-dimensional scanning transmission electron microscopy (4D-STEM), atom probe tomography, density functional theory (DFT), and molecular dynamics (MD) modeling, will be applied to accomplish the goal. We will study the interaction between hydrogen and CSRO, and their coupling effects on stacking fault (SF) formation and twin nucleation. In addition, we will study the hydrogen-CSRO effects on dislocation activities via *fully quantitative* nanomechanical testing using in-situ TEM, complemented with MD simulations. We will focus on the HE processes in equiatomic CoNiV MEA at room temperature.

Figure 1 summarizes our research scope and major research methods. Our approaches will provide detailed mechanistic insights into the interactions between hydrogen, CSRO, and HE in FCC MPEAs. Such fundamental understanding is crucial for improving the existing theory of HE and developing defect engineering strategies, like CSRO engineering, to enhance the performance of materials, particularly their damage tolerance in H-rich extreme environments.

Recent Progress

This project has recently started (8/1/2024). We have initiated our research to first examine the short-range order in NiCoV from both computational and experimental perspectives.

Future Plans

Our central hypothesis is that hydrogen can be trapped by specific CSRO domains, and certain kinds of CSRO-H complex may increase the stacking fault energy and impede the activation of the hydrogen-enhanced localized plasticity. Collectively, the coupling effects are hypothesized to contribute to an enhanced resistance to HE. To tackle this problem, we will pursue answers to three fundamental questions, using a hypothesis-driven approach to ensure steady and reliable progress toward the goals, as schematically demonstrated in Figure 2.

- Scientific Question 1: Will hydrogen be trapped at CSRO?
- Scientific Question 2: How will hydrogen impact the SF energy (SFE) in MPEAs with pre-existing CSRO?
- Scientific Question 3: How will hydrogen impact the dislocation motion in MPEAs with pre-existing CSRO?

Over the next three years, we will study these questions and understand the intricate interplay between hydrogen and CSRO for their consequential impacts on fundamental mechanical properties and on the HE processes in equiatomic CoNiV MEA at room temperature. In Year 1, we will prioritize the CSRO and the H solution behavior in CoNiV. This will involve sample

preparation, H-charging and characterization, NiCoV-H interatomic potential development, H solution quantification, and CSRO-H modeling.

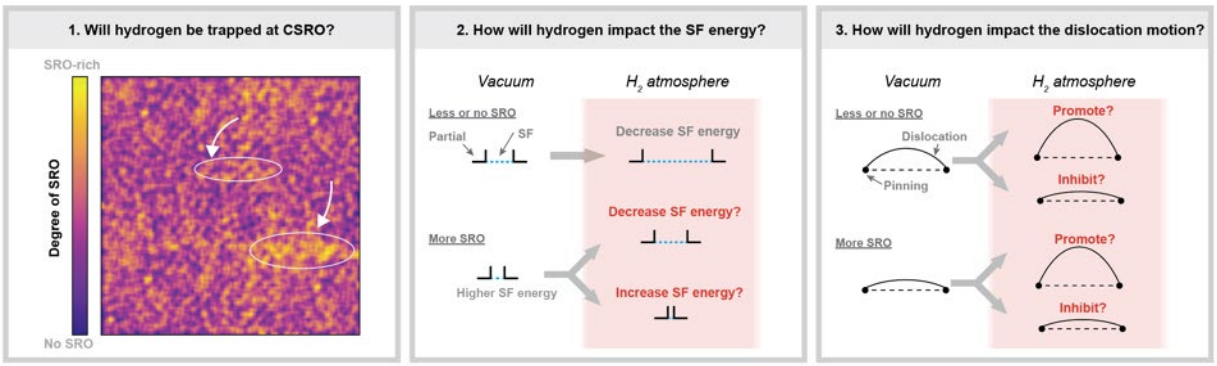

Figure 2. A schematic drawing shows the three major fundamental questions we aim to solve in this project.

References

[1] I.M. Robertson, P. Sofronis, A. Nagao, M.L. Martin, S. Wang, D.W. Gross, K.E. Nygren, Hydrogen Embrittlement Understood, Metall Mater Trans A Phys Metall Mater Sci 46 (2015) 2323–2341. https://doi.org/10.1007/s11661-015-2836-1.

[2] X. Li, X. Ma, J. Zhang, E. Akiyama, Y. Wang, X. Song, Review of Hydrogen Embrittlement in Metals: Hydrogen Diffusion, Hydrogen Characterization, Hydrogen Embrittlement Mechanism and Prevention, Acta Metallurgica Sinica (English Letters) 33 (2020) 759–773. https://doi.org/10.1007/s40195-020-01039-7.

[3] H. Luo, S.S. Sohn, W. Lu, L. Li, X. Li, C.K. Soundararajan, W. Krieger, Z. Li, D. Raabe, A strong and ductile medium-entropy alloy resists hydrogen embrittlement and corrosion, Nature Communications 11 (2020) 1–8. https://doi.org/10.1038/s41467-020-16791-8.

[4] X. Zhou, A. Tehranchi, W.A. Curtin, Mechanism and Prediction of Hydrogen Embrittlement in fcc Stainless Steels and High Entropy Alloys, Physical Review Letters 127 (2021) 175501. https://doi.org/10.1103/PhysRevLett.127.175501.

[5] R. Zhang, S. Zhao, J. Ding, Y. Chong, T. Jia, C. Ophus, M. Asta, R.O. Ritchie, A.M. Minor, Short-range order and its impact on the CrCoNi medium-entropy alloy, Nature 581 (2020) 283–287. https://doi.org/10.1038/s41586-020-2275-z.

Publications

None, as the project just started.

Fundamental Mechanisms of Newtonian Viscous Creep in Structural Alloys

Boopathy Kombaiah, Idaho National Laboratory

Keywords: Diffusional creep, Creep-induced segregation, High entropy alloys, Hydrogen, Multiscale modeling

Research Scope

Stress-driven diffusional mechanisms of atoms and point defects are critical to a wide range of materials phenomena such as creep deformation [1], self-assembly, thin-film growth, and embrittlement. In the Newtonian diffusional creep process, the Nabarro-Herring (N-H) and Coble creep theories postulated that preferential flow of atoms towards the stress direction in exchange of vacancies governs the creep rate in materials. These diffusional creep theories provide a compelling picture for materials scientists to design microstructures improving creep resistance. However, these theories remain vigorously debated due to a dearth of experimental evidence and poor predictions of creep rate [2, 3].

The goal of this proposal is conducting research to understand the Newtonian viscous diffusional creep mechanisms in structural alloys occurring under extreme environments. Motion of vacancies play a pivotal role in diffusional creep, yet it is difficult to image either in situ or postmortem. This challenge inspired our hypothesis that stress-assisted flow of vacancies to specific interfaces would cause elemental segregation in multicomponent materials. Thus, imaging elemental segregation will provide compelling and, in some cases, decisive evidence of creep mechanisms. The project explores the following science questions (SQs) that are relevant to materials in extreme environments: (1) How can we experimentally validate the occurrence of diffusional creep in materials? (2) What are the alloying effects on the diffusional creep in high entropy alloys? (3) How does soluble hydrogen in metallic systems influence the diffusional creep process?

The research methods will employ creep testing and multiscale characterization techniques (i.e., transmission electron microscopy, and atom probe tomography) and multiscale modeling tools (i.e., density functional theory (DFT) and mesoscale phase-field modeling) to quantify and predict chemical segregation at grain boundaries (GBs) of crept alloys. The mechanistic understanding of the diffusional creep mechanisms will enable new pathways for designing advanced creep-resistant materials for extreme environments of high temperature, stress, and corrosion medium.

Recent Progress

SQ 1: How can we experimentally validate the occurrence of diffusional creep in materials?

To answer this question, we conducted creep experiments on 304L stainless steel, nickel-rhenium (Ni-Re) and nickel-chromium (Ni-Cr) alloys to test our primary hypothesis under low-stress and high-temperature conditions that favor diffusional creep processes.

- **Creep-induced segregation (CIS) in alloys**

304 L stainless steel: The segregation measurements at multiple GBs from crept and control (grip) regions of crept 304L alloy demonstrate that Ni segregation at parallel GBs changed from depletion to enrichment because of diffusional creep. Also, the creep deformation produced an effective Cr depletion (via reduction in Cr enrichment) and an effective iron (Fe) enrichment (via reduction in Fe depletion) at the parallel GBs of crept specimen. These observations strongly support our hypothesis proving the operation of diffusional creep mechanisms (Figure 1a-c). In this study, for the first time, we show CIS in an alloy. The occurrence CIS provides compelling experimental evidence for proving the operation of diffusional creep in materials.

To understand the mechanisms of CIS, we developed a single crystal model describing chemo-mechanical coupling of mechanical stress with lattice diffusion and GB vacancy flux. The model predicted segregation at GBs due to stress-assisted vacancy flow and corresponding atomic fluxes. The predictions were qualitatively comparable to the experimental observations of CIS in 304L (Figure 1d-f).

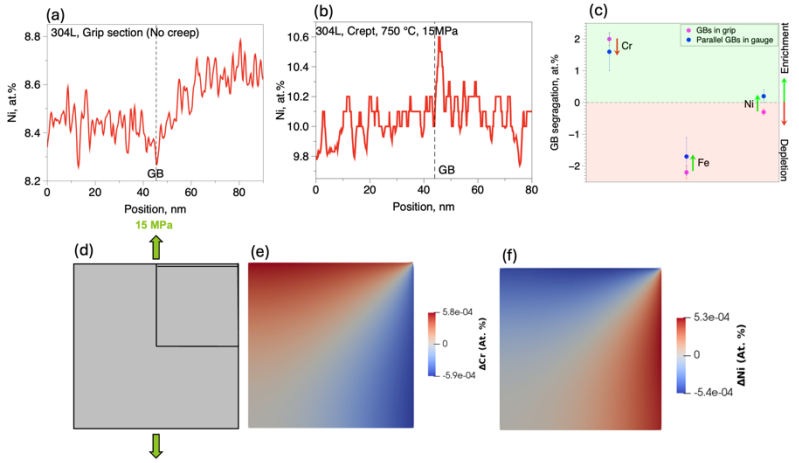

Figure 1. CIS in 304L. (a-c) Experimental data, (d-f) Modeling results.

Ni-Re alloys: Chemical segregation measurements in crept Ni-3 at.% Re alloy revealed Re depletion and Ni enrichment at GBs in the grip section due to thermal processes (Figure 2a-d). However, some GBs parallel to the applied stress in the crept Ni-Re alloy exhibited the opposite trend of segregation, i.e., Re enrichment and Ni depletion. Some parallel GBs in the crept specimen exhibited similar segregation profile compared to that of GBs in the grip section. We speculate that the variability in the stress from one GB to other resulted in different segregation profiles. Additionally, microstructural characterization showed creep-induced grain boundary migration occurring during creep deformation (Figure 2e-h). The GB has left a Re-enriched band in its wake as it migrated. We propose that vacancies flowing into parallel GBs during diffusional creep causes preferential outward flow of the faster element, i.e., Ni, leading to Ni depletion and Re enrichment at GBs. Also, the vacancy flow drives GB migration forming a Re-enriched region inside a grain. The GB migrated region decorated by Ni and Re segregation in each grain will inform us the amount of strain that each grain has undergone due to diffusional

creep alone. This strain information is novel to the research community. Thus, the discovery of this experimental methodology to verify diffusional creep mechanisms in alloys enables development of high-fidelity constitutive equations to predict creep rates.

DFT and self-consistent mean field (SCMF) calculations were used to uncover solute diffusion mechanisms and the solute segregation tendencies at GB vacancy sinks in binary alloys of Ni with solutes Re, Cr, cobalt (Co), molybdenum (Mo), tungsten (W), and tantalum (Ta). The Onsager transport coefficients of solutes were estimated. The solute segregation tendencies were calculated based on the partial diffusion coefficient (PDC) and vacancy drag ratios (Figure 3) as a function of temperature and hydrostatic strain. The calculations point out that Re enriches at GB sinks under the creep test conditions aligning with our experimental observations.

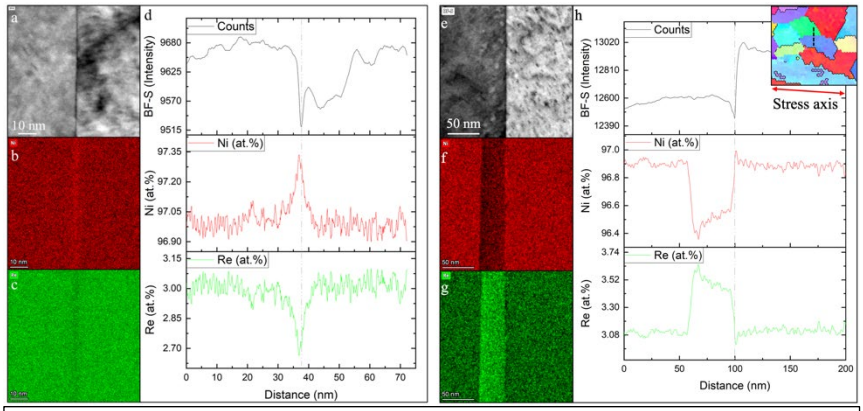

Figure 2. Elemental segregation of Ni and Re at GBs in Ni-3 at.%Re alloy. (a-d) grip section (no creep) and (e-h) parallel GB in crept section (500 °C , 24 MPa).

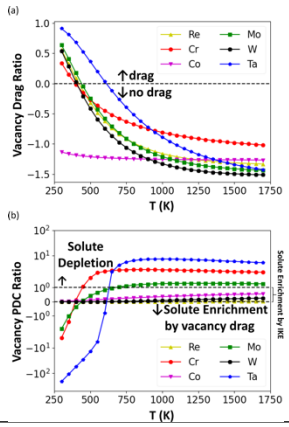

Figure 3. Solute segregation tendencies in Ni calculated using SCMF.

SQ 2: What are the alloying effects on the diffusional creep in high entropy alloys (HEAs)?

- **Elucidating alloying effects on creep of HEAs**

Bulk creep testing and nanoindentation creep methods were employed to systematically investigate the compositional effects on the creep deformation of binary to complex HEAs. A significant observation from the diffusional creep data indicates that increasing the number of elements in the HEAs doesn't necessarily result in more sluggish diffusion and lower diffusional creep rates (Figure 4). For instance, four element HEA (NiCoFeCr) exhibited lower creep rate than five element HEA (NiCoFeCrMn) under similar creep testing conditions. These results provide critical input for alloy design strategies for creep-resistant materials.

Figure 4. Diffusional creep data of alloys

Future Plans

CIS in alloys: Ni-Re alloys exhibited prominent CIS at GBs compared to 304L and Ni-Cr alloys. Therefore, we will focus our efforts on Ni-Re alloy investigating the effect of creep testing parameters such as temperature, stress, and strain and material microstructure like grain size on CIS using bulk creep testing. The chemo-mechanical diffusion model predicted that CIS increases as the grain size of the alloy is reduced.

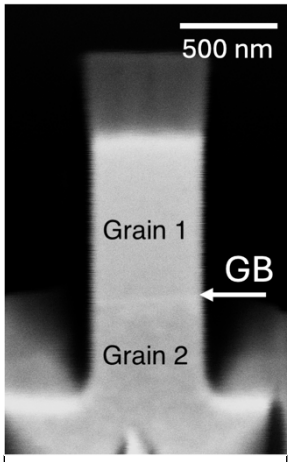

Figure 5. Bi-crystal Ni-Re micropillar

One of the challenges in interpreting CIS is its GB-to-GB variability likely caused probably by different stress states and structure at GBs, making it difficult to accurately predict CIS using models. To resolve this issue, we plan to measure the evolution of CIS at a single grain boundary in a bi-crystal by testing them via micromechanical creep testing. In polycrystalline samples, we will estimate the stress distribution around GBs using crystal plasticity models to account for GB-to-GB variability.

Molecular dynamics (MD) and PF models will be employed to investigate the mechanisms of GB segregation and migration under diffusional creep in bi-crystal and polycrystalline Ni-Re alloys. The coupling between vacancy and atomic fluxes for GB diffusion is not well understood. Specifically, MD will address the nanoscale mechanistic processes behind GB segregation and migration by vacancy flux to GBs. Furthermore, PF modeling will be developed to make a quantitative description of GB segregation and migration processes. With this development, predicted creep rates can be cross-referenced with experimental results.

Elucidating alloying effects on creep of HEAs: Additional diffusional creep data of high entropy alloys will be obtained to understand the effect of chemical composition on sluggish diffusion. Specifically, diffusional creep rates and creep activation energies will be calculated from the creep data. Furthermore, CIS at GBs of HEAs will be measured using advanced characterization techniques such as transmission electron microscopy and atom probe tomography.

Effect of hydrogen on diffusional creep: Under SQ 3, the proposal hypothesizes that the presence of soluble hydrogen in alloys will accelerate the diffusional creep rate and thus hasten CIS through vacancy-atom exchange mechanisms at GBs. We will measure CIS in Ni-3at% Re alloy crept under different hydrogen partial pressures to test this hypothesis.

References

1. F.R.N. Nabarro, *Creep at very low rates,* Metallurgical and Materials Transactions A **33,** 213 (2002).
2. B. Burton and G.L. Reynolds, *In defense of diffusional creep,* Materials Science and Engineering: A **191,** 135 (1995).

3. O.A. Ruano, J. Wadsworth, J. Wolfenstine, and O.D. Sherby, *Evidence for Nabarro-Herring creep in metals: fiction or reality?,* Materials Science and Engineering A-structural Materials Properties Microstructure and Processing **165,** 133 (1993).

Publications

1. S. Shousha, S. B. Kadambi, B. Beeler, and B. Kombaiah, Vacancy-mediated transport and segregation tendencies of solutes in fcc nickel under diffusional creep: A density functional theory study, Physical Review Materials 8, 083605 (2024).

2. M. Nelson, S. Samuha, B. Kombaiah, D. Kamerman, and P. Hosemann, Enhanced stress relaxation behavior via basal <a> dislocation activity in Zircaloy-4 cladding, Journal of Nuclear Materials 601, 155337 (2024)

Interfacial Energy Minimization Mechanisms During Grain Growth

Amanda R. Krause (Carnegie Mellon University), Michael R. Tonks (University of Florida), Joel B. Harley (University of Florida), Michael S. Kesler (Oak Ridge National Laboratory)

Keywords: Grain growth, microstructure, machine learning, Monte Carlo Potts, x-ray diffraction microscopy

Research Scope

The goal of this research program is to establish the mechanisms governing local grain boundary motion, which is needed to design and process desirable microstructures for better performance, by identifying the relative contributions of grain boundary (GB) energy, mobility and stiffness to grain growth. Classical models for grain growth assume that the primary mechanism for reducing the total interfacial energy is area reduction and that GB restructuring is not significant. This assumption implies that grain growth is locally driven by curvature. However, recent experimental observations using new non-destructive 3D x-ray diffraction microscopy techniques (3D-XRM) reveal that classic descriptors (i.e., curvature, number of neighbors, grain size) do not predict real grain growth (1,2). Instead, local GB motion appears to be governed by its energy relative to its neighbors such that low-energy boundaries replace those of higher energy (3). A significant challenge to testing this assumption is due to anisotropic GB mobility. Anisotropic mobility has been hypothesized to cause abnormal grain growth or affect the final grain shapes or growth rate but its true contributions are unknown because it is difficult to measure. As mobility and energy both control GB motion, it is challenging to isolate the local driving forces necessary to test the common assumption that the primary mechanism is area reduction.

The novelty of this work is the use of machine learning tools to capture GB mobility and energy from laboratory-based diffraction contrast tomography (LabDCT, a type of 3D-XRM) measurements in polycrystals to test the common assumption used in grain growth models. Machine learning can capture high-order correlations in dynamic systems like those found in the evolving GB topology. The PIs have previously developed a physics-regularized interpretable machine learning microstructure evolution (PRIMME) model that accurately replicates the grain growth behavior of its trained data set (4). In the current work, PRIMME is being expanded to capture energy and mobility independently from noisy, non-continuous microstructural data from LabDCT. The developed anisotropic PRIMME model will be used to interpret the grain growth behavior of alumina and iron and assess whether GB energy reduction is a primary mechanism for microstructure evolution.

Recent Progress

LabDCT was used to measure the microstructure evolution of Ni and Fe at temperatures between 600°C and 800°C. At higher temperatures, evidence of abnormal grain growth is evident in both materials. Figure 1 shows the 3D microstructural map of a Ni rod before and after heat treating at

800°C for 3 mins with abnormally fast growing grains highlighted in Fig. 1(b). For comparison, Fig. 1(c) shows grains that initially had an equivalent spherical diameter of 90 µm or greater that shrank during grain growth. These grains were comparable in size initially to those that grew abnormally. This measurement is the first known that captures the abnormal grains and their neighborhoods before growth. The grain boundary character and energy (calculated from the function for FCC metals proposed by Ref (5).) were compared for those associated with abnormal growing grains and their neighbors. Figure 2 shows that the population of GBs is indistinguishable and supports the need for higher order descriptors or mobility measurements for predicting abnormal grain growth.

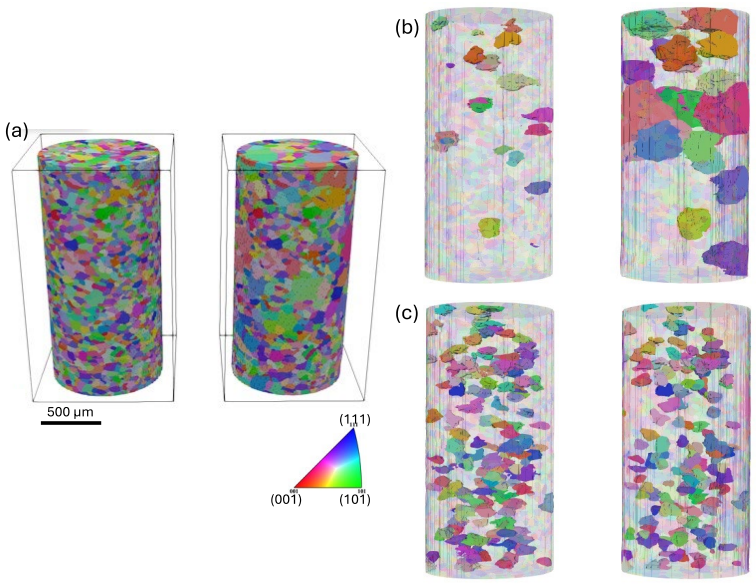

Figure 1: LabDCT microstructural maps of Ni (1mm diameter) collected before and after heat treating at 800°C for 3 mins in forming gas showing grain growth. (A) Full reconstruction of Ni volume measured before and after growth. Examples of (B) large grains that shrank and (C) those that grew abnormally within the same Ni volume are shown in 3D. The maps are colored with respect to the grains' crystallographic direction aligned with the rod's z-axis according to the inverse pole figure key provided.

This study is also comparing grain growth in textured alumina, which develops both anisomorphic grains and a unique grain boundary character distribution, to Monte Carlo Potts (MCP) simulations to identify the role of grain boundary replacement mechanism. In this work, textured Ca-doped alumina is prepared by slip casting in a magnetic field at Oak Ridge National Laboratory and then sintered and heat treated for 1-64 h at 1600°C outside the magnetic field. The grain boundary energy (relative to the surface energy) distribution was measured in the as-sintered condition and after 64 h at 1600°C, at which the grains were highly elongated (see Fig. 2a). The grain boundary energy distribution narrows with time, suggesting a preferential removal of high energy grain boundaries during growth. However, no difference in the grain boundary energy distributions was found for the 'major' and 'minor' grain boundaries associated with the long and short axes of the grains, respectively. Such shape has been attributed to anisotropic mobility in untextured Ca-doped alumina previously. To test this hypothesis, the microstructures of an anisotropic MCP simulations using an anisotropic grain boundary energy or mobility as a function of plane inclination were compared to those found experimentally.

The final grain shape and grain boundary energy distribution after grain growth of textured Ca-doped alumina resembles that of the MCP simulations using an anisotropic GB energy as a

function of plane inclination (Fig. 2b) but not the anisotropic GB mobility function (Fig. 2c). However, the results were sensitive to the shape of the grain boundary energy function, such that energy anisotropy alone was not sufficient to induce anismorphic growth. Specifically, the functions that resulted in elongated grains applied a torque that favored the straightening of low energy grain boundary types. This work supports that grain boundary stiffness (the energy and torque combined) plays an important role in local grain boundary migration and may explain why small differences in GB energy affect grain growth.

We created a new grain growth model, inspired by PRIMME, with the intention to better understand how PRIMME functions. We refer to this model as a mode filter model. We have proven theoretically that this mode filter model solves the same optimization function as the well-known Monte Carlo Potts grain growth model. However, mode filter model is faster than the Monte Carlo Potts and Phase Field simulations. In addition, more recently, we have shown that it more reliably satisfies the properties of traditional isotropic grain growth than the Monte Carlo Potts model. Specifically, we have found lower lattice pinning (Fig. 3) and a stronger agreement with the von Neumann/Mullins law.

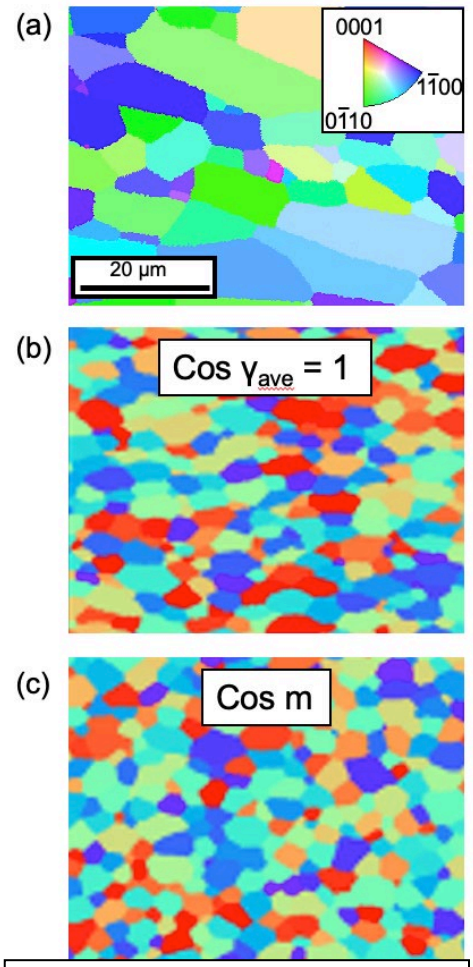

Figure 2: Comparison of microstructures from experiments and MCP simulations with anisotropic GB properties. (a) Electron backscattered diffraction map of textured Ca-doped alumina after 64 h at 1600°C with grains colored according to the provided inverse pole figure key. The microstructures for (b) anisotropic energy considering stiffness and (c) anisotropic mobility when 10,000 grains were reached.

In addition, lessons from the mode filter model are currently being used to improve the PRIMME framework, making it more robust and interpretable. For example, the mode filter has inspired us to change the underlying function being optimized in the PRIMME framework. This change has resulted in less uncertainty and reduced distortions in test simulations with circular grains, which were significant in the original PRIMME framework. In addition, the mode filter model has helped us interpret the output "action likelihoods" of PRIMME, illustrating that anisotropy and grain growth speed are encoded within. This workflow demonstrates a pathway to learning grain boundary energy and mobility information directly from PRIMME's outputs.

Future Plans

The goal is to use the acquired LabDCT data (for Ni, Fe, and alumina) to train the machine learning model, PRMME. To achieve this goal, the next steps are to test the 3D version of PRIMME that includes the full grain boundary character (five degrees of freedom) and is currently being developed. Additionally, PRIMME's robustness to errors and uncertainty in the experimental data is currently being improved with additional training from phase field simulations and by implementing a multi-time step training methodology.

Experimentally, the next steps include processing and measuring the grain growth of textured Fe and alumina with abnormal growth. LabDCT measurements have begun on large grain textured and untextured alumina, which must be prepared at 1800°C to reach measurable grain sizes. This data will be used to train PRIMME as well as analyzed with traditional methods to identify unique grain boundaries worth further study.

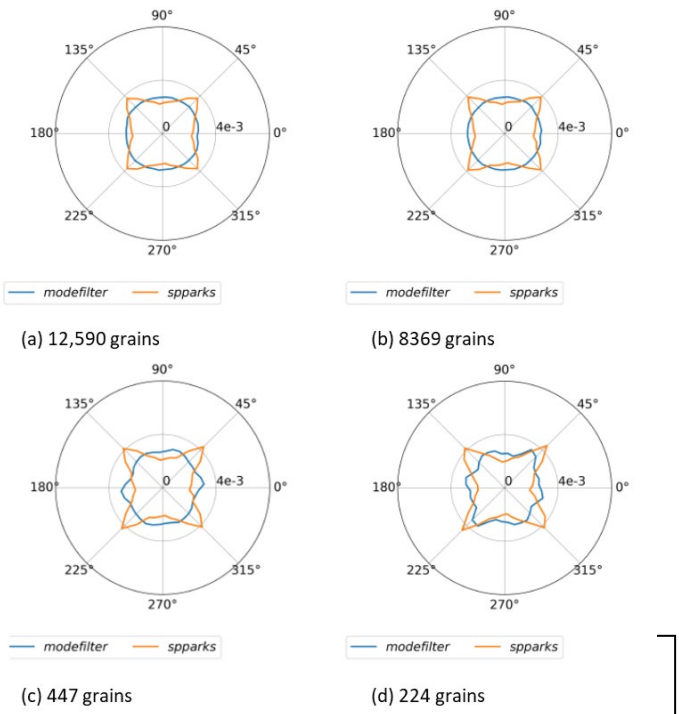

model (as implemented in SPPARKS). (a)-(d) shows how the distribution changes as a function of time. We observe that the mode filter remains isotropic (no direction dependencies) across time while the Monte Carlo Potts model displays significant inclination dependence (i.e., lattice pinning).

References

1. A. Bhattacharya, Y.F. Shen, C.M. Hefferan, S.F. Li, J. Lind, R.M. Suter, C.E. Krill III, G.S. Rohrer, *Grain boundary velocity and curvature are not correlated in Ni polycrystals*, Science **374**, 189-193 (2021).
2. V. Muralikrishnan, H. Liu, L. Yang, B. Conry, C.J. Marvel, M.P. Harmer, G.S. Rohrer, M.R. Tonks, R.M. Suter, C.E. Krill III, A.R. Krause, *Observations of unexpected grain boundary migration in $SrTiO_3$*, Scripta Materialia **222**, 115055 (2023).
3. Z. Xu, Y.F. Shen, S.K. Naghibzadeh, X. Peng, V. Muralikrishnan, S. Maddali, D. Menasche, A.R. Krause, K. Dayal, R.M. Suter, G.S. Rohrer, *Grain boundary migration in polycrystalline α-Fe*, Acta Materialia **264,** 119541 (2024).
4. W. Yan, J. Melville, V. Yadav, K. Everett, L. Yang, M.S. Kesler, A.R. Krause, M.R. Tonks, J.B. Harley, *A novel physics-regularized interpretable machine learning model for grain growth*, Materials & Design **222**, 111032 (2022).
5. V.V. Bulatov, B.W. Reed, M. Kumar, *Grain boundary energy function for FCC metals*, Acta Materialia **65**, 161-175 (2014).

Publications

1. D.P. DeLellis, A.R. Krause, *Large Pores Promote Abnormal Grain Growth Behavior in Calcia Doped Alumina,* Scripta Materialia **245**, 116058 (2024).
2. J. Melvile, V. Yadav, L. Yang, A.R. Krause, M.R. Tonks, J.B. Harley, *Anisotropic physics-regularized interpretable machine learning of microstructure evolution*, Computational Materials Science **238**, 112941 (2024).
3. B. Conry, M. Kole, W.R. Burnett, J.B. Harley, M.R. Tonks, M.S. Kesler, A.R. Krause, *The evolution of grain boundary energy in textured and untextured Ca-doped alumina during grain growth*, Journal of the American Ceramic Society, **107**, 1725-1735 (2024).
4. L. Yang, V. Yadav, J. Melvile, J.B. Harley, A.R. Krause, M.R. Tonks, *A triple junction energy study using an inclination-dependent anisotropic Monte Carlo Potts grain growth model*, Materials & Design **239**, 112763 (2024).
5. J. Melville, V. Yadav, L. Yang, A.R. Krause, M.R. Tonks, J.B. Harley, *A new efficient grain growth model using a random Gaussian-samples mode filter*, Materials & Design **237**, 112604 (2024).
6. I.D. Khurjekar, B. Conry, M.S. Kesler, M.R. Tonks, A.R. Krause, J.B. Harley, *Automated, high-accuracy classification of textured microstructures using a convolutional neural network*, Frontiers in Materials **10**, 1086000 (2023).

Mechanical Behavior of Materials at the Micrometer Scale under Different Environments

Seok-Woo Lee (University of Connecticut)

Keywords: Micromechanical test, Dislocation, Plasticity, Fracture, Size effect

Research Scope

Mechanical behavior of metals at the micrometer scale is often different from that of bulk metals because the plasticity at the micrometer scale is controlled by the intermittent operation of dislocation sources while the plasticity in bulk scale is controlled by continuous and collective evolution of dislocation structures. Temperature is an important factor that affects the motion of dislocation, but the effect of temperature on the source-controlled plasticity at the micrometer scale has not been understood well. For the past decade, the combined effect of temperature and sample dimension on compressive strength and plastic flow has been widely investigated. However, the combined effect of temperature and sample dimension on tensile plasticity and fracture has not been explored. In this project, we study the tensile plasticity of body-centered-cubic (BCC) metals at the micrometer scale using *in-situ* cryogenic mechanical testing and computer simulations. This project aims to understand how the interplay between temperature and sample dimension affects tensile plasticity and fracture of BCC metals at the micrometer scale. The plasticity of BCC metals is strongly temperature-dependent because the motion of screw dislocation is sensitive to temperature change. Sample dimension brings additional complexity in dynamics of screw dislocation because the presence of free surface affects the motion of screw dislocation significantly. To advance the knowledge on metal plasticity, it is crucial to understand how the interplay between temperature and sample dimension influences dislocation dynamics, the tensile ductility, as well as fracture. Research outcomes of this project will provide an important insight into understanding of mechanical behavior of metals at low temperature.

Recent Progress

1. Dislocation density effect on plasticity and fracture in micron-sized niobium (Nb) single crystals under uniaxial tension

The tensile ductility of micron-sized body-centered-cubic (bcc) Nb single crystal was investigated, and it was found that its tensile ductility decreases significantly as the sample size decreases (Figs. 1(a) and 1(b)). The tensile ductility of metals is strongly dependent of how much the motion of mobile dislocations contributes to the total plastic strain until fracture occurs. At small length scales, dislocation multiplication becomes more limited, and the plasticity becomes more localized compared to bulk metals. In addition, we also conducted the micro-tensile test using our custom-built *in-situ* cryogenic micro-mechanical testing system. The result showed that the ductility becomes smaller at lower temperatures due to the limited cross-slip, and even dislocation starvation occurred. Moreover, a high dislocation density with the order of 10^{14}~10^{15} m^{-2} was introduced by pre-straining a bulk Nb crystal before making a micro dog-bone sample. We found

that high dislocation density containing samples exhibit the ductile-to-brittle transition as the temperature decreased. At 56 K, a sample showed the brittle cleavage on {001} plane (Fig. 1(c)). Several papers reported that it is almost impossible to see the {001} cleavage from Nb unlike other bcc metals because of the high mobility of dislocations in Nb [1]. However, the combined effect of size reduction, high dislocation density, and temperature reduction seemed let us to observe a rare {001} cleavage fracture from Nb single crystal. Our micro-tensile experiments confirmed the famous '*Smaller is Stronger*' behavior is still hold under tension. However, the '*Smaller is less ductile'* was observed, too. This means that '*Strength-Ductility Trade-off*', which is usually observed in alloy development, exist in size effect (Fig 1(b)). Our result opens a new challenge regarding how to improve tensile ductility of metals at the micrometer scale.

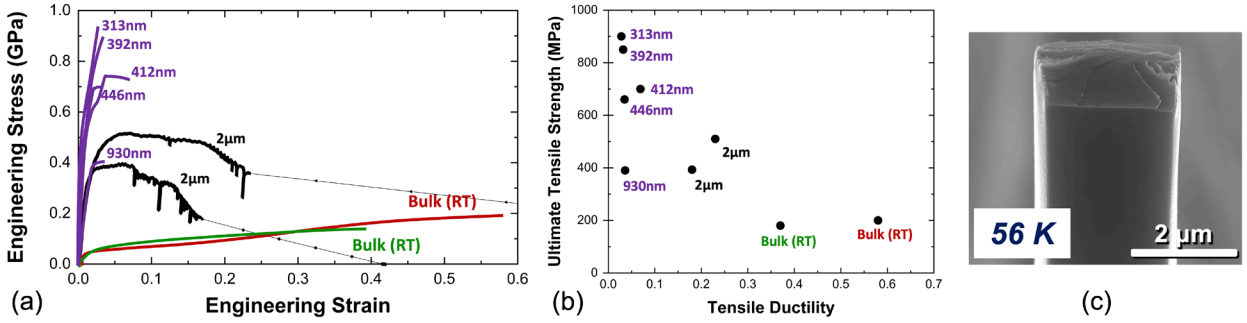

Figure 1. (a) Stress-strain curve of [001] Nb single crystals (the number corresponds to sample size); (b) Strength-ductility trade-off; (c) {001} cleavage fracture of high dislocation density containing micropillar at 56 K.

2. Tension-compression asymmetric behavior of screw dislocation in body-centered-cubic nanopillars

Several papers reported that particularly in bcc metals, a dislocation could be easily multiplied due to the surface-induced cross-slip of screw dislocation, so-called the surface-controlled dislocation multiplication (SCDM) [2]. However, our experimental results showed that dislocation activity seemed to be limited under tension. Thus, we conducted an atomistic simulation to see if the SCDM occurs under tension, too. Surprisingly, our simulation results showed that the SCDM does not occur under tension (Figs. 2(a) and 2(b)). The strong image forces that push a screw dislocation onto two different {121} slip planes were considered as the main driving force of the SCDM. This image forces do not depend on the applied stress, so it must exist even under tension. Then, why does not the SCDM occur under tension? Tension-compression asymmetry of BCC single crystal metals has been observed, and twining/anti-twinning asymmetry of {121}<111> slip has been considered as the most widely accepted model. This model suggests that a screw dislocation prefers different slip planes when the direction of shear stress is changed. In our case, a screw dislocation chooses two {121} slip planes under compression but only one {121} slip plane under tension based on the slip energy barrier (Figs. 2(c) and 2(d)). Under tension, thus, a screw dislocation wants to stay on a single slip plane and simply glides out. This result will

be critical to design a discrete dislocation dynamics model on the plasticity of bcc metals at the nanoscale.

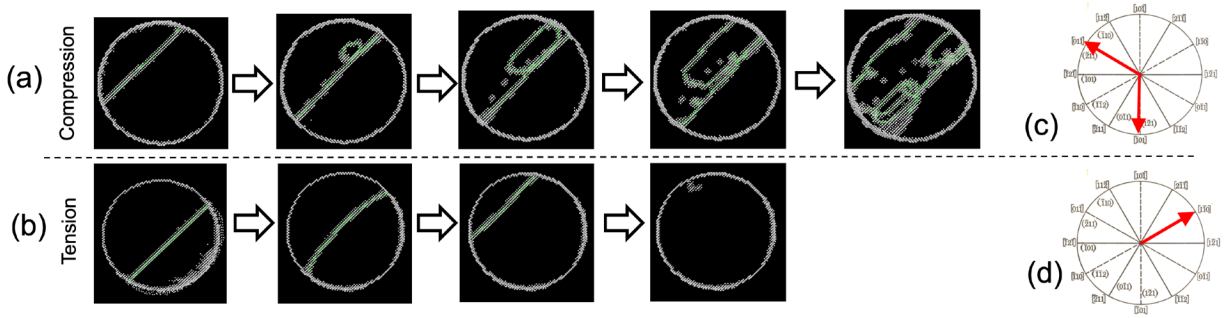

Figure 2. Simulation snapshots of (a) [001] compression and (b) [001] tension of Nb single crystals at 10 K; Twinning slip system (low slip energy barrier) under (c) compression and (d) tension.

3. Critical examination of the scaling exponents of compressive flow strength of bcc metals

Scaling exponent has been regarded as one of the most important quantities that can be measured from the size effect study on strength of materials [3, 4]. We found that the scaling exponent of compressive flow strength of several bcc metals is nearly constant if flow strength is measured at plastic strain over 1% (Fig. 3). This result is surprising because the strain hardening rate is significantly size-dependent. Submicron-sized pillars exhibit several times higher strain hardening rate than micron-sized pillars. The constant scaling exponent over plastic strain means the scaling exponent can be scaled by the power law relation (D^{-n}, D: diameter, n: scaling exponent) of flow strength. This mathematical analysis allows us to extract the scale-free part of strain hardening, leading to a fundamental strain hardening law that does not dependent of sample dimension. If we know a flow strength for a particular sample size, the presence of scale-free part of strain hardening allows us to predict a flow strength of micropillar with other sizes. This result is greatly useful for not only the validation of dislocation dynamics model but also the design of micron-sized metals for engineering applications. It is interesting to find the lower or upper bound at which the scale-free part of strain hardening begins to break down. It is unclear whether scale-free part of strain hardening will break down or not when a sample size increases continuously. It will be necessary to explore the strain hardening rate of pillar with the wide range of diameter.

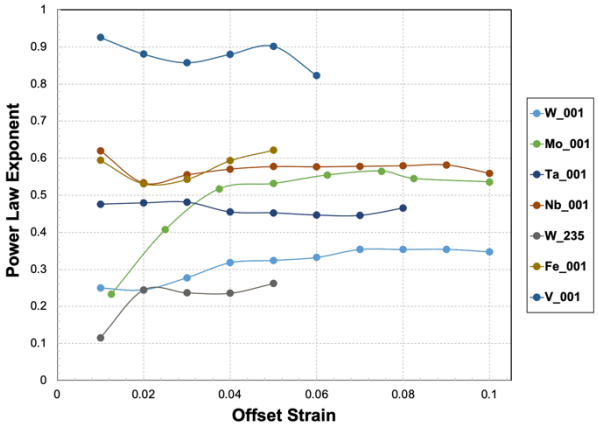

Figure 3. Power-law exponent as a function of plastic strain offset at which a flow strength is measured.

Future Plans

(1) **Micro-tensile test of micropillar with relatively uniform distribution of dislocations:** It could be possible to introduce dislocations if a micropillar with a hard coating is pre-strained. We will try the atomic layer deposition or tungsten deposition on Nb micropillars, prestrain them, and fabricate a micro-tensile sample out of prestrained micropillar. Enhanced tensile ductility could be observed if all dislocations contribute to the plastic deformation.

(2) **Discrete Dislocation dynamics studies of tension-compression asymmetry:** We will incorporate our atomistic simulation results (asymmetric path of screw dislocation on {121} planes) into discrete dislocation dynamics model, obtain stress-strain curves under both tension and compression, compare with the experimental data.

(3) **Detailed analysis of scaling exponent:** The scale-free part of strain hardening has been observed in only a few bcc micropillars at room temperature and under [001] loading. We will check if the scale-free part of strain hardening can also be observed when (1) plastic strain is less than 1%; (2) the temperature is not room temperature; (3) the loading orientation is not [001]; (4) the sample dimension approaches bulk-scale. All these proposed works seem to be very important to advance the fundamental knowledge of dislocation plasticity.

References

1. W. Luo, M. L. Cohen, J. W. Morris Jr., *On the possibility of cleavage in Nb*, Philosophical Magazine Letter **89**, 23-32 (2009).

2. C. R. Weinberger, W. Cai, *Surface-controlled dislocation multiplication in metal micropillars*, PNAS **105**, 14304-14307 (2008).

3. M. D. Uchic, P. A. Shade, D. M. Dimiduk, *Plasticity of micrometer-scale single crystals in compression*, Annual Review of Materials Research **39**, 361-389 (2009).

4. J. R. Greer, Jeff Th. M. De Hosson, *Plasticity in small-sized metallic systems: Intrinsic versus extrinsic size effect*, Progress in Materials Science **56**, 654-724 (2011)

Publications

Three manuscripts are in-preparation.

Understanding The Influence of Ca and Zn on Twinning-Detwinning Behavior in Mg Alloys During In-SEM Cyclic Loading

Aeriel Leonard, Department of Materials Science and Engineering, The Ohio State University, Columbus, OH

Keywords: EBSD; Twinning; Mg Alloys; Fatigue; Cyclic Stress-Strain Behavior

Research Scope

The **research objective** of this project is to understand and quantify the role of twin and twin boundary types on natural crack initiation in unalloyed Mg, Mg-RE, Mg-Zn, Mg-Ca, and Mg-Zn-Ca alloys. The core hypothesis of this work is that damage near and within twin and grain boundaries is driven by dislocation interactions and accumulations (i.e., pileups, penetrated dislocations, slip irreversibility) near these regions leading to a local stress concentration. It is well established that many wrought Mg alloys show a strong initial basal texture, where the c-axis in most grains is aligned normal to the working direction[1]. During cyclic loading the grains with this initial texture favor twinning during compression and the c-axis of the twinned regions are rotated 86.3° toward the working direction. When the load is reversed detwinning occurs and the twins either narrow or are removed altogether. Recent studies have shown that twinning is greatly reduced through the addition of RE elements and/or the combination of Ca and Zn [][2,3]. However current research fails to collectively link dislocation interactions and structures at the nano and micro scale to meso-scale damage accumulation or macro-scale mechanical behavior. To improve the understanding of fatigue crack initiation, this study will involve a multi-scale and multi-modal systematic investigation to understand the mechanisms of damage accumulation leading to crack initiation.

Recent Progress

The cyclic stress strain (CSS) behavior and mechanisms of deformation during cyclic loading are currently being explored in two extruded Mg alloys: Mg-2Nd-1Y-0.1Zr-0.1Ca (rare-earth, RE) and Mg-2Zn-0.5Ca (ZX21) (wt. %) as well as unalloyed Mg. Flat, rectangular, dog bone specimens were extracted from the extruded bars and tested under fully-reversed, strain-controlled, low-cycle fatigue conditions at total strain amplitudes between 0.2-1.2%. A methodology employing a combination of scanning electron microscopy (SEM), in-SEM, and ex-situ loading are used to characterize the evolution of deformation and damage throughout the microstructure. The initial crystallographic texture was measured using electron back scatter diffraction (EBSD) and it was determined that the Mg-RE displayed a random texture. Contrarily, ZX21 showed a very weak basal-type texture. During in-SEM cyclic loading it was found that twins formed in grains where the c-axis was initially oriented normal to the loading direction. It should be noted that not all grains with this orientation nucleated twins during cyclic loading. At low strain amplitudes ($\leq 0.6\%$) twins formed during the first compressive cycle were not completely detwinned during tensile reloading. Alternatively, after the first cycle, these twins

become narrower during tensile reloading and experience growth or thickening during compression for many cycles. As a result, the abrupt compressive yielding associated with twin nucleation disappears after the first cycle and the tension-compression asymmetry is greatly reduced. In-SEM analysis revealed that after the first cycle twin nucleation persistently occurred from the same location throughout the fatigue life. In the Mg-RE alloy, the CSS behavior exhibited stable, symmetric hysteresis loops where the maximum tensile and compressive stresses were similar throughout the fatigue lifetime.

Figure 1: Electron back scatter diffraction (EBSD) inverse pole figure (IPF) maps showing twinning-detwinning behavior during in-SEM cyclic loading of Mg-Zn-Ca. During the first compressive cycle (-0.6% strain) twins form in certain grains (i.e., regions of interest are highlighted by a black square on each map). The sample is then unloaded to 0% strain where there is negligible change within the microstructure. Upon loading to +0.6% strain, twins formed during compression are reduced in thickness indicating some detwinning did occur. After cycling up to 20 cycles, the same behavior persists.

Future Plans

For the upcoming academic year, there are three main goals for the project:

1. Understand the role of non-basal dislocation slip has in deformation of Mg alloys with suppressed or reduced twinning using in-SEM cyclic loading and scanning transmission electron microscopy
2. Characterize the dislocation interactions and accumulation at interfaces associated with deformation twins and grains using STEM and ECCI
3. Quantify the 3D strain along twin interfaces using dark-field X-ray microscopy at ESRF (upon successful proposal submission)

References

[1] A.D. Murphy-Leonard, D.C. Pagan, A. Beaudoin, M.P. Miller, J.E. Allison, Quantification of cyclic twinning-detwinning behavior during low-cycle fatigue of pure magnesium using high energy X-ray diffraction, Int J Fatigue 125 (2019) 314–323. https://doi.org/10.1016/j.ijfatigue.2019.04.011.

[2] T.D. Berman, J.E. Allison, Coupling Thermomechanical Processing and Alloy Design to Improve Textures in Mg-Zn-Ca Sheet Alloys, Jom (2021). https://doi.org/10.1007/s11837-021-04630-0.

[3] R. Roumina, S. Lee, T.D. Berman, K.S. Shanks, J.E. Allison, A. Bucsek, Mg-3 . 2Zn-0 . 1Ca wt. .% alloy using in-situ far field high-energy diffraction microscopy, Acta Mater (2022) 118039. https://doi.org/10.1016/j.actamat.2022.118039.

Fatigue Crack Initiation and Growth in Ultrafine-Grained Magnesium Deformed at Subfreezing Environmental Temperatures

Qizhen Li, Washington State University

Keywords: Magnesium, Fatigue life, Deformation mechanism, Crack initiation and growth, Subfreezing temperature

Research Scope

This project aims to uncover the fundamental mechanisms of fatigue crack initiation and growth in ultrafine-grained magnesium when the testing temperature is below 0ºC. The insight enabled through the project will unveil the activities and interactions of dislocations, twins, and grain boundaries in magnesium at the studied temperatures and cyclic loading conditions. Although there are extensive research efforts devoted to investigate the deformation behaviors and mechanisms of magnesium under a wide range of different loading conditions including static, dynamic, high strain rate, and cyclic loading at room temperature, only very few published papers were focused on the testing temperatures below room temperature [1-4]. It is clear that the testing temperature has a strong effect on mechanical behavior of magnesium [1]. During the winter season, many regions over the world experience cold weather with environmental temperatures much lower than 0°C [5]. The environmental temperatures are the service temperatures for many components of automobiles and aircrafts during the winter season. The major research goal of this project is to understand cyclic mechanical properties, fatigue deformation mechanisms, and fatigue crack behaviors of ultrafine grained magnesium at sub-freezing temperatures through investigating endurance limit and fatigue life, and through exploring grain boundary activities, twinning/detwinning, and dislocation operations.

Recent Progress

Some results from this project indicate the existence of three deformation stages (i.e. Stage A, Stage B, and Stage C) for fine-grained magnesium during fatigue testing at subfreezing temperature, as shown in Figure 1. Stage A went from the first cycle to about the 5000th cycle. During this stage, the material primarily experienced cyclic softening, and ε_{max} and ε_{min} increased with a decreasing rate during the beginning 5000 cycles. The maximum values for ε_{max} and ε_{min} were about 0.91% and 0.51% respectively. Stage B started at the end of Stage A and continued until about the 50,000th cycle. During this stage, ε_{max} and ε_{min} decreased with the increase of N, and cyclic hardening was dominating. At about the 50,000th cycle, the deformation transited to Stage C. The minimum values for ε_{max} and ε_{min} were about 0.72% and 0.30% respectively. In Stage C, ε_{max} and ε_{min} increased at an increasing rate. Overall, the variation of ε_{max} and ε_{min} followed the same trend during the whole test until about the 51,000th cycle. Therefore, $\Delta\varepsilon$ stayed at around

0.41% from the first cycle to about the 51,000th cycle and then increased until fracture. The responses during Stage A and Stage B would be due to the competition between deformation accumulation and strain hardening. At Stage A, the amount of deformation accumulation was low and the corresponding strain hardening was small, thus deformation accumulation was dominating. At Stage B, strain hardening became dominating with all the deformation accumulated during Stage A, the hardened material was harder to deform, and ε_{max} and ε_{min} decreased with N. The material became unstable in Stage C, and ε_{max} and ε_{min} quickly increased until fracture.

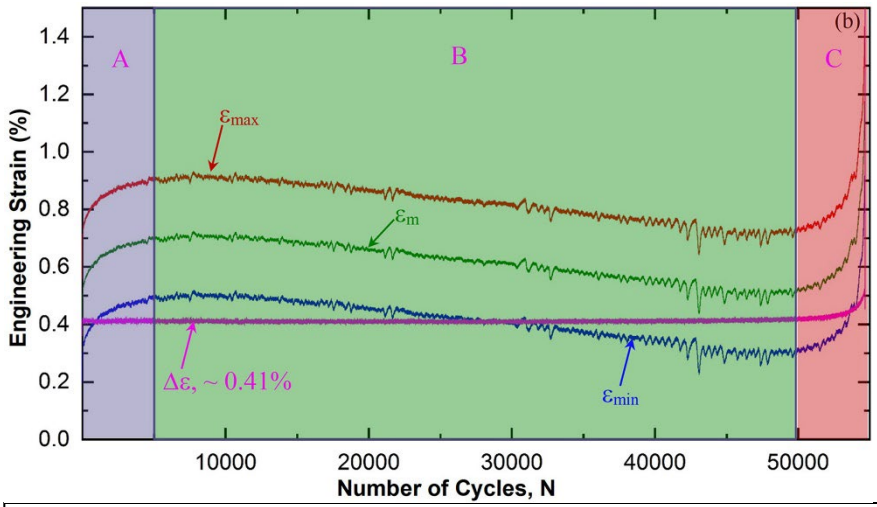

Figure 1. Variations of ε_{max}, ε_{min}, ε_m, and $\Delta\varepsilon$ with the number of loading cycles N. (A, B, and C are the three stages of deformation response of the material under fatigue loading; ε_{max} – maximum strain per cycle, ε_{min} – minimum strain per cycle, ε_m – average strain per cycle, $\Delta\varepsilon$ –strain range per cycle).

SEM microscopic image in Figure 2 reveals that there are secondary cracks. The right edge of this image is the fracture location, and the loading direction is horizontal as labeled. The two ellipses marked two secondary cracks. These cracks are labeled as I and II respectively. Both cracks were originated from the edge of the sample (i.e. the sample surface). They are also roughly along the vertical direction, and thus perpendicular to the loading direction.

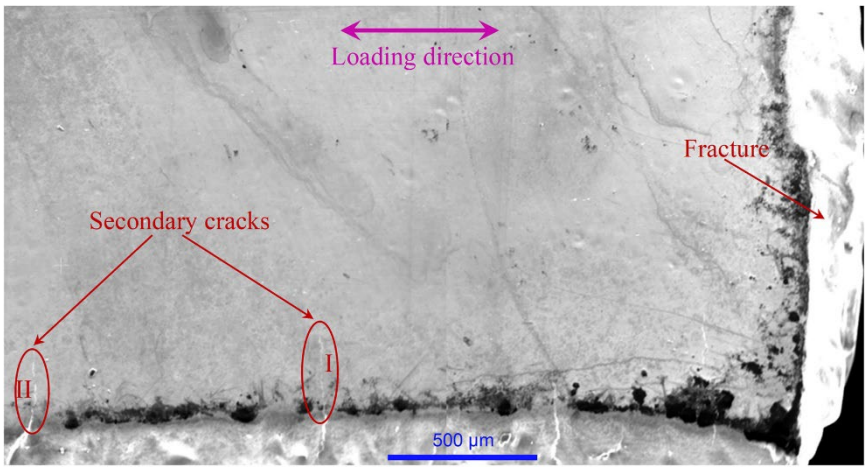

Figure 2. Scanning electron microscopic image of the top face of the fractured sample after the fatigue testing at −30 °C. Regions I and II are secondary cracks.

Region I in Figure 2 was magnified to observe the microstructural features around the secondary crack tip as reported in Figure 3. The SEM image in Figure 3(a) shows that the crack is almost perpendicular to the loading direction while there are some zigzags during the crack propagation as indicated by the dotted circles i and ii. The circle i encloses the bifurcation of the

crack with one branch B1 at about 24° from the loading direction and the other branch B2 at about 51° from the loading direction. The crack continued along the branch B2. The circle ii marks another location with the crack progressing along a direction away from that perpendicular to the loading direction. The left portion in the circle ii followed a direction of about 72° from the loading direction for about 10 μm.

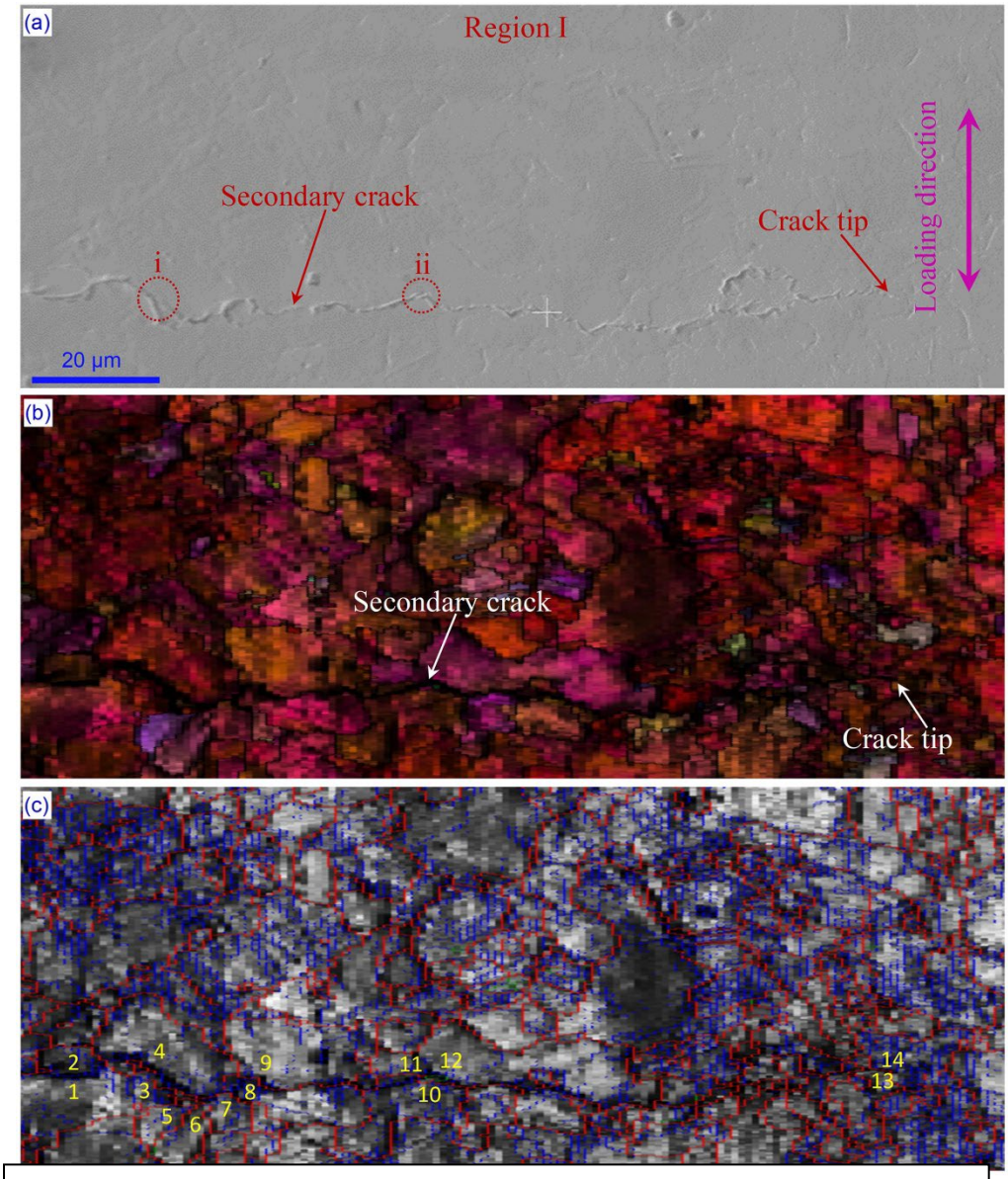

Figure 3. (a) SEM image, (b) the combined inverse pole figure map plus band contrast map, and (c) the grain boundary map for the region around the crack tip of the secondary crack I. (The micro bar in (a) is shared by (b) and (c)).

This region was observed under EBSD and Figure 3(b) provides the combined inverse pole figure map plus band contrast map. According to the crack outline shown in Figure 3(b), the crack propagated along grain boundaries. This feature is displayed more clearly through the grain boundary map in Figure 3(c). The boundaries with the misorientation angles of 2° ~ 15°, > 15°, and 84° ~ 90° are colored in blue, red, and green respectively. The 84° ~ 90° angle range represents tensile twin boundaries (TTBs). There are very few TTBs and the length is about 223 μm. The 2° ~ 15° and > 15° angle ranges refer to the small angle grain boundaries and large angle grain boundaries respectively, and their corresponding lengths are 3.16 cm and 2.12 cm. Figure 3(c) shows that there was no part of the crack along TTBs and the crack progressed along

both small angle grain boundaries and large angle grain boundaries. In addition, mostly the crack propagated along large angle grain boundaries.

Future Plans

The project will continue exploring the fatigue crack initiation and growth mechanisms and fatigue properties through further microstructural and mechanical characterizations for both fine-grained and coarse-grained magnesium samples at sub-freezing testing temperatures.

References

1. Q. Li, *Effect of Subfreezing Testing Temperature on Tensile Mechanical Behavior of Fine-grained Magnesium*, Materials Science and Engineering A **803**, 140457 (2021).

2. D. Jung, J. Kwon, N. Woo, Y. Kim, M. Goto, S. Kim, *S–N Fatigue and Fatigue Crack Propagation Behaviors of X80 Steel at Room and Low Temperatures*, Metallurgical and Materials Transactions A **45**, pp. 654 (2014).

3. O.P. Ostash, I.M. Andreiko, V.V. Kulyk, I.H. Uzlov, K.I. Uzlov, O.I. Babachenko, *Low-Temperature Cyclic Crack Resistance Of Steels Of Railroad Wheels*, Materials Science **44**, pp. 524 (2008).

4. D. Jeong, S. Lee, J. Yoo, J. Lee, S. Kim, *Comparative studies on near-threshold fatigue crack propagation behavior of high manganese steels at room and cryogenic temperatures*, Materials Characterization **103**, pp. 28 (2015).

5. January–february 2019 North American Cold Wave, 2019 https:// en.wikipedia.org/ wiki/ January%E2%80%93February_2019_North_American_cold_wave.

Publications

1. Y. Zhu, D. Hou, Q. Li, *Quasi in-situ EBSD analysis of twinning-detwinning and slip behaviors in textured AZ31 magnesium alloy subjected to compressive-tensile loading*, Journal of Magnesium and Alloys **10**, 956-964 (2022).

2. J. Wang, Q. Li, *Microhardness Distribution of Long Magnesium Block Processed through Powder Metallurgy*, Journal of Manufacturing and Materials Processing **7** (5), 1-17 (2023).

3. W. Zhao, Q. Li, *Effect of Grain Size on Bio-Corrosion Properties of AZ31 Magnesi um Alloy*, Magnesium Technology, 205-209 (2023).

4. Q. Li, *Geometrically Necessary Dislocation Analysis of Deformation Mechanism for Magnesium under Fatigue Loading at 0 oC*, Crystals **13** (3), 490 (2023).

5. Q. Li, *Fatigue crack propagation in fine-grained magnesium under low temperature tension-tension cyclic loading*, Journal of Magnesium and Alloys **11**, 4420-4430 (2023).

Influence of 3D heterophase interface structure on deformation physics

Prof. Nathan A. Mara, University of Minnesota-Twin Cities

Prof. Irene J. Beyerlein, University of California, Santa Barbara

Keywords: Dislocation-interface interactions; Phase Field Dislocation Dynamics; Nanolayered Composites; Electron Microscopy; Enhanced Strength and Ductility

Research Scope:

The goal of this program is to develop an **understanding of the mesoscopic effects of biphase interfaces on their interactions and reactions with dislocations**. Interfaces play a profound role in the response of polycrystalline materials to mechanical deformation through the localized strains and stresses they develop and their resulting impact on the defects that enable plasticity. Not all interfaces produce the same effect and the outcomes of their interactions and reactions with defects depend on the structure of the interface.

This program aims to span processing/microstructure/ property relationships for 3D interface motifs with a combination of experiment and modeling. The critical set of length scales in which 3D interfaces can affect hardening and material strength will be the mesoscopic scales, lying between atomistic simulation and the continuum. We join well-controlled synthesis techniques with mesoscopic modeling to investigate biphase systems where we can control the interface motif. Specific activities include controlled synthesis, characterization with a suite of techniques to define properties before/during/after straining, atomic and mesoscale modeling of motifs with impinging dislocations, and mechanical testing. On the experimental side, the composites are synthesized via physical vapor deposition, a process by which the composition and/or

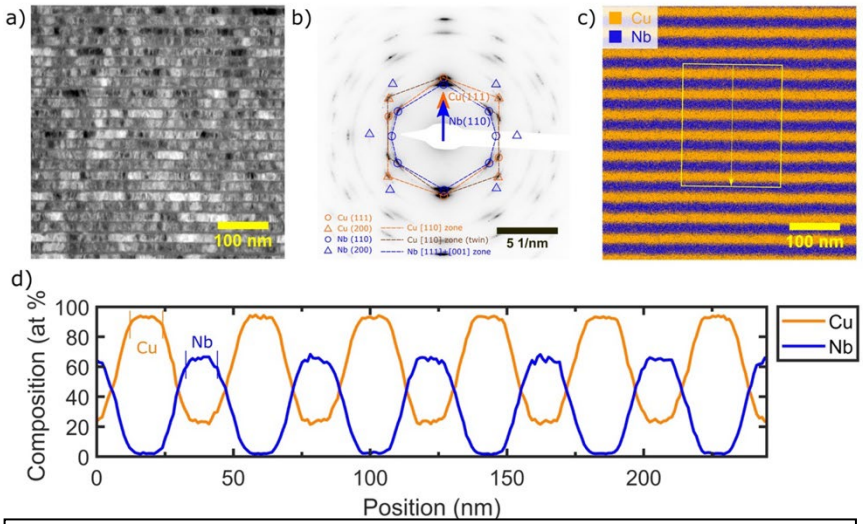

Figure 1: a) HAADF-STEM image of undeformed 10–10 Cu/Nb. **b)** Grayscale-inverted SAD diffraction pattern from near the region shown in a) showing that Cu (111) and Nb (110) planes are parallel to layer directions. Note that the orientation between a) and b) does not change – a direction indicated in reciprocal space in b) is aligned with the same direction in real space in a). **c)** STEM-EDS map of region a) with Cu in orange and Nb in blue. **d)** Elemental profile taken from c) along the direction of the yellow arrow and averaged along the width of the box encompassing that arrow. The layer and interface thicknesses taken from this profile are summarized in Table 2. Note that Nb layers appear impure due to the redeposition of more mobile Cu during FIB preparation of TEM specimens.[2]

structure may be systematically varied in the out-of-plane direction. Microstructural characterization consists of addressing structure at the atomic level (TEM, Atom Probe), as well as mesoscales (X-ray). Mechanical behavior is investigated from atomic-level dislocation-interface interactions (in-situ TEM) to micro scales (in-situ SEM and ex-situ nanomechanical testing). On the modeling side, the desired length scales need to capture the motion of dislocation arrays and simulate the structural stability of 3D interfaces with respect to local dislocation fields. At present, several methods for simulating the dynamic evolution of many discrete dislocations in crystals with interfaces that span this broad range of length scales, namely molecular dynamics (MD), discrete dislocation dynamics (DDD) and phase field dislocation dynamics (PFDD). In this program, we exploit PFDD to simulate multiple dislocation interactions with 3D interfaces with experimental or DFT or MD input on only the most fundamental properties to build models that stretch out to larger time and length scales. PFDD can model a single crystal or polycrystal and recovery processes and the output linked to experimentally determined stress-strain responses.

Recent Progress:

Recently, we discovered that Cu-Nb nanocomposites containing 3D interfaces with layer thickness h = 10 nm and 3D interfacial thickness of h' = 10 nm possess enhanced compressive strength and deformability as compared to similar material with 40 nm pure layer thickness [3]. **(See Figure**

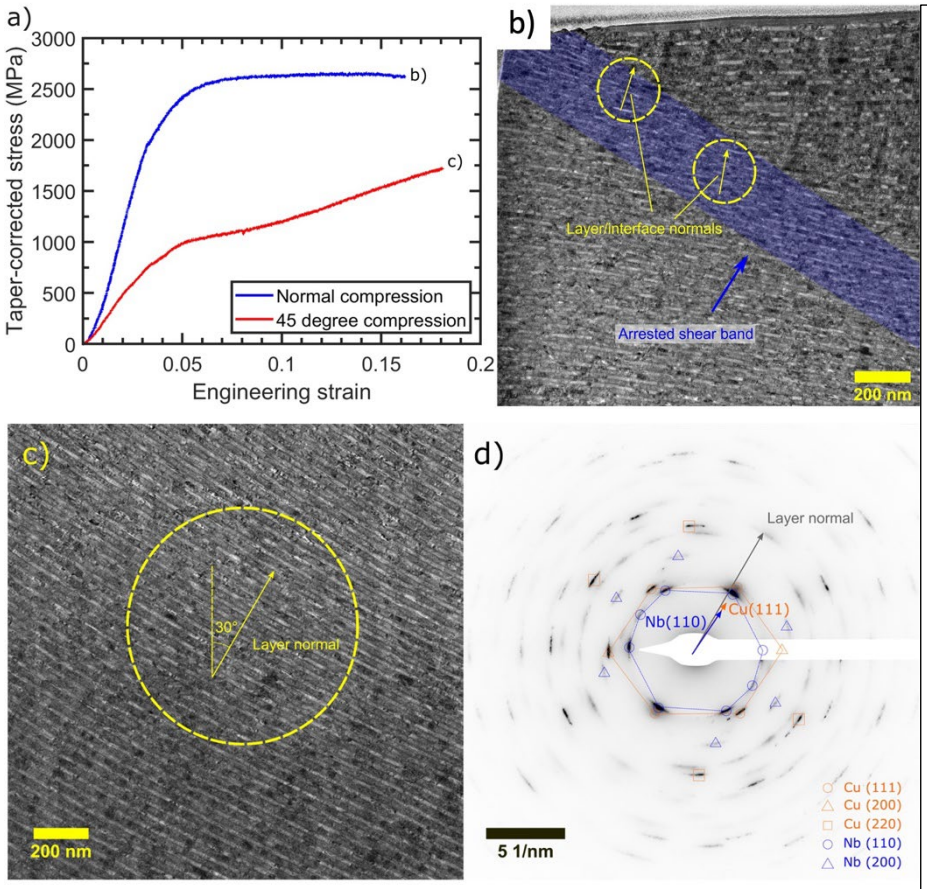

Figure 2: a) Stress-strain curves for normal and 45◦ compression pillars. **b)** CTEM micrograph of an arrested shear band from the top of a layer-normal compression pillar in 10–10 Cu/Nb. Note layer rotation for many layers under the shear band. **c)** CTEM micrograph of area of interest in a) denoted by the dotted yellow box. The final orientation of planes parallel to Cu and Nb layers is depicted with respect to the compression axis. **d)** SAD pattern taken from the area in c) indicated by the dotted yellow circle. Orange and blue arrows depict the orientation of Cu and Nb compact planes that began at 45◦ incidence to the compression axis, respectively. The grey arrow depicts orientation of layer/interface planes after compression. [2]

1) In conventional (2D interface) nanolaminate materials, such a decrease in layer thickness has historically been associated with an increase in strength, but a decrease in deformability [4].

Moreover, we investigated the anisotropy of these same materials using micropillar compression parallel, perpendicular, and at a 45° angle with respect to the interface. When loaded in shear, h = 10 nm h' = 10 nm Cu/Nb exhibits enhanced work hardening, and homogeneous deformation without shear banding before failing via shear banding (Figure 2b) [2]. When 2D Cu/Nb is loaded in shear, local interface sliding leads to softening and fast failure. The 3D interface lends considerable shear strength to the interface, and no localized shear occurs (see Figure 2c), leaving a structure where the layers thin uniformly, but minimal rotation of the layers or the constituent crystals is observed. Utilizing Crystal Plasticity Finite Element (CPFE) modeling (not shown, but available in [2]), we demonstrated that for shear loading of a Cu/Nb nanocomposite with high interfacial shear strength, the cubic symmetry of the constituent materials favors slip across the interface on many slip systems, such that ~90% of slip occurred via transmission across the 3D interface. This finding implies that the 3D interface can enhance both strength and ductility in materials where the Schmid factor on multiple systems in each pure constituent is high. It also leads to the question, could a 3D interface facilitate deformation in a more anisotropic constituent?

To answer this question, we investigated Ti/Nb hcp/bcc nanocomposites. The microstructure of the magnetron sputtered Ti/Nb system in **Figure 3** is characterized by a {1000}basal-hcp//{110}bcc interface plane, where the 3D interface thickness can be nearly atomically sharp as in this example, or made diffuse through co-deposition. The texture from the diffraction pattern in **Figure 3d** is not quite as pronounced as for Cu/Nb (Figure 2d). XRD results (not shown) are consistent with the aforementioned crystallography, and hcp-Ti-based dark field images (Figure 2b) reveal the expected columnar polycrystalline structure and crystallography.
For hcp Ti, basal (0001)⟨11-20⟩ slip and prismatic (10-10)⟨11-20⟩ slip are the preferred slip systems. Our experiments indicated that a 3D interface would strengthen a material over nanocrystalline pure Ti, and we observed a "thicker is stronger" 3D interface effect. However, the mechanism giving rise to this behavior remain elusive. With PFDD, we simulated slip transfer

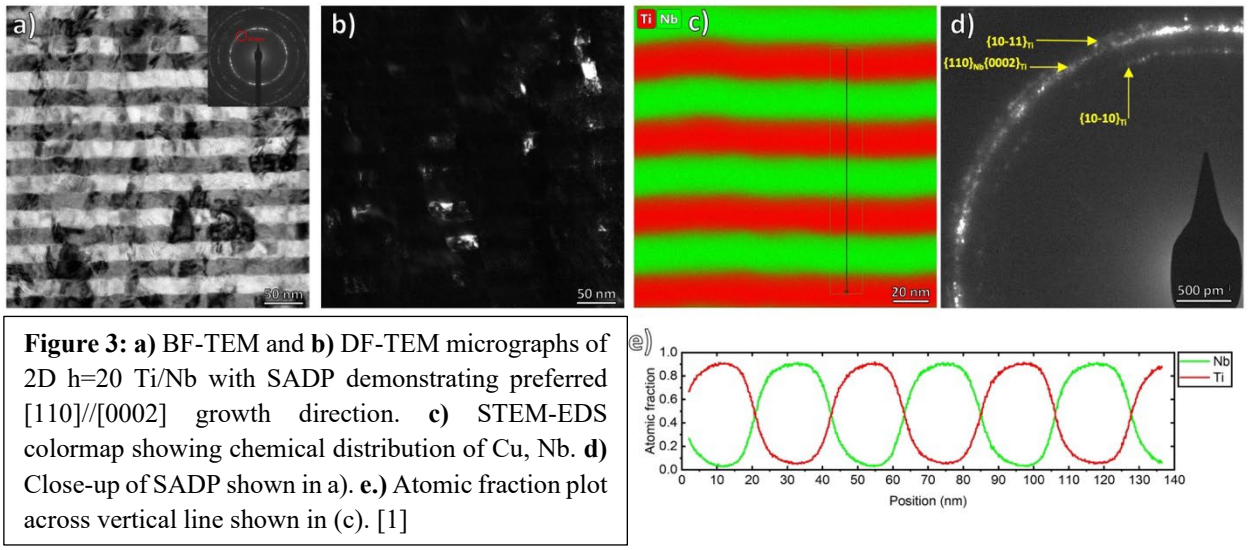

Figure 3: a) BF-TEM and **b)** DF-TEM micrographs of 2D h=20 Ti/Nb with SADP demonstrating preferred [110]//[0002] growth direction. **c)** STEM-EDS colormap showing chemical distribution of Cu, Nb. **d)** Close-up of SADP shown in a). **e.)** Atomic fraction plot across vertical line shown in (c). [1]

across the 3D interface utilizing only experimental measurements and DFT for input on fundamental properties with no adjustable parameters. The model considers changes in stacking fault energies, elastic anisotropy, crystal structure, and lattice parameter among the phases and 3D interface. **Figure 4** shows the simulation cell and predictions on critical slip transfer strength. Two orientation relationships are considered to involve either basal or prismatic slip. We found a strengthening effect as the interface thickened. Interestingly, below a critical h' of ~2 nm, the transmission stress was higher from Nb to Ti. Above it, the transmission stress is higher from Ti to Nb. This was true for both orientations for prismatic and basal slip and motivates our next anisotropy experiments under uniaxial compression.

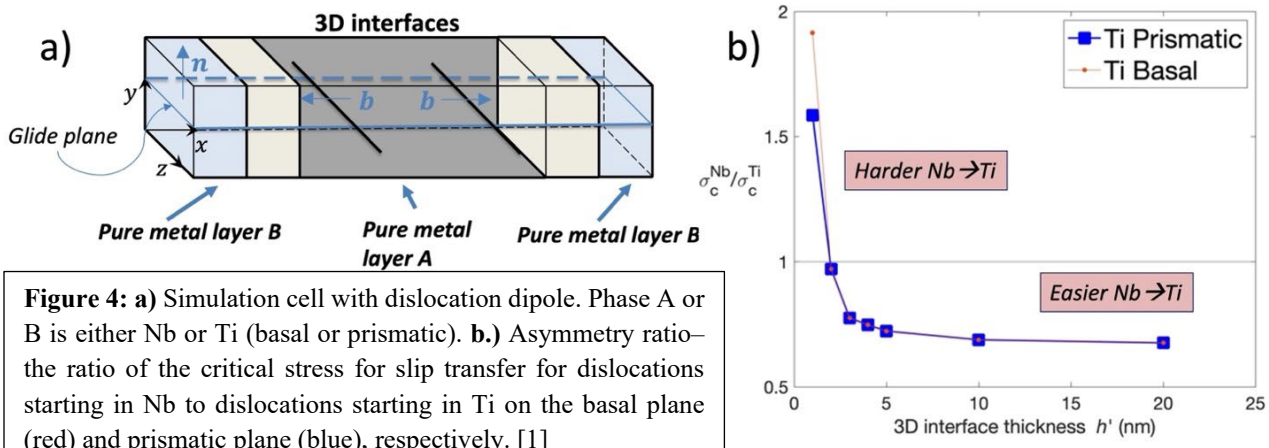

Figure 4: a) Simulation cell with dislocation dipole. Phase A or B is either Nb or Ti (basal or prismatic). **b.)** Asymmetry ratio– the ratio of the critical stress for slip transfer for dislocations starting in Nb to dislocations starting in Ti on the basal plane (red) and prismatic plane (blue), respectively. [1]

Future Plans

Over the next year of our existing grant, we will be carrying out microcompression testing to determine the mechanical anisotropy of Ti-Nb composites, as well as modeling the interfaces that are predominantly observed experimentally under different applied loads. We also plan to understand the effects of dislocation dissociation in Ti. Further, we will carry out thermal stability studies of Ti-Nb with an emphasis on alloying effects of Nb on phase stability of the 3D interface.

References

1. Fuchs-Lynch, N., P. Garg, M.d. Leo, S. Xu, N.A. Mara, and I.J. Beyerlein, *3D interface size effects on slip transfer in Ti/Nb nanolaminates.* in preparation.
2. Cheng, J.Y., J. Wang, Y. Chen, S. Xu, J.G. Barriocanal, J.K. Baldwin, I.J. Beyerlein, and N.A. Mara, *3D interfaces enhance nanolaminate strength and deformability in multiple loading orientations.* Acta Materialia, 2024. **267**: p. 119697. DOI:https://doi.org/10.1016/j.actamat.2024.119697
3. Cheng, J.Y., S. Xu, Y. Chen, Z. Li, J.K. Baldwin, I.J. Beyerlein, and N.A. Mara, *Simultaneous High-Strength and Deformable Nanolaminates With Thick Biphase Interfaces.* Nano Letters, 2022. **22**(5): p. 1897-1904. DOI:10.1021/acs.nanolett.1c04144
4. Beyerlein, I.J., Z. Li, and N.A. Mara, *Mechanical Properties of Metal Nanolaminates.* Annual Review of Materials Research, 2022. **52**(1): p. 281-304. DOI:10.1146/annurev-matsci-081320-031236

Publications

Primary Publications (2022-present):

1. J.Y. Cheng, S. Xu, Z. Li, I.J. Beyerlein, N.A. Mara, *Simultaneous High-Strength and Deformable Nanolaminates With Thick Biphase Interfaces*, Nano Letters **22**, Issue 5, 1897-1904 (2022).
2. I.J. Beyerlein, Z. Li, N.A. Mara, *Mechanical Properties of Metal Nanolaminates,* Annual Review of Materials Research **52**, 281-304 (2022).
3. Z.Li, J.Y. Cheng, J.D. Poplawsky, S. Xu, J.K. Baldwin, I.J. Beyerlein, N.A. Mara, *Critical length scales for chemical segregation at Cu/Nb 3-D interfaces by atom probe tomography,* Scripta Materialia **223**, 115078, (2023).
4. S. Xu, J.Y. Cheng, N.A. Mara, I.J. Beyerlein, *Dislocation dynamics in heterogeneous nanostructured materials,* Journal of the Mechanics and Physics of Solids **168**, 105031 (2022).
5. S. Xu, J.Y. Cheng, N.A. Mara, I.J. Beyerlein, *Thick interface size effect on dislocation transmission in nanolaminates,* IOP Conference Series: Materials Science and Engineering **1249**, 012005 (2022).
6. S. Xu, "Recent progress in the phase-field dislocation dynamics method", *Computational Materials Science,* Volume 210, 111419, (2022).
7. J.Y. Cheng, "The influence of 3D interfaces on mechanical behavior of nanolaminated bimetallic composites", *PhD Dissertation, University of Minnesota*, (2024).
8. J.Y. Cheng, J. Wang, Y. Chen, S. Xu, J.G. Barriocanal, J.K. Baldwin, I.J. Beyerlein, N.A. Mara, "3D interfaces enhance nanolaminate strength and deformability in multiple loading orientations", *Acta Materialia,* Volume 267, 119697, (2024).
9. J.Y. Cheng, Z. Li, D.L. Poerschke, J.K, Baldwin, B.L. Bresnahan, N.A. Mara, "Thermal Stability of 3D Interface Cu/Nb Nanolaminates", *Scripta Materialia (in press)*.
10. A. Hamilton, J.Y. Cheng, M. Odlyzko, M. de Leo, J.K. Baldwin, N.A. Mara "Highly wear resistant Ti/TiN nanolayered composites containing graded interfaces", *Wear (in review).*

Chemical partitioning and radiation damage in concentrated alloys

Emmanuelle Marquis (University of Michigan), Fadi Abdeljawad (Lehigh), Enrique Martinez (Clemson), Suveen Mathaudhu (Colorado School of Mines)

Keywords: Irradiation, grain boundaries, segregation

Research Scope

This program addresses the mechanisms behind radiation-induced segregation (RIS) in concentrated alloys by elucidating the synergies between solute and defects and the interactions between solutes fluxes and extended defects (dislocations, voids, grain boundary network). Focusing on Fe-Ni-Cr based alloys with possible alloying with Mn and/or Co, current work focuses on understanding interactions and of solutes and defects (vacancies and interstitials), quantifying RIS evolution with dose and interactions with microstructure ion ion-irradiated alloys, understanding the mechanisms behind grain boundary migration in some alloys and not others, and understanding the role of grain size on RIS behavior.

Recent Progress

To answer key questions about RIS, a multiprong approach was adopted and we detailed the main achievements below.

Grain boundary thermal segregation

Understanding equilibrium segregation to establish a baseline against which to compare irradiated microstructure is essential. From a modeling standpoint, very little is known about the dependence of defect energies, that are essential to any RIS treatment, on the particular fit of interatomic potentials used in atomistic studies. Abdeljawad published a study that provides a quantitative understanding of the impact of EAM interatomic potential parameters, commonly used in RIS studies, on interfacial properties [1]. Our results reveal that interfacial energies are extremely sensitive to the particular choice of interatomic parameters and highlight the need to consider this effect in studies of RIS. In this project, several interatomic potentials for the alloy system selected are being considered and emphasis will be placed on recovering physical trends rather than recovering specific values. To highlight similarities and discrepancies between computations and experimental data, the team conducted segregation measurements at grain boundaries as a function of temperature on a Cantor alloy, used as a model HEA system.

Role of alloy chemistry on RIS

To understand the role of individual elements on RIS, Offidani and Marquis conducted ion irradiations of Fe-27Ni-10Cr, Fe- 27Ni-10Cr-8Co, Fe-27Ni-10Cr-8Mn (in at.%) and Cantor alloys at different temperatures and doses. Detailed experimental quantification of RIS at large angle grain boundaries is currently on-going. Developing a detailed understanding of the impact of the shallow damage depth inherent to ion irradiation on RIS measurements was first needed to appropriately quantify RIS. The team uncovered a strong dependence of the RIS with irradiation depth, as well as non-negligible grain boundary diffusion away from the irradiated region (**Fig.1**) [4]. In parallel, Jeffries and Martinez have been calculating the transport coefficients in CrFeMnNiCo and associated binary/ternary/quaternary subsystems, which is key to rationalize the

observed RIS behaviors. They have performed molecular dynamics simulations to calculate the transport coefficients for a single point defect (PD), and have published the package for computing these transport coefficients on the Python Package Index (PyPI) (https://pypi.org/project/onsager-coefficients/). They have developed a general model for calculating impurity concentrations in concentrated alloys to rescale these transport coefficients by their corresponding PD concentration. In order to inform a phase-field model to calculate segregation profiles, Abdeljawad and Martinez have developed a lightweight, open-source tool to calculate chemical potentials and fit them to a regular solution model (https://github.com/MUEXLY/chemical_potential). This has potential to reach a much wider audience, aiding in the quantification of thermodynamics of solid solutions as a whole. They also calculated these concentrations depending on short-range order (SRO), also publishing the SRO calculation on PyPI (https://pypi.org/project/cowley-sro-parameters/). Lastly, they have built a Kinetic Monte Carlo (KMC) tool to compute diffusivity in a noisy environment with plans to make it opensource. This tool was used to compute diffusivity as a function of barrier standard deviation, of which we have developed semi-analytical expressions.

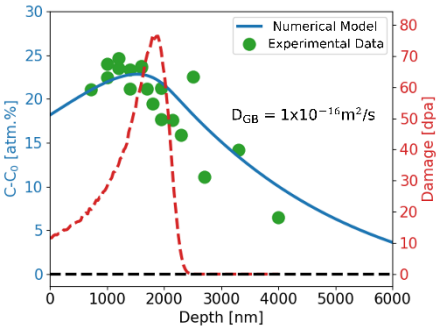

Figure 1. Experimentally measured grain boundary peak Ni concentration obtained from the Fe-Ni-Cr alloy nominally irradiated to 35 dpa, with comparison to the numerical solution of a simple diffusion model that considers grain boundary diffusion away from the irradiated region.

Dependence of RIS with dose and temperature

Focusing initially on characterization of the ternary base alloy, Offidani and Marquis have showed that the extremum of concentration along high angle grain boundaries in the selected Fe-Ni-Cr alloys does not saturate with dose as is normally expected. Furthermore, the width of the region affected by RIS around grain boundaries continuously increases. Phase field calculations by Martinez and Abdeljawad are on-going to understand the origin of the lack of saturation. An initial hypothesis is related to the phase transformation that is presumably irradiation-accelerated and noted in these alloys after irradiation. Wang and Abdeljawad completed the development and initial numerical implementation of a mesoscale model of RIS in multi-component alloys using the Message Passing Interface. The model accounts for chemical thermodynamics of multi-component concentrated alloys; various mass transport mechanisms; and generation, interaction, and recombination of irradiation-induced points defects. As inputs, the model employs mass transport coefficients and chemical potentials which are computed using the atomistic simulation thrust by co-PI Martinez. The output of our mesoscale computational studies will be composition profiles of chemical species and point defects that will be cross-validated with the experimental studies by Offidani and Marquis.

Synergy between irradiation, grain boundary migration, and RIS

The initial experimental analysis of RIS at large angle grain boundaries in the Mn containing alloys (Offidani and Marquis) reveal significant grain boundary migration during irradiation. To understand how grain boundary velocity impacts RIS, Jeffries and Martinez have been studying the effect of grain boundary (GB) velocity, with two GBs moving in opposite directions, on radiation induced segregation (RIS). Fe-Cr alloys are simulated using a KMC algorithm to

calculate the Cr segregation profiles at the moving interfaces. GB motion is achieved by applying stress at both ends of the domain. Current results show the same level of segregation is achieved at lower doses with increasing grain boundary velocity. The segregation profiles are asymmetric at the grain boundaries, as observed experimentally (see **Fig. 2**). The goal is also to find a relationship between velocity and applied stress to understand the role of RIS in GB drag. Future work will investigate the segregation profile at higher temperature.

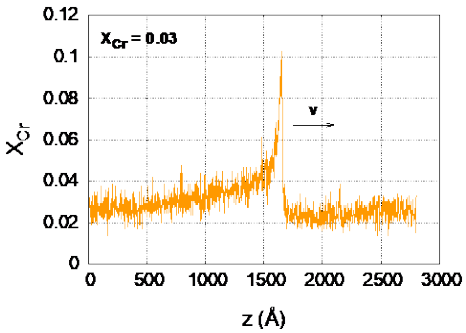

Figure 2: Asymmetric Cr concentration profile in a Fe-3%Cr ferritic alloy under irradiation with concurrent GB motion as obtained with a KMC model.

Role of grain size on RIS

One goal of our project is to understand RIS behavior as a function of grain size, or equivalently GB density, grain boundary orientation, and alloy composition/complexity. Recently, Thomas and Mathaudhu used high pressure torsion (HPT) of a FeCr alloy to achieve grain sizes of ~150 nm and grain growth studies to tailor grain sizes to larger ranges. FeCr samples were ion irradiated at Michigan to 5 dpa at 400 ºC and returned to Mines for TEM chemical and orientation analysis. These collaborative experimental studies will both inform and validate existing theory developed by Martinez on the effect of grain size on RIS. As for modeling efforts related to the impact of grain size (i.e., GB spacing) on RIS behavior, Wang and Abdeljawad used their recently developed atomistically informed mesoscale model of RIS and GB migration to examine the impact of grain size and alloy non-ideality on RIS profiles. As inputs, the model employs transport coefficients from lower length scale simulations by Jeffries and Martinez. For example, using computed transport coefficients of Fe-9%Cr alloy, Figure 3 shows results from mesoscale phase field simulations depicting the impact of grain size on RIS profiles. The steady-state Cr concentration profiles across the simulation domain are shown in **Fig. 3(a)**, whereas Fig. **3(b)** depicts the GB Cr solute excess across as a function of grain size.

Figure 3: For the Fe-9%Cr model alloy, mesoscale phase field simulations depicting the im-pact of grain size on RIS. (a) Cr concentration line scans across the simulation domain. (b) GB Cr solute excess as a function of grain size.

Future Plans

On the experimental side, Offidani and Marquis will finalize the quantification of RIS in our first series of alloys after irradiation at 400 ºC with upcoming additional ion irradiation to reach doses of ~ 60-70 dpa. This will yield a complete description of RIS and microstructure evolution in the base Fe-Ni-Cr alloy with and without Mn or Co and the development of grain boundary migration and its synergy with RIS. To explore a possible synergy between RIS and phase decomposition, irradiation at 500 C where the alloys are predicted to be phase stable will be conducted at two

doses (2 and ~30-40 dpa) to test whether RIS reaches a steady state. In parallel, Thomas and Mathaudhu have prepared a new base alloy (Fe-40Ni-10Cr) that remains as a single phase at the irradiation temperatures (300-500 ºC). They will be processing the alloy to reach grain sizes <100 nm. They will be working with Offidani and Marquis to irradiate the new alloys to understand the effect of grain size on RIS.

On the computational side, Martinez will continue our work on the analysis of the synergy between grain boundary motion and RIS. We are comparing the drag under thermal and irradiation conditions and we plan to validate against experimental observations. Martinez will keep developing a robust suite of scripts to compute transport coefficients as a function of composition from atomistics to inform mesoscale models to reach experimental times. Finally, Abdeljawad will conduct mesoscale computational studies to quantify the impact of grain size and deviations from ideal solution thermodynamics on RIS profiles. Further, the modeling framework is developed to capture RIS in multicomponent alloys. As a result, Abdeljawad will conduct computational studies in ternary alloys, treated as model multicomponent systems, to investigate mechanisms controlling RIS in systems with complex chemistry.

Publications

1. Marie Thomas, Heather Salvador, Trevor Clark, Eric Lang, Khalid Hattar, Suveen Mathaudhu "*Thermal and Radiation Stability in Nanocrystalline Cu*", **Nanomaterials**, 13 (2023) 1211. https://doi.org/10.3390/nano13071211
2. Yasir Mahmood, Murray Daw, Michael Chandross, and Fadi Abdeljawad, "Universal trends in computed grain boundary energies of FCC metals," Scripta Materialia **242** (2024) 115900. https://doi.org/10.1016/j.scriptamat.2023.115900
3. Ryan Schoell, Christopher Barr, Douglas Medlin, David Adams, Yasir Mahmood, Fadi Abdeljawad, Khalid Hattar, "The radiation instability of thermally stable nanocrystalline platinum gold", Journal of Materials Science, **59** (2024) 11497-11509
4. Daniele Fatto Offidani, Enrique Martinez, Emmanuelle A. Marquis, "On the analysis of radiation-induced segregation at ion-irradiated grain boundaries," Journal of Nuclear Materials. Under review
5. Jacob Jeffries, Suveen Mathaudhu, Emmanuelle Marquis, Fadi Abdeljawad, Enrique Martinez "Prediction of dilute impurities in concentrated solid solutions using a Langmuir-like model," Physical Review Materials. Under review. Manuscript available: arXiv:2402.07324

Metal-ceramic interfaces at high temperatures

Yuri Mishin, George Mason University, Fairfax, Virginia

Keywords: Interfaces, metals, ceramics, modeling, simulation

Research Scope

This research program aims to improve the fundamental understanding of metal-ceramic interfaces at high temperatures and develop new methods for computational prediction of their structure, thermodynamics, kinetics, and mechanical responses. This goal will be achieved by large-scale atomistic computer simulations of interfacial shear deformation, interfacial creep, and interface diffusion in several model systems representing metal-nonmetal contacts. The initial stage of the program will focus on Al-Si alloys as prototypical composite materials. However, our long-term goal is to expand this program to other classes of metal-matrix composites. The project can significantly impact the fundamental knowledge of metal-ceramic interfaces at high temperatures. It can also create a theoretical foundation for the design of new creep-resistant composite materials in the future.

Recent Progress

Several key processes occurring at metal-ceramic interphase boundaries (IPBs) are the atomic transport of the chemical components along the IPB, grain boundaries (GBs) in the metallic phase, triple lines between the GBs and between a GB and the IPB, and along dislocations attached to the IPB and extending into the metal. Applied shear stress can cause sliding along the IPB, which at high temperatures has the character of interfacial creep. Our goal is to understand the atomic mechanisms of these processes, quantify their rates, and establish the hierarchy of the diffusion pathways and their relation to the creep kinetics. Our simulation methodology combines classical molecular dynamics and Monte Carlo methods with various statistical data analyses and visualization techniques. The diffusion coefficients are extracted directly from mean-square displacements of atoms without adjustable parameters or model assumptions other than the approximations underlying the interatomic potential. As a starting point, we chose the Al-Si system as a model with a simple eutectic phase diagram and low mutual solid solubility between Al and Si. Al-Si alloys embody prototypical properties of metal-matrix composites, with Al representing a ductile matrix and Si representing a hard and brittle reinforcer.

Three methods were applied to create Al-Si IPBs: phase bonding, simulated epitaxy, and simulated vapor deposition (Fig.1). In the phase bonding method, Al and Si grains with chosen crystallographic orientations are bonded together. The initial orientation relationship between the phases cannot change during the anneal. In the simulated epitaxy and deposition methods, a Si substrate with a chosen crystallographic orientation is brought in contact with liquid Al or Al(Si) vapor, which solidify in a preferred crystallographic orientation. This process is ideal for discovering new orientation relationships. For the deposition on the Si(111) surface, the two most common surface reconstructions were considered: 1x1 and 7x7. In the first case, the deposited Al(Si) film was polycrystalline with columnar grains separated by $\Sigma 3$, $\Sigma 7$, and $\Sigma 21$ GBs with the common [111] axis normal to the substrate. This rich structure presented us with an exciting new opportunity to study the diffusion process in several short-circuit paths in the *same sample*: the

IPB, GBs, GB triple junctions (GBTJs), GB-IPB triple lines (GBTLs), threading dislocations (TDs), and disconnection (DC) loops (Fig. 2). The Al(Si) layer deposited on the 7x7 reconstructed Si(111) is single-crystalline and the IPB contains a network of misfit dislocations.

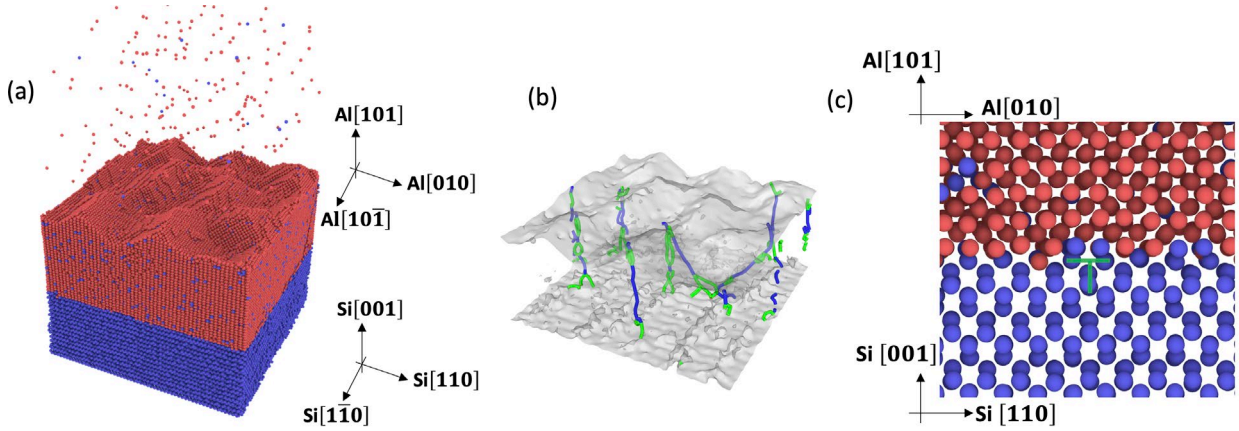

Figure 1: (a) Simulated growth of $Al_{0.93}Si_{0.07}$ layer on the Si(100) substrate by vapor deposition at the temperature of 622 K. (b) Threading dislocations in the growing layer are composed of full (blue) and partial (green) segments. (c) Example of a misfit dislocation in the interface.

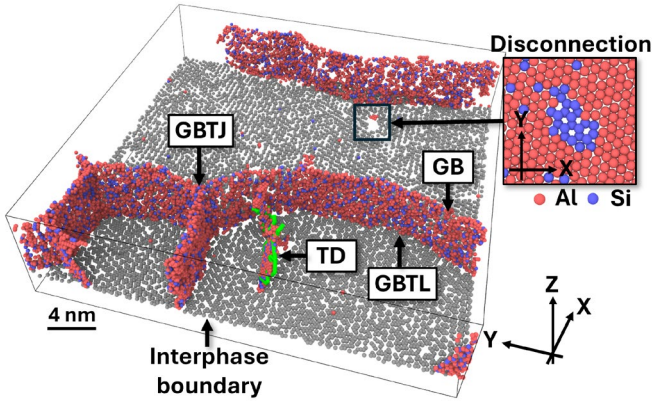

Figure 2: Perspective view of the polycrystalline $Al_{0.93}Si0_{.07}$ layer deposited on a Si(111)-1×1 substrate. The arrows point to the defects used in the diffusion calculations: the interphase boundary (IPB), grain boundaries (GBs), GB triple junctions (GBTJ), GB-IPB triple lines (GBTL), and threading dislocations (TD). The zoomed-in image shows a disconnection (DC) loop at the IPB with the blue and red colors representing the Si and Al atoms, respectively.

The diffusion calculations have shown that GBs exhibit much higher diffusivity than IPBs, with a difference of about two orders of magnitude. This large difference is explained by the ordering effect imposed by the Si substrate: the Si atoms in the substrate are virtually immobile, and their highly ordered arrangement imposes a period constraint on the IPB atoms, reducing their mobility. The anisotropy of GB and IPB diffusion is relatively small. Si diffuses faster than Al in all defect cores. Among the GBs, the $\Sigma 7$ GB has the highest diffusivity and the $\Sigma 3$ GB the lowest. This trend correlates with the strength of Si GB segregation. The diffusivity along the GBTJs and GBTLs strongly correlates with the respective GB diffusivities and is much faster than the diffusivity of both Al and Si in the IPBs. The IPB diffusion is dominated by diffusion along the misfit dislocations in the 7x7 IPB and along GBTLs in the 1x1 IPB. The Arrhenius diagrams in Fig. 3 summarize the diffusion calculation results.

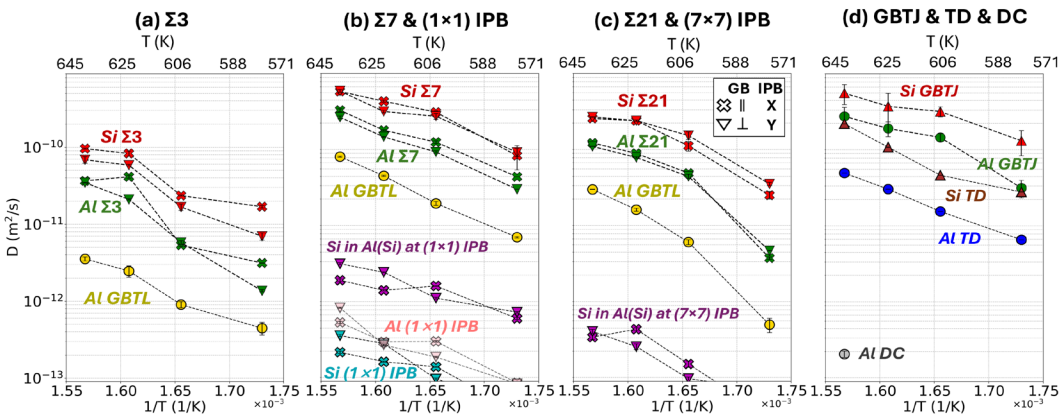

Figure 3: Arrhenius diagrams of Al and Si diffusion at the (a) $\Sigma 3$ GB, (b) $\Sigma 7$ GB and 1x1 IPB, (c) $\Sigma 21$GB and 7x7 IPB. The Al diffusion coefficient at GBTLs is also shown in (a-c). (d) Al and Si diffusion at GBTJs, TDs, and disconnection (DC) loops within the 1x1 IPB.

Collective atomic rearrangements in the form of strings and rings dominate diffusion in the 2D and 1D defects studied here. For GBs, point-defect avalanches were observed in agreement with our prior work [1]. The higher diffusivity is associated with a shorter lifetime and smaller size of the string-like dynamic clusters. An increase in temperature leads to a decrease in the maximum string length and characteristic lifetime and a reduction in the ratio of Si atoms in the clusters.

Some Al-Si interfaces transformed into a more stable state by a new mechanism that we call *interface-induced recrystallization*. In a typical scenario, the interface splits into an IPB with a new orientation of the Al phase and a new GB in the Al phase. This phenomenon can have practical significance. During thermal processing or deformation, a metal-nonmetal interface can transform to a new state by changing the orientation relationship between the phases and injecting a new grain into the metallic matrix. This process and its possible impact on the mechanical properties of metal-ceramic composites is worth further exploration by experiment and modeling in the future.

We have started simulations of sliding along Al(Si)-Si IPBs. An example is shown in Fig. 4 for a single-crystalline alloy layer deposited on Si(100) substrate. This interface contains a network of misfit dislocations. The shear deformation at this interface occurs in increments, producing a saw-tooth behavior of the shear stress. Each sliding event is accompanied by nucleation and rapid growth of additional dislocation loops in the interface region (Fig. 4a). During this brief period, the mean-square displacement of the atoms (relative to the local center of mass) increases, indicating a surge of the interface diffusivity. The accelerated diffusion is especially fast for the Al atoms, suggesting that the shear-amplified diffusion occurs on the Al side of the interface. This was indeed confirmed by tracking the displacement of thin atomic layers normal to the interface. As seen in Fig. 4b,c, the shear is primarily localized within a 1 nm layer on the Al side of the IPB, in which the diffusive scatter of the atoms is more significant than elsewhere in the system. More systematic studies of the interface sliding will be performed to establish the effect of the local shear deformation on the diffusivity and diffusion mechanisms as a function of the IPB crystallography and temperature.

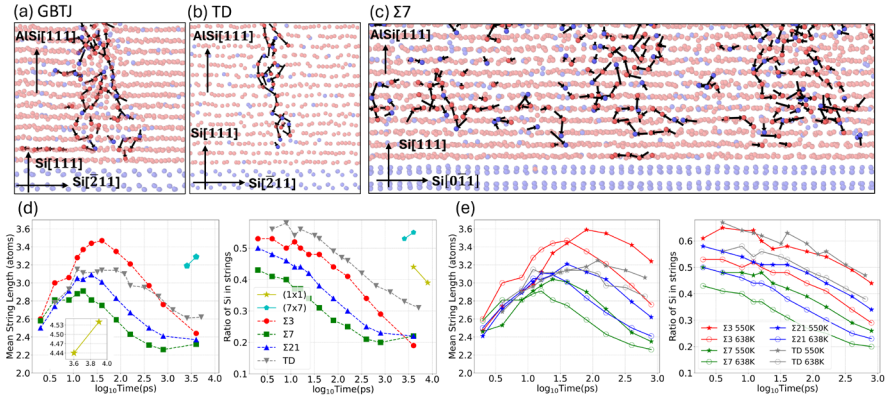

Figure 4: (a-c) Displacement strings in 1D and 2D defect cores. (d) The mean string length and the Si composition in the strings as a function of lifetime. (e) Results at different temperatures for the $Al_{0.93}Si_{0.07}$ system.

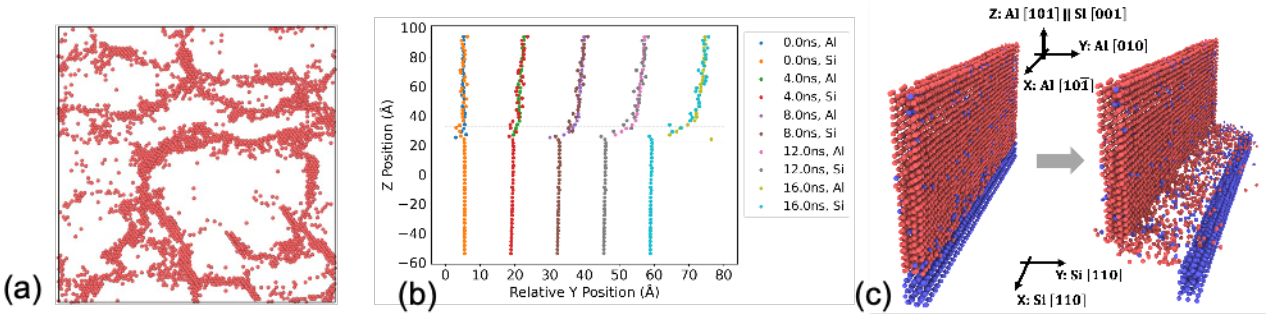

Figure 5: Shearing test of the $Al_{0.93}Si_{0.07}$ layer deposited on the Si(100) substrate at the temperature of 622 K. (a) Top view of the interface showing nucleation and growth of interface dislocations during strain increments. (b) Time evolution of marker lines demonstrating that the localized shear and accelerated diffusion occur in a 1 nm-thin interfacial later. (c) A perspective view of the marker line shows shear-activated diffusion.

Future Plans

- Continue the investigation of Al-Si interfaces at high temperatures, focusing on mechanical responses.
- Understand the atomic-level mechanisms by which the interface shear deformation accelerates interphase boundary diffusion.
- Start expanding the project to more realistic interfaces, such as Al-SiC. The first step is to develop a reliable interatomic potential for the ternary Al-Si-C system, which currently does not exist. This is part of the current work.

References

I. Chesser, Y. Mishin, Point-defect avalanches mediate grain boundary diffusion, *Communications Materials* 3, **90** (2022).

Publications

1. I. Chesser, R. Koju, A. Vellore and Y. Mishin. Atomistic modeling of metal-nonmetal interphase boundary diffusion. *Acta Materialia* **257**, 119172 (2023).
Acknowledgments: This research was supported by the U.S. Department of Energy, Office of Basic Energy Sciences, Division of Materials Sciences and Engineering, under Award # DE-SC0023102. We thank Paul Wynblatt, Dominique Chatain and Eugen Rabkin for useful discussions.

2. I. Chesser, R. K. Koju and Y. Mishin. Atomic-level mechanisms of short-circuit diffusion in materials. *International journal of materials research* **115**, 85-105 (2024).
Acknowledgments: This research was supported by the U.S. Department of Energy, Office of Basic Energy Sciences, Division of Materials Sciences and Engineering, under Award # DE-SC0023102.

3. Y. Li, R. K. Koju and Y. Mishin. Atomistic modeling of diffusion processes at Al/Si(111) interphase boundaries obtained by vapor deposition. Submitted.

4. I. Chesser, R. K. Koju and Y. Mishin. An atomistic study of dislocation diffusion in Al-Si alloys. In preparation.

Plasticity of High-Strength Multiphase Metallic Composites

Amit Misra[1] (PI), Jian Wang[2] (co-PI)

[1]University of Michigan, Ann Arbor; [2]University of Nebraska, Lincoln.

Keywords: dislocations, interfaces, nanoscale eutectics, nanomechanics, atomistic modeling.

Research Scope

In metallic microstructures dominated by planar interfaces such as grain or interphase boundaries, the interactions between interface-confined mobile dislocations and interactions of glide dislocations with interfaces determine the measured flow strength, strain hardening, and ductility. Dislocations can be effectively blocked at, transmitted across, deflected along, or reflected from interfaces (Figure 1) [1]. For grain (or interphase) boundaries involving soft metals, the efficiency of slip transmission can be predicted in terms of geometry of incoming and outgoing slip systems [2]. However, in the case of metal-hard (intermetallic or covalent) phase microstructures, the slip system geometry, although necessary, is not sufficient to predict slip activity since the high Peierls stress of the hard phase [3] may suppress slip transmission in favor of fracture or slip deflection/reflection from interface. Many fine-scale metal-hard phase systems show unique mechanical behavior where flow strength and ductility are simultaneously enhanced due to suppression of catastrophic localized shear bands [4], but there is a critical gap in knowledge of predicting the active dislocation mechanisms and relating it to the strength-strain hardening-plastic co-deformability relationship of a given soft/hard phase microstructure. The goal of this research program is to develop fundamental understanding of the multitude of dislocation-dislocation and dislocation-interface interactions in *multiphase* microstructures with disparate phases. Specifically, how the combination of factors such as the thermodynamic and mechanical properties of the interphase boundary, crystallographic orientation relationships between soft and hard phases, Peierls stress of the hard phase, and morphology of the hard phase (fibrous, lamellae) determine the relative barriers for dislocation transmission or reflection, ($b_{in} \rightarrow b_{out\text{-}T}$) or ($b_{in} \rightarrow b_{out\text{-}R}$), respectively, in Figure 1.

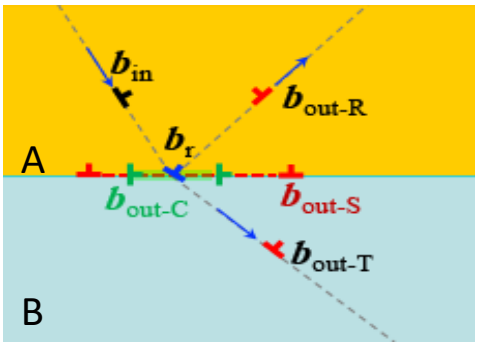

Figure 1. Schematic of dislocation interactions at crystalline A/B interfaces: slip transmission $b_{in} \rightarrow b_{out\text{-}T}$, slip reflection $b_{in} \rightarrow b_{out\text{-}R}$, sliding $b_{in} \rightarrow b_{out\text{-}S}$, interface climb $b_{in} \rightarrow b_{out\text{-}C}$.

The proposed work is organized to test two key hypotheses:

1) High strain hardening rate in metals, including high stacking fault energy metals such as Al that can easily cross-slip, confined by nano-fibers of a hard phase result from a combination of a high density of geometrically necessary dislocations and locks between intersecting dislocations that develop associated with plastic deformation incompatibility, and high strain energy associated with non-linear elasticity in the hard phase.
2) Slip transmission across or reflection from soft/hard interphase boundaries is determined by both defect energetics as well as crystallographic barriers, and slip transmission is favored over

other unit mechanisms only when both defect energetics and crystallographic barriers are reduced below some critical value.

Recent Progress

Our research approach integrates laser processing of Aluminum (Al)-based model nano-eutectics, nanomechanical and scanning/transmission electron microscopy (S/TEM) characterization (*in situ*, high-resolution, quantitative 4D-STEM), and atomistic and crystal plasticity modeling.

1) Dislocation mechanisms of strain hardening in nano-eutectics

The first hypothesis was tested by integrating experiments on model systems of nanoscale fibrous Al-Si eutectics with large-scale molecular dynamics (MD) simulations. This is a model system for behavior dominated by dislocation reflection (as opposed to transmission) from interfaces. *In situ* SEM micro-tensile and micro-compression tests revealed strong dependence of measured yield strength and strain hardening on the orientation of the Si nanofibers with the loading direction and eutectic colony size. The lowest strength and strain hardening is observed when the fibers are nearly 45° to tensile axis where plastic flow is confined to the Al nano-channels. When the Si nanofibers are nearly parallel or perpendicular to the loading direction, the measured tensile strength can exceed 600 MPa with around 5% to 10% ductility. *In situ* tensile tests revealed high strain hardening post-yield and the measured total uniform elongation was limited by sliding or cracking along eutectic colony boundaries and not by fracture of Si nano-fibers (Figure 2(a)-(c)).

Large-scale MD simulations were performed using a simulation cell of 40 nm x 40 nm cross-section and 70 nm height comprising of Al matrix reinforced with Si nanofibers approximately 5 nm in diameter and 15 nm spacing. Dislocation motion in Al nano-channels was observed to be inhibited by Si nanofibers leading to development of dislocation forests with Lomer-Cottrell and Hirth locks, (Figure 2(d)-(e)). The formation of these locks enabled the total (geometrically necessary and statistically stored) dislocation density in the Al matrix to rise to $\approx 10^{17}$ /m^2. The

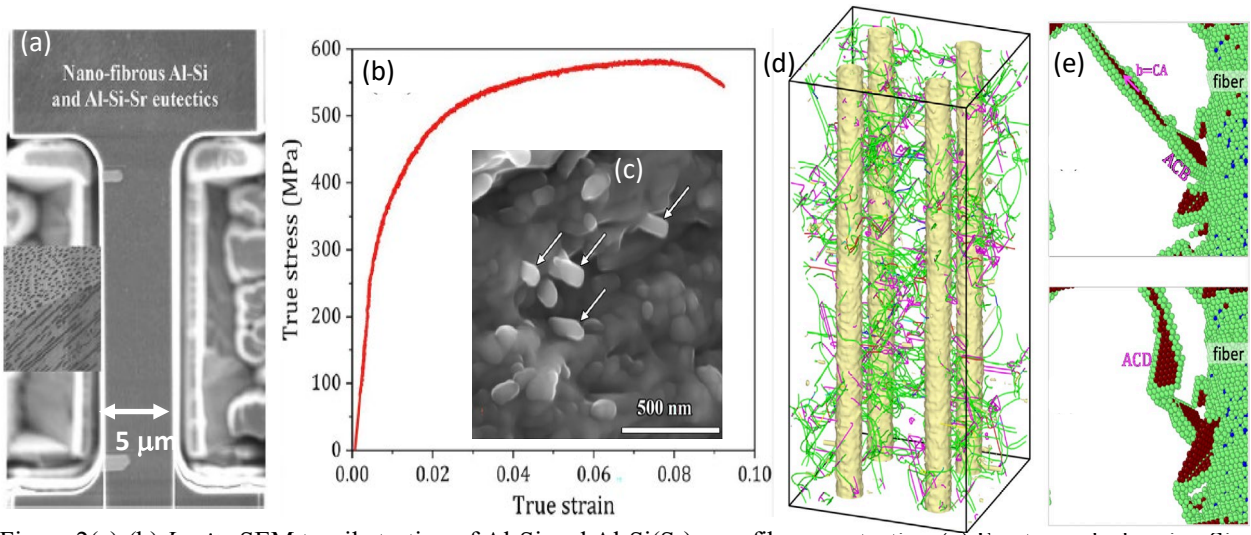

Figure 2(a)-(b) *In situ* SEM tensile testing of Al-Si and Al-Si(Sr) nanofibrous eutectics. (c) Fractograph showing Si nanofibers necked to fracture. (d) MD simulation of tensile strained Al with Si nanofibers showed multiple dislocation junctions (non-green), Lomer-Cottrell locks (1/6<110>, pink) and Hirth locks (1/3<001>, yellow). A statistical analysis estimated dislocation junctions account for up to 30% of total dislocation lines. (e) A screw dislocation is observed to cross-slip from ACB plane onto ACD plane. Atoms colored by common neighbor analysis.

local and average stresses in the two phases and the composite samples revealed build-up of high elastic stresses in the high aspect ratio nanofibers, ≈10% of elastic modulus, prior to fiber cracking. However, the nanoscale dimension of Si fibers limits the nano-cracks to sub-critical lengths that remain confined in the Si nanofibers and do not propagate into Al matrix with increasing tensile strain of ≈15% used in the simulation. The propagation of nano-cracks can be effectively buffered by dislocation-based strain hardening in Al nano-channel, as revealed by both experiments and simulations. The mechanisms of elastic/plastic co-deformation discerned from these simulations on a model Al-nanofibrous Si system apply broadly to nano-confined metallic microstructures reinforced with high aspect ratio hard phases.

2) Partial-dislocation mediated plasticity in the hard phase in nano-eutectics

The second hypothesis was tested by integrating atomistic modeling with experimental characterization of Al-Si nano-eutectics, with and without micro-alloying with Strontium (Sr). Effect of Sr addition is mostly manifested through high degree of impurity induced twinning in the fibers with diameters refined to approximately 30 nm, and high twin density in fibers with spacing of 1–3 nm, resulting in maximum compressive flow strength of ≈840 MPa with stable plastic flow up to ≈26% plastic strain. The Sr-modified nano-fibers revealed a high density of deformation-induced stacking faults, observed only in the deformed samples, not in the as-laser melted state. The fault density was very high in the Sr-modified deformed microstructure but extremely limited in the laser refined Al–20Si without Sr. To our knowledge, this is the first demonstration of partial dislocation-mediated plasticity in covalently bonded Si at room temperature and suggests that the relative barriers for dislocation transmission vs reflection from interfaces are modified in Sr-modified nanotwinned Si to favor dislocation activity in fibers.

It is hypothesized that limited localized plasticity in the Si(Sr) fibers is enabled by glide of partial dislocations that are nucleated heterogeneously from sites such as Al/Si interphase boundary or from atomic-level steps on the growth twins. Local segregation of Sr and Al in Si(Sr) fibers might have important effect in easing nucleation and glide of partial dislocation, which will be discussed in the future work. Examination of deformed microstructure has revealed that Sr-alloyed eutectic

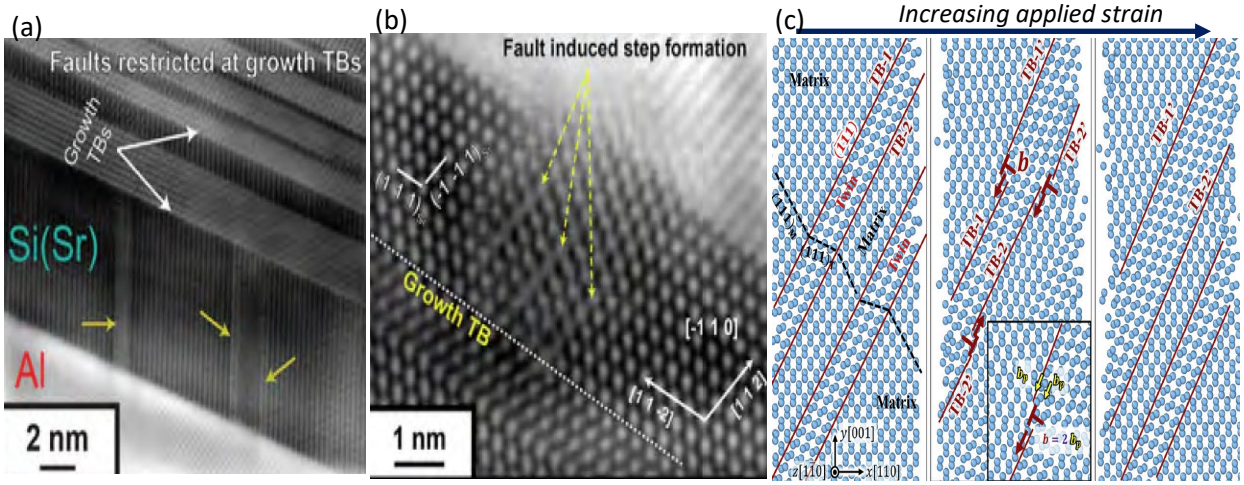

Figure 3 (a)-(b). HR/STEM images showing deformation induced stacking faults (SFs) due to partial dislocation mediated plasticity in nano-twinned Si(Sr) fibers in Al-Si(Sr) nanoeutectics. c) MD simulation showing that the dislocation motion on twin boundary (TB) in the Si(Sr) fiber leads to TB migration.

completely suppressed cracking of nano-fibers while Al–Si nano-eutectic without Sr exhibits a few cracks in the fibers. The suppression of cracking is presumably due to refinement of the fibers compared to earlier studies where cracking was frequently observed in Si fibers that were coarser. In the present study, since both alloys, with and without Sr addition, had similar fiber diameter and aspect ratio but the Sr alloyed sample suppressed cracking more effectively, it is postulated that the partial dislocation activity assists in alleviating the local stresses and delaying the onset of cracking in the harder Si phase.

MD simulations revealed that the Si nanofibers within the Al matrix exhibited large non-linear elastic strains followed by localized plasticity, whereas aligned Si nanofibers in vacuum (no Al matrix) exhibited elastic deformation followed by cleavage fracture. Localized plasticity in Si nanofibers is accomplished by glide of "zonal" partial dislocations with Burgers vector b = a/3<112>, which leads to synchronous shear of two shuffle-sets. Local stress concentration in Si nanofibers due to non-screw segments of dislocation loops around fibers triggers yielding in the nanofibers through the activation of dislocation sources at or near the interfaces but only below some critical fiber diameter, highlighting the role of nanoscale refinement in activating plasticity in embedded Si nanofibers in Al matrix. In addition, the kinetic barriers associated with the glide of edge/screw zonal dislocation in the perfect crystal and twinned crystal are computed using climbing-image nudge elastic band method. A higher mobility of the zonal dislocation in the twinned crystal suggests a lower barrier for dislocation glide parallel to the twin boundary.

The results in this investigation provide direct evidence of enabling plastic co-deformation of Al–Si microstructure at nano-scale, through control of microstructure size, aspect ratio of hard phase, nano-twinning in the hard phase and Sr segregation that may favor partial dislocation mediated plasticity. In other words, microstructural *heterogeneity* at nanoscales enhances flow strength, strain hardening and *homogeneity* of plastic flow in laser processed eutectic alloys.

Future Plans

The effects of chemical (solute) and structural (growth twin boundary) defects on dislocation mobility in the Si phase will be elucidated. Atomistic calculations using first principles density functional theory will be performed to compute the role of solutes (and solute clusters) on Peierls energy barriers for dislocation glide in Si with diamond cubic structure, with solutes of interest being (i) Al, (ii) Sr, (iii) Sr and Al, and (iv) Ge. This work will help deconvolute the relative effects of twin boundaries versus solutes in facilitating partial dislocation motion in alloyed Si nano-fibers in Al-Si-X eutectics. Experimental characterization of tensile stress-strain response from fully eutectic microstructures and characterization of dislocation activity in the hard phases of Al-Ge, Al-Si(Ge) and Al-Si(Sr) eutectics will be integrated with the atomistic modeling results. The binary Al-Ge system will be compared with Al-Si to understand the role of hard phase morphology in nano-refined eutectic microstructures: both Si and Ge have diamond cubic crystal structures but Al-Ge is lamellar while Al-Si is fibrous eutectic.

References

1. J. Wang, Q. Zhou, S. Shao, A. Misra, *Strength and Plasticity of Nanolaminated Materials*, Materials Research Letters, **5**, 1-19 (2017).

2. M.D. Sangid, T. Ezaz, H. Sehitoglu, I.M. Robertson, *Energy of slip transmission and nucleation at grain boundaries,* Acta Materialia, **59** (2011) 283-296.

3. J.J. Gilman, *Why Silicon is hard*, Science **261** (1993) 1436.

4. H. Wu and G. Fan, *An overview of tailoring strain delocalization for strength-ductility synergy*, Progress in Materials Science, **113** (2020) 100675.

Publications from this grant (2022-2024)

1. W.Q. Wu, M. Gong, B.Q. Wei, A. Misra, J. Wang, *Atomistic Modeling of Interface Strengthening in Al-Si Eutectic Alloys*, **Acta Materialia,** 225**,** 117586 (2022).
2. H.-H. Lien, J. Wang, A. Misra, *Plastic deformation induced microstructure transition in nano-fibrous Al-Si eutectics*, **Materials & Design**, 218, 110701 (2022).
3. B.P. Sahu, J. Wang, A. Misra, *Deformation behavior of crystalline/amorphous Al/Si nanocomposites with nanolaminate and nanofibrous microstructures*, **Physical Review Materials**, 6(9), 094002 (2022).
4. W.Q. Wu, B.Q. Wei, A. Misra, J. Wang, *Atomistic simulations of nano-fiber-confined metal plasticity*, **Scripta Materialia** 235, 115619 (2023).
5. A. Ghosh, B.P. Sahu, W.Q. Wu, J. Wang, A. Misra, *Enabling plastic co-deformation of disparate phases in a laser rapid solidified Sr-modified Al-Si eutectic through partial-dislocation-mediated-plasticity in Si*, **Materials Science & Engineering A**, 885, 145648 (2023).
6. B.Q. Wie, W.Q. Wu, A. Ghosh, M. Kayitmazbatir, A. Misra, J. Wang, *In situ SEM characterization of tensile behavior of nano-fibrous Al-Si and Al-Si-Sr eutectics*, **Journal of Materials Science**, The Physics of Metal Plasticity: in honor of Professor Hussein Zbib, 59(3), 1-14, (2023).
7. J. Wang, A. Misra, *Plastic Homogeneity in Nanoscale Heterostructured Binary and Multicomponent Metallic Composites*, **Current Opinion in Solid State & Materials Science**, 27, 101055, (2023).
8. W.Q. Wu, B.Q. Wei, A. Misra, J. Wang, *Atomistic Simulations of Dislocation Activity in Si Nanofibers in Al-Si Eutectics*, **Acta Materialia**, 264, 119569, (2024).
9. B.P. Sahu, M.T. Andani, A. Ghosh, J. Wang, A. Misra, *Crystallography and Interface Structures in As-Arc Melted and Laser Surface-Remelted Aluminum–Silicon Alloys with and without Strontium Addition*, **Crystals**, 14, 283 (2024).
10. **W.Q. Wu, B.Q. Wei, C. Zhou, A. Misra, J. Wang, *The influence of twin boundary on character and motion of dislocations in silicon*, Acta Materialia, in review.**

Mechanisms of Defect Cluster Dynamics from Automated Massive Scale Defect Characterization and Molecular Simulation

Dane Morgan, University of Wisconsin; Paul M. Voyles, University of Wisconsin; Kevin Field, University of Michigan

Keywords: Defect Dynamics, Ni-Cr Alloys, (S)TEM, Machine Learning, Simulation

Research Scope

Radiation-induced microstructural evolution, specifically the motion of defect clusters, is a poorly understood yet significant factor affecting materials under high-temperature and irradiation conditions, such as those found in nuclear reactors. This research aims to identify, understand, and quantify the mechanisms driving the movement of defect clusters in Ni-Cr alloys. By focusing on defect clusters like cavities and dislocation loops, the project seeks to elucidate the effects of composition, irradiation conditions, local environments, and other factors on the kinetics and stability of these clusters. Utilizing advanced scanning transmission electron microscopy ((S)TEM) with automated analysis via machine learning[1,2], along with comprehensive molecular dynamics simulations, the goal is to generate statistically significant data on many interacting defect clusters at unprecedented scales (in terms of counting statistics and temporal fidelity) to inform and enhance material performance prediction models under extreme conditions.

Recent Progress

Several key tools needed to investigate many interacting defects at scale have been developed by the project team and are currently being optimized in preparation for the start of the project. Specifically, we have explored the development of a fully automated method for the 3D reconstruction of highly defective structures using machine learning. This method entails machine learning-enabled object detection coupled with an in-house custom code derived from Obtain3D, which takes a stereo-pair of images and automatically reconstructs the microstructure based on the principles of stereomicroscopy. We have deployed the object-oriented bounding box (OBB) variant of the YOLOv8 (You Only Look Once[3,4]) machine learning architecture to automatically detect dislocation loops and cavities formed in an FCC irradiated microstructure. The OBB variant enables the definition of non-constrained rotated bounding boxes to determine loop normals within the 3D volume of the TEM specimen.

The results of the OBB method, shown in Fig. 1, demonstrate that individual loop orientations and spatial relationships to cavities can be accurately reconstructed, providing further characteristics based on a priori knowledge of the material system. These characteristics include loop inclination, loop Burgers vector, and the spatial correlation of these characteristics between different loop types and the cavities present in the microstructure. A full 3D representation of the microstructure enables better parametrization of molecular dynamics models. More importantly, the technique demonstrated in Fig. 1 can run on an edge computing device equipped with a

Graphical Processing Unit (GPU), achieving reconstructions in under one second—significantly faster than conventional methods that can take hours or days. This computational speed will allow us to perform real-time 3D reconstructions, providing a full temporal and spatial description of each defect in-situ, capturing the entire dynamics within a single field of view regardless of whether single or hundreds of defects are present. This capability will enable the parameterization of the model in both spatial and temporal domains during the planned in-situ TEM ion irradiations and in-situ TEM annealing experiments.

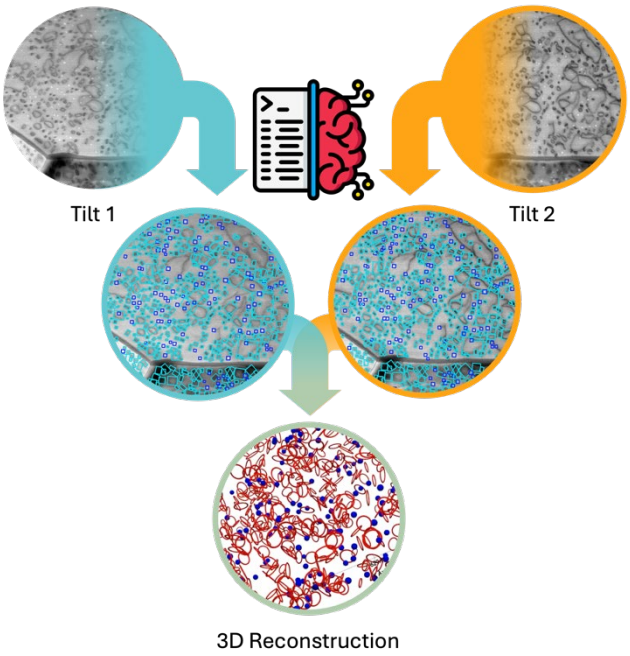

Fig. 1: Schematic showing the uses of TEM tilt pairs and machine learning to rapidly (<1 s) form 3D reconstructions of complex irradiated microstructures where the red polygons are loops detected as cyan bounding boxes in the second level and the blue polygons and detection bounding boxes are cavities in the 3D reconstruction.

Additionally, a technique is being developed using the same machine learning-enabled object detection for video/drift stabilization. This technique is unique in that it does not require stable key points or cross-correlation analysis, thus enabling all features in the field of view to be mobile. This approach is ideal for studying many interacting defects, as it allows for fully dynamic events to occur while stabilizing the field of view. The stabilization provides more accurate determination of changes in size, shape, defect gain, defect loss, and other characteristics of features with no additional artifacts from changes in the field of view within the same region of interest. To date, preliminary work has established the workflow, but the defect tracking algorithms are still undergoing extensive optimization to generalize the approach to all expected dynamic events that are predicted to occur within this study.

Future Plans

In the immediate future, we aim to further refine our established workflow shown in Fig. 1 for increased accuracy and computational efficiency. We will explore the use of common inference accelerators for machine learning models such as TensorRT to enhance the defect detection framework. Concurrently, we will begin deploying the framework on the in-situ TEM ion irradiation facility at University of Michigan to enable real-time 3D reconstructions during in-situ irradiations. In parallel, we will optimize are multiple object tracking (MOT) algorithms to improve defect tracking and our video stabilization pipeline through an extend hyperparameter search.

On a larger scale, our future plans aim to assess our hypotheses on the mechanisms driving defect cluster dynamics in Ni-Cr alloys: (1) cavities move primarily by surface vacancy mediated mechanisms, showing strong coupling to cavity size, temperature, irradiation, composition, and local sinks, with weak coupling to strain or helium; and (2) small dislocation loops move through cluster reorganization, showing strong coupling to cluster size, irradiation, composition, and local strain, with modest coupling to temperature and weak coupling to helium and other defects. To comprehensively test these hypotheses, we will systematically sample a range of variables including defect size, local microstructural environment, materials composition, sample temperature, and irradiation conditions, including dose rate, damage level, and helium content.

Initially, we will execute a series of ex-situ irradiations across different Ni-Cr compositions (pure Ni, Ni90Cr10, Ni80Cr20). These ex-situ irradiations will provide baseline experimental insights into the material systems and enable better focusing of subsequent in-situ irradiations. This phase will be completed within the first six months of the project. Phase 2 will consist of primary studies using 4D-STEM post-irradiation annealing to measure temperature dependence of defect mobility and in-situ TEM ion irradiations to assess the impact of damage and damage rate on defect dynamics. Using the data reservoir from Phase 1 and Phase 2 experiments on pure Ni, we will extend and parameterize our atomistic simulation efforts to encompass a broader range of defect types and environmental variables. Model and simulation efforts will also include optimizing machine learning object detection and segmentation models to improve overall recall and counting statistics of all experiments. With the established frameworks in place for pure Ni, we will then explore the impacts of compositional variability on defect mobility and interactions in Phase 3.

Overall, the combined experimental and computational approach will refine our scientific hypotheses, achieving a detailed mechanistic understanding of defect cluster dynamics in metallic alloys. The outcomes will significantly contribute to the development of more resilient materials for extreme radiation environments.

References

1. Shen, M. et al. *Multi defect detection and analysis of electron microscopy images with deep learning.* Comput Mater Sci **199**, 110576 (2021).

2. Shen, M. et al. *A deep learning based automatic defect analysis framework for In-situ TEM ion irradiations*. Comput Mater Sci **197**, 110560 (2021).

3. Redmon, J. & Farhadi, A. *YOLOv3: An Incremental Improvement*. arXiv:1804.02767 (2018).

4. Redmon, J. & Farhadi, A. *YOLO9000: Better, Faster, Stronger*. arXiv:1612.08242 (2016).

Publications

None to list, new project start.

Modeling the Molecular Mechanisms of Interfacial Welding in Self-Healing Polymers

Thomas C. O'Connor, Materials Science & Engineering, Carnegie Mellon University

Keywords: Polymers, Self-Assembly, Self-healing, Thermoplastic Elastomers, Mechanical Welding

Research Scope

Intrinsically self-healing polymers are plastics that rapidly repair damage when two broken interfaces are brought into contact. Self-healing plastics have garnered interest as sustainable alternatives to conventional plastics that can be repaired and reused, reducing plastic waste accumulation.[1,2] However, designing self-healing plastics remains challenging because the molecular mechanisms governing self-healing remain poorly understood in many polymer systems.[3] We lack this knowledge because self-healing occurs at nanoscale polymer interfaces, and experiments cannot easily access these details while systems heal.[4] The objective of our project is to combine molecular dynamics simulations and mechanical welding experiments to identify the molecular mechanisms that mediate the self-healing process in a diverse class of self-healing polymers: precisely sequenced thermoplastic elastomers. Molecular simulations can directly resolve the molecular-scale details that are difficult to observe and directly relate them to the time-dependent recovery of mechanical strength measured in experiments. This combined approach will build fundamental relationships relating the chemical structure of polymer chains to the speed at which they recover specific mechanical properties like strength, stiffness, and yield stress during interfacial welding. Our findings will guide the molecular design and synthesis of new self-healing plastics with improved mechanical properties and repairability.

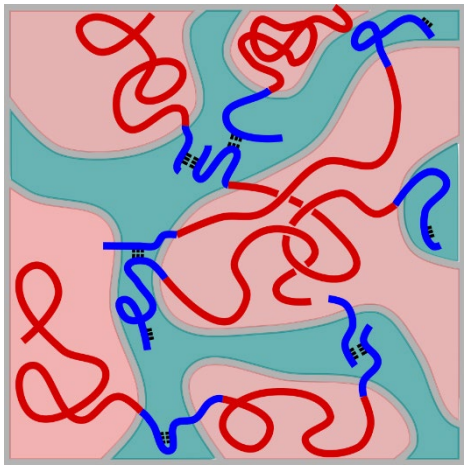

Schematic of a self-healing TPE nanostructure. Chains simultaneously form a network of associative bonds and a microphase separated nanostructure of mobile (red) and glassy (blue) domains. Our work aims to understand the relative roles of both structures in mechanical welding.

Recent Progress

This project is newly awarded and we have no substantial progress to report at this time.

Future Plans

Our current plans are to execute the aims outlined in our project proposal that was recently awarded. Ongoing preliminary efforts continue to indicate that these are promising directions to pursue. Our approach will combine MD simulations and collaborative experiments to study the mechanical welding of precisely sequenced self-healing P(MMA-co-BA) thermoplastic

elastomers. We are using copolymer sequence as a *scientific tool* to gradually suppress nansotructure formation while keeping the overall density of associative monomers fixed. This will allow us to isolate and quantify the separate roles of nanostructure and intermolecular association on weld dynamics and mechanical recovery. Our mechanistic hypothesis is that the kinetics of welding of self-healing polymers is controlled by the dynamics of nanostructural domains and not by the diffusion of individual chains across interfaces. We will test our hypothesis by pursuing 3 aims which will measure the relative roles played by glassy nanostructures and intermolecular associations in controlling the mechanical behavior of TPEs in bulk, welding, and post-fracture conditions.

Aim 1: Bulk Mechanics of Self-healing TPEs **–** self-healing TPEs occupy a poorly understood region of copolymer compositions that form disordered continuous rubbery/glassy nanostructure. MD simulations tuned and validated against mechanical experiments will identify quantify the molecular mechanisms mediating the elastic and plastic mechanical response of these complex material states

Aim 2: Mechanical Recovery During Interfacial Welding – MD simulations of interfacial welding will directly measure molecular diffusion and nanodomain restructuring and relate both to the recovery of elastic stiffness, yield stress, and ultimate strength.

Aim 3: Nanostructure Reorganization at Free Surfaces– we will study how self-assembled nanostructures reorganize at freshly cleaved interfaces at different temperatures and how this impacts subsequent welding. Simulation predictions will be validated by AFM measurements of free-surface structures and experimental measurements of auto-adhesion after surface annealing protocols.

References

(1) P. Wool, *Self-Healing Materials: A Review*, Soft Matter, *4* (3), 400, (2008)

(2) S. Wang, M.W. Urban, *Self-Healing Polymers*, Nat. Rev. Mater., *5* (8), 562–583, (2020)

(3) G. Raos, B. Zappone, *Polymer Adhesion: Seeking New Solutions for an Old Problem,* Macromolecules, *54* (23), 10617–10644, (2021)

(4) T. Ge, F. Pierce, D. Perahia, G.S. Grest, M.O. Robbins, *Molecular Dynamics Simulations of Polymer Welding: Strength from Interfacial Entanglements*, Phys. Rev. Lett., *110* (9), 098301 (2013)

Publications

NA

Understanding Irradiation-Assisted Plasticity in Complex Concentrated Alloys

Hyunseok Oh, University of Wisconsin-Madison

Keywords: TiZrNb-O, complex concentrated alloy, bcc phase stability, planar defect-mediated delocalized plasticity, oxygen complex

Research Scope

This project aims to address the strength-toughness trade-off challenge in structural metals under irradiation at intermediate temperatures (<0.4 melting point). Under these conditions, irradiation and mechanical stress result in hardening and embrittlement via significant strain localization at dislocation channels [1]. Leveraging recent advancements in complex-concentrated alloys (CCAs), this project investigates the effects of multi-scale structures on irradiation-assisted plasticity in CCAs and identifies scientific principles for enhanced resistance to irradiation embrittlement while maintaining hardening. Our focus is on reducing strain localization by tailoring the unique deformation mechanisms of CCAs, a process referred to in this project as planar defect-mediated delocalized plasticity (PMDP).

PDMP has been shown to strongly influence mechanical behavior in unirradiated CCAs. The mechanisms typically initiate from planar slip, which facilitates strain localization through the glide-plane softening effect. However, in some CCAs, synergetic interactions between planar defects and other features, such as dislocation cross-slip tendencies from different stacking fault energies (SFEs) or non-shearable precipitates, can lead to unprecedented strain delocalization and work hardening effects [2,3].

In the first phase of the project, we have explored potential CCA compositions exhibiting PMDP mechanisms in both refractory metal-based *bcc* CCAs and transition metal-based *fcc* CCAs. Previously reported CCAs with PMDP mechanisms often have thermodynamically metastable matrix phases and, hence, a high propensity for transformation to the *hcp* phase during cooling, deformation, or even aging. Furthermore, these alloys contain combinations of interstitial elements that form local chemical ordering or long-range ordering to regulate dislocation behavior, which can lead to precipitate formation under diffusive environments. Therefore, our initial aim is to identify alloy compositions and processing conditions that ensure phase stability and PMDP behavior at intermediate temperatures.

In this presentation, we focus on the phase stability of TiZrNb-O CCAs. TiZrNb-O CCAs have been reported to exhibit high strain hardenability in the as-cast condition due to improved Frank-Read source activation from oxygen complexes [2]. The recrystallization and aging behavior has not yet been reported. Considering the complex transformation behavior of similar β-Ti alloys, e.g., α phase precipitation, it is necessary to ensure high stability of the *bcc* phase while maintaining high strain hardenability at intermediate temperatures (~600 °C).

Recent Progress

We first assess the as-cast TiZrNb alloy with 2 at.% O, referred to here as the Low Zr-2O CCA, which is reported to exhibit PMDP [2], to determine its suitability for this research. The as-cast alloy, fabricated using arc melting, exhibits a typical grain size of 100–200 μm (Fig. 1a). This large grain size might not be beneficial for irradiation embrittlement resistance due to the limited crack deflection effect and significant strain localization at the intersections between irradiation channels and grain boundaries. Moreover, this large grain size makes it challenging to analyze lattice distortion and misfit volume using synchrotron sources (e.g., extended X-ray absorption fine structure (EXAFS), high energy X-ray diffraction (HEXRD)). Therefore, recrystallization is necessary to reduce the grain size to below 100 μm. Additionally, after aging treatment at 600 °C for 12 h, the alloy exhibits precipitation of the *hcp* phase and cracking along grain boundaries (Fig. 1b). This behavior is similar to that of other β-Ti alloys, where O thermodynamically stabilizes the *hcp* phase and causes precipitation during aging at intermediate temperatures.

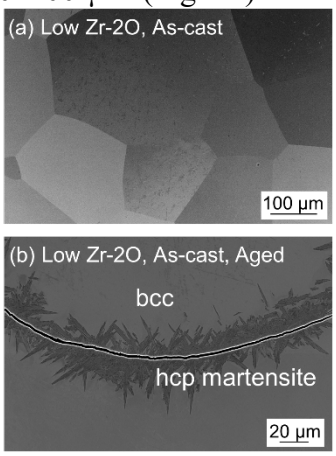

Figure 1. Microstructure of TiZrNb-2O CCA at (a) As-cast and (b) Aged states.

To address these challenges, we have designed new compositions to secure high *bcc* phase stability during recrystallization and aging treatments. To improve *bcc* phase stability, typical β-stabilizing elements used in Ti alloys can be added. However, most β-stabilizing elements reduce oxygen solubility. Therefore, we have divided the design steps into two parts: (1) Investigating the effect of Zr on phase stability, as it does not reduce oxygen solubility and has the potential to increase the stability of the bcc phase [4], and (2) Adding more β stabilizers, such as Nb, Fe, and Mo, to increase *bcc* phase stability, while the addition should be minimal to maintain high oxygen solubility.

The as-cast alloys with different Zr, Nb, and O contents all exhibit good cold rolling capability, achieving up to 80–90% thickness reduction without any cracks. Fig. 2a and b show the recrystallized microstructure of the alloys with different Zr content (low Zr, high Zr) with 2 at.% O, annealed at 900 °C for 15 min. The alloys exhibit a single *bcc* microstructure with equiaxed grains and a random texture. The average grain sizes are 50–70 μm, indicating successful recrystallization. The inset shows the microstructure of a recrystallized Low-Zr alloy without O, which exhibits the formation of the *hcp* phase. This behavior is similar to typical β-Ti alloys, where oxygen kinetically suppresses athermal martensite formation during cooling, likely due to the formation of O nanodomains.

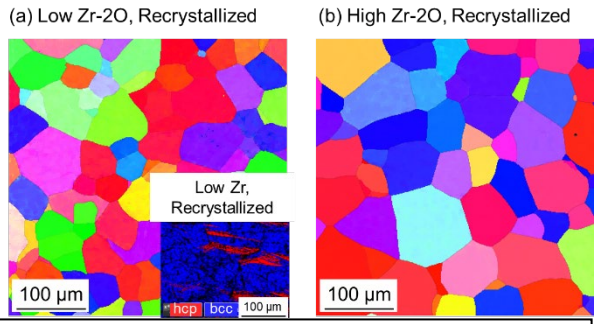

Figure 2. Recrystallized microstructure of (a) Low Zr-2O and (b) High Zr-2O CCAs. Inset: Low Zr-0O CCA.

After aging, the needle-shaped *hcp* phase is formed in both alloys. However, the amount of the *hcp* phase is reduced from ~35% to ~17% with an increase in Zr content (Fig. 3a and b). EDS analysis reveals that Zr is enriched in the *bcc* region, while Nb and Ti contents are higher in the *hcp* phase. This observation deviates from β-Ti literature, where both Zr and Nb are typically enriched in the *bcc* region, suggesting a different origin of phase stability induced by Zr [4]. This result also indicates that the formation of the *hcp* phase is likely due to compositional modulation of Zr rather than O. Further detailed investigation is in progress.

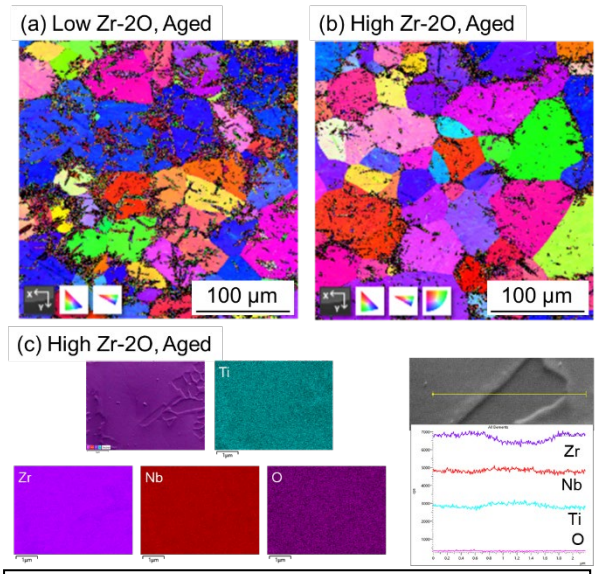

Figure 3. Aged microstructure of (a) Low Zr-2O and (b) High Zr-2O CCAs. (c) EDS maps and line scans showing lower Zr content in the hcp phase.

Although not detailed here, optimizing the β-stabilizing elements to ensure the stability of the bcc phase during aging at intermediate temperatures over 500 °C, while maintaining sufficient oxygen solubility, is currently in progress. For instance, increasing the Nb content further improves the phase stability of the *bcc* phase, while potentially maintaining O solubility.

Future Plans

In the long term, we plan to develop deformation maps of CCAs with interstitial elements to enable PMDP mechanisms during irradiation at intermediate temperatures. In the short term, the project involves post-irradiation deformation at intermediate temperatures. To achieve this aim, once the phase stability-targeted design is completed, the future plans include the following activities:

1. PMDP mechanisms across broad temperature ranges: The mechanical behavior of the CCAs will be investigated over a broad range of temperatures, from room temperature to intermediate temperatures, to identify the conditions that activate PMDP mechanisms. The detailed mechanistic origins required for activating PMDP mechanisms in these alloys will be further analyzed to extend the applicable temperature and time ranges through additional design efforts. *In situ* scanning electron microscope tensile testing at intermediate temperatures will be conducted to elucidate the strain localization behavior of these alloys.

2. Lattice distortion of the developed CCAs: EXAFS analysis will be conducted to understand the lattice distortion around each element [5] and the preferential interactions between the interstitial and substitutional elements. The volume misfit of each element will also be measured using high-energy X-ray diffraction to understand the solid-solution hardening behavior of these alloys. This information will be correlated with irradiation behavior, such as point defect formation.

3. Building a thermodynamic database for the TiZrNb-O system: We have collaborated with Computherm to update the thermodynamic database for the TiZrNb-O system to facilitate further designing and investigation of phase stability. Experimental results have shown discrepancies with the calculated results regarding the fraction of the *hcp* phase. Therefore, we plan to develop a pseudo-binary phase diagram of the system to better understand its phase transformation behavior and provide the necessary data for updating the thermodynamic database.

4. Ion beam irradiation experiments: Ion beam irradiation at intermediate temperatures will be performed on the designed alloys. Microstructural and nanoindentation analyses will be conducted to elucidate the irradiation-modified plasticity behavior of the alloys.

5. *fcc* CCAs with negative and medium SFE values at intermediate temperatures: Simultaneously, two other systems—fcc CCAs with negative SFE (CoCrNi-N-…) and medium SFE (FeMnAl-C-…)—have been designed for superior phase stability and PMDP mechanisms. These alloys will also undergo the aforementioned analyses for further investigation.

References

1. M.D. McMurtrey, B. Cui, I. Robertson, D. Farkas, G.S. Was, *Mechanism of dislocation channel-induced irradiation assisted stress corrosion crack initiation in austenitic stainless steel*, Curr Opin Solid State Mater Sci **19** 305–314 (2015).

2. M. Jiao, Z. Lei, Y. Wu, J. Du, X.Y. Zhou, W. Li, X. Yuan, X. Liu, X. Zhu, S. Wang, H. Zhu, P. Cao, X. Liu, X. Zhang, H. Wang, S. Jiang, Z. Lu, *Manipulating the ordered oxygen complexes to achieve high strength and ductility in medium-entropy alloys*, Nat Commun **14** 806 (2023).

3. H.S. Oh, M. Xu, S. Wei, F.F. Worsnop, J.M. LeBeau, C.C. Tasan, *Composition-dependent transformation-induced plasticity in Co-based complex concentrated alloys*, Acta Mater **262** (2024).

4. M. Abdel-Hady, H. Fuwa, K. Hinoshita, H. Kimura, Y. Shinzato, M. Morinaga, *Phase stability change with Zr content in β-type Ti-Nb alloys*, Scr Mater **57** 1000–1003 (2007).

5. H.S. Oh, K. Odbadrakh, Y. Ikeda, S. Mu, F. Körmann, C.J. Sun, H.S. Ahn, K.N. Yoon, D. Ma, C.C. Tasan, T. Egami, E.S. Park, *Element-resolved local lattice distortion in complex concentrated alloys: An observable signature of electronic effects*, Acta Mater **216** (2021).

Fundamental Studies of the Mechanical Behavior of Charged Hetero-Interfaces

Nitin P. Padture (PI) and Yue Qi (co-PI), Brown University

Keywords: Fracture, Interfaces, Defects, Electric Field, Charge

Research Scope

Mechanical adhesion of hetero-interfaces, which are ubiquitous in energy-conversion and -storage multi-layer devices, is key to their reliability. However, accumulated charge at those interfaces, which is also ubiquitous in these devices that are invariably subjected to external stimuli (electric field, light) during operation, are typically not considered in the measurement and analyses of mechanical adhesion. This represents a critical knowledge gap in interface science. The project is designed to address that gap, with the overarching objective of gaining fundamental understanding of the possible effects of accumulated charge, modulated by external stimuli (electric field, light), on the adhesion and fracture behavior of a range of hetero-interfaces. The project sets out to answer the following broad scientific questions towards achieving the above overarching objective. (1) To what extent do accumulated charges at hetero-interfaces modulated by the application of external stimuli (electric field, light), influence the adhesion toughness of those interfaces? (2) How do the characteristics of the charge accumulation affect the hetero-interface fracture behavior? (3) Can these effects be tuned by introducing engineered interfacial layers?

The project focuses on hetero-interfaces between brittle 'soft' and 'hard' semiconductors relevant to halide perovskite solar cells (PSCs), which provides a model platform for this fundamental study. However, the basic experimental and computational tools that will be developed here will be general, with the potential for extending their application in the future to more complex interfaces and operating conditions relevant to other energy devices such as electrochemical batteries and fuel cells. In this study the 'soft' semiconductor is a metal halide perovskite (MHP) and the 'hard' semiconductor is an oxide which serves as electron transport layer (ETL) or hole transport layer (HTL). Thus, the specific objectives are: (a) Understand quantitatively the effects of external stimuli (electric field, light) on the interfacial adhesion and fracture of a range of MHP/ETL and MHP/HTL interfaces. (b) Understand quantitatively the roles played by the nature and distribution of the accumulated charges, modulated by the external stimuli, on the interfacial adhesion and fracture of the above interfaces. (c) Elucidate the possible role of engineered interfacial layers, such as self-assembled monolayers (SAMs), with electrostatic dipole moments on the interfacial adhesion and fracture quantitatively.

Recent Progress

This project started on August 1, 2024, and we are in the process of hiring graduate students and postdoc to work on the project.

Future Plans

The project integrates experiments and modeling to achieve the above overarching and specific objectives. This comprises the following interrelated and iterative tasks, and they are designed to answer the three scientific questions articulated above. (i) Materials selection: MHP of various compositions, and oxides that serve as ETL and HTL materials, will be selected. (ii) Specimen design: multi-layer stacks in a double-cantilever (DCB) specimen will be designed, where simultaneous electric field and light can be applied during the interfacial adhesion toughness (G_C) measurement. (iii) Synthesis and processing: various DCB specimens of MHP/ETL and MHP/HTL interfaces comprising high-quality thin-film layers, without and with SAMs, will be fabricated. (iv) Materials and interfaces characterization: the layers and the interfaces will be characterized using spectroscopy and microscopy techniques. *Operando* microscopy and *in situ* spectroscopy techniques will also be used to quantify the interfacial potentials and charge accumulation. (v) Coupled mechanical testing: G_C measurements will be performed on the various MHP/ETL and MHP/ETL interface specimens as a function of applied electric field and/or light to mimic PSC operating conditions. (vi) Characterization and analyses: The tested specimens will be characterized, and the results will be critically analyzed to provide input to computational modeling. (vii) Theory and computational modeling: a suite of density-functional theory (DFT)-informed-continuum space-charge layer models will be developed, and they will be combined with the chemical stress model, to fully understand the impact of charge on interface fracture energy.

References

None

Publications

None

Determining the rate-controlling, grain-boundary-mediated mechanisms in ultrafine grained Au films: strain rate and grain size effects

Josh Kacher, Ting Zhu, Olivier Pierron, Georgia Tech

Keywords: In situ TEM, activation volume, grain boundary, dislocation, disconnection

Research Scope

The main goal of this research project is to acquire a fundamental understanding of grain boundary (GB) mediated mechanisms active in ultrafine grained (ufg) metallic films, and the extent to which they dictate plastic flow kinetics. Our approach consists of a synergistic integration of *in situ* transmission electron microscopy (TEM) deformation experiments, nanomechanical testing, and transition state theory based atomistic modeling, in order to provide a linkage between GB-mediated dislocation processes and their deformation kinetics. We recently focused on understanding the discrepancy we observed between our experimental and atomistic characterization of activation volume in ultrafine grained Au thin films. We previously obtained experimental activation volumes around 10 b^3 (average grain size: 140 nm), whereas atomistic activation volumes of 20 and 40 b^3 were obtained for surface and GB dislocation nucleation mechanisms (grain size of atomistic simulations: 10 nm, using symmetric tilt GBs). This discrepancy is further amplified by the known grain size effect on activation volume, captured by Conrad's model, which suggests an increase in activation volume with increasing grain size.

Based on our recent progress (described below), the atomistically determined activation volumes for GB dislocation nucleation in asymmetric tilt GBs (~13 b^3 for Au) compare more favorably to the experimental activation volumes at large strain rates (~20 b^3). In addition, we have started characterizing the activation volumes and strain rate effects on two annealed Au films with larger grain sizes (average grain sizes: 290 and 770 nm). The limited data are qualitatively consistent with the expected scaling effect from Conrad's model, and increase with grain size. These results indicate that GB dislocation nucleation is a strong candidate for the rate-controlling process in ultrafine grained thin films.

Recent Progress

We recently improved our in situ TEM technique by switching from capacitive sensing to image-based sensing, which enables local strain measurements along the specimen gauge length (and more accurate plastic strain rate measurements for activation volume calculation) and testing at larger strain rates (exceeding 10^{-1} s^{-1}) [1]. Fig. 1(a) shows the effect of applied strain rate on the monotonic curves, clearly highlighting strain rate effects. Fig 1(b) shows the evolution of yield stress versus applied strain rate. The slope (strain rate sensitivity, m) is not constant through the entire range of applied strain rate. Instead, the slope m is larger for low applied strain rate ($<10^{-4}$ s^{-1}), and decreases with increasing applied strain rate ($> 10^{-2}$ s^{-1}). This translates into a change in physical activation volume between low and high applied strain rate (see Fig. 1(c)). At 400 MPa,

the activation volume increases from $10b^3$ (our previous results) at low strain rate to ~20 b^3 at large strain rates (above 10^{-2} s^{-1}).

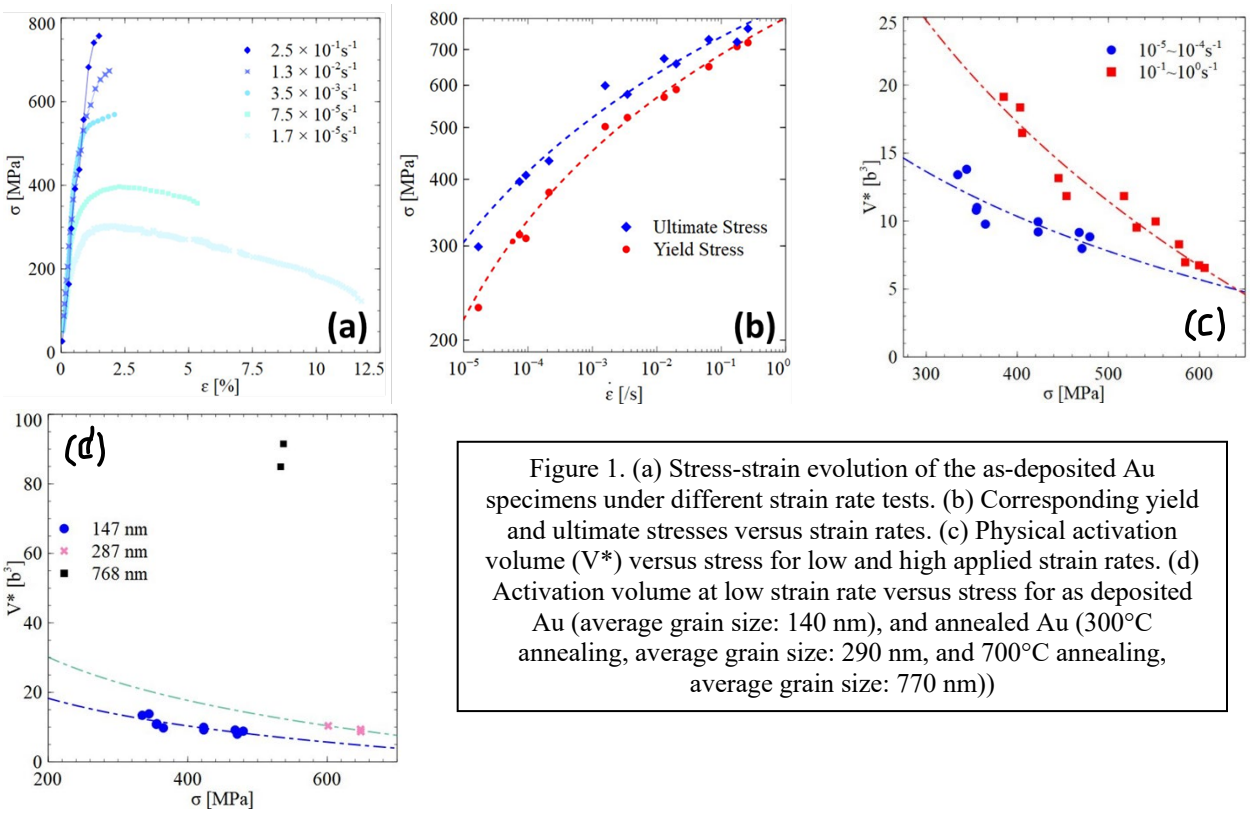

Figure 1. (a) Stress-strain evolution of the as-deposited Au specimens under different strain rate tests. (b) Corresponding yield and ultimate stresses versus strain rates. (c) Physical activation volume (V*) versus stress for low and high applied strain rates. (d) Activation volume at low strain rate versus stress for as deposited Au (average grain size: 140 nm), and annealed Au (300°C annealing, average grain size: 290 nm, and 700°C annealing, average grain size: 770 nm))

Fig. 2 illustrates the dynamic evolution of a grain in Au films under high strain rate loading up to approximately 600 MPa and maintained for relaxation over 6 minutes. A complex network of multiple slip systems is observed with intense dislocation activities within the first very initial stage of the relaxation post-loading. The rapid response is in stark contrast to the subdued activity observed under low strain rate conditions, where dislocation is mainly confined to single slip systems. The junctions function in the capacity of barriers to dislocation movement, which can explain why high strain rate activation volume values are generally larger than that of low strain rate (Fig. 1(c)). The transition of deformation mechanism upon changing strain rate is likely a direct consequence of the activation of multi-slip system.

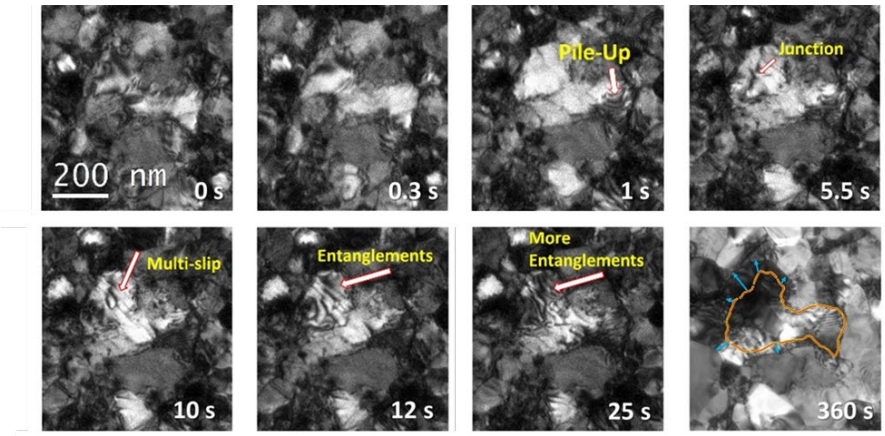

Figure 2. In-situ TEM images capturing the progression of dislocation activity during the relaxation phase following high strain rate loading to 600 MPa, indicating the onset of multiple slip systems.

We are currently investigating the effect of grain size on activation volume for Au. Fig 1(d) shows the preliminary results for activation volume as a function of stress for as deposited Au (low strain rate, average grain size: 140 nm) and annealed Au at 300°C (average grain size: 290 nm) and 700°C (average grain size: 770 nm). The activation volume for the annealed Au was measured at low strain rates. Preliminary results show little strain rate effects compared to what was observed for as-deposited Au. These data will be completed and analyzed over the next year.

In the recent literature, most atomistic studies of GBs focus on coincident site lattice (CSL) GBs, characterized by their reciprocal density of coincident sites (Σ), of the symmetric tilt type [2, 3]. However, asymmetric GBs, instead of symmetric GBs, are more commonly observed in polycrystalline metals [4, 5], indicating that asymmetric GBs are more energetically favorable than symmetric tilt GBs. We focused on free-end nudged elastic band (FENEB) calculations of the activation energies and activation volumes of dislocation nucleation at asymmetric tilt GBs. We studied a representative asymmetric GB observed by in situ atomic-resolution TEM straining experiments by Wang et al. [5]; see Fig 3(a). This asymmetric <110> tilt GB has a misorientation angle of 20.1° between adjoining grains. The magnified atomic structure at this GB is shown in Fig. 3(b). It is seen that both the upper and lower grains are aligned with the <110> zone axis. The face of the lower grain exhibits a close-packed {111} atomic plane, while the face of the upper grain exhibits a high-index {331} atomic plane. Notably, this GB consists of two sets of ½ <110>{111} lattice dislocations to accommodate the lattice misorientation and misfit between adjoining grains. A typical misorientation and a misfit dislocation are marked by symbol "⊥" at the termination of their extra half-plane, respectively, as shown in Fig. 3(b). Interestingly, these two dislocations combine to form a GB Lomer lock, featuring the characteristic core structure of a five-membered unit (marked by a pentagon). The simulation box has the dimensions of 14.0 nm × 24.5 nm × 14.4 nm, and contain 203,193 atoms. Free surface conditions are applied along the x and y directions, and periodic boundary conditions are applied along the out-of-plane direction.

We determined the minimum energy paths (MEPs) of dislocation nucleation in Au using the above GB setup. Fig. 4(a) shows the stress-dependent activation energy of GB dislocation nucleation as a function of RSS in Au. This mode of GB dislocation nucleation becomes unable

when the RSS is larger than 950 MPa. The corresponding activation volume is plotted in Fig. 4(b). The extrapolated activation volume is ~13b^3 when the energy barrier is 0.7 eV. These results indicate that the activation volume for asymmetric tilt GBs is significantly lower than ~40b^3 for symmetric tilt GBs in Au.

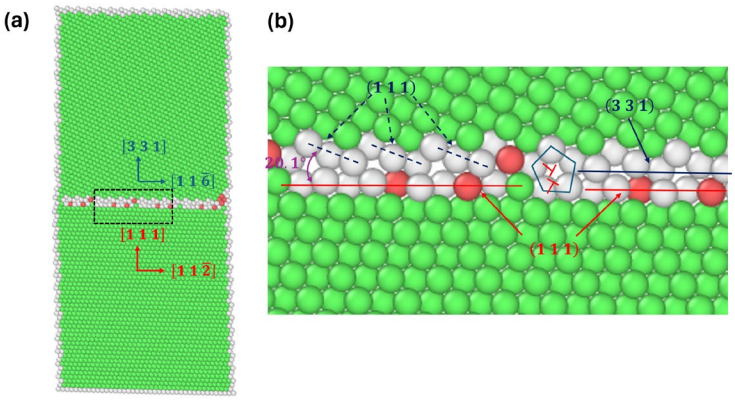

Figure 3: (a) Atomic configuration of a bicrystal containing an asymmetric tilt GB. (b) Magnified image of the black-boxed GB region in (a). Atoms are colored by the common neighbor numbers.

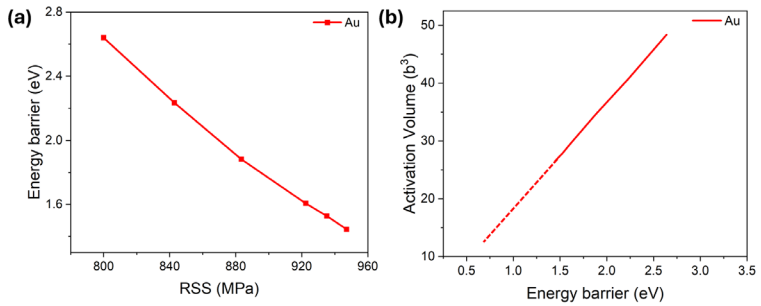

Figure 4: FENEB results of GB dislocation nucleation at an asymmetric GB in Au. (a) Activation energy as a function of resolved shear stress. (b) Activation volume as a function of energy barrier.

Future Plans

In the next year, we will perform the same complete in situ TEM activation volume characterization (as a function of applied stress and applied strain rate) to two sets of annealed Au thin films with larger grain sizes, 290 and 770 nm. These results will be compared to our atomistic simulations and Conrad's model predicting grain size effect on activation volume. Given that the initial grain size of the as-deposited Au films is large (140 nm), we will also fabricate Ni thin films that are known to have an initial grain size of ~10-20 nm, and an average grain size of ~200 nm after annealing (based on characterization for a different project). The full in situ TEM characterization of activation volume of these two sets of Ni thin films will provide another valuable investigation of grain size effect on activation volume and rate-limiting mechanisms, especially because the as-deposited Ni films have a grain size similar to that of the atomistic simulations. On the modeling side, we will employ FENEB simulations to examine the statistical variation of activation volumes from different types of asymmetric GBs. We will also carry out FENEB simulations of dislocation nucleation from asymmetric GBs in other FCC metals such as Al and Cu. These efforts will enable us to establish dislocation nucleation at asymmetric GBs as the rate-controlling process in ultra-fine-grained metals.

References

[1] S. Stangebye, X. Liu, L. Daza Llanos, Y. Yang, T. Zhu, J. Kacher, O. Pierron, Comparison of electrical sensing and image analysis for in situ transmission electron microscopy nanomechanical testing of thin films, Thin Solid Films 787 (2023) 140125.
[2] P. Lejček, M. Šob, V. Paidar, Interfacial segregation and grain boundary embrittlement: An overview and critical assessment of experimental data and calculated results, Progress in Materials Science 87 (2017) 83-139.
[3] H. Grimmer, W. Bollmann, D. Warrington, Coincidence-site lattices and complete pattern-shift in cubic crystals, Acta Crystallographica Section A: Crystal Physics, Diffraction, Theoretical and General Crystallography 30(2) (1974) 197-207.
[4] G.S. Rohrer, The distribution of grain boundary planes in polycrystals, Jom 59 (2007) 38-42.
[5] G.S. Rohrer, E.A. Holm, A.D. Rollett, S.M. Foiles, J. Li, D.L. Olmsted, Comparing calculated and measured grain boundary energies in nickel, Acta Materialia 58(15) (2010) 5063-5069.
[6] L. Wang, Y. Zhang, Z. Zeng, H. Zhou, J. He, P. Liu, M. Chen, J. Han, D.J. Srolovitz, J. Teng, Tracking the sliding of grain boundaries at the atomic scale, Science 375(6586) (2022) 1261-1265.

Publications from past two years

1. S. Stangebye, K. Ding, Y. Zhang, E. Lang, K. Hattar, T. Zhu, J. Kacher, O. Pierron, *Direct observation of grain-boundary-migration-assisted radiation damage healing in ultrafine grained gold under mechanical stress*, Nano Letters, v **23** n 8 pp. 3282-3290 (2023)
2. S. Stangebye, X. Liu, L. Daza-Llanos, Y. Yang, T. Zhu, J. Kacher, O. Pierron, *Comparison of electrical sensing and image analysis for in situ TEM nanomechanical testing of thin films*, Thin Solid Films, v **787** 140125 (2023)
3. S. Stangebye, K. Ding, T. Zhu, O. Pierron, J. Kacher, *Grain size effects on stress-assisted grain boundary migration in polycrystalline Au thin films under tension*, Nano Today, revised manuscript under review
4. Y. Yang, K. Ding, X. Liu, T. Zhu, J. Kacher, O. Pierron, *Strain-rate-dependent in situ transmission electron microscopy activation volume measurements: revealing the governing plastic deformation mechanisms in ultrafine grained Au films*, to be submitted shortly

Damage-Tolerance in Structural Materials

Robert O. Ritchie, Mark Asta, and Andrew M. Minor
Lawrence Berkeley National Laboratory

Keywords: High-entropy alloys, Deformation, Fracture, Toughness, *fcc vs. bcc* alloys

Research Scope

The attainment of strength and toughness is a vital requirement for structural materials; unfortunately, these properties are often mutually exclusive. Indeed, the development of damage-tolerant materials has traditionally been a compromise between hardness *vs*. ductility. Using an approach that combines multiscale mechanical testing and characterization with theoretical and machine-learning informed computational methods, we are examining strategies to solve this "conflict" in advanced metallic alloys by focusing on the interplay between the individual mechanisms that contribute to strength and toughness, that of plasticity and crack-tip shielding, noting that these phenomena may originate at wildly different structural length-scales. Our central objective is to seek a fundamental understanding of the scientific origins of damage-tolerance in multiple-element (largely single-phase) metallic alloys at atomistic to near-macroscopic length scales. Our focus is currently on medium-/high-entropy alloys (M/HEAs), which can display excellent mechanical properties due to a novel combination of mechanisms arising from their disordered structures. We first examined face-centered cubic (*fcc*) CrCoNi-based M/HEAs which we revealed exhibited some of the highest fracture toughnesses ever recorded. Their strength, ductility and toughness are achieved by a synergistic sequence of deformation mechanisms (slip, stacking-fault formation, nano-twinning and phase transformation, catalyzed we believe by local chemical ordering) which serves to promote prolonged strain hardening. The damage-tolerance of these alloys is further enhanced at cryogenic temperatures and ultrahigh strain rates. In stark contrast, the body-centered cubic (*bcc*) refractory high-entropy alloys (RHEAs), which are now our focus, are characterized by high strength at ultrahigh temperatures. Although they look impressive when tested in compression, we have shown that in tension, they are invariably plagued by severe brittleness, *e.g*., NbTaMoW. However, we have shown that RHEAs with Group IV elements, specifically NbTaTiHf, can display remarkable fracture toughness over a wide temperature range from 20K to 1200°C, with minimal evidence of strain hardening. The mechanical properties of NbTaTiHf are essentially unique for *bcc* alloys, and involve (especially at higher temperatures) the fascinating phenomenon of kink band formation. Our ultimate aim here is to uncover the relationships between atomic-scale phenomena and macroscopic mechanical behavior, which is the basis of the damage-tolerance of these structural materials.

Recent Progress

The two major highlights of our recent work pertain to the deformation and fracture behavior in extreme environments – the record fracture toughness (exceeding 450 MPa$\sqrt{m}$) of the *fcc* CrCoNi at 20K,[1] and the remarkable fracture toughness of the *bcc* NbTaTiHf at 77K to 1200°C associated with twinning and especially kink band formation.[2] Indeed, our most recent (unpublished) work

has shown that this latter alloy displays no ductile-to-brittle transition with an astounding fracture toughness of ~100 MPa√m in a liquid helium environment at 20K.

We have now examined several *bcc* RHEAs, but most notably, have provided a dramatic comparison between two alloys with somewhat similar compositions, namely NbTaTiHf and NbTaMoW, both of which are nominally single phase. Atomistic simulations of the precursor conditions to fracture of these two RHEAs show precise Rice-Thomson behavior: NbTaTiHf undergoes crack-tip blunting by dislocation emission indicative of its ductile behavior, whereas NbTaMoW, which is brittle, initiates fracture by breaking atomic bonds at the crack tip.[3] These simulations are completely consistent with the experimental fracture results described below.

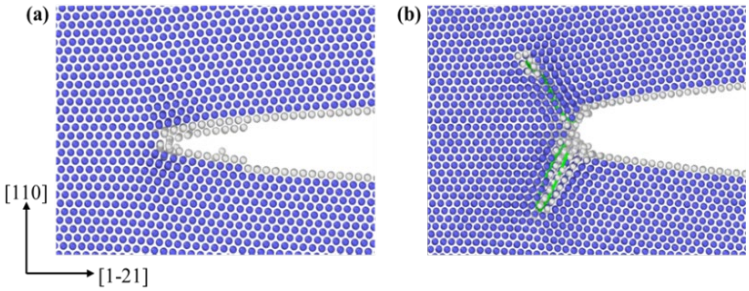

Fig. 1. Atomically sharp crack propagation at 0 K in (a) $Nb_{45}Ta_{25}Ti_{15}Hf_{15}$ and (b) NbMoTaW. At applied stress intensity factor, K_I of ~0.93 MPa√m, $Nb_{45}Ta_{25}Ti_{15}Hf_{15}$ fractures via a ductile mode: the crack tip is blunted by the emission of ½ <111> dislocations, and NbMoTaW fractures via brittle mode: the crack advances by bond breaking and remains sharp.

NbTaMoW is a well-known RHEA for its high strength at ultrahigh temperatures - it retains a yield strength of 400 MPa at 1600°C – however, its mechanical properties have been largely measured in compression. We tested this alloy in tension and found ductility values two orders of magnitude lower than in compression due to nominally elastic fracture below its compression yield strength. It also develops oxygen embrittlement in the grain boundaries at high temperatures, leading to brittle intergranular fracture.[4] Not unlike many *bcc* RHEAs, this alloy is a highly brittle material, with measured fracture toughnesses generally below 10 MPa√m.

The single phase NbTaTiHf RHEA, which comprises Group IV elements, conversely displays remarkable tensile ductility and toughness over a very wide temperature range from 20K to 1200°C,[2] properties unlike most other *bcc* alloys. With a K_{JIc} of 90 to 100 MPa√m between 77 and 20K, we believe this is one of the toughest *bcc* alloys reported to date, yet unlike the *fcc* HEAs, it displays virtually no strain hardening (Fig. 2).[2]

The fracture resistance of materials depends on deformation mechanisms active ahead of the crack tip and microstructural features such as grain size, texture, and morphology/distribution of precipitates/inclusions. These factors could be divided into three categories for HEAs: (i) The intrinsic ductility of the materials is influenced by the characteristics of the metallic bond, and different deformation mechanisms are activated ahead of a crack tip by varying the electronic state of the atoms. The material's fracture resistance depends on the ability of these deformation mechanisms to be activated and their effectiveness in spreading the damage away from the crack tip, avoiding strain localization at a gross scale. The deformation mechanisms glide/cross-slip of complete and partial dislocations, twinning-induced plasticity, transformation-induced plasticity, and possibly kink bands are activated by altering the stacking fault energy (SFE) of the materials through compositional modulations at atomic scale (Fig. 3). A reduced SFE can activate TWIP or TRIP in *fcc* HEAs. (ii) Strengthening factors work conversely with intrinsic ductility and increase

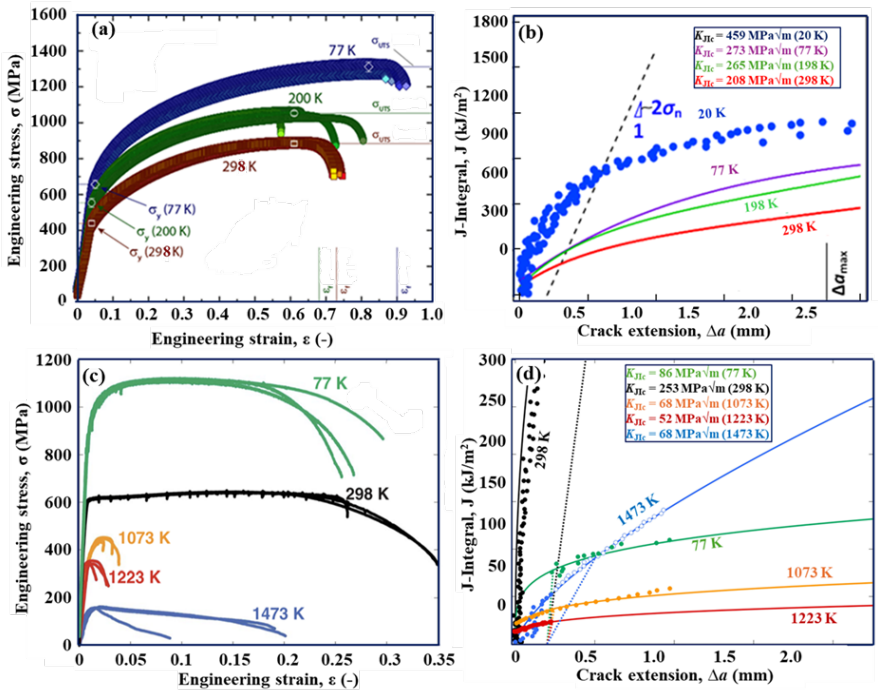

Fig. 2. (a) Engineering stress-strain plots of an *fcc* high-entropy alloy, CrCoNi, at temperatures 77 K, 200 K, and 298K. (b) The energy release rate, *J*, *vs.* crack length, Δa, plots (*J*-R curves) of CrCoNi at temperatures 20 K, 77K, 198K, and 298K. (c) Engineering stress-strain plots of a *bcc* high-entropy alloy, $Nb_{45}Ta_{25}Ti_{15}Hf_{15}$, at temperatures 77K, 298K, 1073K, 1223K, and 1473K. (d) *J vs.* Δ*a* plots of $Nb_{45}Ta_{25}Ti_{15}Hf_{15}$ at 77K, 298K, 1073K, 1223K, and 1473K.

fracture resistance by resisting the spread of plastic damage away from the crack tip. A stronger material will show a relatively higher K_{JIc} because higher stress is required to achieve the same equivalent plastic strain at the crack tip. Consequently, the single-phase solid solutions have relatively higher toughness than the pure metal counterparts. Nonetheless, if the plastic damage is not effectively distributed and the strain is localized at the crack tip, the strengthening could inversely affect the fracture resistance. This is primarily observed in *bcc* alloys, where strengthening is associated with strong directional bonding, high Peierls-Nabarro forces, and limited dislocation mobility. (iii) Metallurgical extrinsic factors also affect the fracture resistance of the HEAs. These factors are microstructurally weak links providing a path of least resistance for crack propagation either by microvoid nucleation or cleavage/intergranular fracture.

Future Plans

The discovery of novel HEAs with exceptional properties has sparked significant interest among materials scientists. Some indications are that these exceptional properties originate from atomic scale variations instilled from mixing multiple elements, promoting dislocation glide and cross slip, stacking fault formation, nano-twinning, and kink bands during deformation. Along with searching for novel M/HEAs, a detailed investigation of these deformation mechanisms is required to develop a deeper understanding so that they can be harnessed to accelerate the discovery of structural materials suitable for more extreme environments. We intend to have a holistic approach to understanding the atomic state changes and their effect on nucleation and propagation energies of defects and mesoscale properties—strength and toughness—for utilizing the full potential of M/HEAs. We will continue focusing on the *bcc* RHEAs, which present exciting possibilities for developing ultrahigh-temperature structural materials.

Our approach to the technological ductility/toughness challenge is to gain a fundamental

understanding of the ductile-to-brittle transition in these alloys through atomistic simulations and a comprehensive assessment of their deformation and fracture mechanisms *under tensile loading* at nano- to macro-scales (the community has largely focused on compression testing to date which can mask the extreme lack of damage-tolerance in these RHEAs). As these alloys invariably fail by intergranular fracture at high temperatures, grain boundaries are clearly critical as they can lead to a dramatic reduction in fracture toughness due to segregation of multiple alloying elements, the resulting formation of new grain-boundary structures or complexions, the precipitation of intergranular nitrides and carbides, and consequent high-temperature stress-corrosion/creep mechanisms.

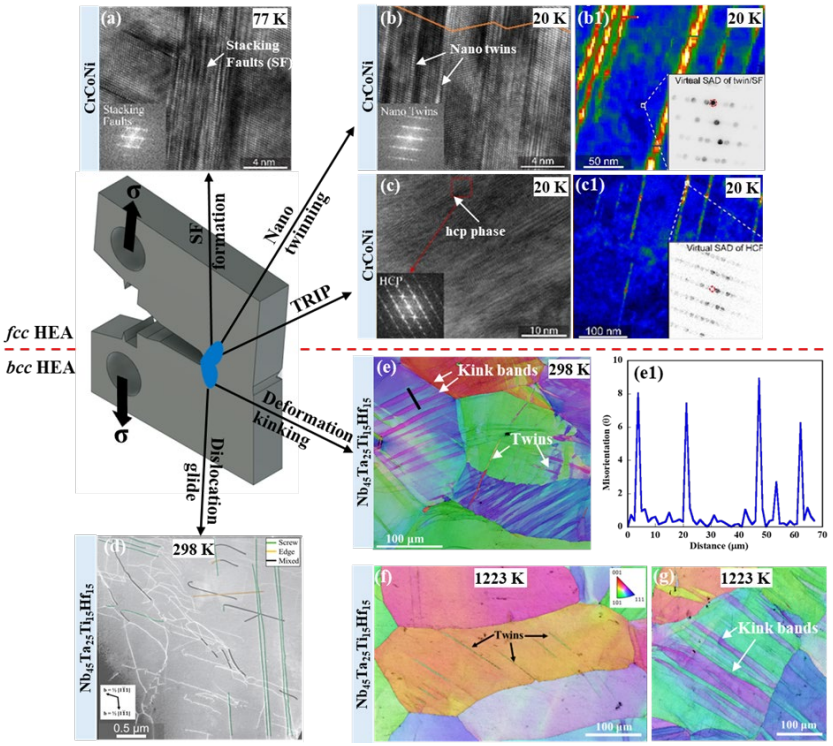

Fig. 3. Different deformation mechanisms activated at the crack tip in CrCoNi (*fcc* HEA) and $Nb_{45}Ta_{25}Ti_{15}Hf_{15}$ (*bcc* HEA). In the *fcc* HEAs, deformation mechanisms (a) stacking fault formation, (b) nano twinning, and (c) transformation-induced plasticity are activated across a temperature range of 298 K-20 K. In bcc HEA, (g) edge and screw dislocations, (b) twins, and (c) forms during deformation across the temperature range of 77 K-1223 K.

Our overall plan is a focus on developing capabilities to model, characterize and advance fundamental understanding of the origins of the unique properties of compositionally and structurally complex "high-entropy" materials. This pertains to the discovery of structural materials utilizing computational and experimental methods including AI/ML, for high throughput prediction and verification of novel alloys focusing on high-entropy alloys

References

1. D. Liu, Q. Yu, S. Kabra, M. Jiang, P. Forna-Kreutzer, R. Zhang, M. Payne, F. Walsh, B. Gludovatz, M. Asta, A. M. Minor, E. P. George, R. O. Ritchie, *Exceptional fracture toughness of CrCoNi-based medium- and high-entropy alloys at 20 kelvin*, Science, 378 (6623), 978 (2022).
2. D. H. Cook, P. Kumar, M. I. Payne, C. H. Belcher, P. Borges, W. Q. Wang, F. Walsh, Z. Li, A. Devaraj, M. Zhang, M. Asta, A. M. Minor, E. J. Lavernia, D. Apelian, R. O. Ritchie, *Kink bands promote exceptional fracture resistance in a NbTaTiHf refractory medium-entropy alloy*, Science, 384 (6692), 178 (2024,
3. W. Q. Wang, P. Kumar, D. H. Cook, D. Farkas, R. O. Ritchie, M. Asta, *Unveiling the fundamentals of intrinsic ductility in $Nb_{45}Ta_{25}Ti_{15}Hf_{15}$ and NbMoTaW RHEA via machine learning potentials*, article in preparation (2024).
4. P. Kumar, X. Gou, D. H. Cook, M. I. Payne, N. J. Morrison, W. Wang, M. Zhang, M. Asta, A. M. Minor, R. Cao, Yi Li, R. O. Ritchie, *Degradation of the mechanical properties of NbMoTaW refractory high-entropy alloy in tension*, Acta Materialia, 279, 120279 (2024).

Publications

1. F. Walsh, R. O. Ritchie, M. Asta, *Theoretical Antiferromagnetism of Ordered Face-Centered Cubic Cr-Ni Alloys*, Physical Review Materials, 6 (11), 113602 (2022)

2. M. Zhang, Q. Yu, C. Frey, F. Walsh, M. I. Payne, P. Kumar, D. Liu, T. M. Pollock, M. Asta, R. O. Ritchie, A. M. Minor, *Determination of Peak Ordering in the CrCoNi Medium-Entropy Alloy via Nanoindentation*, Acta Materialia, 241, 118380(2022). .

3. D. Liu, Q. Yu, S. Kabra, M. Jiang, P. Forna-Kreutzer, R. Zhang, M. Payne, F. Walsh, B. Gludovatz, M. Asta, A. M. Minor, E. P. George, R. O. Ritchie, *Exceptional Fracture Toughness of CrCoNi-Based Medium- and High-Entropy Alloys at 20 Kelvin*, Science, 378 (6623), 978 (2022).

4. S. Zhao, S. Yin, X. Liang, F. Cao, Q. Yu, R. Zhang, L. Dai, C. J. Ruestes, R. O. Ritchie, A. M. Minor, *Deformation and Failure of the CrCoNi Medium-Entropy Alloy Subjected to Extreme Shock Loading*, Science Advances, 9 (18), eadf8602 (2023).

5. F. Walsh, M. Zhang, R. O. Ritchie, A. M. Minor, M. Asta, *Extra Electron Reflections in Concentrated Alloys do not Necessitate Short-Range Order*, Nature Materials, 22 (8), 926 (2023).

6. P. P. P. O. Borges, R. O. Ritchie, M. Asta, *Local Lattice Distortions and the Structural Instabilities in bcc Nb-Ta-Ti-Hf High-Entropy Alloys: An Ab Initio Computational Study*", Acta Materialia, 262, 119415 (2024).

7. W. Q. Wang, F. Walsh, R. O. Ritchie, M. Asta, *Elucidating the Roles of Chemistry, Compositional Complexity, and Short-Range Order in the Dislocation Energetics of Body-Centered-Cubic Concentrated Solid Solutions*, Physical Review Materials, 8 (1), 013608 (2024).

8. Y. Yang, S. Yin, Q. Yu, Y. Zhu, J. Ding, R. Zhang, C. Ophus, M. Asta, R. O. Ritchie, A. M. Minor, *Rejuvenation as the Origin of Planar Defects in the CrCoNi Medium Entropy Alloy*, Nature Communications, 15, 1402 (2024).

9. D. H. Cook, P. Kumar, M. I. Payne, C. H. Belcher, P. Borges, W. Q. Wang, F. Walsh, Z. Li, A. Devaraj, M. Zhang, M. Asta, A. M. Minor, E. J. Lavernia, D. Apelian, R. O. Ritchie, *Kink Bands Promote Exceptional Fracture Resistance in a NbTaTiHf Refractory Medium-Entropy Alloy*, Science, 384 (6692), 178 (2024,

10. F. Walsh, M. Zhang, R. O. Ritchie, M. Asta, A. M. Minor, *Multiple Origins of Extra Electron Diffractions in fcc Metals*, Science Advances, 10, eadn9673 (2024).

11. P. Kumar, X. Gou, D. H. Cook, M. I. Payne, N. J. Morrison, W. Wang, M. Zhang, M. Asta, A. M. Minor, R. Cao, Yi Li, R. O. Ritchie, *Degradation of the Mechanical Properties of NbMoTaW Refractory High-Entropy Alloy in Tension*, Acta Materialia, 279, 120279 (2024).

Understanding and Engineering the Damage Tolerance of Amorphous Grain Boundary Complexions

Timothy J. Rupert - Johns Hopkins University

Keywords: complexions, grain boundaries, nanocrystalline, interfacial engineering

Program Scope

Grain boundaries often act as failure nucleation sites during plastic deformation. This project aims to understand how amorphous grain boundary complexions can be used to toughen these critical weak points, and then subsequently engineer these complexions to further improve damage tolerance. Specifically, we focus on nanocrystalline metals, as these materials are notorious for failing prematurely. Our primary focus is on mechanical damage due to dislocation-based plasticity, although we pursue some limited avenues of investigating the ability of amorphous complexions to act as point defect sinks as well. Complexion thickness is first studied, followed by the investigation of structural short-range order (SSRO) as a key descriptor of internal complexion structure.

Recent Progress

The description of our progress here is organized based on our efforts to test two core hypotheses: (1) Thicker amorphous complexions will be more damage tolerant. (2) SSRO patterning will influence damage nucleation and growth. In both cases, efforts are made to modify these structural descriptors by varying processing conditions and/or dopant selection.

Thickness of Amorphous Complexions

While our simulation work on bicrystal models suggests that thicker amorphous complexions can absorb more dislocations before a crack nucleates, experimental validation is needed to ensure that such behavior translates into macroscopic plasticity and to understand how failure commences in a random polycrystalline microstructure. Nanocrystalline Cu-Zr alloys were created by ball milling and then consolidated with hot pressing, followed by a heat treatment to induce amorphous complexion formation. The bulk pieces were exposed to a quenching/cooling gradient by placement on a heat sink, with subsequent samples taken from either near the contact location (fast-quenched) or far away (slow-quenched). Figs. 1(a) and (b) show how amorphous complexion thickness can be measured and a distribution of thicknesses calculated for each sample. The faster quenched sample has thicker complexions than the more slowly quenched sample. Micropillar compression experiments, performed to different strains and at different loading rates (not all details shown here, for brevity), show that the sample with thicker complexions experiences more homogeneous plasticity (Fig. 1(c)). In contrast, localized deformation and failure was more often observed in the sample with thinner complexions, as shown in Fig. 1(d).

Complexion thickness was also found to influence the ability to absorb point defect content brought by irradiation. Our team has started a collaboration with Prof. Janelle Wharry, also a PI

in this program, who has shown that ion irradiation can create amorphous interfacial complexions in Cu-Ta. These features are observed at both grain boundaries (separating two Cu crystals) and interphase boundaries (separating a Cu crystal from a Ta-rich particle). Fig. 2(a) and (b) shows a Cu-Ta sample before and after ion irradiation, respectively. Worth noting is that the amorphous complexions observed here do not form from heating and quenching, with the irradiation itself providing a driving force for amorphization. Fig. 2(c) shows that the local internal structure of the complexions is different in Cu-Ta than in our Cu-Zr standard, with the former having stronger spatial gradients in local atomic volume. Atomistic simulations of collision cascades near different interface types confirm that amorphous complexions are efficient point defect sinks, whether at a Cu-Cu grain boundary or at a Cu-Ta phase boundary, with less damage observed as complexion thickness is increased (Fig. 2(d).

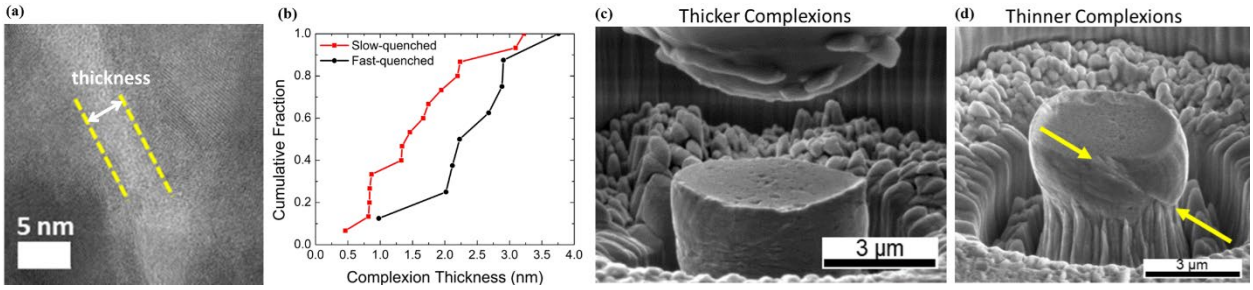

Figure 4. (a) An amorphous complexion in Cu-Zr. (b) Statistical distributions of complexion thickness measured from samples with slow and fast quenching. (c) Samples with thicker complexions exhibit more uniform plasticity. (d) Sample with thinner complexions were more likely to experience localized failure.

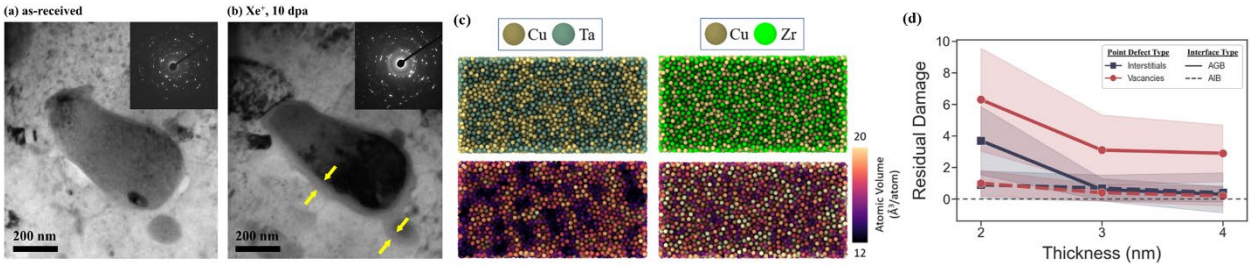

Figure 5. (a) As-received Cu-Ta had ordered grain boundaries while (b) ion irradiated Cu-Ta contained amorphous complexions at both grain and interphase boundaries. (c) Cu-Ta metallic glass has more pronounced variations in local atomic volume than a Cu-Zr comparison. (d) Residual damage from primary-knock-on-atom simulations is reduced as complexion thickness increases.

Our team recently developed thermally-stable Al-rich nanocrystalline alloys that could maintain amorphous complexions even after slow cooling. Bulk Al-Mg-Y pieces were created (Fig. 3(a)) and macroscale compression experiments (Fig. 3(b)) were carried out on these samples to understand how the remaining amorphous complexions affected strength and plasticity. The time for hot pressing was varied to allow for evolution of carbide and intermetallic precipitates in the samples. Fig. 3(c) shows a compilation of compressive stress-strain curves, showing that a number of samples had outstanding combinations of strength and ductility. These results demonstrate that the atomic-scale mechanisms study in this project can result in real gains in macroscopic performance.

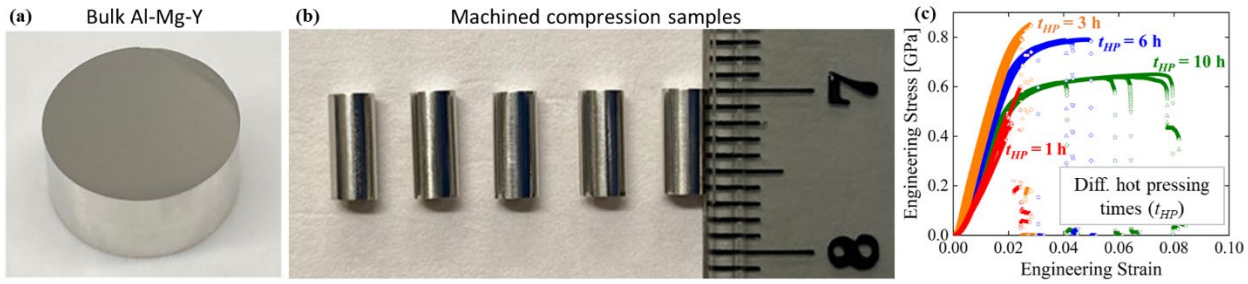

Figure 6. (a) bulk piece of nanocrystalline Al-Mg-Y with a small grain size and amorphous complexions. (b) Macroscale compression samples were machined and (c) compressive stress-strain curves were measured, showing both high strength and appreciable plasticity.

Structural Short-Range Order (SSRO) of Amorphous Complexions

An individual amorphous complexion can be characterized in terms of its local packing motifs or SSRO, marking another important descriptor that is hypothesized to impact damage tolerance. Metallic glasses serve as an important comparison, where disordered Voronoi polyhedra are the most common motif. Atomistic modeling of amorphous complexions shows that the interior of an amorphous complexion has a similar structure to a glass, but there are important deviations where the complexion meets the grains in a region that can be called the amorphous-crystalline transition region (ACTR). An example is shown in Fig. 4(a), where the most common atomic packing motifs at the ACTRs are ordered Voronoi polyhedra that are only slightly different than the perfect face-centered cubic structure. We have uncovered how crystallography influences the patterning of this SSRO, with relief of grain boundary strain being the critical mechanism. We discovered that subtle differences in SSRO patterning can led to large toughness differences. Fig. 4(b) shows two amorphous complexions where the overall densities of ordered and disordered packing is the same, but the location of the more ordered ACTR is different. Fig. 4(c) shows molecular dynamics simulations of plasticity and damage for these two complexions, demonstrating that it is beneficial to have the more disordered (and therefore more easily deformed) region further away from the site where the dislocation is absorbed. This allows the entire complexion volume to participate in the absorption event, distributing the strain more homogeneously and avoiding localization.

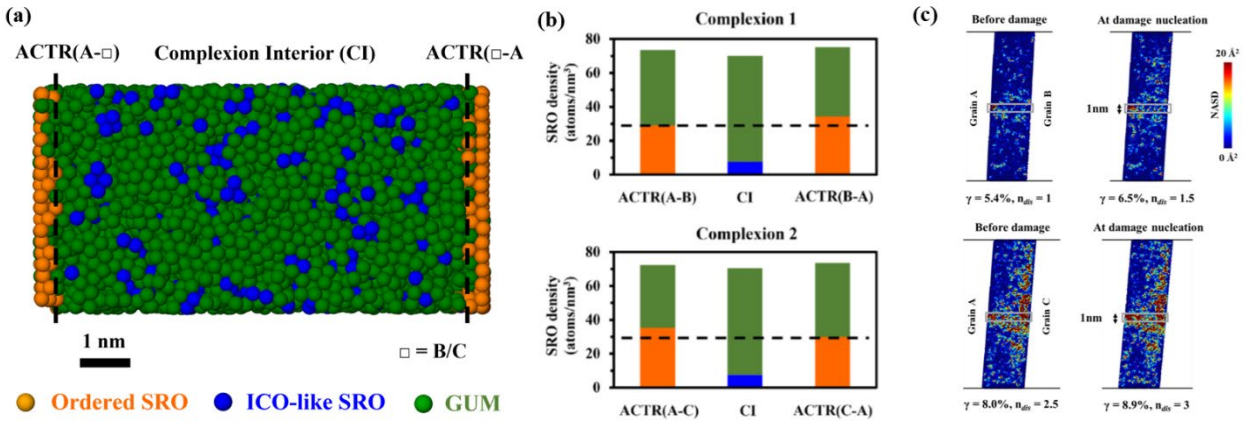

Figure 7. (a) An amorphous complexion, with atoms colored according to their SSRO type. (b) Two complexions were chosen that had different relative SSRO at the two ACTRs. (c) The sample with more disorder at the ACTR further away from the dislocation absorption site is more damage tolerant.

Current efforts are focused on quantifying SSRO in experimental samples with 4D-STEM. Early efforts on our ball milled materials have been unsuccessful here, as the grain size stays very small , resulting in curved boundaries and overlapping grains. We are pursuing a sputter deposition route to make model films designed to align the features of interest with an electron beam for detailed characterization. A thick layer of pure Cu is first deposited, followed by co-sputtering of multiple elements to match the desired grain boundary composition, and then finally another thick layer of pure Cu. High temperature heat treatments evolve the material from the as-deposited configuration to an equilibrium state containing an amorphous complexion along a planar orientation in the middle of the sample that is confined by larger grains on either side, creating a model row of interfaces. An example of an as-deposited film is shown in Fig. 5. Heat treatment of these samples is being performed with an in situ TEM heating chip, to allow for super fast quenching of the microstructures.

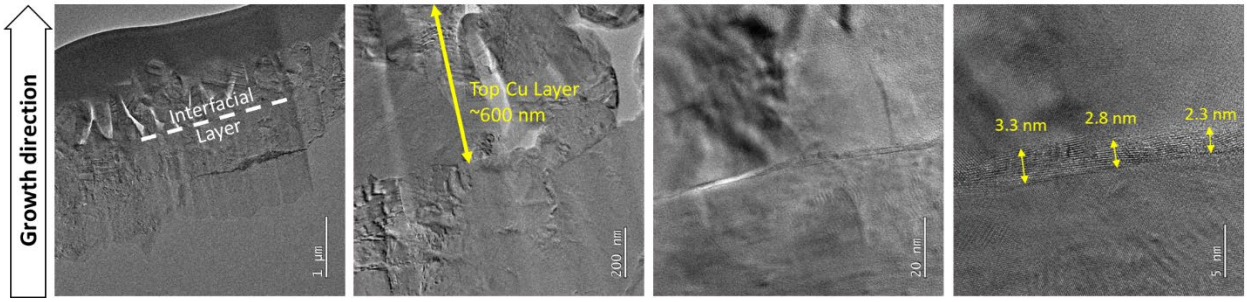

Figure 8. An as-deposited planar complexion sample, where the amorphous complexions will be aligned for TEM imaging and nanoscale diffraction analysis of SSRO.

We are also working to create new alloys with the intent of breaking up the ordered SSRO patterns along the ACTRs. Our high resolution transmission electron microscopy results have shown that Nb in a ternary Cu-Zr-Nb alloy and Nb+Ti in a quaternary Cu-Zr-Nb-Ti alloy have their highest concentrations at the ACTRs. These elements prefer to form ordered grain boundaries when studied by themselves in Cu-rich binary alloys, leading to the conclusion that they prefer the ACTRs. As increasing the compositional complexity has been shown to result in more disordered metallic glasses, we hypothesize that multi-component grain boundary segregation will be a pathway to toughening for amorphous complexions.

Future Plans

We will work to characterize SSRO distributions in our real world alloys using 4D-STEM nanodiffraction. A specific challenge in this area is the difficulty of interpreting local diffraction patterns. Even with 4D-STEM, clusters of multiple atoms will be probed. We plan to create a database of atomic-scale diffraction patterns associated with different SSRO types and orientations with respect to the electron beam, followed by the application of image recognition to identify the SSRO distribution from experimental data. Atomistic simulations, where we know the exact packing motifs, are expected to be important benchmarks. Once we have samples with controlled variations in the SSRO patterns, mechanical testing of the film samples will commence. Overall behavior will be probed with mandrel bending tests while individual interfaces will be tested with in situ mechanical testing modalities.

Publications (August 2022 - August 2024)

PUBLISHED:

1. D. Aksoy, P. Cao, J.R. Trelewicz, J.P. Wharry, T.J. Rupert. *Enhanced radiation damage tolerance of amorphous interphase and grain boundary complexions in Cu-Ta*, JOM, **76**, 2870 (2024).
2. P. Garg, T.J. Rupert. *Local structural ordering determines the mechanical damage tolerance of amorphous grain boundary complexions*, Scripta Materialia, **237**, 115712 (2023).
3. T. Lei, E.C. Hessong, D.S. Gianola, T.J. Rupert. *Binary nanocrystalline alloys with high glass forming ability of the interfacial region: Complexion stability, segregation competition, and diffusion pathways*, Materials Characterization, 206, 113415 (2023).
4. P. Garg, T.J. Rupert. *Grain incompatibility determines the local structure of amorphous grain boundary complexions*, Acta Materialia, 244, 118599 (2023).

UNDER REVIEW:

1. E.C. Hessong, T. Lei, M. Xu, T. Aoki, T.J. Rupert. *Chemical partitioning within multi-component amorphous interfacial complexions*, Submitted.

Segregation and Shear Localization in Nanocrystalline Alloys

Frederic Sansoz

Department of Mechanical Engineering, The University of Vermont, Burlington VT (USA)

Keywords: Nanocrystalline alloys, heterogeneous GB segregation, GB strengthening.

Research Scope

Solute segregation to grain boundaries (GBs) plays a crucial role in shaping the mechanical properties and thermal stability of nanocrystalline (NC) alloys. While stabilizing nanoscale interfaces can harden metals through extreme grain refinement, GB segregation is also associated with a well-known ductile-to-brittle transition, driven by two dominant concentration-dependent deformation mechanisms: GB embrittlement, which accelerates intergranular cracking, and glass-like shear localization, which leads to catastrophic softening. This research aims to deploy advanced atomistic simulations and micromechanical tensile experiments to gain a fundamental understanding of how GB solute segregation influences both GB strengthening and shear localization in NC alloys. The focus is on binary Ag alloys containing either Cu or Ni solutes, which exhibit a range of segregation mechanisms. These alloys are of particular interest due to their inherently heterogeneous GB segregation behavior, characterized by the formation of solute atom clusters or uneven solute distribution across the GB network. Some GB regions are rich in solute, while others remain solute-free. The ultimate goal is to advance the design of NC alloys by developing new strain de-localization mechanisms, induced by heterogeneous segregation, that could potentially suppress GB segregation embrittlement.

Recent Progress

Experimental study of three regimes of concentration-dependent tensile strength in sputtered NC Ag-Cu alloys:

In the past two years, a significant focus of our program was placed on conducting micromechanical tensile experiments on NC Ag-Cu alloys, produced by magnetron sputtering with varying Cu concentrations, to identify three distinct tensile strength regimes: (1) classical segregation hardening at low Cu concentrations (up to 3.5 at.%), (2) strength softening at high Cu concentrations (above 8.5 at.%), and (3) a regime of maximum strength at intermediate Cu concentrations, termed NC sterling Ag alloys, which was demonstrated experimentally for the first time in this study and confirmed the findings of our previous atomistic simulation studies [1].

The ultimate tensile strength of NC sterling Ag metals was 604 MPa, which is 44% higher than that of standard rolled sterling Ag foils (420 MPa). The key experimental findings of this study are summarized in Figure 1: A concentration-dependent plateau in maximum strength divides the tensile behavior into three distinct regimes, with direct evidence of heterogeneous Cu solute segregation across the GB network, particularly at intermediate Cu concentrations from 3.5 to 8.5 at.%. This heterogeneous segregation involves the formation of Cu-Ag alloy clusters at GB junctions and an uneven distribution of Cu solute atoms across different interfaces. We did not attribute the strength plateau to solute clustering at GB junctions, as these clusters were observed at all concentrations, even below 3.5 at.%. Instead, we propose that partially active GB segregation mechanisms, caused by the uneven distribution of Cu solute, may explain the three tensile strength regimes in NC alloys, in contrast to the two regimes with homogeneous segregation.

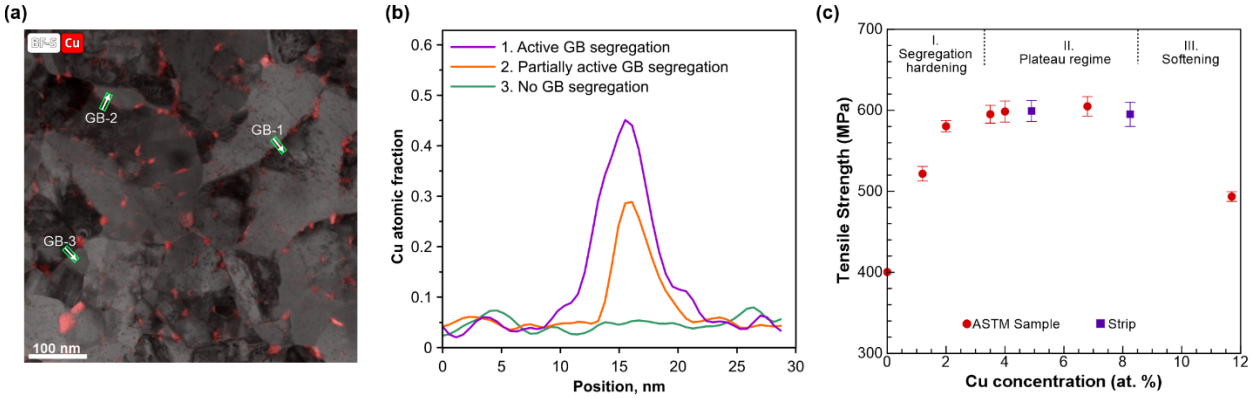

Figure 1. STEM analysis and micromechanical tensile experiments on sputtered NC Ag-Cu alloys with varying Cu concentrations, exhibiting a maximum strength plateau at intermediate solute concentrations and dividing the strength into three distinctive regimes. (a) Inhomogeneous solute segregation at GBs in NC Ag-4.9at% Cu obtained by mixed bright field (BF-S) STEM and EDX imaging with the selection of three individual GBs and **(b)** their concentration line profiles. **(c)** Effect of Cu concentration on tensile strength of sputtered NC Ag-Cu alloy ASTM dog-bone and strip specimens.

Based on our STEM analysis, a mechanistic model was developed to explain the three concentration-dependent strength regimes in NC alloys (Figure 2), incorporating partially active and heterogeneous solute segregation to GBs. With homogeneous segregation, the mechanical behavior shifts from dilute GB solute strengthening (Regime I), driven by reduced GB free volume, to strain-localization softening (Regime III), when all GB sites are occupied by solute atoms. However, in Regime II (2–8.5 at.% Cu), Cu atoms are forced into less favorable sites due to solute attraction, forming solute clusters and uneven solute distribution. This heterogeneous GB segregation influences tensile properties, as high-solute regions block GB plasticity, while lower-concentration regions remain active, leading to local stress concentrations that emit lattice dislocations [1]. It can be shown that the critical stress intensity to emit those dislocations is independent of solute concentration [2], which validates the existence of a strength plateau over extended concentrations.

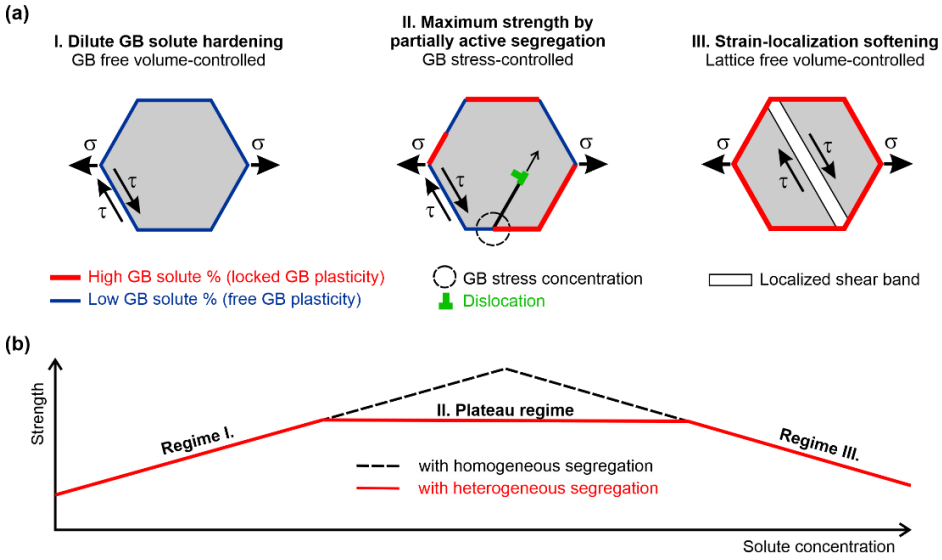

Figure 2. Mechanistic interpretation of three strength regimes in NC alloys with heterogeneous GB solute segregation. (a) Proposed plastic deformation mechanism transitions from low to intermediate and high solute concentrations. **(b)** Effect of partially active segregation (heterogeneous segregation) on tensile strength, in contrast to the two regimes with homogeneous segregation.

Theoretical study of the interplay of GB junction and long-range solute attraction effects on GB solute clustering in polycrystals

Spectral analysis of local atomic environments has become a valuable tool for studying the segregation and interaction of dilute solute atoms at GBs in NC alloys [3-5]. When applied to single ordinary GBs, our spectral analysis has revealed that solute interaction effects can be either attractive or repulsive, with long-range attractive effects increasing the tendency for solute cluster nucleation [6], as shown in Figure 3(a).

Recently, we combined this type of analysis with a new GB structure descriptor based on GB atom coordination, to investigate the influence of GB junctions on solute atom segregation in polycrystals. Specifically, we systematically characterized the tendency for solute cluster nucleation at different types of ordinary grain boundaries, triple junctions, and high-order junctions in Ag polycrystals containing either Ni or Cu solute atoms, as shown in Figure 3(b).

Our findings revealed that a strong interplay between high-order GB junctions and long-range solute attraction effects governs GB solute cluster nucleation, as shown in Figure 3(c). This finding highlights the multiscale nature of solute segregation at crystalline interfaces and provides deeper insights into the complex phenomena of heterogeneous solute segregation and short-range order in polycrystalline alloys.

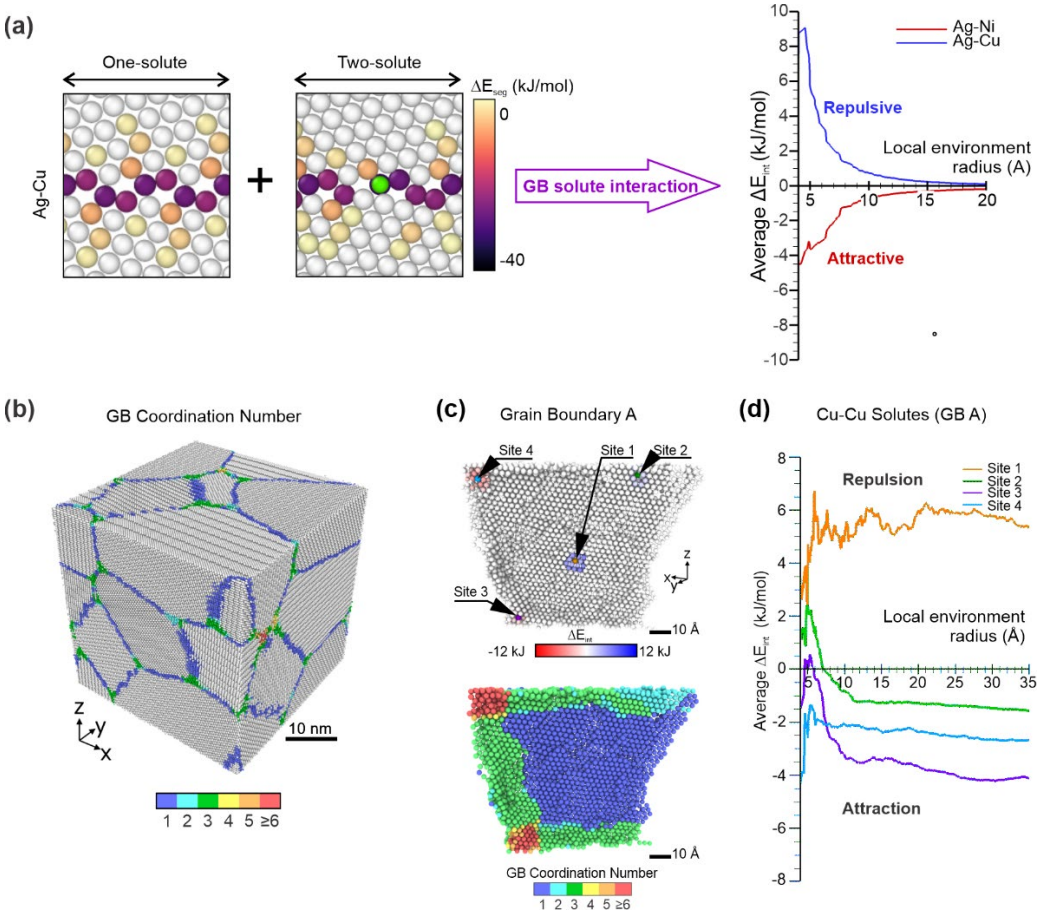

Figure 3. Local atom environment analysis of short-range and long-range dilute solute interactions at GBs in a symmetric bicrystal and a random polycrystal. (a) Simple ordinary GB interface predicting either solute attraction (Ni solute) or solute repulsion (Cu solute) in a Σ9(221) bicrystal. **(b)** GB atom coordination number algorithm applied to an Ag-Cu polycrystal. **(c)-(d)** The interplay of GB junction and long-range solute attraction effects shown in in a GB of this polycrystal.

Future Plans

For the next phase of this program, the primary plan is three-fold:

(1) to extend the local atom environment analysis to study how solute cluster size influence long-range solute attraction effects at GBs in polycrystals.

(2) to study the effects of solute concentration on microstructure and tensile mechanical behavior of sputtered deposited Ag-Ni alloys, because Ni-Ni solute interactions are strong. This research necessitates extensive STEM analysis of solute clustering mechanisms.

(3) to train more accurate physics-based machine-learning embedded-atom-method (ML-EAM) interatomic potentials to study GB segregation and solute clustering in Ag-Cu alloys by atomistic simulations. Particularly, our goal is to elucidate how solute clustering at GB junctions was observed in our experiments, despite weak attractions between Cu solute atoms predicted in previous atomistic simulations.

References

1. F. Sansoz and X. Ke. *Hall-Petch Strengthening Limit through Partially Active Segregation in Nanocrystalline Ag-Cu Alloys*. Acta Materialia, 225, 117560 (2022)
2. R.J. Asaro, S. Suresh, *Mechanistic models for the activation volume and rate sensitivity in metals with nanocrystalline grains and nano-scale twins*, Acta Materialia 53(12) (2005) 3369-3382.
3. M. Wagih, C.A. *Schuh, Spectrum of grain boundary segregation energies in a polycrystal*, Acta Materialia 181 (2019) 228-237.
4. M. Wagih, P.M. Larsen, C.A. Schuh, *Learning grain boundary segregation energy spectra in polycrystals*, Nature Communications 11(1) (2020).
5. M. Wagih, C.A. Schuh, *Grain boundary segregation beyond the dilute limit: Separating the two contributions of site spectrality and solute interactions*, Acta Materialia 199 (2020) 63-72.
6. T. Nenninger and F. Sansoz. *Local atomic environment analysis of short and long-range solute-solute interactions in a symmetric tilt grain boundary*. Scripta Materialia, 222, 115045 (2023)

Recent Publications

1. P. Nikitin, M. Guinel de France and F. Sansoz. *Maximizing Tensile Strength by Partially Active Solute Segregation to Grain Boundaries in Nanocrystalline Ag-Cu Alloys*. Under review.
2. F. Sansoz, M. R. Pringle, J. Oh, L. Zhou, R. T. Ott, Y. Liu, G. Zhu, C. Deng. *Short-Range Order Enhances Strength and Tensile Ductility in Nanocrystalline Silver with Intercalation of Amorphous Nickel Nanolayers*. Under review.

3. L. Capaldi and F. Sansoz. *High-temperature Active Oxidation of Nanocrystalline Silicon-Carbide: A Reactive Force-Field Molecular Dynamics Study*. Acta Materialia, 258, 119229 (2023).
4. T. Nenninger and F. Sansoz. *Local atomic environment analysis of short and long-range solute-solute interactions in a symmetric tilt grain boundary*. Scripta Materialia, 222, 115045 (2023)
5. E. A. Picard and F. Sansoz. *Ni Solute Segregation and Associated Plastic Deformation Mechanisms into Random FCC Ag, BCC Nb and HCP Zr Polycrystals*. Acta Materialia, 240, 118367 (2022)
6. F. Sansoz and X. Ke. *Hall-Petch Strengthening Limit through Partially Active Segregation in Nanocrystalline Ag-Cu Alloys*. Acta Materialia, 225, 117560 (2022)

Crack-Tip Mechanisms Driving Environmental Degradation

D.K. Schreiber, A. Devaraj, K. Kruska, K.M. Rosso, M.L. Sushko, C. Wang

Pacific Northwest National Laboratory

Keywords: corrosion, fracture, diffusion, grain boundaries, microscopy

Research Scope

Environmental degradation and associated stress corrosion cracking (SCC) are persistent materials science challenges that affect energy systems that operate in high-temperature, hostile environments. Recent research has revealed many processes that underpin material degradation, including elemental selectivity for reactions, interface-dominated transport kinetics, and vacancy-driven acceleration of mass transport. Despite these advances, a comprehensive understanding of the atomic-scale crack-tip mechanisms that underpin environmental degradation remains elusive. For example, contradictory behaviors have been observed for degradation in gaseous and aqueous environments under nominally identical oxidizing potentials, and SCC responses can diverge significantly from the kinetics of visible degradation processes. It is, therefore, the long-term vision of this program to both elucidate the mechanistic processes occurring at the atomic scale and build definitive connections to meso-to-macroscale cracking of materials under high-temperature, corrosive conditions. In this program we focus on the roles of different corrosive media under similar electrochemical potentials, evolving alloy microstructures, and targeted alloy additions to affect these behaviors. To do so, we integrate a suite of in situ and ex situ microscopy techniques, multiscale mechanistic modeling, and macroscale mechanical testing under controlled environments to produce a comprehensive picture of the roles that environment, hydrogen insertion, applied stress, alloying additions, surfaces, interfaces, and microstructural defects have in the resulting behaviors. In doing we seek to advance our fundamental understanding of the atomic scale crack tip processes driving micro-to-macroscale environmental degradation and SCC.

Recent Progress

Our research is motivated, in part, by a consistent observation that SCC in high-temperature environments (~200–600 °C) is driven by selective oxidation of more reactive alloying elements (e.g., Cr over Ni), especially along alloy grain boundaries (GBs). To understand this oxidation and subsequent alloy embrittlement process, we must also understand how mass transport and reactions proceed at the atomic level. Advanced characterization methods, including operando transmission electron microscopy (TEM) and isotope-sensitive atom probe tomography (APT), in combination with atomistic simulations (molecular dynamics [MD] and density functional theory [DFT]), have been employed to probe these local processes and reveal new insights on alloy degradation in a variety of model alloy systems and corrosive environments that can then be compared with realistic macroscale SCC testing behaviors.

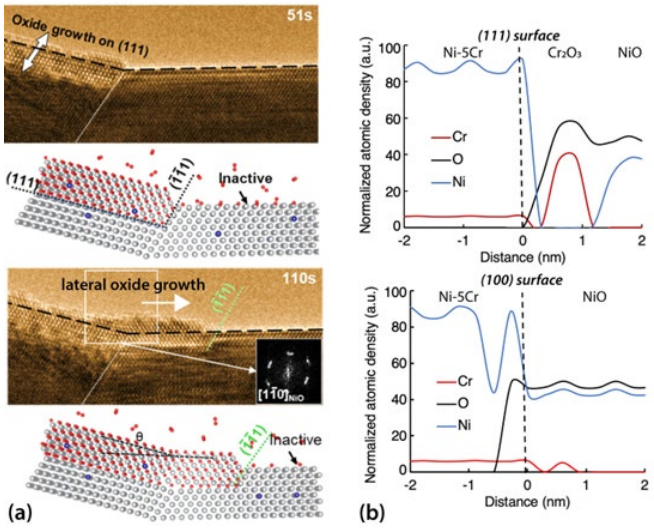

Fig. 1: Operando TEM and modeling reveal crystallographic differences in early-stage oxidation on Ni-Cr surfaces. (a) Operando TEM reveals that surprisingly faster initial oxidation on the (111) vs. (100) surfaces of Ni-5Cr transitions into lateral fast-oxide growth over the adjacent grain. (b) cDFT simulations show that faster Cr diffusion facilitates these kinetic differences. [1]

In a recent study [1] operando TEM oxidation of Ni-5Cr was used to understand how crystallographic differences alter initial and long-term oxidation kinetics. As shown in Fig. 1, a bare Ni-5Cr alloy surface was exposed to a low pO_2 atmosphere (1×10^{-4} mbar, 350 °C) and the evolving surface oxidation was monitored at the atomic level in real time in a dedicated environmental TEM (ETEM). Strong differences were observed in the initial oxide formation on the (111) and (001) alloy surfaces (Fig. 1a). The (111) surface exhibited rapid initial oxide formation within 51 s, while the (001) surface showed no apparent oxide formation. As oxidation extended to 110 s in the second image, the oxide on the (111) surface grew laterally into and over the adjacent (100) surface. This observation is intriguing because an opposite crystallographic dependence is expected during long-term oxidation behavior and confirmed by operando ETEM at longer oxidation times (not shown). To understand this incipient response, complementary DFT and classical DFT (cDFT) simulations (Fig. 1b) were performed of the interfacial transport between the (111) metal/oxide and (100) metal/oxide interfaces. These simulations showed that the (111) metal/oxide interface had more facile Cr diffusion, enabling rapid formation of an initial Cr-rich oxide, while Cr diffusion was more difficult across the (100) oxide/metal interface. Together these results showed that the initial surface oxidation (i.e., Cr-rich oxides) favors the (111) surface that inhibits thick oxide growth, while long-term oxidation (NiO dominant) eventually favors the (100) surface. Further studies are needed to fully understand when and how these transition points occur, especially with varying alloy content and environmental conditions.

Isotopic tracers in concert with 3D APT have also been used recently to show that oxide/metal interfaces are the dominant diffusion pathway through and around both surface and intergranular oxides to enable further metal corrosion (Fig. 2). [2] Using isotopic tracers in two-stage oxidation experiments wherein the oxidizing environment changes from initially natural abundance (~99.8% ^{16}O) to an isotopically altered (~95%+ ^{18}O) environment in a second stage, it is possible to discriminate the initial oxide formation (^{16}O) from subsequent oxidation (^{18}O). Thus, the ^{18}O

isotopic distribution can document active diffusion pathways and reaction sites using 3D APT in model Ni-Cr alloys. In the example highlighted in Fig. 2, a Ni-20Cr alloy was exposed to a controlled gas mixture of CO/CO_2 at 600 °C with a low pO2 to enable selective oxidation of Cr, similar to the hydrogenated water conditions used in our previous SCC testing of similar alloys. [3] Representative APT measurements show that ^{18}O penetrated deep into the alloy GB along the metal/oxide interface with very little isotopic intermixing. The absence of ^{18}O decoration along oxide/oxide GBs, which would be readily apparent by the 3D nature of the APT reconstruction, also proves that the oxide/metal interface itself is the primary short-circuit diffusion pathway enabling ongoing penetrative oxidation. This observation makes clear that mitigation of further oxidation should seek to inhibit mass transport along the alloy / oxide interface and that diffusion along oxide GBs is relatively unimportant.

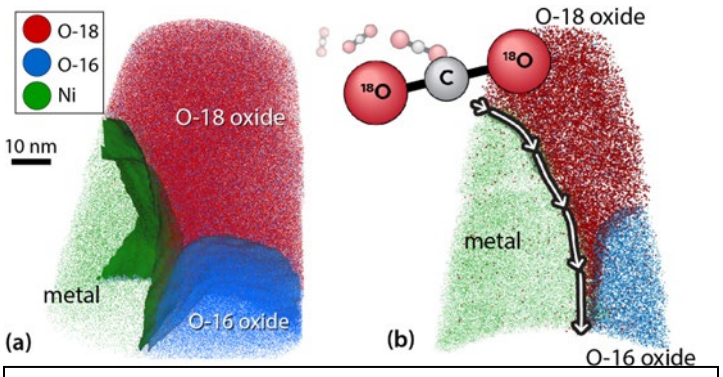

Fig. 2: Two-stage $^{16}O/^{18}O$ oxidation reveals nanoscale GB oxidation and diffusion pathways. (a) Isotope-sensitive 3D APT analysis identifies GB oxides formed during the ^{16}O (stage 1) and ^{18}O (stage 2) phases. (b) A 10 nm cross-section view of the oxide/metal interface reveals that ^{18}O diffuses along the ^{16}O-oxide/metal interface to form new oxides. [2]

As selective oxidation of Cr proceeds in Ni-Cr alloys such as those highlighted in Fig. 2, we oftentimes observe rapid diffusion and migration of the alloy GB, leading to severe local Cr depletion in the underlying metal. To understand these behaviors and complement our experimental efforts, we have also developed atomistic simulations of bulk and GB diffusion behavior. Most recently we considered bulk and GB diffusion in a Ni-Cr alloy under premelt conditions (~0.9 TM), as highlighted in Fig. 3. [4] Diffusion at low-energy GBs was very similar to bulk diffusion across the system, with Cr exhibiting faster diffusion than Ni. Diffusion at high-energy GBs revealed surprising differences, with Ni exhibiting liquid-like diffusion four orders of magnitude faster than in the bulk, and also diffusing faster than Cr. Chromium GB diffusion was limited by its tendency to cluster along the GB, as depicted in Fig 3. As the GB migrated, Cr from the matrix coalesced into trapped GB clusters. The reversal of the faster-

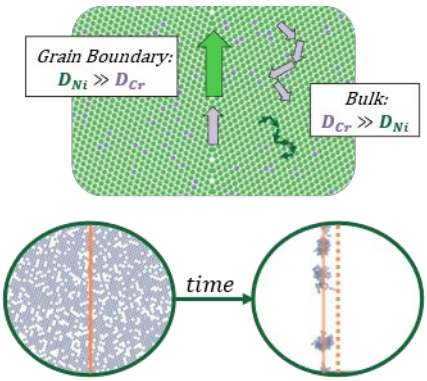

Fig. 3: [top] Molecular dynamics (MD) simulations compare the movement of Ni (green arrows) and Cr atoms (purple arrows) at a GB and through the bulk. Both are faster at the GB, but Cr is faster than Ni in the bulk, while Ni is much faster than Cr at the GB. [bottom] Cr atoms cluster at the GB, slowing their mobility relative to Ni at the GB. [4]

diffusing species at the high-energy GB versus the matrix could explain why, even in the case of severe Cr depletion, we experimentally do not see evidence for excess Cr vacancies leading to void formation along corroding alloy GBs. Put another way, these data suggest that Ni and Cr diffusion may be more comparable than expected from previous DFT calculations due to a combination of faster-than-expected Ni diffusion and possible formation of Cr clusters. Going forward, we look to extend these simulations to lower temperatures and applying other external stimuli, including uniaxial stresses and/or vacancy sources, to more accurately represent realistic SCC conditions.

Future Plans

Looking forward, we will continue to develop and employ novel in situ and operando experimental methods to reveal the atomistic details of material degradation with newfound fidelity. Cryogenic APT, newly developed on a complementary early career research program [5], will be used to map H distributions around alloy GBs with particular attention to the possible local trapping of H to dealloyed zones or dislocations ahead of propagating crack tips. This will be combined with in situ mechanical testing to understand how local H distributions directly impact alloy deformation and subsequent SCC behavior. In a second research direction and building upon the isotopic tracer APT experiments in Fig. 2, we will seek to reveal how dilute alloying with reactive elements (e.g., Y) alters both ongoing alloy corrosion and specifically isotopic diffusion along previously identified short-circuit diffusion pathways, especially oxide/metal interfaces. In both of these exemplar experiments, we will synergistically pursue complementary multiscale modeling of controlling processes ranging from the atomistic-to-mesoscale in tandem with macroscale SCC of similar alloys and environmental conditions to build connections between atomistic degradation phenomena and macroscale SCC behaviors.

References

1. S. Li, L. Yang, J. Christudasjustus, N.R. Overman, B.D. Wirth, M.L. Sushko, P. Simonnin, D.K. Schreiber, F. Gao, and C. Wang, *Selective atomic sieving across metal/oxide interface for super-oxidation resistance*, Nature Communications **15**, 6149 (2024).
2. M. Weiser, M.J. Olszta, M.H. Engelhard, Z. Zhu, and D.K. Schreiber, *Visualizing oxygen transport pathways during intergranular oxidation in Ni-Cr*, npj Materials Degradation **7**, 70 (2023).
3. S.M. Bruemmer, M.J. Olszta, M.B. Toloczko, and D.K. Schreiber, *Grain boundary selective oxidation and intergranular stress corrosion crack growth of high-purity nickel binary alloys in high-temperature hydrogenated water*, Corrosion Science **131**, 310 (2018).
4. P. Simonnin, D.K. Schreiber, B.P. Uberuaga, and K.M. Rosso, *Atomic diffusion, segregation, and grain boundary migration in nickel-based alloys from molecular dynamics simulations*, Materials Today Communications **35**, 105768 (2023).
5. D.J. Barton, D.T. Nguyen, D.E. Perea, K.A. Stoerzinger, R.M. Lumagui, S.V. Lambeets, M.G. Wirth, and A. Devaraj, *Towards quantitative analysis of deuterium absorption in ferrite and austenite during electrochemical charging by comparing cyclic voltammetry and cryogenic transfer atom probe tomography,* International Journal of Hydrogen Energy **50**, 30 (2024).

Publications (2023-2024)

1. M. J. Olszta and K. R. Fiedler, *Nanocartography: Planning for success in analytical electron microscopy*, Elemental Microscopy, https://doi.org/10.69761/DNKA1581 (2024).

2. S. Li, L. Yang, J. Christudasjustus, N.R. Overman, B.D. Wirth, M.L. Sushko, P. Simonnin, D.K. Schreiber, F. Gao, and C. Wang, *Selective atomic sieving across metal/oxide interface for super-oxidation resistance,* Nature Communications **15**, 6149 (2024).

3. K. Kruska, M.J. Olszta, J. Wang, and D.K. Schreiber, *Intergranular corrosion of Ni-30Cr in high-temperature hydrogenated water after removing surface passivating film*, npj Materials Degradation **8**, 25 (2024).

4. S.-H. Kim, S. Bhatt, D.K. Schreiber, J. Neugebauer, C. Freysoldt, B. Gault, and S. Katnagallu, *Understanding atom probe's analytical performance for iron oxides using correlation histograms and ab initio calculations*, New Journal of Physics **26**, 033021 (2024).

5. G. Zhou, K.A. Unocic, C. Wang, Z. Shan, S.J. Haigh, and J.C. Yang, *Revealing atomic-to-nanoscale oxidation mechanisms of metallic materials,* MRS Bulletin **48**, 852 (2023).

6. Y. Yang, W. Zhou, S. Yin, S.Y. Wang, Q. Yu, M.J. Olszta, Y.-Q. Zhang, S.E. Zeltmann, M. Li, M. Jin, D.K. Schreiber, J. Ciston, M.C. Scott, J.R. Scully, R.O. Ritchie, M. Asta, J. Li, M.P. Short, and A.M. Minor, *One dimensional wormhole corrosion in metals*, Nature Communications **14**, 988 (2023).

7. M. Weiser, M.J. Olszta, M.H. Engelhard, Z. Zhu, and D.K. Schreiber, *Visualizing oxygen transport pathways during intergranular oxidation in Ni-Cr*, npj Materials Degradation **7**, 70 (2023).

8. S.D. Taylor, K.H. Yano, M. Sassi, B.E. Matthews, E.J. Kautz, S.V. Lambeets, S. Neuman, D.K. Schreiber, L. Wang, Y. Du, and S.R. Spurgeon, *Resolving diverse oxygen transport pathways across Sr-doped lanthanum ferrite and metal-perovskite heterostructures*, Advanced Materials Interfaces **10**, 2202276 (2023).

9. P. Simonnin, D.K. Schreiber, B.P. Uberuaga, and K.M. Rosso, *Atomic diffusion, segregation, and grain boundary migration in nickel-based alloys from molecular dynamics simulations*, Materials Today Communications **35**, 105768 (2023).

10. A.Y. Gerard, E.J. Kautz, D.K. Schreiber, J. Han, S. McDonnell, K. Ogle, P. Lu, J.E. Saal, G.S. Frankel, and J.R. Scully, *The role of chromium content in aqueous passivation of a non-equiatomic* $Ni_{38}Fe_{20}Cr_xMn_{21-0.5x}Co_{21-0.5x}$ *multi-principal element alloy (x = 22, 14, 10, 6 at%) in acidic chloride solution*, Acta Materialia **245**, 118607 (2023).

Towards High-Throughput Computation of Phase-and-Defect Diagrams

Christopher A. Schuh
Department of Materials Science and Engineering, Northwestern University, 2145 Sheridan Road, Evanston, IL 60208, USA
Department of Materials Science and Engineering, Massachusetts Institute of Technology, 77 Massachusetts Avenue, Cambridge, MA, 02139, USA

Keywords: Thermodynamics, Defects, Grain Boundary, Segregation, Atomistic Simulation

Research Scope

Spectral information, which captures the full distribution of local atomic environments in the grain boundary (GB) network, has been shown in recent years to be necessary to accurately capture the energetics of GB segregation in polycrystals. Furthermore, a recent push has been made towards constructing "phase-and-defect" diagrams, which seek to place defects on an equal thermodynamic footing with bulk thermodynamic phases, with the goal of mapping equilibrium defect concentrations, compositions, and structures onto the existing phase diagrams of alloys. An example of this is shown in Fig. 1, from our work developing an analytical expression for the free energy of segregated polycrystals using a spectral regular solution model.

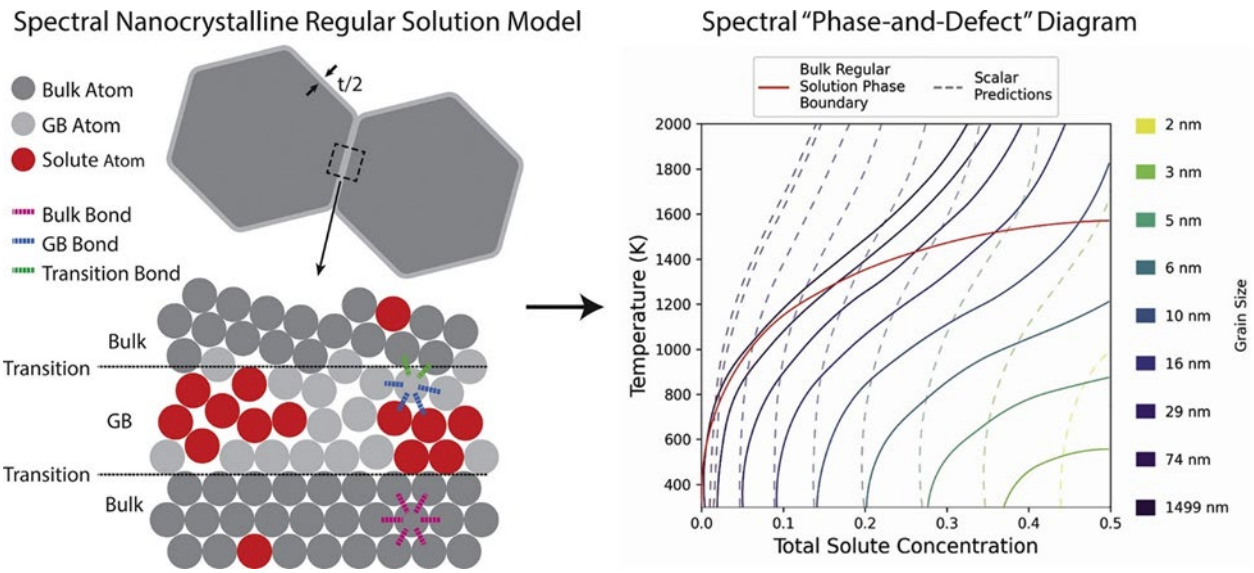

Figure 1. The spectral nanocrystalline regular solution model illustrated in (a) can be used to calculate (b) solubility limit at various grain sizes which is influenced by the bulk solute depletion due to grain boundary segregation.

However, until the work of this project, there has been a complete lack of the spectral data that is required to populate phase-and-defect diagrams in practice, due to excessive computational cost. Our recent DOE-funded work [1-3] has addressed this lack of polycrystalline GB data by cataloging the many components of the spectral free energy of segregation - spectral segregation enthalpies, solute-solute interactions, and excess vibrational entropies, using a combination of atomistic simulation and accelerated learning frameworks, summarized in Table 1. These spectral

databases include results from hundreds of available interatomic potentials spanning 80-250 unique binary alloys. Furthermore, using hybrid quantum mechanics/molecular mechanics calculations, we have started populating an atlas of spectra with ab-initio accuracy, for Al and V as the base solvent to date.

Table 1. Summary of available methods and databases of spectral segregation parameters.

	Segregation Enthalpy	Solute Interactions	Excess Entropy
Interatomic Potentials	~ 430 NIST interatomic potentials	~200 NIST EAM potentials	~150 NIST EAM potentials
Ab-Initio Accuracy	~50 Al-base and 50 V-base alloys	In progress	N/A

These databases allow us to populate the thermodynamic models required to construct phase-and-defect diagrams, but experimental validation of the spectral model remains sparse. Some of our recent works, focused on Al(Au), Fe(P), and Pd(H), have attempted to experimentally capture spectral behavior and directly establish the need for spectral modeling. As a result, the need to refine and extend spectral databases to full ab-initio accuracy, as well as encompass more complex behaviors, such as interstitial alloys and triple-junction effects, has become increasingly apparent. Here, we recap these recent experimental studies, and how they reflect on our computational efforts to accurately catalog the spectral energetics of the full range of alloy systems.

Recent Progress

Our recent efforts allow for a more rigorous mapping between the defect chemistry predicted from modeling and that observed in experiments. Starting with Fig. 2a, we conducted an evaluation of the Al(Au) binary system, a carefully choses system in which the classical approach to grain boundary segregation, using a Miedema-based model suggests no preference for segregation. However, when a spectral model is employed there is in fact a portion of the site spectrum at grain boundaries that favors segregation. This is thus a very clear-cut test of the spectral model, because it predicts the opposite of the classical one (segregating vs. non-segregating). Our experiments convincingly validate the quantum-accurate spectral model in this case.

Moreover, our quantitative frameworks enable us to calculate spectral parameters from previously reported experimental solute content. From those experiments, a spectrum of segregation energies

is implied and can be quantitatively estimated. We have shown specific case studies on Pd(H) [4] in Fig. 2b where the atomistic model identifies multiple interstitial site types in GBs which suggests a bimodal distribution as a priori distribution shape. This model, while not a perfect match to the experimentally-extracted single-mode distribution, provides an excellent qualitative match that again validates the spectral approach generally.

Lastly, we demonstrate a case study of Fe(P) [5] in Fig. 2c on interpreting experimental characterized solute concentrations spectrally to improve interpolation and extrapolation, which is extremely limited in the classical McLean model. This analysis shows that while many models can be fitted to experimental data, the use of a full spectral model is needed to achieve the right order of magnitude of the thermodynamic parameters (segregation energy, entropy, interactions, and their interrelationships).

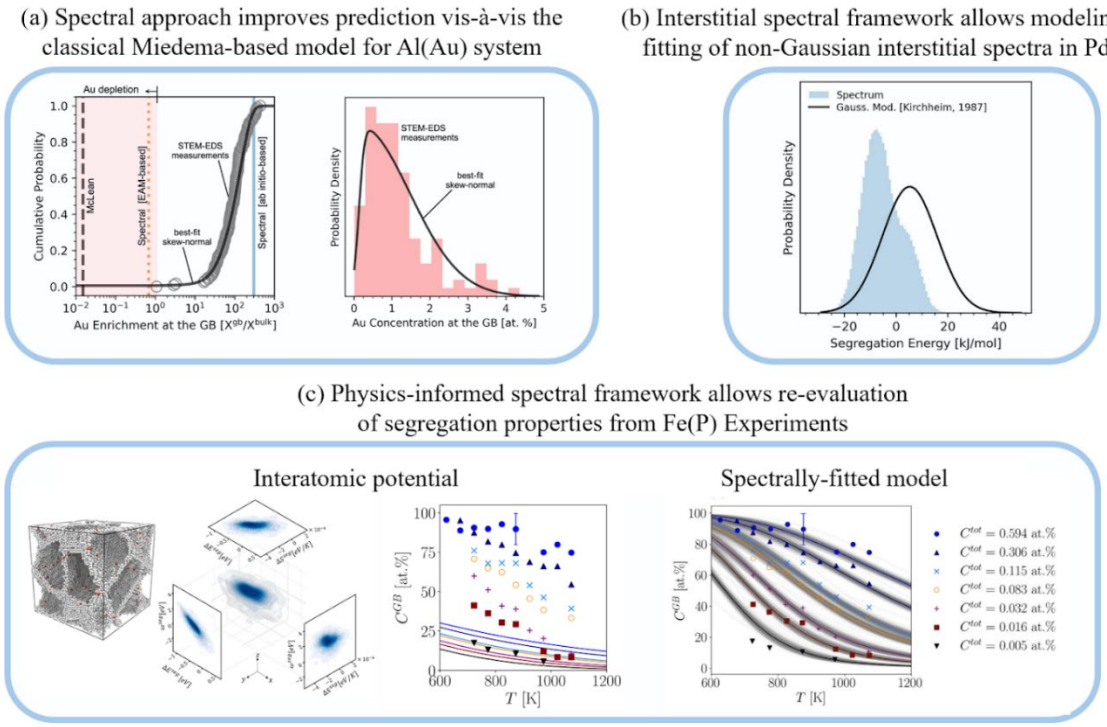

Figure 2 Our recent effort in applying GB spectral models to better understand and quantify GB properties from experiments. In (a), we show that Al(Au) predicted to be non-segregating with the classical model is in fact segregating the system from the ab-initio spectral model. The development of the interstitial spectral model also allows us to identify and fit bivariate Gaussian-like solute energy distribution in Pd(H) systems [4]. Lastly, with the multiphysics framework consisting of dilute segregation energy, solute-solute interactions and excess vibrational entropies, we can re-assess reported experimental results which are traditionally fitted to a single site or McLean model such as the case of Fe(P) shown in (c) [5].

Future Plans

We aim to close the gap between modeling and experiments by developing a full physics spectral model for free energies of grain boundary defects. Our work in the coming year involves tasks on both the modeling and experimental sides. First, we are developing models that relax the random

mixing assumption (which hinders correct evaluation of system configurational entropies that are critical to quantify equilibrium GB states). While Quasichemical models or cluster variational approaches can attempt to capture these states, they are not trivial for arbitrary cluster types in spectral GBs. We have begun tackling this aspect of grain boundary segregation by introducing a lattice-based Monte Carlo method to demonstrate physical short-range ordering that shows a more complex distribution of solute compared to full phase-separation. We are also working to include excess vibrational entropy in solute-solute interactions and interstitial problems which will help address the multiphysics problems in GB segregation as well. Second, on the experimental side, we are beginning to design experiments that test some of the new predictions of the spectral model. This includes ternary alloying effects where solutes compete or cooperate to occupy grain boundary sites, and systems in which segregation entropy is so dominant that unexpected GB occupation states can be achieved.

References

1. M. Wagih, C.A. Schuh, *Learning Grain-Boundary Segregation: From First Principles to Polycrystals*, Physical Review Letter **129**, 046102 (2022).
2. T.P. Matson, C.A. Schuh, *A "bond-focused" local atomic environment representation for a high throughput solute interaction spectrum analysis*, Acta Materialia **278**, 120275 (2024).
3. N. Tuchinda, C.A. Schuh, *Computed entropy spectra for grain boundary segregation in polycrystals*, Npj Computational Materials **10**, 72 (2024).
4. T. Mütschele, R. Kirchheim, *Segregation and diffusion of hydrogen in grain boundaries of palladium*, Scripta Metallurgica. **21**, 135–140 (1987).
5. H. Erhart, H.J. Grabke, *Equilibrium segregation of phosphorus at grain boundaries of Fe–P, Fe–C–P, Fe–Cr–P, and Fe–Cr–C–P alloys*, Metal Science **15**, 401–408 (1981).

Publications

1. N. Tuchinda, C.A. Schuh, *The vibrational entropy spectra of grain boundary segregation in polycrystals*, Acta Materialia **245**, 118630 (2023).
2. M. Wagih, C.A. Schuh, *The spectrum of interstitial solute energies in polycrystals*, Scripta Materialia **235**, 115631 (2023).
3. N. Tuchinda, C.A. Schuh, *Triple junction solute segregation in Al-based polycrystals*, Physical Review Material **7**, 023601 (2023).
4. M. Wagih, C.A. Schuh, *Viewpoint: can symmetric tilt grain boundaries represent polycrystals?*, Scripta Materialia **237**, 115716 (2023).
5. T.P. Matson, C.A. Schuh, *Phase and defect diagrams based on spectral grain boundary segregation: A regular solution approach*, Acta Materialia **265**, 119584 (2024).
6. N. Tuchinda, C.A. Schuh, *Computed entropy spectra for grain boundary segregation in polycrystals*, Npj Computational Materials **10**, 72 (2024).
7. T.P. Matson, C.A. Schuh, *A "bond-focused" local atomic environment representation for a high throughput solute interaction spectrum analysis*, Acta Materialia **278**, 120275 (2024).
8. A. Reichmann, N. Tuchinda, C. Dösinger, D. Scheiber, V. Razumovskiy, O. Peil, T.P. Matson, C.A. Schuh, L. Romaner, *Grain boundary segregation for the Fe-P system: Insights from atomistic modeling and Bayesian inference*, Acta Materialia **279**, 120215 (2024).
9. N. Tuchinda, C.A. Schuh, *Triple Junction Excess Energy in Polycrystalline Metals*, Acta Materialia **279**, (2024) 120274.

Microparticle Impacts for Extreme Mechanics

Christopher A. Schuh

Department of Materials Science and Engineering, Northwestern University, 2145 Sheridan Road, Evanston, IL 60208, USA

Department of Materials Science and Engineering, Massachusetts Institute of Technology, 77 Massachusetts Avenue, Cambridge, MA, 02139, USA

Keywords: Strength, Hardness, High Strain Rates, Impact, Deformation Mechanisms

Research Scope

Over the past few years, the laser-induced particle impact test (LIPIT) has emerged as a new quantitative tool for extreme-conditions materials mechanics. The principle of the approach is shown in Fig. 1a, where a short green laser burst is used to ablate a target, and that ablation in turn is used to launch a particle (typically 5-50 μm) at high velocities. Depending on the power of the laser and the properties of the particle, the velocities attained can be as low as ~10 m/s and as high as ~1500 m/s. Importantly, the LIPIT also involves a second laser used for imaging of the particle in flight and during its collision with a substrate target.

In most conventional high rate experiments, the pressures are very high (Fig. 1c), and the resulting hydrodynamic condition is one where solids flow like fluids. However, in contrast, LIPIT accesses

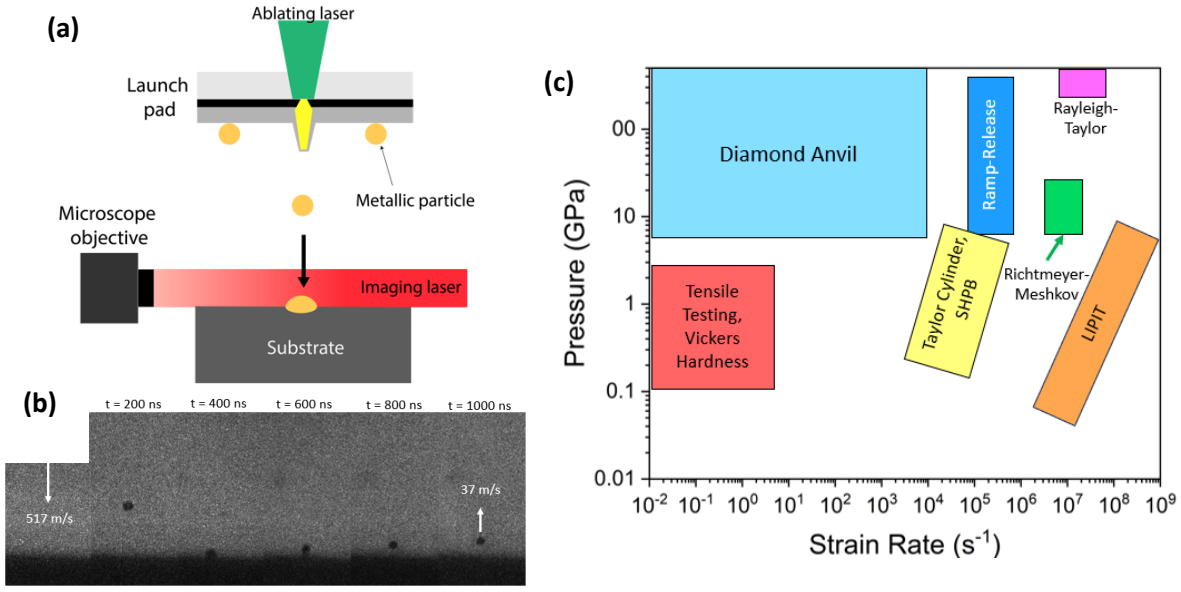

Fig. 1(a) The laser-induced particle impact test (LIPIT) is shown schematically. (b) The particle flight, impact and rebound are captured in-situ on camera, in this example for 14 μm alumina particles striking copper. (c) The combination of high velocity and small particle size leads to a unique mechanical test at high strain rates but rather low pressures.

extreme strain rates at pressures far lower than other test methods. Put another way, LIPIT is free of shock effects and yet achieves the highest possible strain rates. The reason that low pressures are important is that this is the range where materials considerations matter: microstructure controls strength and deformation, and thus the true strain-rate dependent materials properties can be accessed without being overpowered by hydrodynamic effects. Before LIPIT, essentially all measurements of materials properties at these strain rates involved conflation with shock physics. LIPIT measurements offer a unique "clean" view on the role of material structure on properties at strain rates over 10^5 s^{-1}. This motivates many materials science questions that have remained open until now, and which drive our current research.

Recent Progress

One high strain-rate materials response that has been expected for many decades is the onset of ballistic dislocation transport, where phonon drag is rate limiting to the dislocation motion. This deformation mechanism has been very hard to study quantitatively because it occurs at the highest rates and prior existing experiments are conflated with strong shocks. LIPIT has recently proven to access this regime with quantitative detail.

Perhaps the most important signature of ballistic transport is that it is NOT thermally activated, but rather increases with temperature. Thus, a critical experimental observable for this concept is that higher temperature should lead to higher strength. High temperature LIPIT experiments have only recently been enabled by our development of new equipment and methodology, including hot stages and also new launch pads made from heat-resistant materials. We recently published those methods [1], and applied them to the study of pure copper in the range where we expected to see the phonon-drag/ballistic transport regime.

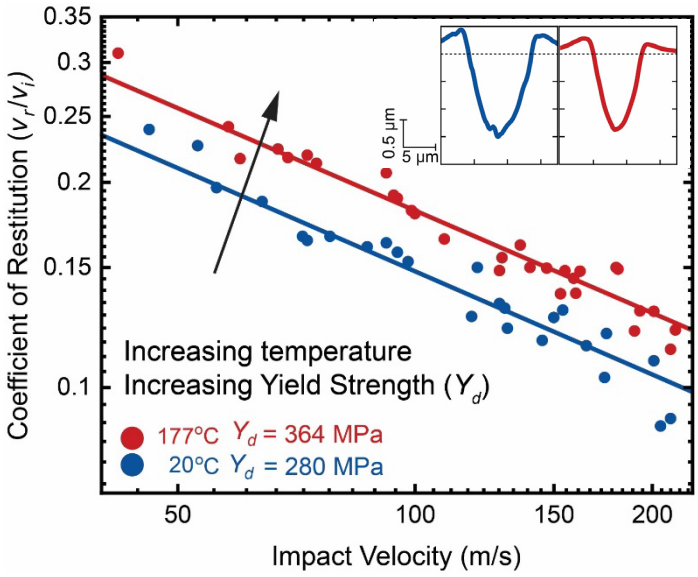

Fig 2: LIPIT data on the rebound of alumina particles from annealed copper substrates at 20 °C (blue) and 177 °C (red). Insets show profilometry scans of impact craters at the same impact velocity for each temperature: higher temperatures produce smaller craters, which matches the increased dynamic strength implied by the CoR.

The results in Fig. 2 are a subset of our full dataset for well-annealed copper [3], impacted by sapphire spheres. These data are typical LIPIT measurements, in which the camera was used to measure the inbound (impact) velocity v_i as well as the rebound velocity v_r, and their ratio is

presented as the coefficient of restitution (CoR = v_r/v_i). The CoR curves here show that less plastic energy dissipation occurs in copper as we heat it up to 177° C: the rebounds are greater for an otherwise identical test. In the inset, we show that this indeed corresponds to smaller impact craters. In short, copper is stronger at higher temperatures in these experiments at 10^7 s^{-1}, opposite of conventional thermal activation. These experiments thus provide direct experimental evidence of anti-thermal strengthening behavior at extreme strain rates outside of shock conditions, a defining signature of ballistic dislocation transport. A full analysis of these data shows that they are quantitatively consistent with phonon drag plasticity, and experiments on several other pure metals confirms that this is a general physical phenomenon not isolated to copper [3].

As discussed above, another issue with most conventional high-rate tests that involve shocks and high pressures is that the material strength is of little to no consequence in plasticity. By extension, most published high-rate experiments are not much influenced by materials microstructure considerations. In contrast, we believe that LIPIT should be sensitive to microstructure at velocities in the low-pressure regime. Another taskline of our current research is to explore the role of microstructure explicitly and quantitatively at extreme rates. In Fig. 3, we compare LIPIT data on pure copper in two different states: fully annealed and fully work hardened, each impacted with sapphire spheres. In validation of our working hypothesis, these data indeed show that microstructural effects are important to LIPIT, as the harder copper exhibits more pronounced rebounds (higher CoR), which is a result of lower plasticity and thus higher strength [5].

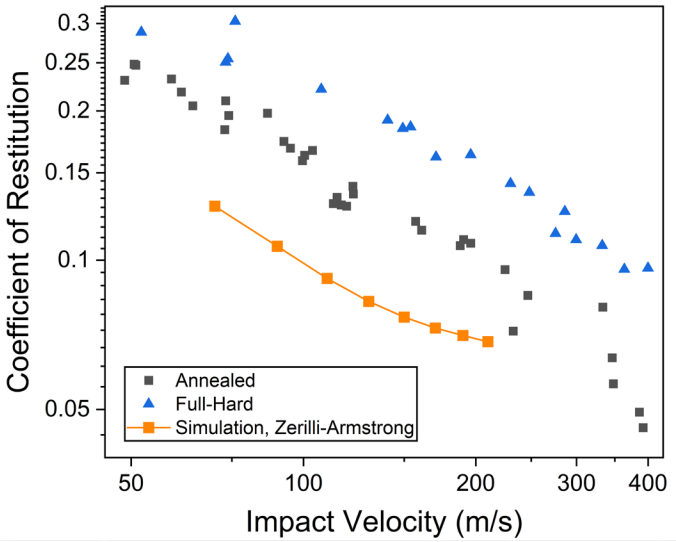

Fig. 3: Coefficient of restitution rebound data from LIPIT experiments of sapphire on copper, in either an annealed or fully work-hardened condition. The fact that microstructure affects the LIPIT measurements is prima facie evidence that these experiments are in the "low pressure" regime where shocks do not swamp out microstructural considerations. In that regime, classical constitutive laws such as the Zerilli-Armstrong model used in finite element modeling here, are miscalibrated and can now be updated to capture the true material response at high rates (free of shock effects).

Given that prior work on constitutive laws for extreme loading states did not have access to microstructure-dependent high strain rate data such as these, the current "best" constitutive laws for high rate deformation are certainly missing details. This is borne out by comparison with our group's finite element modeling of impacts for this system, which are shown in Fig. 3 using the current state-of-the-art parameterization of the Zerilli-Armstong constitutive law modeled on ALE3D from Lawerence Livermore National Lab [5]. The model does not match either set of

experimental data, almost certainly because it has been calibrated with previously available high-rate data with strong shock conflation, which are (i) not sensitive to microstructure and (ii) generally taken at lower rates ($<10^5$ s^{-1}) on Kolsky bar impact experiments. We therefore view the advent of LIPIT as a major opportunity to improve material models used widely in the community.

Future Plans

The above experiments illustrate the interesting new opportunities for structure-property connections in the regime of extreme strain rates, but low pressures. This is an underexplored regime compared with the typical shock experiments that dominate the literature at these rates, and importantly, this regime is sensitive to materials microstructure (where shocks typically are not). The ballistic, or phonon-drag, regime has been mysterious for decades, and with LIPIT we stand poised to not only calibrate phonon drag models to experimental data, but also to chart out its limits on the deformation mechanism map. We are currently looking at two complementary dimensions along which we expect phonon drag to give way to other mechanisms.

First, we are exploring the role of temperature far above the range where anti-thermal hardening has been seen in Fig. 2. Clearly metals cannot harden with temperature indefinitely; at some point they will be molten. However, the way in which ballistic transport breaks down as the melting point is reached has never been studied before. We are working on higher temperature experiments that can probe the crossover between mechanisms in quantitative detail.

Second, we are exploring the role of structural obstacles to dislocation motion, in the form of solutes (alloying elements). As the density of dislocation obstacles increases, the competition between classical obstacle bypass and phonon drag increases, and a cross-over between those mechanisms is expected. We are systematically exploring that cross-over in alloys of controlled composition.

Publications

1. A. Reiser, C.A. Schuh, *Microparticle impact testing at high precision, higher temperatures, and with lithographically patterned projectiles*, Small Methods, **7**, 2201028 (2023).
2. A.A. Tiamiyu, T. Lucas, E.L. Pang, X. Chen, J. LeBeau, C.A. Schuh, *Heterogeneous microstructural evolution during hydrodynamic penetration of a high-velocity copper microparticle impacting copper*", Materials Today, **72**, 71-86 (2024).
3. I. Dowding, C.A. Schuh, *Pure metals strengthen with increasing temperature when deformed at extreme strain rates*", Nature, **630**, 91-95 (2024).
4. V. Panova, C.A. Schuh, *Towards a quantitative understanding of bonding in supersonic single particle impacts: a three-dimensional FIB-SEM exploration*, Acta Materialia, **276**, 120105 (2024).
5. T. Lucas, A.M. Saunders, C.A. Schuh, *Microstructure effects on high velocity microparticle impacts of copper*, Acta Materialia, **280**, 120329 (2024).

6. A. Reiser, C.A. Schuh, *Towards an understanding of particle-scale flaws and microstructure evolution in cold-spray via accumulation of single particle impacts*, Acta Materialia, in press (2024).

Toughening mechanisms in ceramic nanocomposites

Principal Investigators: Brian W. Sheldon, Brown University; Jun Lou, Rice University

Co-Investigators: Huajian Gao and Nitin P. Padture, Brown University

Keywords: fracture, nanomaterials, small-scale testing, multiscale modeling

Research Scope

The brittleness of ceramic materials prevents their use in applications that could exploit their unique properties, such as high hardness, high strength, corrosion resistance, light-weight, etc. One of the most effective ways to improve their poor fracture resistance is by creating ceramic matrix composites (CMCs) based on long fiber reinforcements. The promise of extending this approach to create tougher nanoscale ceramics via nanotube and nanoplatelet reinforcements is supported by prior research, in spite of the conventional understanding that moving to smaller length scales in advanced ceramics typically leads to stronger but less tough materials. Determining whether these conventional scaling ideas are fully applicable to nanoceramic composites is a primary motivation for the research described in this project.

The overall goal of our work is to evaluate and understand the ways in which the inherently smaller microstructural length scales in ceramic nanocomposites will impact toughening mechanisms. The key objectives of these efforts are:

- Evaluate the failure and toughening mechanisms that occur in ceramic matrices reinforced with different nanoreinforcements. A major focus is on the use of in situ mechanical testing methods that make it possible to investigate phenomena over a broad range of length scales. The interpretations of these measurements are closely integrated with related multiscale modeling and analysis.
- Quantitatively evaluate the toughening contributions from phenomena that occur in 2-D reinforcements. This includes inelastic deformation mechanisms in reduced graphene oxide (*r*-GO), increased fracture resistance in *h*-BN sheets (compared to graphene-related sheets), and strength-limited interfacial debonding at small-scales (compared to the classical energy-limited debonding that occurs at larger length scales).
- Determine how the toughening mechanisms that operate in 2-D reinforced materials differ from those that operate in other composites (i.e., at larger length scales, with fiberous reinforcements, etc).
- Make detailed comparisons between *r*-GO and *h*-BN reinforced composites with the full range of platforms that are being employed in this work (i.e., nanocomposites produced by spark plasma sintering (SPS), nanosheet pull-out tests, deformation and fracture of single nanosheets).

Recent Progress

Early research on ceramic nanocomposites focused on carbon nanotubes (CNTs), however, more recent work has demonstrated significant toughening by graphene-based 2-D reinforcements. A “broad hypothesis” that has emerged is that 2-D reinforcements (graphene) are more effective at toughening than 1-D reinforcements (CNTs). In particular, prior work in this DOE-BES project has examined ceramics reinforced with reduced graphene oxide (r-GO) platelets, which generally exhibit toughness enhancements than multilayer graphene (i.e., where the latter have more “perfect” graphene structures with fewer defects). Recent experiments are largely focused on

extending these investigations to 2-D *h*-BN (hexagonal boron nitride) reinforcements in ceramic matrices (primarily silicon nitride produced by SPS). These comparisons are motivated by experiments which indicate that there are significant differences between the mechanical behavior of these different types of reinforcements. Recent work at Rice has focused on measurements of individual *h*-BN reinforcements. This work demonstrates that the intrinsic 2D fracture mechanism in *h*-BN differs from that in *r*-GO, and leads to substantially higher *platelet* fracture toughness. Understanding the relationships between these individual platelet properties and the overall fracture process in ceramic nanocomposites is a central goal of our current efforts.

Two central features of the current experiments at Brown are: (1) direct measurements of crack growth resistance curves (R-Curves) using the indirect compliance method, and (2) in situ observations of stable crack propagation inside a scanning-electron microscope (SEM). To quantitatively investigate the fracture process in these materials we are also continuing to employ and improve the small-scale testing methods that have been developed in this DOE-BES funded program. This includes microcantilever and micropillar measurements (at both Brown and Rice). The specific experiments at both Brown and Rice are also closely integrated with detailed modeling conducted by co-PI Gao. This overall effort is designed to create a broad, integrated understanding of nanocomposite fracture mechanisms where the full set of modeling results are more than the sum of the individual parts. The full framework is built around the idea that crack propagation in nanocomposites with dispersed reinforcements is accompanied by a finite fracture process zone (FPZ), within which the crack surfaces are bridged by multiple reinforcements. This includes a semi-analytical discontinuous crack-bridging model to analyze toughening due to multiple reinforcements. This approach provides a powerful and flexible framework to integrate each part of this program, evolving as we obtain a better understanding of the bridging mechanisms. For example, employing this to describe nanoplatelets makes it possible to describe multiple bridging events. This model is designed to incorporate specfic results obtained from the experiments, including pull-out and failure of reinforcements (direct SEM observations), crack arrest (microcantilever tests), and interfacial sliding (single sheet pull-out tests). Based on this information, a size-dependent constitutive law of the bridging force σ_{br} is currently being developed. This is designed to predict the overall crack bridging contributions based on the classical linear elastic crack-tip field analysis.

Future Plans

More extensive comparisons will be made between *r*-GO and *h*-BN, based on nanocomposites with the same reinforcement volume fraction and the same matrix phase, using the experimental methods at Brown and Rice that are outlined above. Based on our work to date, we anticipate that the *h*-BN reinforced materials will exhibit notable differences when compared with *r*-GO based composites. New work will also include experiments at elevated temperatures (up to 500 °C). This is high enough to significantly alter the compressive thermal stress imposed by the ceramic matrix (which generally has a higher CTE than the reinforcements). In prior work we proposed that these stresses can substantially enhance energy dissipation during pull-out. In principle, this effect can be directly investigated by conducting experiments at elevated temperature (at 500 °C we do not anticipate significant chemical changes in the materials of interest). This approach will enable

systematic investigations over a wide range of residual stresses by employing composites that are processed with SPS. Matrices with different CTE values (Al_2O_3 and Si_3N_4) will be used to produce a wide range of thermal stresses.

The direct interpretation of the experiments with both nanocomposites and individual reinforcements will require detailed modeling. This effort is designed to overcome the limitations of previous models, which are based almost exclusively on extending models of toughening by embedded fibers. Our experiments to data have demonstrated that toughening mechanisms associated with 2-D nanomaterials differ from these descriptions, and new modeling will be based on these observations.

Publications

- Xing Liu, Christos E. Athanasiou, Cristina López-Pernía, Ting Zhu, Nitin P. Padture, Brian W. Sheldon, and Huajian Gao, "Tailoring the toughening effects in two-dimensional nanomaterial-reinforced ceramic matrix composites", *Journal of Applied Mechanics* **91**, 011003 (2024).
- Z. Song, B. Zhang, Y. Yang, G. Gao, Q. Fang, Y. Zhang, B. Shin, D. Steinbach, Q. Ai, X. Zhao, Y. Han, N. Padture, B.W. Sheldon, T. Taniguchi, K. Watanabe, H. Gao and J. Lou, "Fracture of Multilayer Hexagonal Boron Nitride: Flaw-size Induced Mechanical Interlayer Coupling and Edge-reconstruction Embrittlement", *Nature Materials*, revision in review (2024).
- B. Zhang, W. Tu, X. Liu, D. Steinbach, Y. Zhu, J. Zhang, B.W. Sheldon, H. Gao, J. Lou, "3D printed mechanically robust h-BN reinforced silica nanocomposites", *ACS Nano*, submitted (2024).
- D. Steinbach, B. Zhang, F. Arifurrahman, R. Xin, B. Shin, Y. Camacho, N. Balaji, M. RW Brake, M. Tang, Q. Li, and J. Lou, "A Nanomechanical Tensile Testing Method at High Strain Rates", *Materials Today Communications*, submitted (2024).
- B. Zhang, X. Liu, D. Steinbach, W. Tu, Q. Ai, T. Taniguchi, K, Watanabe, B.W. Sheldon, H. Gao, J. Lou, "Engineering Interfacial strength and toughness of h-BN/PDC nanocomposites", *Small*, to be submitted (2024).
- Cristina Lopez Pernia, Aleksander Mijailovic, Xing Liu, Jun Lou, Huajian Gao, Nitin Padture, and Brian W. Sheldon, "R-Curve behavior and in situ observation of toughening mechanisms in Si_3N_4 ceramic composites reinforced with BN nanosheets", in preparation (2024).

- Christos E. Athanasiou, Xing Liu, Boyu Zhang, Truong Cai, Cristina Ramirez, Nitin P. Padture, Jun Lou, Brian W. Sheldon, and Huajian Gao, "Integrated simulation, machine learning, and experimental approach to characterizing fracture instability in indentation pillar-splitting of materials", *J. Mech. Phys. Solids* **170**, 105092 (2023).
- Zhenghong Dai, Meaghan C. Doyle, Xing Liu, Mingyu Hu, Qizhong Wang, Christos E. Athanasiou, Yuching Liu, Brian W. Sheldon, Huajian Gao, Shengzhong Frank Liu, and Nitin P. Padture, "The mechanical behavior of metal-halide perovskites: Elasticity, plasticity, fracture, and creep", *Scripta Mater* **223**, 115064 (2023).
- B. Ni, D. Steinbach, Z. Yang, A. Lew, B. Zhang, Q. Fang, M.J. Buehler, J. Lou, "Fracture at the two-dimensional limit," *MRS Bulletin* **47**, 848 (2022).
- Y. Yang, Z. Song, G. Lu, Q. Zhang, B. Zhang, B. Ni, C. Wang, X. Li, L. Gu, X. Xie, H. Gao, and J. Lou, "Intrinsic toughening and stable crack propagation in hexagonal boron nitride," *Nature* **594**, 57 (2021).

The Brittle Ductile Transition in Nanoporous Gold

Karl Sieradzki, Fulton School of Engineering, Arizona State University, Tempe, AZ 85287

Keywords: bi-continuous morphology, ligament diameter, micron-scale tensile tests, pico-indenter

Research Scope:

In metallic alloys some elemental components are more susceptible to electrochemical dissolution than others and such a dealloying process can result in the formation of a nanoporous bi-continuous morphology. Large enough volumes of these structures contain dangling ligaments and clusters of these ligaments can be viewed as a three-dimensional crack. The prototypical example of this is the dealloying of Ag-Au alloys under free corrosion in nitric acid, during which Ag is selectively dissolved, forming nanoporous Au (NPG) [1]. If structures containing nanoporous morphologies are subjected to tensile loading, a form of stress corrosion cracking (SCC) that we term dealloying induced SCC can occur. The NPG morphology that initiates the SCC fracture is brittle [2].

NPG is known to undergo a brittle to ductile transition as a function of the average ligament size, $< \mathcal{L} >$, and smallest length, R (often the sample thickness), characterizing the sample size. For conventionally sized NPG tensile samples with $< \mathcal{L} >$ =100 nm and R = 125 μm, the behavior is brittle, but for $< \mathcal{L} >$, greater than about 200 nm the behavior is ductile. Previous work suggests [3, 4] that this transitional behavior is a smooth rather than a sharp transition, that results from statistical fluctuations in the NPG ligament size distribution.

We believe that our observations of the ductile versus brittle behavior of NPG are connected to the so-called weakest link theory, which says that a large structure is more prone to brittle failure than a small one. In the case of NPG and similar structures, the "measuring stick" corresponds to a ligament length. At fixed sample volume then, a small ligament length correspond to a large sample for which brittle behavior is observed. On the other hand, for large enough ligament lengths, the damage during tensile loading is more distributed, resulting in a ductile response. Assuming that the cracks composed of the dangling ligaments do not interact with one another, the brittle or ductile response of the morphology is determined by the number of critical flaws that exist. The smaller the number, the more brittle the behavior. Distributed damage results in ductile fracture. The cumulative Weibull distribution has the form,

$$F(\sigma; V) = 1 - \exp\left[-V\left(\frac{\sigma}{\sigma_o}\right)^m\right],$$

where $F(\sigma; V)$ is the brittle failure probability, V is the sample volume, σ_o is the shape factor and m is the modulus. When comparing two samples, V, and a reference, V_{REF}, at constant probability of brittle failure, $\sigma_o/\sigma_{REF} = (V_{REF}/V)^{1/m}$. The shape parameter determines the spread

of the distribution. A large value indicates a distribution with a large spread while a small value indicates a tighter spread. The modulus determines the shape of the distribution. A small value (< 1) indicates a distribution with a long tail while a large value (> 1) indicates a shorter tail. As the modulus increases the value of the variance decreases.

Our hypothesis is that as a function of a characteristic measure of the NPG morphology (such as the mean ligament diameter, $< \mathcal{L} >$, there is a minimum NPG volume or sample dimension, $\mathcal{R}_{crit}$, required for macroscopically brittle behavior. For conventionally sized tensile samples, displaying brittle behavior, $<\mathcal{L}>/\ \mathcal{R}_{crit}$ is about 1000. Our aim is to validate that weakest link theory applies to the ductile/brittle response of NPG. For example, at $< \mathcal{L} >$ 100 nm and $\mathcal{R}_{crit}$ = 2 μm, we expect the brittle/ductile response to be borderline, i.e., ductile failure is possible.

We use a push-to-pull micro-electromechanical systems (P2P MEMs) device to perform the micron-scale tensile tests. The average NPG ligament diameter $< \mathcal{L} >$ is varied between 15 nm – 150 nm, at a fixed R = 2 μm. In our tensile tests, R corresponds to the thickness dimension within the gage length of the dog bone shaped samples. The NPG ligament distribution is characterized using digital image analysis and the sample displacement within the gage length is measured using digital image correlation (DIC).

In order to perform these experiments, we initiated a collaboration with Brad Boyce at Sandia National Laboratory. The CINT facility there has a Bruker Hysitron PI89 pico-indenter which is necessary for our experiments. The post-doctoral scholar working on this project, Qingguo Bai, travels to Sandia to perform these experiments with Kevin Garner, a member of Brad Boyce's group.

Recent Progress

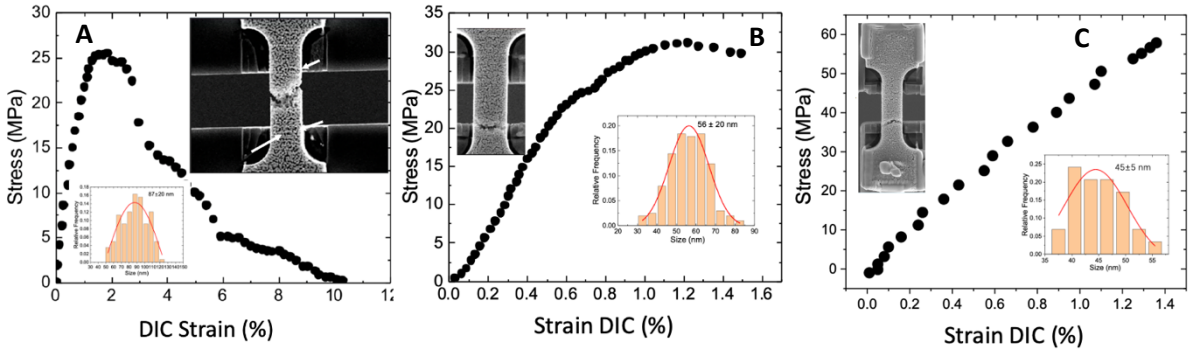

Fig. 1. P2P MEMs based micro-tensile test results. A. $< \mathcal{L} >$ = 87 nm NPG showing ductile behavior. The white arrows point to distributed crack damage in the morphology. **B**. $< \mathcal{L} >$ = 56 nm NPG shows a transitional ductile/brittle response. **C**. $< \mathcal{L} >$ = 45 nm NPG shows a fully brittle stress-strain curve, similar to that obtained for conventionally sized tensile samples [4]. The insets show the ligament distributions and the samples at fracture.

Fig. 1 shows some of our representative results for the micro-tensile tests. The most surprising thing is the sensitivity to the average ligament size. As we change $< \mathcal{L} >$ from about 90 nm to 45 nm we move from an entirely ductile response showing distributed damage to completely brittle behavior.

Future Plans

We plan to examine the full spectrum of average ligament sizes at $\mathcal{R}_{crit}$ = 2 μm in order to define the sharpness of the transitional region. This will include $< \mathcal{L} >$ values of 50, 60, 70 and 80 nm. We will also be varying $\mathcal{R}_{crit}$ from 2 μm to 2.5 or 3 μm to see how this affects the $< \mathcal{L} >$ value at which the transition occurs.

Since the microscale tensile samples are single-crystals, we also plan to use electron backscatter diffraction to determine the sensitivity of the brittle/ductile response to the crystallographic orientation of the tensile samples and loading direction.

References

1. J. Erlebacher, M.J. Aziz, A. Karma, N. Dimitrov, K. Sieradzki. Evolution of nanoporosity in dealloying. *Nature* **410,** 450 – 453 (2001).

2. S. Sun, X. Chen, N. Badwe, K. Sieradzki, Potential-dependent dynamic fracture of nanoporous gold. *Nat. Mater*. **14,** 894–898 (2015).

3. R. Li, R., K. Sieradzki, Ductile-brittle transition in random porous Au. *Phys. Rev. Lett*. **68**, 1168–1171 (1992).

4. N. Badwe, X. Chen, K. Sieradzki, Mechanical properties of nanoporous gold in tension. *Acta Mater*. **129,** 251-258 (2017).

Publications

X. Chen, E.K. Karasz, N. Badwe, K. Sieradzki, Dynamic fracture and dealloying induced stress-corrosion cracking*, Corros. Sci*, **187,** 109503 (2021).

Micromechanics of Migrating Interfaces

Ryan Sills, Department of Materials Science and Engineering, Rutgers University

Keywords: grain boundary, phase boundary, interface migration, disconnection, dislocation

Research Scope

In the last decade, it has become widely accepted that the primary mechanism of interface migration is formation and migration of disconnections—interfacial line defects characterized by a Burgers vector and a step height [1]. Despite this progress, numerous recent experimental observations have brought into question basic tenets of the theory of interface migration [2]. This source of discrepancy between experimental observations and theory is a lack of knowledge about how disconnections form and what controls their migration rate; the focus of this project is to fill these knowledge gaps through molecular dynamics (MD) simulations of grain and phase boundaries. Capabilities developed previously under this project, including tools for predicting line defect structures and identifying interfacial line defects in MD simulations, uniquely enable the research methods. The hypothesis guiding the work is that interactions with dislocations—both in the bulk and within the interface—govern the formation and migration rates of disconnections. The project is comprised of three research tasks aimed at (1) predicting and classifying line defect structures for a variety of interfaces, (2) identifying disconnection formation mechanisms and quantifying formation rates, and (3) understanding how interfacial dislocations affect formation and migration of disconnections.

Recent Progress

Two major challenges have hindered advances in our understanding of interface migration: (1) predicting what line defect structures are present in interfaces and (2) identifying individual line defects and their dynamics over time in MD datasets. Two software tools have been developed and released as open-source under this project which solve these challenges. The first tool called AIDADA (Arrangement of Interfacial Dislocation And Disconnection Arrays) is an extension of a tool developed by Sangghaleh and Demkowicz [3] which uses the Frank-Bilby equation to identify all possible line defect structures—including dislocations and disconnections—for a given interface. Using AIDADA we have shown that interfaces typically have 100s of possible line defect structures which are similar

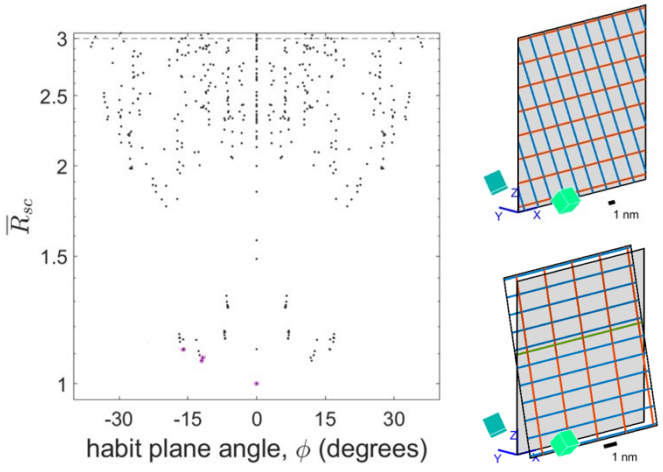

Figure 1. Spectrum of estimated line defect energies obtained with AIDADA for a Nishiyama-Wasserman interface in Fe (normalized by the lowest predicted energy level) as a function of interface habit plane angle. Line defect structures for the two lowest energy solutions are shown.

in energy and thus expected to exist in interfaces with similar frequency (see Figure 1). The second tool called ILDA (Interfacial Line Defect Analysis) automatically identifies and extracts line defects in crystalline interfaces, quantifying their Burgers vectors and step heights. Figure 2 shows the workflow for how ILDA operates. Using ILDA, detailed analyses can be performed to tie specific dislocation/disconnection mechanisms with migration behaviors, as shown below.

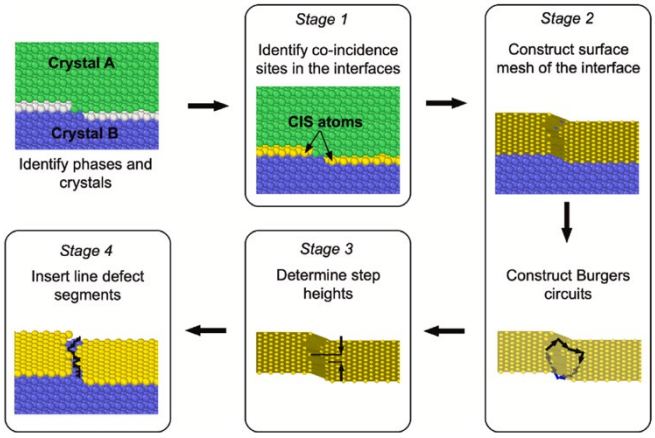

Figure 2. Workflow for the ILDA tool, based around a surface mesh connecting co-incidence site (CIS) atoms in the interface.

One core question we are making progress on answering is how the migration rates of individual disconnections are tied to the overall migration rate of interfaces. Using ILDA, we can track the migration rate of the interface along with the line densities of different disconnections. We can then use this information to determine how different disconnections contribute to the overall migration rate and also extract the apparent mobility of each disconnection. Figure 3 presents one example result from this analysis, showing different line defect densities as a function of grain boundary migration distance. A few simulation snapshots of interfacial line defect structures are also shown.

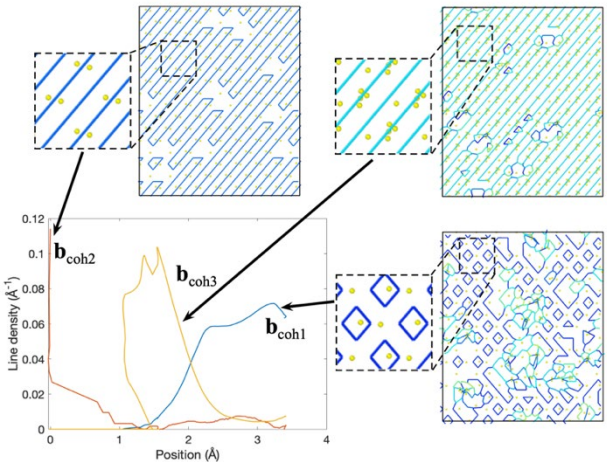

Figure 3. Densities of three different line defects (discohesions) in an FCC grain boundary as a function of migration distance. Snapshots show representative line defect structures which are dominated by the three different discohesions.

While examining line defect structures in grain and phase boundaries, we have identified a new class of coherent interfaces. These interfaces feature local, non-affine distortions within the interface which increase the number of co-incident site (CIS) atoms shared by the crystals. Figure 4 presents this idea schematically. These non-affine deformations are equivalent to the insertion of disconnection dipoles or loops, and we argue that they represent a new class of line defects which we called discohesions. An interface whose coherency is enhanced by the presence of discohesions is termed a discoherent interface. So far we have identified discoherent phase, twin, and grain boundaries in FCC, BCC, and HCP systems. Atomic structures predicted in discoherent interfaces have also been validated against high-resolution transmission electron microscopy,

thanks to a collaboration with Douglas Medlin of Sandia National Laboratories. As an example of a discoherent interface, the grain boundary shown in Figure 3 is discoherent and the line defect densities shown in the plot represent three different discohesions observed in the interface. As the interface migrates, the defect structure switches from one discoherent state to another, as exemplified by changes in the defect densities.

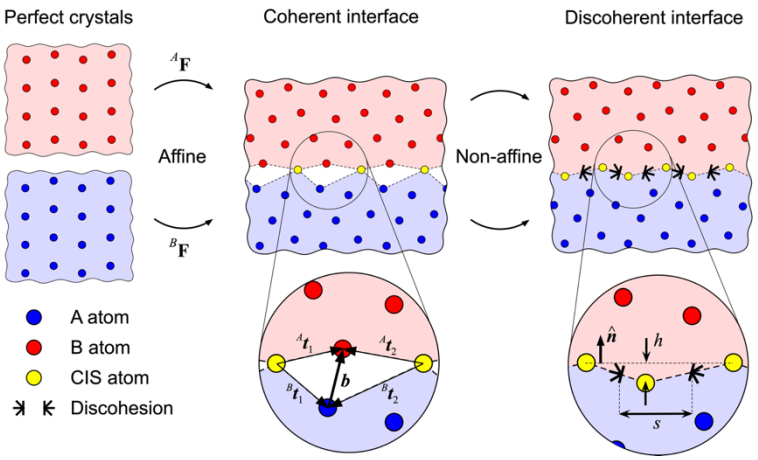

Figure 4. Schematic depiction of how a discoherent interface is construction through insertion of discohesions—disconnection dipoles which increase the number of CIS atoms in the interface.

Future Plans

Future efforts will be focused on leveraging the previously developed tools to reveal basic mechanisms of disconnection formation and migration. This will include a survey of line defect structures across a range of grain and phase boundaries using AIDADA. By pairing this analysis with previously published databases of MD simulations [4], we can identify important correlations between defect structures and migration behaviors. Using our own MD simulations, we will use ILDA to test the validity of commonly used interface migration models. For example, disconnections are commonly assumed to obey linear mobility laws with mobilities that vary Arrheniusly with temperature. Both of these assumptions can be directly interrogated by applying ILDA to interface migration simulation results. Finally, we will use ILDA to investigate mechanisms of disconnection formation through homogeneous nucleation and intersections with bulk line defects. These analyses will allow us to determine the most likely source of disconnections in migrating interfaces.

References

1. G. S. Rohrer, I. Chesser, A. R. Krause, S. Kiana Naghibzadeh, Z. Xu, K. Dayal, and E. A. Holm, *Grain Boundary Migration in Polycrystals*, Annual Review of Materials Research **53**, 347-369 (2023).

2. A. Bhattacharya, Y.-F. Shen, C. M. Hefferan, S. F. Li, J. Lind, R. M. Suter, C. E. Kill III, and G. S. Rohrer, *Grain boundary velocity and curvature are not correlated in Ni polycrystals*, Science **374**, 189-193 (2021).

3. A. Sangghaleh and M. J. Demkowicz, *AIDA: A tool for exhaustive enumeration of solutions to the quantized Frank-Bilby equation*, Computational Materials Science **145**, 35-47 (2018).

4. E. R. Homer, G. L. W. Hart, C. B. Owens, D. M. Hensley, J. C. Spendlove, and L. H. Serafin, *Examination of computed aluminum grain boundary structures and energies that span the 5D space of crystallographic character*, Acta Materialia **234**, 118006 (2022).

Publications

1. N. Deka, C. Alleman, D. Medlin, and R. B. Sills, *Energy and stochasticity: The yin and yang of dislocation patterning*, Material Research Letters, **11**, 289-295 (2023).

2. N. Deka, A. Stukowski, and R. B. Sills, *Automated extraction of interfacial dislocations and disconnections from atomistic data*, Acta Materialia, **256**, 119096 (2023).

Internal normal pressure balance: the driving mechanism of elastomeric nanocomposite reinforcement from low strain to void formation

David S. Simmons, University of South Florida

Keywords: Nanocomposite, Polymer, Nonlinear Mechanics, Toughness, Molecular Dynamics Simulation

Research Scope

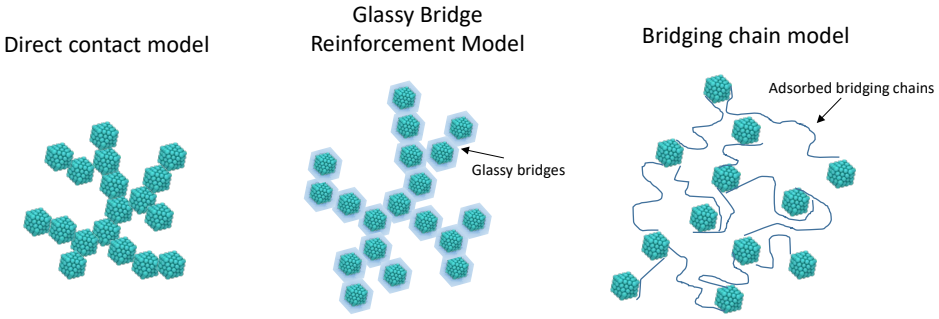

Figure 9. Proposed models of nanoparticulate reinforcement of soft polymers: percolation via direct nanoparticle contacts; percolation via glassy polymer bridges between particles; and percolation via tie or interentangled chains.

Introduction of nanoparticles to elastomers and other polymers can greatly enhance mechanical toughness, an effect essential for a wide range of material applications demanding mechanical robustness under load. At high (nonlinear) strain, the primary mechanism of this enhancement is a dramatic enhancement in energy dissipation. However, the precise molecular mechanism by which this enhanced energy dissipation occurs remains unsettled. Is the primary origin of dissipation direct particle-particle friction? Is it plastic deformation of glassy domains induced by surface interactions in gaps between particles? Is it the dragging of polymer chains across the surface, or dissipation linked to transient physical crosslinking of chains by particles? Each of these mechanisms (see Figure 1) has been proposed in the literature[1–3]; the conditions (if any) under which each dominates remain unresolved. The goal of this project is to resolve the mechanisms of mechanical reinforcement and energy dissipation underlying nonlinear mechanical response in elastomeric nanocomposites.

Recent Progress

This year, work on this project has led to an emerging cohesive picture of the origin of nanoparticulate driven elastomer reinforcement, from low strain to failure. Over the last several decades, it has become increasingly clear that jamming or network formation of nanoparticles plays a central role in mechanical reinforcement of elastomers in the linear low-strain regime. Prior work by our group pinpointed a Poisson ratio mismatch between the elastomeric matrix and a co-existing percolated granular solid as playing a central role in this reinforcement, with this mismatch causing the elastomer's bulk modulus (order GPa) to contribute to the composites Young's modulus (order MPa in neat elastomers).

A central open question is thus how this linear-regime reinforcement, which is predominated by energy storage, transitions to the nonlinear regime, where reinforcement is dominated by energy dissipation. Our results *point to a fundamental transition from a solid-like nanoparticulate response to a plastic nanoparticulate response, at a strain corresponding to the Payne-effect strain softening*. By decomposing the stress response into contributions from the polymer and filler, our work reveals that the filler response becomes almost entirely dissipative beyond several tens of percent strain, pointing to a post-yield plastic filler response. On its own, this raises a new question. Particulate media do not normally exhibit plastic behavior under extensional strain due to their lack of cohesion. Why are they able to do so here?

Our results suggest that the Poisson ratio mismatch implicated in low strain reinforcement continues to play a central role under nonlinear deformation. In the linear regime, this mismatch leads to a massive internal stress balance, wherein a compensation between a large negative polymeric normal stress and a large positive particulate normal stress sums to zero. Our results demonstrate that this internal normal stress balance persists in the nonlinear response regime, indicating that the volume of the system remains intermediate between that preferred by the polymer and that preferred by the filler. These data suggest a remarkable situation wherein, during nonlinear strain, a large normal compressive stress applied by the polymer to the filler preserves filler cohesion and likely a near-jammed state, enabling the emergence of a plastic nanogranular response under extensional strain. This plastic granular response, in turn, provides a large dissipative addition to the mechanical response of the composite, leading to high-strain toughening.

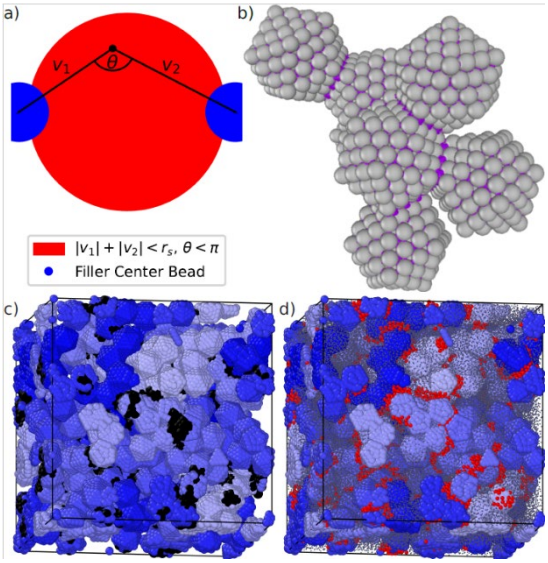

Figure 10. (a) geometry for identification of particle contact regions and interfiller polymer; (b) image of a filler cluster; (c) image of filled polymer with contacting filler beads shown in black; (d) image of same system with interfiller polymer shown in red.

Analysis of highly local stress response behavior (Figure 2) adds additional support to these interpretations. In particular, these analyses indicate that stress at high strain is highly enhanced at particle-particle contact point, *but only in the normal direction*. To the contrary, stress in the extensional direction is actually *reduced* at particle-particle contact points. This supports a scenario wherein internal normal stress imposed by the polymer matrix maintains near-jammed contacts between particles, facilitating emergence of a plastic response. In contrast, in the extensional direction filler-filler contacts are elastic weak points since they lack the covalent interconnectivity of the elastomeric matrix. Similarly, results indicate that small bridges of polymer between particles do not exhibit enhanced mechanical response. This is reflective of the fact that these simulations are at relatively high temperatures where glassy bridge effects are

absent, and it supports the hypothesis that direct particle-particle contacts are most important in this regime.

Finally, the most recent work in this project identifies a new mechanism, also emanating from the internal pressure balance above, that drives ultimate failure. At high strains, the plastic deformation particulate regime described above ends with a re-jamming phenomenon, wherein lateral compression causes particles to re-jam and cease plastic flow. In the approach to this phase, the particles increasingly form a heterogeneous structure wherein particle 'pillars' in the normal direction are interspersed with particle poor regions (Figure 3a). We believe this leads to spatially heterogeneous normal pressures, in which filler-rich pillars exhibit positive normal pressures while filler-poor regions exhibit large negative normal pressures. This effect quickly leads to pressure-induced cavitation in the filler-poor regions (Figure 3b, Figure 4), which is follows by void growth and eventual failure. The formation of voids

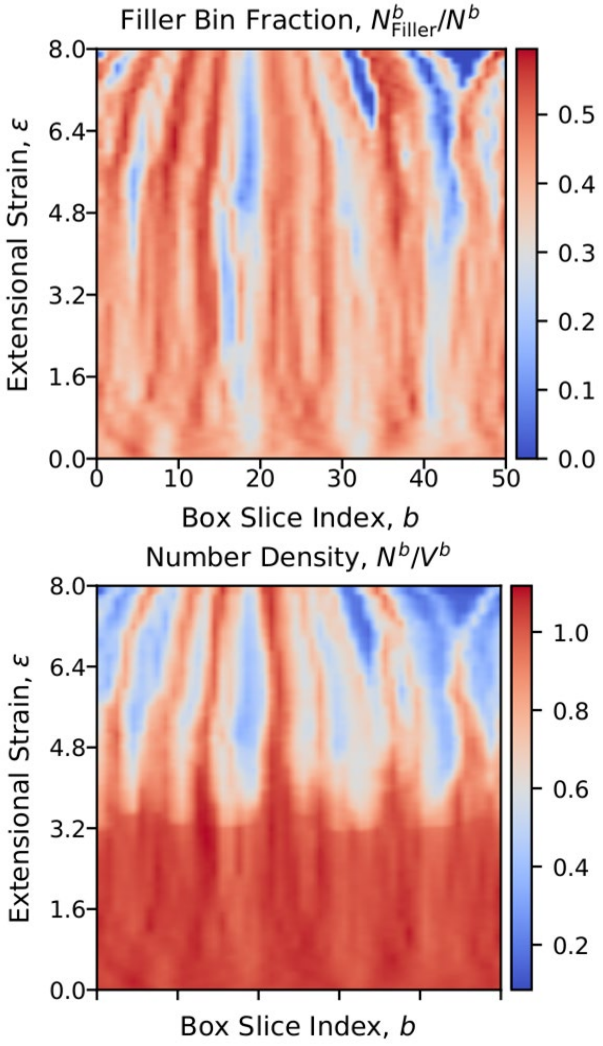

Figure 11. Heat maps of local number fraction of filler beads (a) and density (b) vs fractional location in the box in the deformation direction (x axis) and extensional strain (y axis). The figures illustrate that filler-poor stripes develop normal to the deformation direction and serve as precursors for cavitation and void formation.

Simulations across a range of nanoparticle loadings and structures indicate that this phenomenon is closely coupled to and driven by the normal-pressure-driven reinforcement at lower strains. Systems with higher loading or more structured particles exhibit higher low-strain reinforcement driven by a larger internal normal stress balance buildup; this in turn leads to earlier pressure-induced cavitation and failure. Collectively, these findings recast the mechanism of nanoparticle-based elastomer reinforcement

Figure 12. Snapshot of a simulation illustrating formation of voids in particle-poor regions that evolved during earlier deformation stages. Red outlines highlight two major cavitation regions, with the cavities in these regions spanning the period boundaries of the box.

as being driven by Poisson-ratio-mismatch and normal-stress-balance effects from the linear regime through the initiation of failure.

Future Plans

A final remaining question is how the presence of strong polymer-filler attractions related to postulated glassy bridge effects would modify the picture above. Preliminary simulations suggest that these effects both enhance normal-direction particulate jamming and introduce an additional particle-extensional-reinforcement mechanism at second order. Ongoing simulations and analysis aim to complete this element of the mechanistic picture of nanoparticulate-based elastomer reinforcement.

Publications

1. Kawak P., Bhapkar H., and Simmons, D. S., "Central Role of filler-polymer interplay in nonlinear reinforcement of elastomeric nanocomposites", *Macromolecules,* accepted manuscript.

Chemical short-range and radiation effects in ceramics

Izabela Szlufarska, Department of Materials Science & Engineering, University of Wisconsin - Madison

Keywords: carbides, borides, high-entropy ceramics, radiation effects, corrosion**.**

Research Scope

The overall goal of this project is to discover scientific principles that control defect kinetics and radiation damage recovery processes in high entropy ceramics (HECs) to lay a foundation for rational design of new materials for the extreme environments of advanced nuclear reactors. The specific scientific hypotheses that will guide this research are: (1) Local chemical heterogeneities enhance radiation resistance of HECs; (2) HECs with lower thermal conductivity have a better radiation resistance; (3) HEC can undergo significant radiation-induced segregation (RIS); (4) C stoichiometry in HECs has a significant impact on radiation resistance of HEC.

Recent Progress

Radiation-induced segregation (RIS) and its impact on corrosion in binary carbides and borides. We have previously discovered the existence of radiation-induced segregation (RIS) in structural ceramics, even if these ceramics form line compounds and therefore have a strong thermodynamic drive to stoichiometry. This discovery was made in irradiated SiC [1]. We have since demonstrated that RIS is more common in such ceramics than previously assumed as we have recently demonstrated that it is also present in TiB_2 [2]. Mechanisms of RIS in ceramics are distinct from those found in metals and they are intimately related to the complex defect energy landscape. The mechanisms are also not the same in the different ceramics. For example, in SiC RIS is controlled by short-range energy barriers to C Frenkel pair recombination (which are larger than migration energy barriers), whereas in TiB_2 RIS is controlled by formation of B_{Ti} antisite defects. Generalizable principles that govern RIS in ceramics still need to be determined. We have also shown that RIS in ceramics has a significant impact on properties relevant to nuclear reactor applications. For example, we found that irradiated SiC exposed to high-temperature water has slower grain boundary corrosion than unirradiated SiC grain boundary (see Fig. 1) [3]. These

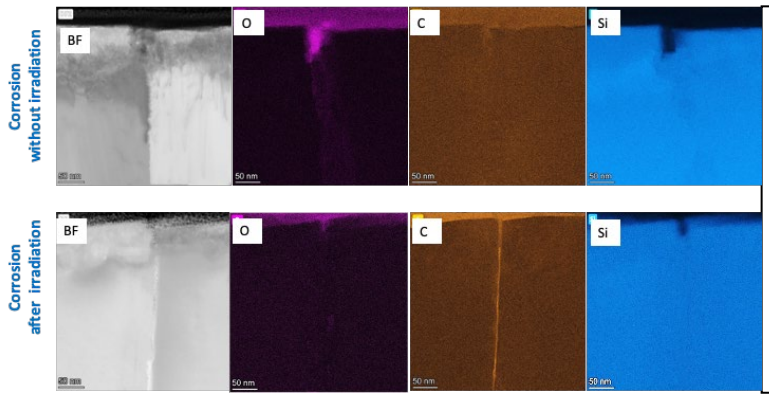

Fig. 1. Grain boundary in irradiated SiC after exposure to high-temperature water (360C) for 30 days. Top row: Corrosion of an unirradiated bicrystal. Bottom row: Corrosion of irradiated bicrystal with the same grain boundary misorientation. C-enrichment due to irradiation suppresses Si dissolution during high-temperature corrosion in SiC. Mechanisms explained by atomistic simulations.

experimental observations have been explained by our multi-scale models of defect evolution. Briefly, the positive impact of radiation on suppressing GB corrosion of SiC in water can be explained by C segregation to GBs due to RIS. Our atomistic simulations based on the density functional theory confirmed that C suppresses corrosion in SiC and the mechanisms of corrosion have been elucidated [4, 5].

Chemical short-range order (CSRO) in high-entropy ceramics and its impact on radiation resistance.

We have demonstrated for the first time the existence of CSRO in high-entropy carbides (HECs) using a combination of high-resolution scanning transmission electron microscopy (STEM) and 4D-STEM, combined with atomistic simulations (Fig. 2). Atomistic simulations were performed using machine learning potentials developed in this project. While CSRO has been previously observed in high-entropy metal alloys, it had not been reported in high-entropy structural ceramics. Experiments and simulations were performed on (TiVZrNb)C (referred to as Zr-HEC) and (TiVMoNb)C (referred to as Mo-HEC) and both methods showed an excellent agreement with each other. Zr-HEC was found to have a stronger CSRO than Mo-HEC and CSRO was determined to be due to clustering of heavy elements. To isolate the effects of CSRO, we annealed Mo-HEC at high temperature (1773K), which resulted in a significant reduction of the CSRO compared to as-sintered samples. The presence of CSRO has been shown to have a significant positive impact on radiation resistance. Specifically, Mo-HEC irradiated right after sintering (higher level of CSRO present) exhibited less radiation-induced swelling than Mo-HEC irradiated after annealing at high temperature (lower level of CSRO present). We hypothesize that the desirable impact of CSRO on reducing of radiation-induced swelling stems from a slower diffusion of defects in the presence of CSRO. However, the impact of CSRO on defect diffusion and the relation between diffusion and radiation resistance need to be investigated. We are addressing these scientific questions using atomistic simulations based on our newly developed machine learning potentials. While annealing Mo-HECs proved excellent in isolating the effects of CSRO on radiation resistance, CSRO alone does not explain trends in radiation resistance when comparing Zr-HEC

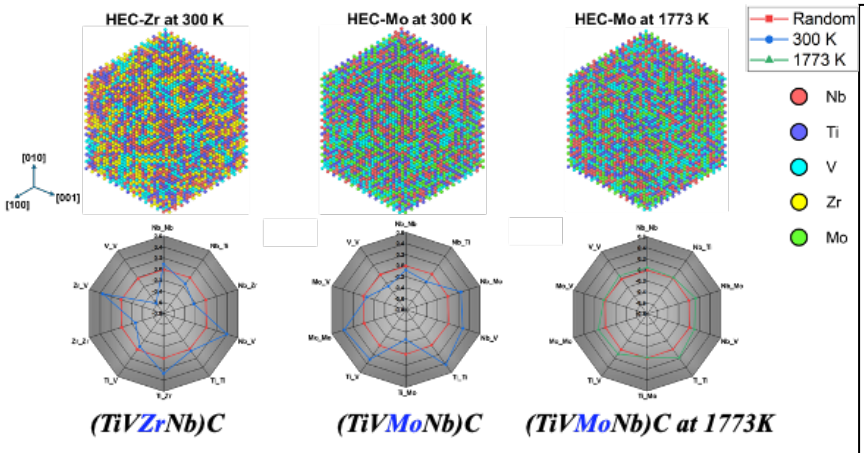

Fig. 2. Hybrid molecular dynamics / Monte Carlo simulations of HECs based on newly developed machine learning potentials. Top: visualization of the atomic structure. Bottom: Warren-Cowley parameter quantifies the amount of CSRO and confirms that Zr-HEC has a higher level of CSRO than Mo-HEC and annealing reduces CSRO in Mo-HEC.

and Mo-HEC. Specifically, Zr-HEC had a significantly higher radiation-induced swelling, despite having a higher level of CSRO than Mo-HEC. These results demonstrate that CSRO is not only common in HECs, but that it can also be controlled by selecting chemical elements and though synthesis. The interplay between chemical bonding, CSRO, and radiation is now being investigated.

Predictions of phase stability in high-entropy ceramics using DFT-based free energy models.

While the vast compositional space of high-entropy ceramics provides an unprecedented opportunity for design of materials with fine-tuned properties, it also creates a significant challenge in selecting elements that will form the often-desirable single-phase materials or lead to controlled precipitation. CALPHAD methods are excellent in this regard, but they suffer from lack of comprehensive experimental data for high-entropy ceramics needed for fitting of the free energy

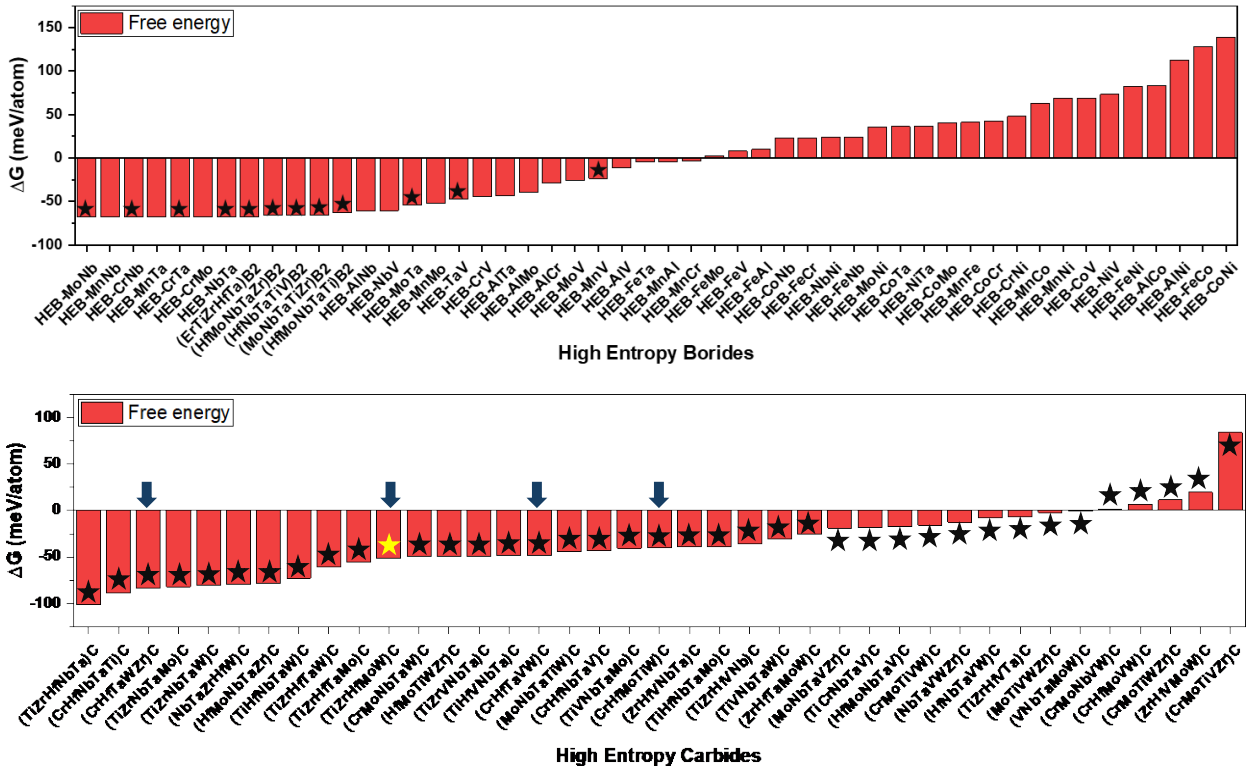

Fig. 3. Predictions of phase stability in high entropy-borides (top) and high-entropy carbides (bottom) using our DFT based free energy calculations. Negative values of ΔG indicate single-phase stability. Stars indicate existing experiments. The model agrees with experiments, except for the potential disagreement for the four compositions indicated by arrows in the lower panel. These arrows correspond to W containing HECs where our model predicts single phase and previous experiments reported multi-phase materials. To test predictions of our model, we synthesized experimentally the composition shown by a yellow star and found that in fact it does form a single phase, confirming predictions from our model. It appears that W containing high-entropy ceramics might be difficult to synthesize, as mixed experimental reports have also been reported for W containing high entropy borides, sometimes for the same composition and by the same authors.

models underlying CALPHAD calculations. Another approach that recently gained attention in the scientific community involves development of descriptors that can be calculated relatively quickly from atomistic simulations (especially density functional theory, DFT) and that correlate with single-phase stability of high-entropy ceramics. Some of the most promising descriptors include entropy forming ability, lattice strain, and DEED. However, although such descriptors are physically motivated, they are not built on an underlying scientific framework or model. As a result, if a descriptor fails to predict a certain range of compositions, there is no obvious path to improvement of a given descriptor. To address this challenge, we have developed a new approach to predicting phase stability of high-entropy ceramics based on free energies calculated from DFT. While it is obvious that free energies can in principle be used to predict phase stability, it had not been clear whether DFT accuracy and approximations to free energy terms that are needed at present to make such calculations computationally efficient, are robust enough to make predictions of phase stability reliable. Here, we have developed a framework for calculation of enthalpic and entropic contributions and found that predictions from our model are in a very good agreement with existing experiments and with new experiments performed by us in this project. Our DFT based free-energy model has been tested on high entropy borides and high entropy carbides (Fig. 3).

Future Plans

Our plans for the near future include: (i) atomistic simulations to explain the impact of chemical short-range order on radiation effects in HECs, and on the competition/coupling between CSRO and chemical bonding (chemical identities) of atoms when it comes to their effects on radiation resistance. (ii) The presence of RIS in high entropy ceramics and fundamental defect behavior that controls RIS when it is observed.

References

1. X. Wang, H. Zhang, T. Baba, H. Jian, C. Liu, Y. Guan, O. Elleuch, T. Kuech, D. Morgan, J-C Idrobo, P. M. Voyles, I. Szlufarska, *Radiation-induced segregation in a ceramic*, Nature Materials **19**, 992 (2020).
2. S. Wei, M. W. Qureshi, J. Xi, J. Y. Kim, X. Wang, J. Wei, R. Su, L. Liu, W. O. Nachlas, J. H. Perepezko, H. Zhang, I. Szlufarska, *Radiation induced segregation in titanium diboride*, Acta Materialia **267**, 119739 (2024)
3. J. Xi, H. Zhang, R. Su, S. Wei, X. Hu, B. Queylat, T. Kim, A. Couet, I. Szlufarska, *Coupling of radiation and grain boundary corrosion in SiC*, npj Materials Degradation, **8**, 16 (2024)
4. J. Xi, I. Szlufarska, *Control of surface chemical reactions through solid stiffness*, Phys. Rev. Lett. **129**, 106101 (2022)
5. J. Xi, C. Liu, D. Morgan, I. Szlufarska, *Deciphering water-solid reactions during hydrothermal corrosion of SiC*, Acta Materialia, **209**, 116803 (2021)

Publications

1. S. Wei, M. W. Qureshi, J. Xi, J. Y. Kim, X. Wang, J. Wei, R. Su, L. Liu, W. O. Nachlas, J. H. Perepezko, H. Zhang, I. Szlufarska, *Radiation induced segregation in titanium diboride*, Acta Materialia **267**, 119739 (2024)
2. J. Xi, H. Zhang, R. Su, S. Wei, X. Hu, B. Queylat, T. Kim, A. Couet, I. Szlufarska, *Coupling of radiation and grain boundary corrosion in SiC*, npj Materials Degradation, **8**, 16 (2024)
3. J. Xi, I. Szlufarska, *Control of surface chemical reactions through solid stiffness*, Phys. Rev. Lett. **129**, 106101 (2022)
4. J. Y. Kim, H. Zhang, J. Xi, I. Szlufarska, *Trends in behavior of point defects in MB and MAB phases*, Chemistry of Materials, **34**, 7807-7816 (2022)
5. J. Y. Kim, L. Gelczuk, M. Polak, D. Hlushchenko, D. Morgan, R. Kudrawiec, I. Szlufarska, *Native Deep-Level Defects in Transition Metal Dichalcogenides – Experimental Verification of Theoretical Predictions*, npj 2D Materials and Applications, **6**, 1-11 (2022)
6. J. Xi and I. Szlufarska, *Control of surface chemical reactions through solid stiffness*, Phys. Rev. Lett**.**, **129,** 106101 (2022)
7. J. Y. Kim, H. Zhang, R. Su, J. Xi, S. Wei, P. Richardson, L. Liu, E. Kisi, J. H. Perepezko, I. Szlufarska, *Defect recovery processes in Cr-B binary and Cr-Al-B MAB phases: structure-dependent radiation tolerance*, Acta Materialia, **235**, 119099 (2022)

Grain Boundary Microstates: Exploring the Metastability of Sink Efficiency

Mitra Taheri (Johns Hopkins), Michael Falk (Johns Hopkins), and Jaime Marian (UCLA)

Keywords: Grain Boundary, Denuded Zone, Microstate, Order, Metastability

Research Scope

Materials under radiation are far from equilibrium, however metastable interfaces pose an opportunity to tailor radiation damage tolerance, which is an important goal outlined in the *Basic Research Needs (BRN) Workshop for Future Nuclear Energy* report. This project builds on a multi-scale characterization framework developed to understand the interplay of defects with metastable interfaces (i.e., grain boundaries (GBs)) under irradiation. We will investigate how defect absorption events alter the resulting internal GB structure, resulting in metastable interfaces which improve radiation damage tolerance over time. The target materials in this project are those which incorporate self-healing strategies through enhanced control of GBs as defect sinks. Chemical complexity is of critical importance when considering the sink strength of materials, therefore this multi-PI effort seeks to define how metastability is altered in pure/dilute materials versus novel chemically complex alloys (CCAs). In such materials possessing a complex energetic landscape, we hypothesize that the role of the GB vicinity, in addition to the GB itself, affects the ability of a GB to act as an efficient defect sink. To address our hypotheses, we will leverage our toolset of multiscale modeling, experiment, and machine learning tools, to pave a pathway to more predictive design and optimization of modern energy concepts. Our approach will allow for otherwise "unseen" grain boundary structures and order landscapes to be utilized for key outcomes such as radiation tolerance, providing new insight into these critical material systems, as outlined in the *BRN Workshop for Scientific Machine Learning: Core Technologies for Artificial Intelligence*.
In our current program, we seek to pursue the following overarching questions:

- Will we observe more transient behavior near GBs due to defect landscape heterogeneity?
- Does bulk defect bias heterogeneity translate to the GB? In other words, in dilute systems, the bias should be constant, whereas in CCAs there should an increase in the heterogeneity in defect bias toward the GB by virtue of the CCA order landscape.
- Ultimately, will chemical heterogeneity and its implications on defect bias allow for GBs to leverage microstates more effectively for extended absorption efficiency?

Recent Progress

To address the questions above, the team employs a combination of experimental, meso-, and atomistic scales to gain a wholistic understanding of CCA GBs under irradiation. Our focus is aimed toward understanding the fundamental nature of each alloy's chemical landscape, the interplay of chemistry with defect properties, and the resulting effect on sink efficiency, with highlights elaborated including:

1. GB stabilizes metastable structural properties through elastic landscape development;
2. Metastability allows for absorption to persist and for GBs exhibit renewed sink efficiency;
3. Compositional complexity enables GBs to exist in more inherently metastable configurations. Evidence supports the notion that through increasing compositional complexity, prevalence coexistence of structural unit configurations is enhanced;
4. Multi-component alloys exhibit a greater distribution of defect shape and size in comparison to their dilute counterparts, supporting prior defect formation hypotheses.

Pathways for defect migration are limited by elastic effects from lattice distortion defect bias landscape, which we believe dependent on material parameters, such as alloy stoichiometry and defect formation energies;

5. Efficiency of HEA GB defect absorption response will be dictated by (1) defect mobility pathways to boundary mediated by energetic landscape of matrix and (2) interface purity;

Mechanisms Behind the Stabilization of Interfacial Metastable Phases. Results from transmission electron microscopy (TEM) experiments and multiscale modeling efforts provide evidence of dynamic elastic structural evolution of a GB under irradiation [1]. We recognize the absorption proficiency is not a static property. Instead, we propose that as the microscopic structure of the damaged GB is changing during irradiation, the elastic landscape within the boundary ecosystem can transform to promote defect reduction phenomena. An important outcome of our work is highlighting that not only does an enhanced near-GB strain state enhance point defect (PD)-GB interaction, but also enables the coexistence of metastable GB phases. This is illustrated in **Figure 1**, where we see a strain network extending from the boundary at elevated damage doses for a suite of multimodal bicrystalline Cu studies.

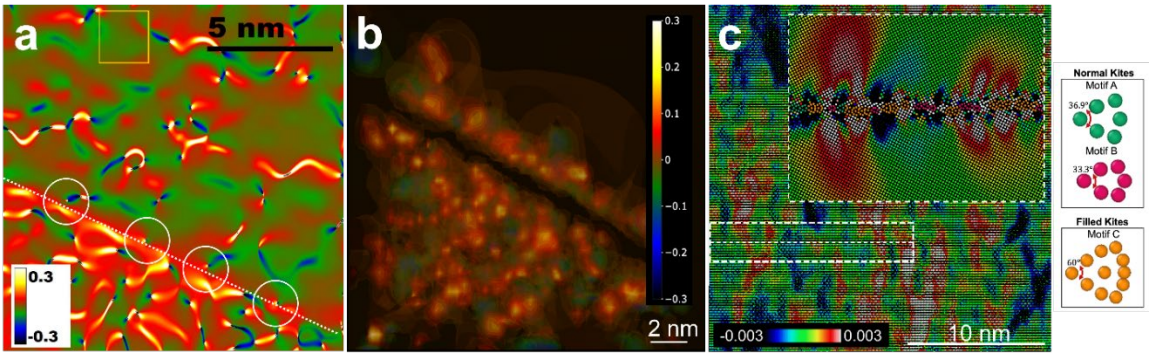

Figure 1. Elastic strain (ε_{yy}) extension from GB in a) irradiated Cu bicrystal experiment at 0.5 dpa, b) relaxed physics-based loop network GB simulation for ∑5 Cu at 1 dpa [2], and c) MD simulation cell stabilizing coexistence of metastable GB phases at 0.5 dpa.

Role of Metastability in Promoting Transient Absorption States. Our results aimed at understanding the GB elastic landscape evolution is most noteworthy considering its implications on GB sink efficiency. Quantitative machine-learning enabled by YOLOv5 object detection framework assisted observations of spatiotemporally dependent defect densities. Work was compared to a molecular dynamics (MD) simulation of a loaded boundary, highlighting emission events caused by ion damage. Here, emission, or "self-healing", is responsible for defect concentration manipulation. We assert that localized emission to reduce saturation restores a GB to a previous absorption state. While the MD and TEM scales differ greatly, we anticipate localized GB emission events must still occur, albeit randomly and immeasurably, in physical systems. Emission will instead compile as long-time defect concentration oscillations detectable within the microstructure as production and annihilation of dislocation loops or clusters.

Compositional Complexity as an Anchor for Metastable Phase Coexistence. MD simulations were conducted on FCC Σ5 bicrystals of varying complexity (Ni, Ni-5Cr, CoCrNi) to pinpoint the effect of chemical complexity on a GB's response to bombardment [3]. Self-interstitial atoms (SIAs) were deposited into the GB to mimic a vacancy bias condition where SIAs arrive at sinks in higher proportions than vacancies. Simulations revealed impacts of damage and chemical complexity

push a system towards greater microstate availability via expansion of the energetic range of GB structural unit. We witness (1) new motifs as irradiation occurs and (2) energy-level-splitting enabling additional motif variations. This work demonstrates a direct observation of open microstate stability pathways through chemistry- and irradiation-induced phase expansion and phase coexistence on a single boundary (**Fig. 2**), which in turn enhances sink efficiency.

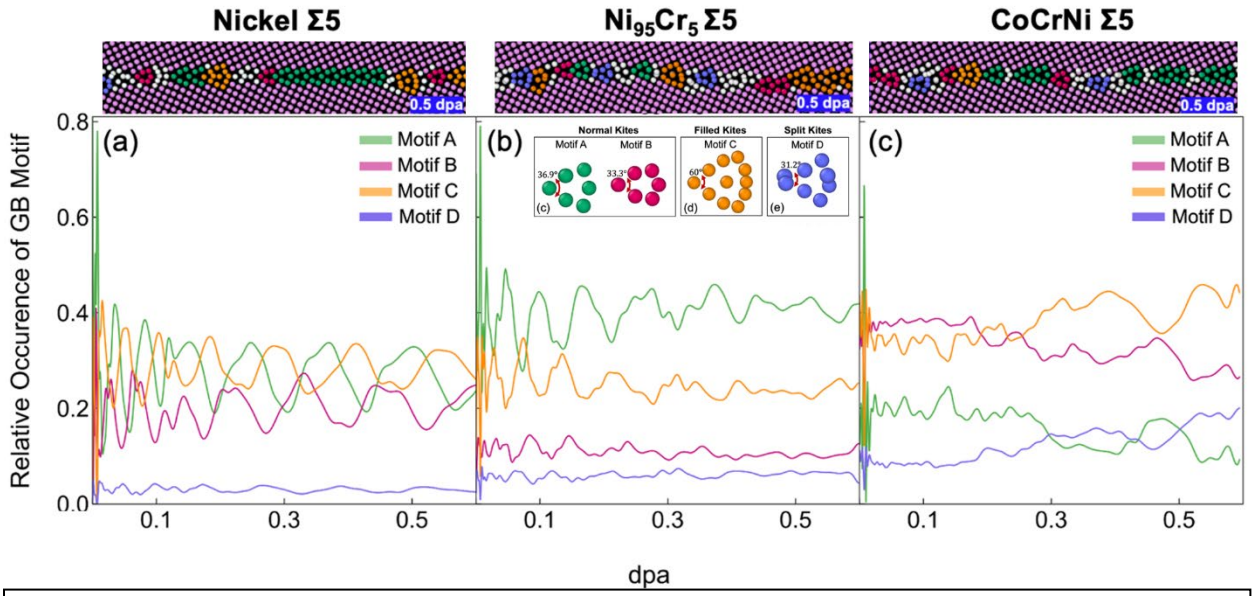

Figure 2**.** Ni, Ni-5Cr, and CoCrNi ∑5 GBs showing GB phase motifs against fraction of motif occurrence as a function of dose. a) GB is free from, or b) with minor solute interactions experience oscillations in structure upon an interstitial flux into the boundary. Increasing the chemical complexity of the grain boundary (c) dynamically alters the mechanism of point defect accommodation and results in global structural evolution.

Quantification of Defect Heterogeneity in Compositionally Complex Alloys. Experiments conducted on CCA compositions against their dilute counterparts exhibit heterogeneous dislocation shapes and sizes. This is consistent with hypotheses posed earlier in the program, where it was anticipated that CCAs would not exhibit a wide variation in defect shape and size due to defect bias landscape influences. An example of this behavior is quantified in **Figure 3**.

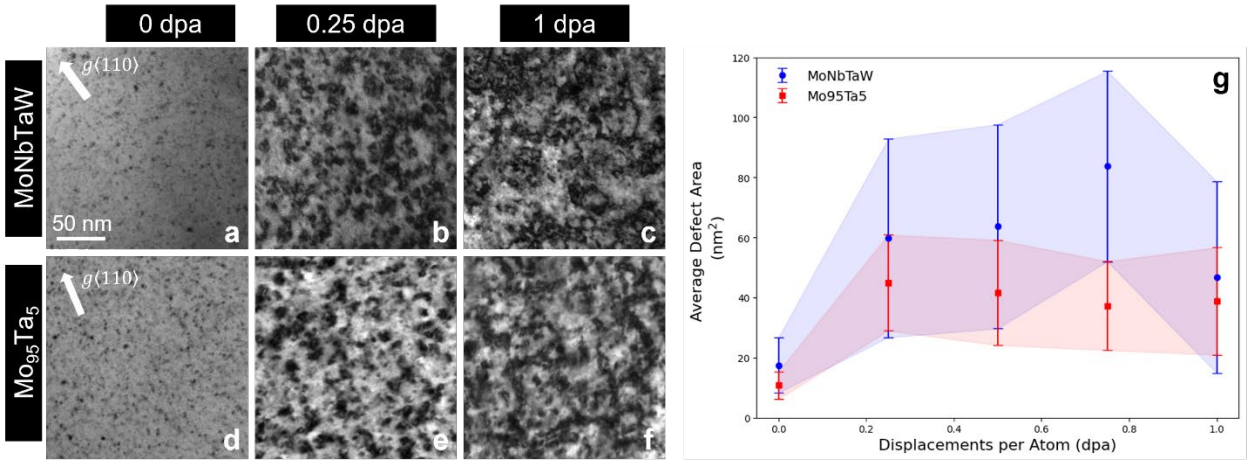

Figure 3**.** a-f) Micrographs from *in situ* irradiation experiment using 1 MeV Kr^{2+} ions at 300°C. g) Comparison of average defect area as a function of damage dose, showing large variation in HEA defect size vs. dilute alloy.

Manipulating Defect Bias: The Implications of Altering Defect Mobility via Vacancy Immobilization. Results from this period explore samples irradiated with dual- 1 MeV Kr^{2+} and 18 keV He^{+} ions in comparison to single-beam (Kr^{2+}). Interestingly, we find the dual beam irradiated sample exhibits suppression of loop size and evidence of severe lattice distortion induced by radiation damage. The experiment presents an opportunity to investigate impact of system vacancy mobility on microstructure via vacancy biasing.

Observing Lattice Distortion as a Passage for Defect Mobility. We investigated the dimensionality and orientation of interstitials in MoNbTaW to determine how lattice distortion and chemical complexity alter the SIA structures from those observed in pure and dilute alloys. It was discovered that SIA mobilities are low in MoNbTaW [4], however the local defect properties are extremely sensitive to chemistry and temperature. Upon increasing temperature, there is a change in diffusion dimensionality from 1-to-3D at 600K. In experiments, we find that defects in MoNbTaW form readily at 573K (**Fig. 3**), and are not visible at higher temperatures, 873K and 1273K.

Exploring Challenges in Compositionally Complex Alloy Design and Impacts on GB Absorption. Recent works have prompted complementary studies given commonly found oxides at CCA GBs. Although much work has yet to be completed, results indicate a difference in absorption capacity between pure interfaces and those that have been inundated with nucleated oxides. Oxidation is a common problem in manufacturing CCAs; therefore, our team is interested in exploring this tangential avenue for translation to more practical applications.

Future Plans

We intend to thoroughly investigate the interplay of chemistry with defect properties and work to define the effect of heterogeneous energetic environments on GB sink efficiency in CCAs. While it is well supported that BCC CCA GBs will exhibit enhanced metastable properties [5], we aim to establish a framework for the implications of this metastability on microstructure through multi-modal techniques, including advanced microscopy and computational efforts.

Pursuits will address the following overarching questions:

1. Will we observe more transient behavior at CCA GBs given anticipated enhancement of metastable GB structural properties?
2. How will elemental localization and lattice distortion influence translate to GB sink strength? More specifically, how spatial deviations in average lattice configuration, including short-range order and GB segregation, impact the GB's ability to accommodate radiation-induced defects?

References

1. Mang, E.H., Barnett, A.K., He, S., Nathaniel II., J.E., Jacobs, R., Morgan, D., Falk., M.L., Marian, J., & Taheri, M.L., (2024). *Metastable grain boundary sink behavior revealed through deep-learning image analysis* [In Review at Nature Communications].
2. He, S., Mang, E. H., Leff, A. C., Zhou, X., Taheri, M. L., & Marian, J. (2024). Complex dislocation loop networks as natural extensions of the sink efficiency of saturated grain boundaries in irradiated metals. *Science Advances*, *10*(18), eadj8395.
3. Barnett, A., Marian, J., Falk, M.L., Taheri, M.L., (2024) *Compositional complexity dictates grain boundary metastability thresholds in fcc metals* [Submitted to Physical Review Letters].
4. Zhou, X., Barnett, A., Mang, E. H., Falk, M. L., Taheri, M. L., & Marian, J. (2024). Self-interstitial atom properties in Nb–Mo–Ta–W alloys. *Computational Materials Science*, *234*, 112765.
5. Geiger, I., Apelian, D., Pan, X., Cao, P., Luo, J., Rupert, T. (2024). Frustrated metastable-to-equilibrium grain boundary structural transition in NbMoTaW due to segregation and chemical complexity, *Acta Materialia*, Volume 272, 119939.

Publications

1. He, S., Mang, E. H., Leff, A. C., Zhou, X., Taheri, M. L., & Marian, J. (2024). Complex dislocation loop networks as natural extensions of the sink efficiency of saturated grain boundaries in irradiated metals. *Science Advances*, *10*(18), eadj8395.
2. Zhou, X., Barnett, A., Mang, E. H., Falk, M. L., Taheri, M. L., & Marian, J. (2024). Self-interstitial atom properties in Nb–Mo–Ta–W alloys. *Computational Materials Science*, *234*, 112765.
3. Foley, D. L., Barnett, A. K., Rakita, Y., Perez, A., Das, P. P., Nicolopoulos, S., Spearot, D. E., Beyerlein, I. J., Falk, M. L., & Taheri, M. L. (2024). Diffuse electron scattering reveals kinetic frustration as origin of order in CoCrNi medium entropy alloy. *Acta Materialia*, *268*, 119753.
4. El-Atwani, O., Barnett, A. K., Martinez, E., Han, J., Leff, A. C., Hung, C.-Y., Nathaniel, J. E., He, S., Mang, E. H., Woryk, L. M., Hattar, K., Uberuaga, B. P., Srolovitz, D. J., Falk, M. L., Marian, J., & Taheri, M. L. (2024). *Grain boundary metastability controls irradiation resistance in nanocrystalline metals* (arXiv:2404.10144). arXiv [In Review at Science Advances].
5. Mang, E.H., Barnett, A.K., He, S., Nathaniel II., J.E., Jacobs, R., Morgan, D., Falk., M.L., Marian, J., & Taheri, M.L., (2024). *Metastable grain boundary sink behavior revealed through deep-learning image analysis* [In Review at Nature Communications].
6. Foley, D.L., Mang, E.H., Wang, Y., & Taheri, M.L., (2024). *Low frequency band-pass Fourier filtering for irradiation damage analysis in the transmission electron microscope* [Under Review at Ultramicroscopy].
7. Barnett, A., Marian, J., Falk, M.L., Taheri, M.L., (2024) *Compositional complexity dictates grain boundary metastability thresholds in fcc metals* [Submitted to Physical Review Letters].
8. Taheri, M.L., Anber, E., Barnett, A., Billinge, S., Birbilis, N., DeCost, B., Foley, D.L., Holcombe, E., Hollenbach, J., Joress, H. and Leigh, G., 2023. *Understanding and leveraging short-range order in compositionally complex alloys*. MRS Bulletin, ***48*(12)**, pp.1280-1291.
9. Hartshorne, M., Leff, A., Vetterick, G., Hopkins, E.M. and Taheri, M.L., 2023. *Grain Boundary Plane Measurement Using Transmission Electron Microscopy Automated Crystallographic Orientation Mapping for Atom Probe*

Mechanisms of Irradiation-Induced Grain Subdivision

Michael R Tonks, Simon Phillpot, Assel Aitkaliyeva (University of Florida)

Keywords: Irradiation-induced grain subdivision, High burnup structure, continuous dynamic recrystallization, atomistic simulation, ion irradiation.

Research Scope

In irradiation-induced grain subdivision (IIGS), metals and ceramics form nanocrystalline grains under irradiation [2,3]. There is debate on whether IIGS results from subgrain formation that forms low angle grain boundaries (LAGBs) or from recrystallization that forms high angle grain boundaries (HAGBs). The understanding of IIGS is incomplete in part because samples have always been characterized post irradiation [2]. Recent experimental results by co-PI Aitkaliyeva and others [1,4] have revealed that subgrains with LAGBs that form during IIGS may transition to form HAGBs, as illustrated in Figure 1. This process is like what occurs during continuous dynamic recrystallization (CDRX) [5] and therefore comparing the two processes will provide critical insights into the fundamental mechanisms of both IIGS and CDRX. In this project, we are identifying the mechanisms driving IIGS in metals and ceramics and compare them to CDRX mechanisms to better understand both phenomena. The project is built on three central hypotheses:

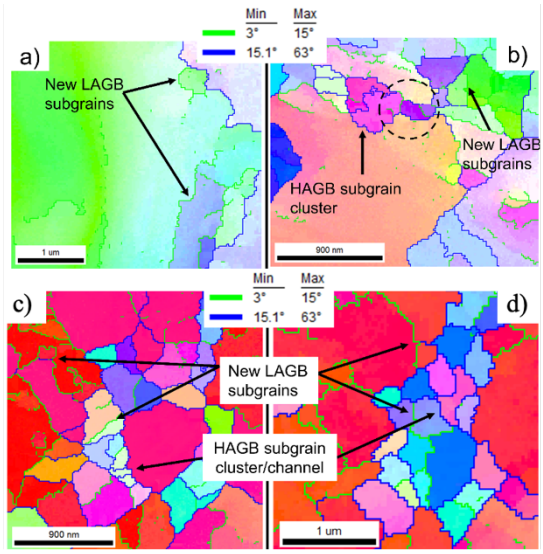

Figure 13: GB misorientation in low fission density (a) and (b) and high fission density (c) and (d) U-Mo fuels, highlighting formation of LAGBs and their transformation to HAGBs [1].

(1) The governing mechanisms for IIGS are the same as for CDRX, except that dislocations are produced by irradiation rather than deformation.
(2) An additional source of stress is required to drive the motion of dislocations produced by irradiation to transform LAGBs to HAGBs.
(3) The IIGS mechanisms are the same in metals and ceramics since the dislocations are generated due to radiation damage and do not require significant ductility.

These hypotheses are being tested using a combination of ion irradiation experiments, atomistic simulation, and mesoscale modeling.

Recent Progress

In the first year of the project, we are focusing on the first hypothesis in which we are seeking to define the governing mechanisms for IIGS using both modeling and ion irradiation experiments and compare them with the mechanisms of CDRX. CDRX has been shown to form via three steps [5]:

(1) Severe plastic deformation results in the formation of extended dislocation networks.
(2) The dislocation networks become LAGBs between subgrains.
(3) The LAGBs gradually become HAGBs as they continuously absorb dislocations.

Based on Hypothesis 1, we predict that during IIGS materials undergo Steps 1 and 2, except that in Step 1, dislocations form from radiation damage rather than from severe plastic deformation. We are using in-situ ion irradiation to observe these steps during irradiation, with specific goals of defining how radiation damage results in dislocation networks, the formation of LAGBs from dislocation networks, and the transition of LAGBs to HAGBs. The experiments in this task are being carried out without an applied load, so we predict that we will not see the transition of LAGBs to HAGBs based on our Hypothesis 2. We are also using atomistic simulations to provide more information about how dislocations form from radiation damage.

Experimental Progress

Preliminary ex-situ ion irradiations are being used to determine temperatures and ion irradiation conditions at which grain subdivision occurs in Al. We are beginning by irradiating at room temperature because room temperature 50 keV He-ion irradiations of Al alloys have been shown to produce dislocation loops and walls, which are precursors to IIGS. We are beginning with room temperature irradiations using He and will gradually increase ion fluence from 1×10^{14} cm^{-2} to 1×10^{17} cm^{-2}. This will allow us to capture the threshold at which grain subdivision begins. In addition to varying ion fluence, we will vary accelerating energies from low (tens of keV) to high (MeV range) and temperatures from room temperature to elevated temperatures. We have obtained polycrystalline samples of pure aluminum and are preparing them for ex situ ion irradiation at Texas A&M. We are also characterizing the initial microstructure of the sample using electron back-scatter diffraction (EBSD) in a scanning electron microscope/focused ion beam (SEM/FIB) instrument. Immediately following irradiation, specimen surface will be characterized again in the same manner. If grain subdivision occurs at a specific ion fluence, the specimen will be sectioned using Ga ion beam in a FIB, and EBSD characterization of the sectioned cross-section collected to verify that subdivision is not confined to the specimen surface.

Atomistic Simulation Progress

To reveal more detailed information about how the clusters grow into loops and collapse into dislocation networks, we are using molecular dynamics (MD) simulations to characterize the

defect generation during irradiation of polycrystalline Al. We will compare the dislocation type and density evolution from the simulations with measured values from the experiments. We are using the LAMMPS software with the Mishin 2004 Al potential and the Ziegler-Biersack-Littmark screened nuclear repulsion potential to screen high-energy collisions. Many different Al potentials were evaluated, and the Mishin 2004 potential was found to be the most accurate with regards to the stacking fault energy and elastic constants. Simulations of Al bicrystals and polycrystals are being carried out to investigate the defect evolution under irradiation. Irradiation will be simulated by directly representing primary knock-on atoms (PKA) and by the Irradiation-Induced Point Defect (IIPD) method in which many point defects, both vacancies and interstitials, are inserted into the microstructure and their subsequent evolution simulated.

We have started with PKA simulations in bicrystal aluminum, as shown in Figure 2. We have constructed bicrystals with various types of GBs (see Figure 2(a)). We have carried out PKA simulations in Al using energies like what we are expecting from our ion irradiation experiments. Simulations are still ongoing for the other two GB structures, but results obtained for the Σ5 (1-20)/100 structure with three different distances between the PKA position and the GB (40 Å, 60 Å, 100 Å) show that the 60 Å shows maximum defect production and optimal annealing of defects. We are now analyzing the result defect generation across the bicrystal resulting from the PKAs (Figure 2(d)). There is a denuded zone around the GB, but it is asymmetric, with more defects remaining on the side where the PKA occurred. We believe this is due to a shielding effect of the GB. We are continuing these simulations with repeated PKAs to see the development of more complex defect structures as possible precursors to IIGS.

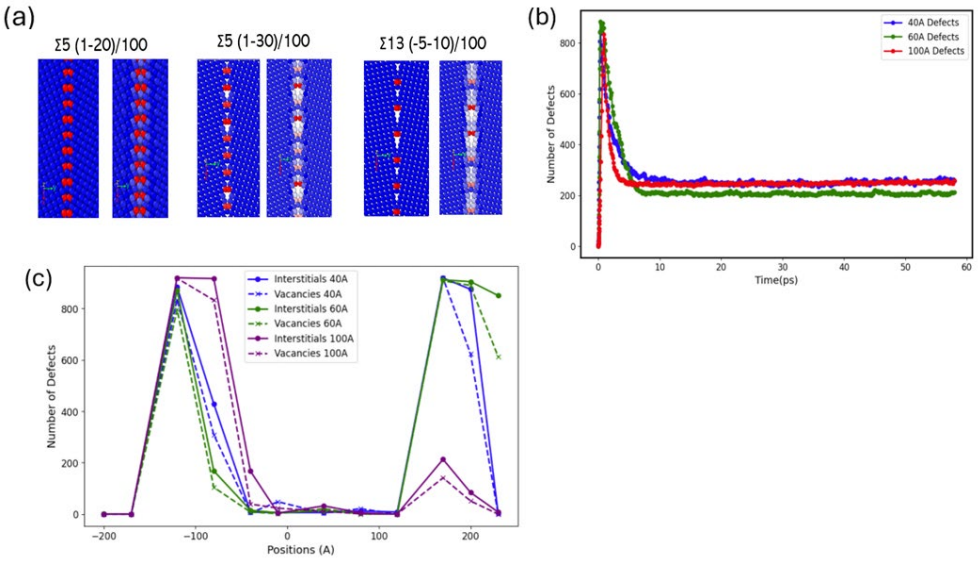

Figure 14: PKA bicrystal simulations using MD, where (a) shows the three GB types used in the simulation, (b) shows the defect production versus time during PKA simulations with various initial PKA distances from the GB and (d) shows the final defect distributions across the bicrystals.

Future Plans

Our future plans are summarized below:

Test Hypothesis 1

- Finish ex situ irradiations of Al to determine conditions for IIGS.
- Carry out in situ irradiations of Al to compare IIGS and CDRX mechanisms.
- Complete MD simulations of Al to investigate dislocation behavior.
- Integrate experimental and atomistic simulation data into theory encompassing our mechanistic understanding of IIGS.

Test Hypothesis 2

- Carry out in situ irradiation of Al with applied stress and quantify any change in crystal orientations.
- Complete MD simulations of subgrain reorientation with and without applied stress.
- Add the mechanism of subgrain reorientation to our theory building on concepts from crystal plasticity.

Test Hypothesis 3

- Repeat ion irraditions using yttria-stabalized zirconium (YSZ) samples and compare with results from Al.
- Repeat MD simulations using YSZ and compare basic mechanisms Al.
- Evaluate theory for YSZ and make modifications as necessary.

References

[1] C.A. Smith, S. Biswas, B.D. Miller, B. Kombaiah, D. Frazer, D.D. Keiser, A. Aitkaliyeva, *High burnup structure formation in U-Mo fuels,* J. Nucl. Mater. **563,** 153617 (2022).

[2] V.V. Rondinella, T. Wiss, *The high burn-up structure in nuclear fuel*, Mater. Today **13,** 24–32 (2010).

[3] L.M. Wang, S.X. Wang, R.C. Ewing, A. Meldrum, R.C. Birtcher, P. Newcomer Provencio, W.J. Weber, H. Matzke, *Irradiation-induced nanostructures*, Mater. Sci. Eng. A, **286,** 72–80 (2000).

[4] T.J. Gerczak, C.M. Parish, P.D. Edmondson, C.A. Baldwin, K.A. Terrani, *Restructuring in high burnup UO_2 studied using modern electron microscopy,* J. Nucl. Mater. **509,** 245–259 (2018).

[5] H.K. Zhang, H. Xiao, X.W. Fang, Q. Zhang, R.E. Logé, K. Huang, *A critical assessment of experimental investigation of dynamic recrystallization of metallic materials*, Mater. Des., **193,** 108873 (2020).

Publications

None so far

Irradiation Defect Formation and Evolution in Doped Metallic Interfaces

Jason R. Trelewicz, Andrea M. Hodge

Keywords: radiation effects, nanocrystalline alloys, amorphous complexions, disconnections

Research Scope

Tailored hierarchical microstructures incorporating grain and interphase boundaries provide energetically favorable sites for combating displacement damage due to irradiation as well as cavity formation from gaseous impurities introduced by implantation or transmutation. Stabilizing a microstructure with a high density of interfacial sinks requires segregated dopants, which will ultimately impact the clustering of gaseous impurities and subsequent formation of bubbles. This research project is studying the impact of dopant species on the mechanisms of gas bubble formation and evolution in interfaces guided by the hypothesis that, at doped metallic interfaces, changes in the local energy landscape due to chemical contributions from the solute species and corresponding structural transitions promote distributed nucleation of bubbles, which in turn delays the critical concentration for bubble coalescence and grain boundary decohesion. Focus of the research has been on synthesis and subsequent helium exposure of nano-metallic multilayers (NMMs) containing amorphous-crystalline interfaces (ACIs) to probe the effect of chemical species and interface structure on bubble nucleation, growth, and coalescence transitions experimentally leveraging previously reported X-ray scattering techniques developed under this project. Atomistic simulations complementing the experiments have expanded on the mechanistic understanding of bubble growth transitions as a function of interface structure and solute concentration, with findings pointing to interfacial transitions that motivated the study of grain boundary disconnection transitions in the presence of solute segregation.

Recent Progress

NMM films featuring ACIs were synthesized within the Fe-W system for an in-situ study of interfacial stability and subsequent helium ion irradiation. Two distinct sample configurations were examined: a laminate multilayer structure denoted as 20-5, comprising a repeating pattern of 5 nm thick amorphous Fe-W layers (with 38 at.% W) combined with 20 nm thick nanocrystalline Fe layers; and the other, a 20-20 configuration consisting of 20 nm thick Fe-W amorphous layers with 20 nm thick nanocrystalline Fe layers. TEM micrographs of the initial multilayer architectures, and their evolution with temperature, are shown for the more stable 20-20 configuration in Figure 1 with elemental mapping and nanobeam diffraction confirming the presence of the Fe-W amorphous layers. The enhanced stability of the 20-20 sample relative to the 5-20 sample was attributed to the intrinsic stability of the Fe-W amorphous alloy disrupting propagating phase transitions in the nanocrystalline Fe layers. This observation provides a critical

insight on the stability of the NMMs, which is critical to selecting implantation temperatures for accessing different defect mobility regimes and central to our hypothesis.

Expanding the Fe-W system to doped grain boundary (DGB) configurations, arrays of 169 combinatorial Fe-W samples were synthesized using magnetron co-sputtering with compositions ranging from 54 – 91 at.% Fe, as depicted in Figure 2. This work has been primarily focused on elucidating the influences of composition, microstructure, and film characteristics on thermal instabilities and early recrystallization. An example of the indexed microstructures are shown with each sample's classification as fully crystalline, mixed, and amorphous based on its respective SAED pattern. Notably, the two spots selected from the mixed nanocrystalline-amorphous regime share the composition of Fe-25 at.% W yet differ significantly in the amorphous content with spot 97 showing an ACI transition. In the context of our hypothesis, the solute distribution in the nanocrystalline samples is of particular interest for accessing doped Fe grain boundary configurations for comparison with the ACI behavior.

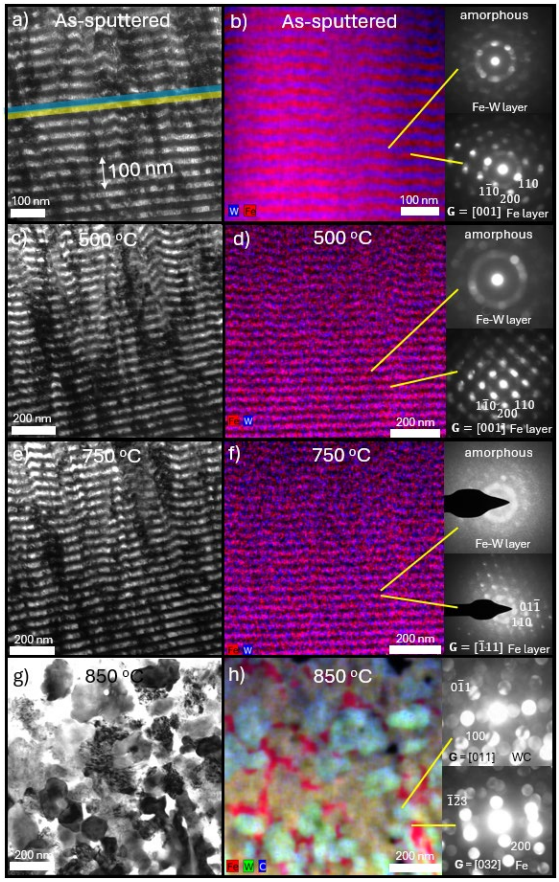

Figure 1. S/TEM results captured during the in-situ experiment of the 20-20 nm Fe-W NMM

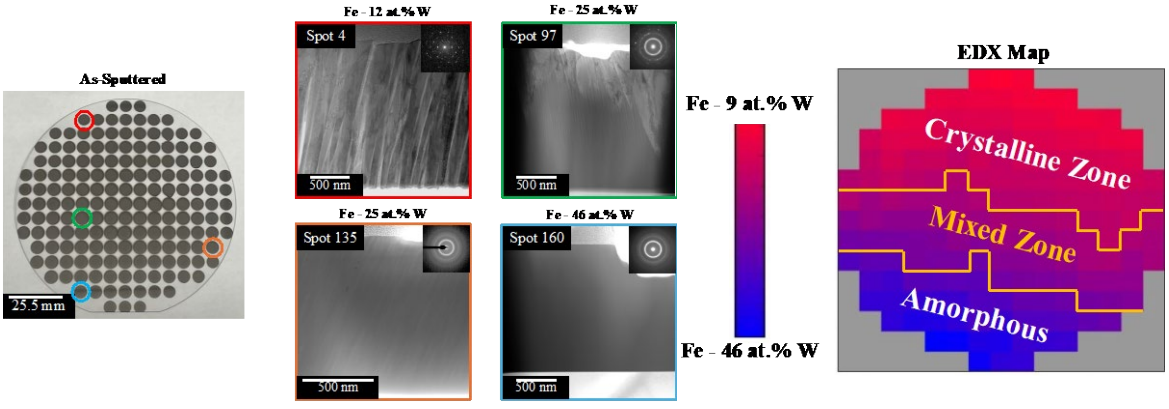

Figure 2. As-sputtered Fe-W material library with color-coded circles indicating samples that were selected for TEM. Four cross-sectional S/TEM micrographs with inset SAED patterns indicating varying degrees of crystallinity, as reflected on the compositional EDS map.

The final set of systems investigated includes three new Fe alloys selected for their propensity to remain crystalline but with doped grain boundaries and amorphous interfaces, commonly termed amorphous complexions. Highlighted in Figure 3 are results on nanocrystalline

Fe-Zr, Fe-Ti, and Fe-Ti-Y alloys where high-resolution imaging combined with EDS maps and FFT patterns indicated the formation of amorphous complexions during quenching from 800 and 1100°C. Grain size mapping and dark-field (DF) TEM images demonstrate a marked enhancement in thermal stability, which is attributed to amorphous complexion formation. The most stable configuration was the Fe-Ti-Y alloy, which maintained its nanocrystalline structure up to 1100°C with thick amorphous complexion formation as confirmed through high-resolution TEM. These materials now provide the stable microstructure needed to explore defect behavior in different mobility regimes, which was limited in Fe-W to > 800°C.

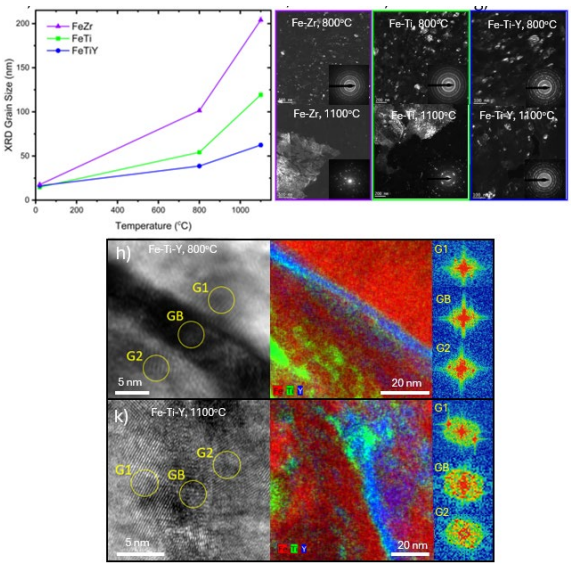

Figure 3. Grain size and DF micrographs for e) Fe-Zr, f) Fe-Ti, and g) Fe-Ti-Y samples. HRTEM, EDS maps, and FFT patterns form the interfacial regions in Fe-Ti-Y powders water-quenched from h) 800°C and k) 1100°C.

Direct probing of interfacial effects on the helium bubble behavior was accomplished via atomistic simulations of three grain boundaries: Σ5{130} tilt, Σ11{110} twist, and Σ13{100} twist, each characterized by unique grain boundary planes and symmetries. Our simulations uncovered a pivotal metric for capturing structural differences on helium defect transitions: the flexibility volume, which is the product of the vibrational mean squared displacement and the average atomic spacing – effectively representing the vibrational capacity of atoms within their sites. Figure 4 illustrates the flexibility volume for each atom across the three boundaries. Introducing 7 helium atoms into a single vacancy within each boundary revealed a correlation between the relaxed bubble volume and the average flexibility volume, demonstrating this metric as an effective indicator for the onset of He bubble formation. Using flexibility volume, He bubble growth was revealed to be a complex interaction involving defect generation, local deformation and structural transformation, stress concentrations, and dislocations.

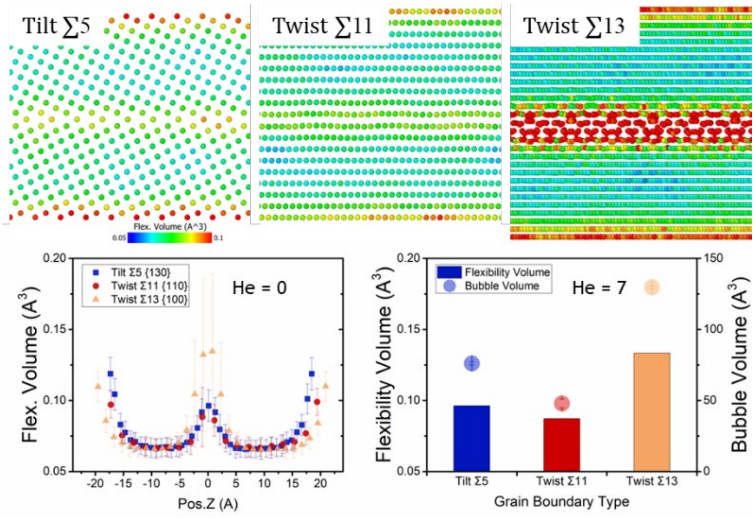

Figure 4. Simulated Fe grain boundary structures with the upper panel showing three grain boundary types colored by flexibility volume. Flexibility volume distribution in different atomic planes parallel to the grain boundary with the average value plotted for each grain boundary type along with the initial He bubble size.

With disconnections serving as mediators of grain boundary plasticity, such as the local changes that transpire upon He bubble growth in the boundary plane, understanding their role in accommodating grain boundary structural transitions during bubble nucleation and growth can provide crucial input for the testing of our hypothesis. Atomistic simulations were therefore designed to measure how alloying affects nucleation barriers for different disconnection modes and uncover how doping influences grain boundary plasticity and defect exchange. Our results indicate that for many GBs, these processes are limited not by the formation, but by the migration of disconnections as the mobility of different modes can vary by orders of magnitude. Low-barrier modes can be suppressed by low mobility, but in cases where low-mobility modes remain favorable, slow-moving disconnections accumulate and roughen the GB and introduce nucleation sites for new disconnections. These findings now connect the observed behavior to local atomic mechanisms transpiring in the grain boundary and provide model systems for exploring the interdependencies of disconnections on helium bubble evolution.

Future Plans

Future plans are focused on completing the multimodal characterization experiments on the helium irradiated Fe-Fe/W multilayers to provide the necessary insights into helium cavity evolution in disordered doped interfaces. The combinatorial sputtering and thermal stability work will key in on compositions exhibiting nanocrystalline grain structures and identify conditions that produce doped grain boundary configurations. The modeling effort will focus on completing the analysis of existing simulation data and translating these results into four planned publications covering cascades and He effects in doped Fe grain boundaries. Collectively, these results provide critical insights into our driving hypothesis on the role of local structural motifs and the underlying interfacial energetics in shifting helium defect transitions in doped metallic interfaces.

Publications

1. Killeen, C., Zhang, Y., Cunningham, W.S., Sprouster, D.J., Trelewicz, J.R., Helium Defect Transitions in Ultrafine Grained Tungsten Revealed Through Microstructurally Informed Synchrotron X-Ray Analysis, Acta Materialia, **under review** (2024)
2. Russell, K., Killeen, C. Peter, N.J., Schwaiger, R., Trelewicz, J.R., Hodge, A.M., *Microstructure and Thermal Stability of Crystalline/Amorphous Fe/FeW Nanomultilayers*, Scripta Materailia, **42**, 115962, 2024
3. Aksoy, D., Cao, P., Trelewicz, J.R., Wharry, J.P., Rupert, T.J., *Enhanced damage tolerance of amorphous interphase and grain boundary complexions in Cu-Ta*, JOM, **76**, 2870–2883, 2024
4. W.S. Cunningham, S.T.J. Mascarenhas, J.S. Riano, W. Wang, S. Hwang, K. Hattar, A.M. Hodge, J.R. Trelewicz, *Unraveling Thermodynamic and Kinetic Contributions to the Stability of Doped Nanocrystalline Alloys using Nanometallic Multilayers*, Advanced Materials, 2200354 (2022)
5. C. D. Appleget, J.S. Riaño, A.M. Hodge, *An Overview of Nano Multilayers as Model Systems for Developing Nanoscale Microstructures*, Materials, **15**, 382 (2022)

Disorder & Diffusion in Complex Oxides: Towards Prediction & Control

Ben Derby, Caitlin Kohnert, Cortney Kreller, Brianna Musico, Yongqiang Wang, Blas Pedro Uberuaga

Los Alamos National Laboratory

Keywords: complex oxides, radiation damage, conductivity, disordering, defect kinetics

Research Scope

To understand damage evolution in irradiated materials, it is imperative to understand how non-equilibrium defects evolve. However, in complex oxides such as spinels, pyrochlores, and perovskites, the kinetics of defects is not a simple function of crystal structure and chemistry. As a material is irradiated, the distribution of cations changes, often from an ordered state to a disordered state. The material can also undergo a phase transformation to a new structure. These changes impact the kinetic properties of those defects. This project is focused on understanding the relationship between these irradiation-induced metastable states and transport. We use irradiation as a tool to modify the structure of the material and then probe the consequences on conductivity. Experimental studies are complemented by computational modeling to provide a comprehensive view of mass transport in these systems. While in the past we have focused extensively on pyrochlores and spinels, we have shifted our attention to sesquioxides, including Bi_2O_3 and interlanthanide oxides, containing two lanthanide cations. The phase diagrams of these Ln sesquioxides display many phases, including several that are disordered [1], which suggest that they may exhibit interesting behavior under irradiation. Our efforts reveal new insight into the structure-property relationship between cation ordering/disorder and mass transport, informing materials design and optimization for a wide-range of applications from nuclear energy systems to fast ion conductors.

Recent Progress

Over the last two years, we have targeted radiation-induced metastability in oxides and the resulting impact on properties. Specifically, we have focused on Ln oxides and Bi_2O_3.

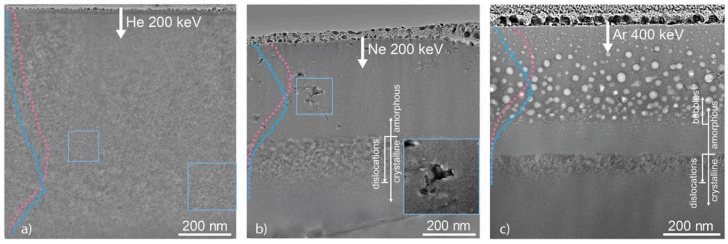

The bubble structure in Bi_2O_3 as a function of implanting species. When He is implanted, the material remains crystalline and the bubbles that are formed are very small (barely visible in this micrograph). However, when the material amorphizes when implanted by Ar, bubble kinetics is enhanced and the bubbles coarsen significantly.

Bi_2O_3 has been extensively studied for its application as a fast-ion conductor. In particular, this compound exhibits multiple polymorphs and the high temperature delta phase – δ-Bi_2O_3 – exhibits high conductivity. In contrast, the low temperature polymorph α-Bi_2O_3 does not. The question we posed is whether radiation could induce the phase transformation to the higher temperature phase and those provide a route to stabilizing this phase at lower temperature. We did not observe such a phase transformation but the resulting behavior was still quite interesting.

We irradiated α-Bi_2O_3 at room temperature with three different ion species – He, Ne, and Ar – chosen because their masses are sufficiently different and thus the nature of the damage process associated with each would also be different [2]. He is expected to produce dispersed Frenkel pairs while Ar will create dense collision cascades; Ne is somewhere in between. In the case of He, we saw little structural changes to doses of 2.5 dpa. However, with Ar, even doses as low as 0.1 dpa induced amorphization. We attribute the difference to differences in electronic stopping powers.

However, even more interesting is the behavior of the implanted gas as a function of the irradiation-induced amorphization. In the case of He, where we saw no amorphization, the bubbles remain small and dispersed. However, when irradiated with Ar, the resulting bubbles coarsen and become much larger. This indicates that atomic transport is much higher in the amorphous phase. Further, when irradiating α-Bi_2O_3 with Ar at 300 C, there is no amorphization and the bubbles remain smaller. These results highlight how we can use ion irradiation to indirectly inform us about defect kinetics in the material. Further, we were able to correlate the local changes in microstructure with the electronic structure: the amorphous regions exhibited a larger band gap than the crystalline regions, further emphasizing the impact of irradiation on the properties of the material.

Regarding the Ln oxides, we have begun our efforts examining the metastability of different polymorphs using density functional theory (DFT) [3,4]. Starting with Ln_2O_3 compounds, we computed the energy of the metastable phases and determined the sequence in which they would form as energy is supplied to the system, across the entire Ln series. Using Lu_2O_3 as a prototype, we then irradiated the material to various fluences and determined the phase evolution as a function of dose using grazing incidence x-ray diffraction. Different phases appeared in Lu_2O_3 as more dose – more energy – was supplied to the system in precisely the same sequence as was predicted theoretically, providing validation of the theoretical treatment.

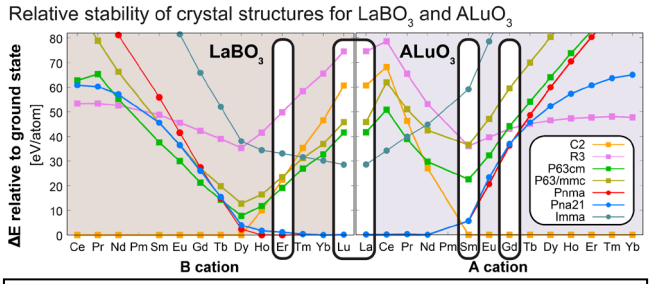

DFT calculations reveal that the phase stability of interlanthanide oxides is very sensitive to the chemistry. In particular, the ground state varies with the cation chemistry, as does the ease of metastable phase formation, which we hypothesize correlates with the radiation damage response of the compound.

We then considered the interlanthanide sesquioxides LnLn'O_3. These compounds are interesting as, depending on the chemistry, they can form either a fluorite-based bixbyite structure or a perovskite structure. In addition, they exhibit a complex phase diagram in which, at high temperature, disordered phases can occur, in contrast to other perovskite compounds such as $LuAlO_3$ which is a line compound up to the melt. This suggests that the radiation damage behavior of the LnLn'O_3 compounds could be much more interesting. Our DFT calculations support this supposition, revealing that, depending on the chemistry of the compound, the propensity to form metastable phases varies significantly. Compare, for example, $ErLuO_3$ and $SmLuO_3$. Both adopt

the cubic bixbyite structure in their ground state. However, the lowest metastable phase for $SmLuO_3$ is a perovskite phase that is only about 5 eV/atom above the ground state while that for $ErLuO_3$ is a hexagonal phase that is nearly 50 eV/atom above the ground state. This suggests that $SmLuO_3$ is much more flexible in terms of the cation coordination and thus potentially more resilient against radiation damage than $LuSmO_3$.

To validate this hypothesis, we are currently synthesizing these materials. Using wet chemistry approaches, we have successfully synthesized $LaLuO_3$ (which crystallizes in the perovskite structure in its ground state), $ErLuO_3$ and $SmLuO_3$, both of which form the bixbyite structure as predicted. The resulting materials are single phase and are currently being irradiated and characterized to determine any differences in radiation damage response of the three interlanthanide sesquioxides.

Pucks of interlanthanide oxides as synthesized and sintered for three different chemistries. XRD confirms that the first two crystalize in the bixbyite structures while the last is in the perovskite structure, consistent with our DFT calculations.

Future Plans

Our future plans involve correlating any observed differences in radiation damage response of the interlanthanide sesquioxides with the predicted differences in metastable phase formation. There are a number of intriguing aspects we will focus on. First, as mentioned, the first metastable phase for $SmLuO_3$ is perovskite structured, which is a much more ordered compound than the essentially solid-solution bixbyite. If irradiation can lead to the formation of a more ordered compound, this would be quite interesting and surprising, as typically (though not universally) irradiation is thought to promote disorder. Second, while the next metastable phase for $LaLuO_3$ is significantly higher in energy than the ground state, the phase diagram of the La interlanthanide sesquioxides tend to exhibit disordered phases at high temperature, suggesting that a cation order-disorder transition is possible, perhaps accompanied by a structural phase transformation at the same time. The extent to which the $LaLuO_3$ compound differs in its response to irradiation as compared to other perovskite compounds is very interesting. Finally, there is the question, as posed above, as to whether there is any correlation between the propensity to form metastable phases and radiation-induced structural changes.

A key focus of this project is to understand how these radiation-induced changes, including cation disorder and phase transformations, impact defect kinetics. To that end, we will be performing AC impedance spectroscopy on materials before and after irradiation to understand how the radiation-induced structural changes impact the conductivity. These measurements require growing thin films of our compounds on substrates that are electrochemically very different to distinguish the conductivity of the material of interest from the substrate, similar to what we've done in the past with other materials [5]. We will also examine the radiation-induced changes in conductivity in situ, using a new capability developed in part as part of this project. Our preliminary molecular dynamics simulations reveal that the conductivity is sensitive to the base

chemistry of the oxide. How radiation-induced conductivity is further modified by the compound chemistry will be very interesting.

While our irradiation studies of α-Bi_2O_3 provided unique insight into the dependence of gas kinetics on the structure of the compound, we were unable to induce a phase change to the fast-ion conducting delta phase. However, we have recently been able to grow a thin film in that structure. We will characterize the behavior of radiation damage in this system and determine if a radiation-induced phase transformation to either the more stable alpha phase or to an amorphous structure is more likely. We will characterize how the kinetics of defects and the ionic conductivity are impacted by the radiation-induced structure. This will further inform how radiation impacts fundamental transport mechanisms in ceramics.

Finally, we will follow up on our recent theoretical discovery of what we called double spinels, low energy ordered compounds that contain three cations in the spinel structure. We have previously unsuccessfully attempted to synthesize these through ball milling techniques. With the new access to wet chemistry methods, we will revisit these compounds, attempt to synthesize the most stable versions, and examine their disordering behavior under irradiation.

References

1. J. Coutures, A. Rouanet, R. Verges, and M. Foex, *Etude a Haute Température Des Systèmes Formes Par Le Sesquioxyde de Lanthane et Les Sesquioxydes de Lanthanides. I. Diagrammes de Phases (1400°C < T < T Liquide),* Journal of Solid State Chemistry **17**, 171 (1976).
2. E. R. Kennedy, J. A. Valdez, Y.-Q. Wang, S. Ribet, K. E. Sickafus, C. R. Kreller, B. P. Uberuaga, and B. Derby, *Insights into Defect Kinetics, Mass Transport, and Electronic Structure from Spectrum Effects in Ion-Irradiated Bi_2O_3*, under review.
3. V. Kocevski, J. A. Valdez, B. K. Derby, Y.-Q. Wang, G. Pilania, and B. P. Uberuaga, *Predicting and accessing metastable phases*, Materials Advances **4**, 1101 (2023).
4. V. Kocevski, G. Pilania, and B. P. Uberuaga, *Thermodynamics of phase stability and disorder in Inter-Lanthanide ternary ABO_3 oxides from first principles*, Materials & Design **228**, 111830 (2023).
5. C. R. Kreller, J. A. Valdez, T. G. Holesinger, J. Morgan, Y.-Q. Wang, M. Tang, F. H. Garzon, R. Mukundan, E. L. Brosha, and B. P. Uberuaga, *Massively enhanced ionic transport in irradiated crystalline pyrochlore*, Journal of Materials Chemistry A **7**, 3917 (2019).

Publications

1. V Kocevski, G Pilania, and BP Uberuaga, *Thermodynamics of phase stability and disorder in Inter-Lanthanide ternary ABO_3 oxides from first principles*, Materials & Design **228**, 111830 (2023).
2. V Kocevski, JA Valdez, BK Derby, YQ Wang, G Pilania, and BP Uberuaga, *Predicting and accessing metastable phases*, Materials Advances 4, 1101 (2023).
3. V Kocevski, G Pilania, and BP Uberuaga, *How inversion relates to disordering tendencies in complex oxides*, Physical Chemistry Chemical Physics **25**, 27189 (2023).
4. SK Pinzon, JA Valdez, V Kocevski, JK Baldwin, BP Uberuaga, CR Kreller, and BK Derby, *Effects of processing parameters on the morphologies of complex sesquioxide thin films*, Journal of Vacuum Science & Technology A **41**, 033404 (2023).

Understanding the Competition between Plastic Flow and Fracture in BCC Transition Metals

Christopher R. Weinberger, Colorado State University
Gregory B. Thompson, University of Alabama

Keywords: Brittle-to-Ductile Transition, Fracture, Dislocations

Research Scope

The ductility and formability of body-centered-cubic (BCC) metals can vary significantly, with the origins for such differences being rather elusive. For example, molybdenum and tungsten are quite limited in their ductility and formability while niobium and tantalum easily deform. For those with limited formability, engineering solutions, such as thermomechanical processing and alloying, are primarily used to improve these properties. In this program we will test the hypothesis that extrinsic point defects, *i.e.*, impurities, are more influential to the ductility of certain BCC metals than others. Through an integrated experimental and modeling approach, we will understand the origins of embrittlement regarding extrinsic impurities, both the impurity types and their concentration. The experiments will examine the change in material properties with respect to impurity level, including dislocation mobility and intrinsic fracture behavior, that will be used in a semi-analytic coupled plasticity-fracture model of the brittle-to-ductile transition temperature (BDTT). This model will enable us to fundamentally determine if and how impurities influence these BCC metals' mechanical properties lending fundamental insight into the use of alloying engineering solutions that are currently employed.

Recent Progress

We have developed a 2-dimensional discrete dislocation dynamics (DDD) model coupled with a crack to simulate the soft brittle-to-ductile transition (BDT) in BCC refractory metals, Fig. 1(a). This model can reproduce the thermally activated nature of the BDT through the incorporation of the thermally activated nature of plasticity in BCC metals and accounting for the crack tip shielding effects of dislocations based on the work of Roberts *et al.* [1-2].

A major advancement of this work is to demonstrate that the activation energy of the BDT, E_{BDT}, is directly related to the activation energy for dislocation motion, ΔH, through an effective stress of the simulation τ_e, in other words $\Delta H(\tau_e) = E_{BDT}$ as shown in Figure 1(b). This holds true regardless of the functional form of the activation enthalpy of the dislocation mobility and that the effective stress, τ_e, is independent of the choice of the dislocation mobility. Thus, the effective stress depends on other parameters in the simulation. We have further shown that the effective stress is related to the source position, s, and intrinsic fracture resistance, K_C^T, as: $\tau_e = \alpha K_C^T/\sqrt{s}$, as shown in Figure 1(c). This is significant because it creates a direct relationship between experimental parameters such as the crack tip toughness K_C^T, which is related to surface energy,

and source position, s, which is related to processing and microstructure to the activation energy for the BDT through the dislocation mobility.

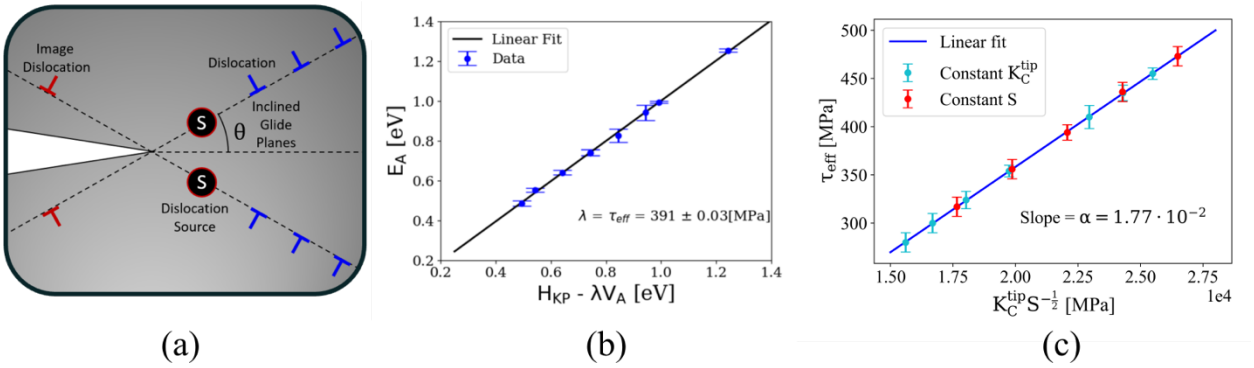

(a) (b) (c)

Fig. 1 (a) A schematic illustrating the 2D discrete dislocation dynamics model including the crack, dislocation sources, and dislocations. (b) A plot of the activation energy of the BDT as a function of the dislocation mobility law demonstrating that they are equal with an effective stress of 391 MPa. (c) A plot of the effective stress versus $K_C^{tip} S^{-1/2}$ demonstrating linearity with a slope of 0.0177.

To address our original question about the BDT between tantalum and tungsten, we have also utilized our model to predict the differences in BDT temperature for these two metals. The BDTT for a nominal loading rate gives a value of 430 K for W and 59 K for Ta. The main parameters for our models are the activation energy for dislocation motion, which comes from experiments, the source position, which we keep the same, and the intrinsic fracture resistance. The intrinsic fracture resistance of W was reported in experiments and match calculations of surface energies of the {001} surfaces, so we have used the DFT computed surface energy for Ta to estimate its intrinsic fracture resistance. Thus, our initial results from this work suggest that indeed intrinsic dislocation mobility can explain the differences in the BDTT of Ta and W. However, extension of this work to the other BCC metals for which we have dislocation mobility parameters (Mo, Nb, and Fe) provide fewer convincing results. Notably the BDTT of Nb is too high – of order 160 K where Nb's reported BDT being somewhere between 4-77 K. This indicates that intrinsic dislocation mobility can explain some of the differences but cannot fully differentiate Nb from W.

To support the computational modeling, a series of experimental tests of the BDTT is required. This requires enough measurements of fracture toughness across temperature ranges and, for this project, impurity levels, to be significantly different in deviations from measurement-to-measurement. This facilitates the requirement for a large number of samples. To address this need, we have developed a method to fabricate microscale samples for determining fracture toughness. This was achieved by combining electrojet polishing to single crystal tungsten samples to thin them into the microscale thickness after which a focus ion beam (FIB) process to cut the cantilever beam sides out. This combined jet-polish – FIB preparation eliminates this undercutting of the

cantilever beam thereby significantly reducing the time to produce a beam by approximately one-third compared to only using FIB milling. And, if multiple beams are made simultaneously, the time savings is compounded. This procedure is schematically shown in Figure 2, with further details reported in our recent paper [3].

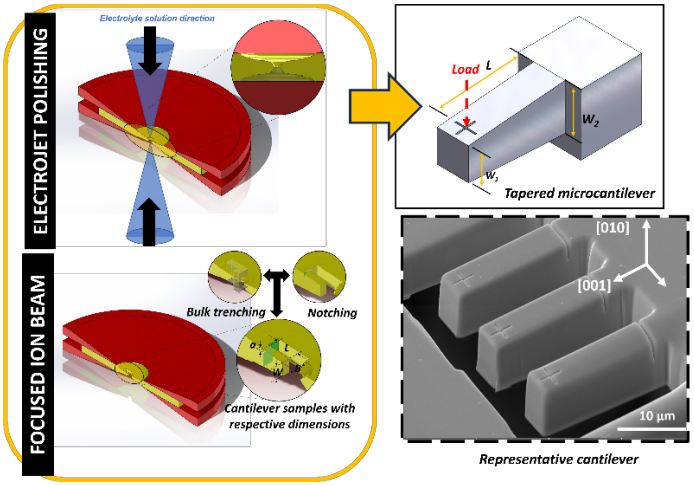

Fig.2 Rapid microcantilever preparation technique using electrojet polishing and focused ion beam fabrication (The prepared microcantilevers are indicated in the bottom right corner along [001] direction determined by electron backscatter diffraction mapping)

Finally, in order to accurately report fracture toughness values, it is critical to have a well-established cracks profiles and depths as the analysis of fracture toughness assumes constant cross-sections and straight crack profiles. However, this is often not achieved from FIB machining. Thus, prior to examining the BDT and the role of impurities, we initiated a study of the role of FIB cut crack profiles and its influence on the reported fracture toughness. Notably, we found that the crack depth profile can be influenced by the way the material is cut from the bulk sample using the FIB. If the crack is cut with direct access a free surface, the notch depth on either beam side is much deeper than those found in the center of the beam. Access to the free surface facilitated the readily removal of material on the sides but not in the interior portions of the beam creating an inverted parabolic notch profile. This asymmetry has the potential to create substantial experimental uncertainty in the evaluation of the fracture toughness. To help correct this, we have now found that varying the cutting procedure, notably cutting the notch first and then the sides, has the potential to greatly improve the consistency of the crack profile and measurements to support our models. We anticipate that these results will have substantial impact on FIB-based micromechanical preparatory procedures for the community.

Future Plans

Previously, we computed the influence of point defects on the cleavage energy for tantalum and tungsten. With the full development of our discrete dislocation dynamics models, we will now use these cleavage energies as inputs to these models to understand how impurities affect the BDT. While we expect these changes to be modest, it is now important to see if this can rationalize the differences seen between the group IVB and VB transition bcc metals.

Anticipating that impurity concentrations will be too low to alter cleavage energies sufficient to influence the BDT temperatures, we are also planning to examine how point defects themselves affect dislocation mobility. Here, we will examine how the point defects bind to the dislocation cores to determine their effects on mobility from which we will propagate these results into our discrete dislocation dynamics model. We will then use this outcome to examine if the effects of point defects can indeed alter dislocation mobility sufficiently to explain the BDT temperatures.

The result of the effective stress above led us also to consider another factor on the BDTT - the role of non-singular stresses. To this point, we have to date only considered singular stress fields through the applied stress intensity factor, which follows traditional fracture mechanics. However, our results suggest that τ_e is of the order of hundreds of MPa's, which means in certain cases the applied stress could affect dislocation mobility near the crack and hence the BDT. We plan on using our model to explore this possibility and determine what this may imply in terms of size effects on fracture toughness measurements.

We are now positioned to use a rapid means for mechanical testing (paper below) with a correct FIB-based notching process to determine the BDT temperature of pure tungsten as a control. After which, we will systematically implant different impurity solute types (oxygen and nitrogen) and vary their concentrations to measure how the BDTT changes. These experimental results will then be compared to our model to understand if and how impurities affect the cleavage energy, dislocation mobility, or both, and how that changes the BDTT.

References

1. A. Giannattasio , Z. Yao , E. Tarleton and S.G. Roberts, *Brittle–ductile transitions in polycrystalline tungsten*, Philosophical Magazine, **90**, 3947 (2010).

2. E. Tarleton and S.G. Roberts, *Dislocation dynamic modelling of the brittle–ductile transition in tungsten*, Philosphical Magazine, **89**, 1478 (2009).

3. M. T. Islam, C. R. Weinberger, and G. B. Thompson, *Rapid microcantilever preparation for conditional fracture toughness evaluation*, Journal of Materials Research and Technology **30**, 5444-5454 (2024).

Publications

1. M. T. Islam, C. R. Weinberger, and G. B. Thompson, *Rapid microcantilever preparation for conditional fracture toughness evaluation*, Journal of Materials Research and Technology **30**, 5444-5454 (2024).

DE-SC0020150: Irradiation Tailoring of Deformation-Induced Phase Transformations

Janelle P. Wharry (Purdue University)

Keywords: Voids, Deformation-Induced Martensite, fcc Alloys, Phase Transformations

Research Scope

The ***objective of this project is to understand how irradiation enables deformation-induced phase transformations in fcc alloys***. Low-temperature deformation of face centered cubic (fcc) metals and alloys can occur through several modes, one of which is martensitic transformation, wherein fcc γ-Fe austenite reverts to hexagonal close packed (hcp) ε-martensite or body centered cubic (bcc) α'-martensite. Irradiation is believed to enhance the tendency for this transformation to occur, considering that irradiation similarly enhances other low-temperature deformation modes such as dislocation channeling and deformation twinning. However, the mechanisms underlying the irradiation enhancement of martensitic transformations remain unknown. Many studies have ascribed any martensites to twinning associated with irradiation-induced dislocation loops [1-2]. But more recently, porosity has been shown to enhance the martensitic transformation in shape memory alloys [3-4] through surface energy effects. Thus, the role of both interstitial-type (e.g., loops) and vacancy-type (e.g., cavities) irradiation defects on the phase transformation must be understood. An altered tendency to phase transform can have severe implications on the performance of load-bearing materials exposed to irradiation, such as nuclear reactor structural materials. More scientifically, using irradiation to tailor the austenite-to-martensite phase transformation can facilitate materials design and innovation across numerous energy generation applications. Thus, there is a critical need to understand exactly how irradiation affects and enables the deformation-induced martensitic phase transformation.

This hypothesis will be tested using a multiscale approach that combines novel small-scale mechanical testing and *in situ* electron microscopy investigations with mechanics models that will help us interpret and expand the parametric space of our experiments. Work will focus on Fe-*x*Mn alloys irradiated with He and/or other ions to create tailored microstructures that are dominated either by vacancy-type or interstitial-type defects, or some combination of these extremes. We will utilize small-scale mechanical testing techniques to introduce deformation. Nanoindentation will rapidly check for twinning or martensitic transformations over a range of irradiation and loading conditions, and post-indentation microstructure characterization will enable us to associate specific irradiation conditions with deformation mechanisms. Transmission electron microscopic (TEM) *in situ* deformation will reveal nano/micro-scale mechanisms of twinning and deformation-induced martensite nucleation at specific irradiation-induced defects. Molecular dynamics (MD) simulations will elucidate exactly how deformation mechanisms initiate and propagate at and around irradiation-induced defects.

Recent Progress

Experimental – We fabricated five Fe-xMn (x = 34, 36, 39, 41, 46 in at%) alloys that have a stable fcc austenitic structure that we believe will transform to martensite when irradiation **and**

strain are applied. Thus far, we have determined deformation mechanisms before irradiation using nanoindentation on targeted grains with subsequent focused ion beam (FIB) milling to extract transmission electron microscopy (TEM) lamellae that enable us to observe the deformation microstructure. The Fe-34Mn exhibited extensive deformation twinning, confirmed by selected area electron diffraction (SAED) at the mesoscale, with high resolution TEM (HR-TEM) revealed the atomic structure at deformation twin interfaces, and fast Fourier transformation (FFT) confirmed the twinning reflections, Figure 1(a). Near the indent (i.e., at a higher strain), deformation twins intersected with strain-induced ε-hcp martensite needles only a few atomic layers thick, as confirmed by streaks in the FFT pattern, Figure 1(b). Higher Mn content appeared to suppress deformation twinning and martensitic transformation in favor of dislocation-mediated deformation. In Fe-46Mn, dark field TEM of the deformation microstructure revealed a high dislocation density, especially along annealing twin boundaries, Figure 1(c-d).

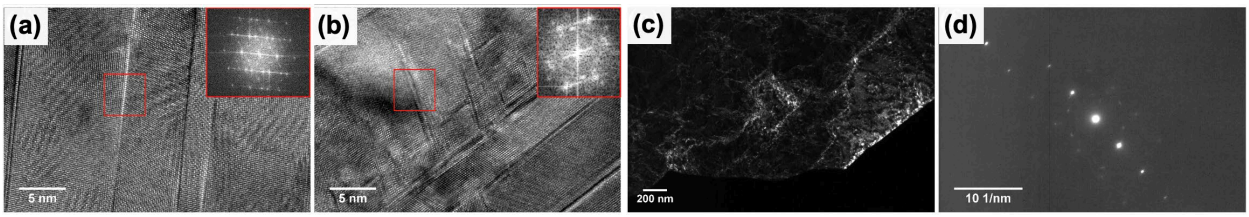

Figure 1: Nanoindentation induced deformation microstructures in (a-b) unirradiated Fe-34Mn showing HR-TEM and FFT images confirming deformation twinning; and in unirradiated Fe-46Mn showing (c) weak-beam dark field image and (d) the corresponding diffraction condition confirming dislocation-mediated deformation.

We have prepared and irradiated two sets of specimens of all five alloys. Since irradiation can compromise surface quality and subsequently make grain orientation mapping by electron backscatter diffraction (EBSD) impossible, we conducted EBSD grain orientation mapping of all five specimens in each set before irradiation. The mapped areas were marked with fiducials, and we identified at least one <100>, <101>, and <111> grain that could be identified post-irradiation. We then conducted two irradiations:

1. *Bubble-dominated microstructure:* 1 MeV He^{+} ions, 500°C, fluence 2 x 10^{16} ions/cm^2
2. *Defect-dominated microstructure:* 2 MeV protons, 300°C, fluence 1 dpa

Simulations **–** An embedded-atom method (EAM) potential for Fe-Ni-Cr [5] was used to simulate strain-induced transformations in Fe-50Ni using molecular dynamics (MD). We selected this system rather than the Fe-Mn system we are studying in parallel experiments, because of a lack of a reasonable interatomic potential for Fe-Mn that can meaningfully describe fcc-bcc-hcp transformations. We set up four unique simulations that were loaded uniaxially (in the z-direction) with strain rate 0.001 ps^{-1}, to a total strain of 0.15 as follows:

1. pristine fcc single crystal – i.e., reference simulation
2. fcc single crystal with random vacancies at a concentration of 10^{-4} (atomic %)
3. fcc single crystal with 1.26 nm radius (5 atoms) spherical void at center of simulation cell
4. fcc single crystal with 2.02 nm radius (8 atoms) spherical void at center of simulation cell

Strain distributions and crystallographic orientation relationships are shown in Fig. 5 for the reference and 1.26 nm void simulations. Phase and shear strain maps of a two-dimensional slice taken parallel to the loading axis reveal that martensite phases exist wherever the shear strain is

larger than ~0.15, confirming that the fcc-bcc transformation is strain-induced. High shear strain around the void (Fig. 5e) can explain the concentration of bcc phases around the void (Figs. 5c, 5f). Both the Kurdjumov-Sachs (KS) and Nishiyama-Wassermann (NW) orientation relationships (ORs) are present and are consistent across all of the simulation cells (though Fig. 5g shows only the 1.26 nm void simulation for clarity of illustration); no intermediate hcp martensite phase is found. Voids become unstable at high strains (Fig. 5h), leading to loss of material integrity, which explains the peaks in the stress-strain and bcc%-strain curves in the voided simulations.

The effect of vacancies on the strain-induced martensite transformation is not sufficiently significant to resolve, at least at the vacancy concentrations studied. By contrast, voids aid in the martensite transformation. In order for the fcc-to-bcc transformation to occur, local stress must reach a critical value to induce $1/6\{111\}\langle 211\rangle_{FCC}$ partial dislocation generation and movement. A void can cause stress concentration, increasing the likelihood that local stresses reach the critical value needed for partial dislocation generation and sliding. Additionally, strain may accumulate at the void, as the void acts as an obstacle for dislocation movement.

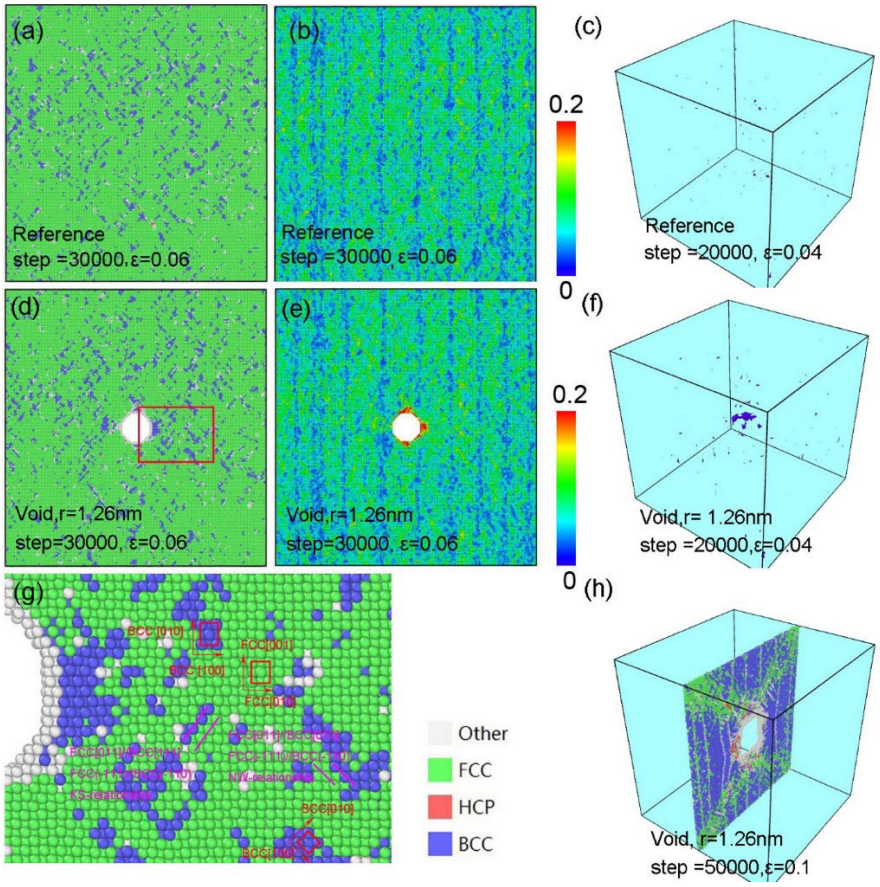

Figure 2: Snapshots of (a) reference simulation phase map, (b) shear strain map, (c) bcc surfaces in simulation box; and small void simulation (d) phase map, (e) shear strain map, (f) bcc surfaces in simulation box, (g) higher resolution view of framed region in (d) showing fcc-bcc orientation relationships, (h) high strain phase map showing void distortion and indicating the position of the 2D maps in taken from the simulation box.

Stress-Induced Transformations – We have also studied stress-induced (i.e., reversible) martensitic transformations to draw contrasts with the strain-induced transformations described previously. We conducted MD simulations of Ni-50Ti containing various point defects: (a) pristine, no defects; 10^{-4} at% concentration of (b) vacancies, (c) interstitials, and (d) anti-site defects; and (e) vacancy clusters formed by equilibration of 10^{-3} at% concentration of vacancies. Both the forward (B2 to B19') and reverse transformations were simulated. In this system, defects inhibited the transformation relative to the pristine simulation, with the vacancy clusters having the most pronounced effect on slowing the transformation. These results are notably different from our observations on strain-induced transformations, which suggest that cavities (which are not unlike the vacancy clusters here) should enhance the transformability by reducing the critical transformation stress. However, these results indicate that irradiation-like defects may suppress transformability to some degree. We are intrigued by these contrasting behaviors and hope to ascertain a unifying explanation for the role of defects on martensitic transformations at varying SFEs and for strain- versus stress-induced modes.

Future Plans

We will test and characterize the post-irradiation Fe-Mn specimens. We will use our pre-irradiation SEM EBSD grain orientation maps to guide us in conducting nanoindentation, conduct FIB to extract lamella, then finally use TEM/HR-TEM to characterize the deformation microstructures. We will also consider Ni-based alloys with higher SFE, in order to reveal the role of SFE on how deformation mechanisms respond to irradiation-induced defects. We will also analyze and interpret results from our recently conducted ion irradiations, nanoindentation, and post-indent TEM characterization of a model Ni alloy, consistent with those done for Fe-xMn specimens, specifically:

1. *Defect-dominated microstructure:* 2 MeV protons, 500°C, fluence 1 dpa
2. *Bubble-dominated microstructure:* 1 MeV He^+ ions, 500°C, fluence ~10^{16} ions/cm^2

References

1. A.H. Cottrell, B.A. Bilby, *LX. A mechanism for the growth of deformation twins in crystals*, Philosophical Magazine **42**, 573-581 (1951).
2. N. Hashimoto, S.J. Zinkle, A.F. Rowcliffe, J.P. Robertson, and S. Jitsukawa, *Deformation mechanisms in 316 stainless steel irradiated at 60°C and 330°C*, Journal of Nuclear Materials **283-287**, 528-534 (2000).
3. M. Chmielus, X.X. Zhang, C. Witherspoon, D.C. Dunand, and P. Müllner, *Giant magnetic-field-induced strains in polycrystalline Ni-Mn-Ga foams*, Nature Materials **8**, 863-866 (2009).
4. W.Z. Han, J. Zhang, M.S. Ding, L. Lv, W.H. Wang, G.H. Wu, Z.W. Shan, and J. Li, *Helium nanobubbles enhance superelasticity and retard shear localization in small-volume shape memory alloy*, Nano Letters **17**, 3725-3730 (2017).
5. G. Bonny, N. Castin, and D. Terentyev, *Interatomic potential for studying ageing under irradiation in stainless steels: the FeNiCr model alloy*, Modeling and Simulation in Materials Science & Engineering **21**, 085004 (2013).

Publications

1. P.H. Warren, C.D. Clement, Y. Sun, J. Ciston, C. Ophus, Y. Yang, and J.P. Wharry, *Ion implantation-induced plastic phenomena in metallic alloys*, JOM **76**, 2858-2869 (2024).
2. C.D. Clement, C. Yang, and J.P. Wharry, *Unexpected deformation-induced martensitic phase transformations in Ni-Cr alloys*, Materials Science & Engineering A **892**, 146029 (2024).
3. A. Hinojos, D. Hong, H. Sriram, L. Feng, C. Yang, J.P. Wharry, X. Gao, K. Hattar, N. Li, J. Schaffer, Y. Wang, M.J. Mills, and P.M. Anderson, *Taming the pseudoelastic response of Nitinol using ion implantation*, Scripta Materialia **226**, 115261 (2023).
4. C. Yang and J.P. Wharry, *Role of point defects on stress-induced martensitic transformation in NiTi shape memory alloy: a molecular dynamics study*, Physical Review B **105**, 144108 (2022).
5. A. Hinojos, D. Hong, L. Feng, C. Yang, J.P. Wharry, X. Gao, N. Li, J. Schaffer, K. Hattar, M.J. Mills, and P.M. Anderson, *Modulating the pseudoelastic response of Nitinol using ion implantation*, Advanced Materials & Processes **180**, 49-53 (2022).
6. C. Yang, Y. Pachaury, A. El-Azab, and J.P. Wharry, *Molecular dynamics simulation of vacancy and void effects on strain-induced martensitic transformation in an Fe-50at%Ni concentrated solid solution alloy*, Scripta Materialia **209**, 114394 (2022).

Understanding Elevated-Temperature Plasticity in Refractory Complex Concentrated Alloys

Mingwei Zhang, Department of Materials Science and Engineering, University of California, Davis

Keywords: refractory complex concentrated alloys, high entropy alloys, deformation mechanisms, strength, creep

Research Scope

The overarching goal of this research is to fundamentally understand the novel deformation mechanisms that control the high temperature-yield strength of refractory complex concentrated alloys (RCCAs). The most important objective of the research is to experimentally address the hypothesis that **the high-temperature yield strength in RCCAs are controlled by a competition among screw dislocation motion, edge dislocation motion, and the diffusion of the primary constituent atoms** in a quantitative manner. The research will combine experimental work in advanced processing, high-temperature testing, and advanced characterization to provide a critical scientific foundation for the development of next generation RCCAs.

More specific project objectives are:

1. Probing the rate-controlling barriers for screw or edge dislocation motion at macroscopic yielding in RCCAs as a function of alloy composition, temperature, and strain rate to determine the key deformation mechanism in different RCCAs.

2. Elucidating the equilibrium vacancy concentration in RCCAs by *in-situ* neutron diffraction and scanning transmission electron microscopy to rationalize the observed temperature dependence of yield strength.

The proposed project aims to study high-temperature plasticity in bulk annealed, homogenized, coarse-grained, and nominally single-phase BCC RCCAs. Interface-dominated effects such as dynamic recrystallization, grain boundary sliding, and grain boundary embrittlement, albeit important, are beyond the scope of the current project. The materials considered in this study will be nominally homogeneous and fully recrystallized single-phase specimens with room temperature tensile ductility, where the tests will be performed below their dynamic recrystallization temperatures under vacuum. This limits the material system selected in this study to be NbTaTi-based RCCAs. We note that although ductility will be explored in this study via the tensile tests and creep tests proposed below, a detailed study of mechanisms that control tensile or creep ductility, damage tolerance, and fracture in RCCAs is beyond the scope of the current project.

Recent Progress

The decrease of yield strength in RCCAs shows a plateau at intermediate temperatures, which is extremely favorable for high temperature applications because of the retention of strength. To date, the origin of this plateau remains elusive. Recently, it is shown that drastically different yield strength plateau behaviors exist among several NbTaTi-based RCCAs. **Fig. 1** shows a compilation of available data [1-3] for their temperature dependent yield strengths. It is evident that NbTaTiV shows a clear plateau starting from approximately 0.35 T_m whereas high temperature data that indicate the end of the plateau is unavailable. This contrasts with NbTaTiHf-based RCCAs that show steeper plateaus at a lower temperature range (between 0.15-0.4 T_m). It has been shown by recent neutron scattering and STEM characterization [1] that plastic deformation in NbTaTiV is controlled predominantly by edge dislocation motion from RT to 1173 K (0.55 T_m) (**Fig. 2**), and the percentage of edge dislocations detected increases with increasing temperature. On the contrary, our preliminary STEM work has shown that deformation in a $Nb_{45}Ta_{25}Ti_{15}Hf_{15}$ alloy is controlled by screw dislocation motion at 1173 K, or 0.46 T_m.

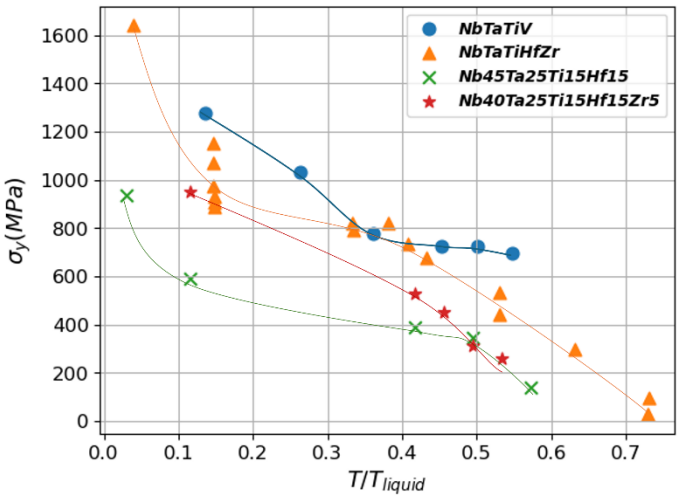

Fig. 1 Temperature dependent yield strengths of NbTaTiV, $Nb_{45}Ta_{25}Ti_{15}Hf_{15}$, $Nb_{40}Ta_{25}Ti_{15}Hf_{15}Zr_5$, and NbTaTiHfZr. Data adapted from Refs. [1-3].

It is therefore hypothesized that the distinct plateau behavior exhibited in the NbTaTiV RCCA is governed by glide of edge dislocations, and switching from a NbTaTiHf-based RCCA to NbTaTiV can facilitate a transition from screw to edge dislocation control. Vanadium is a potent alloying element for BCC alloys because of the large misfit volume caused by its small atomic radius compared to other refractory BCC elements. We thereby further hypothesize that the large atomic misfit or local lattice distortion caused by vanadium can drastically reduce the

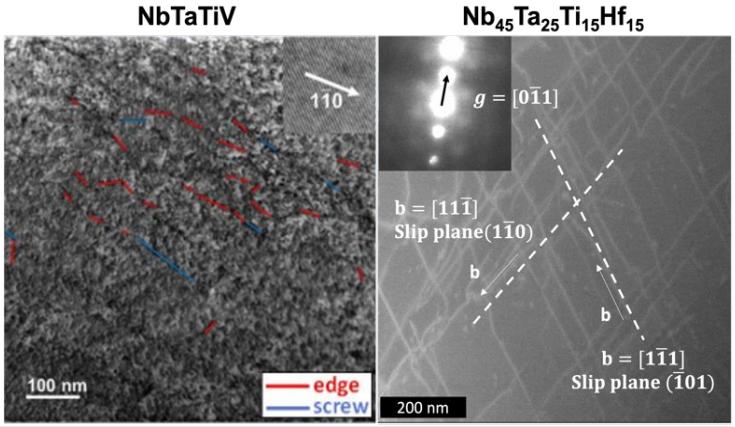

Fig. 2 STEM micrographs of deformation microstructure in NbTaTiV and $Nb_{45}Ta_{25}Ti_{15}Hf_{15}$ at 1173 K. The deformation in NbTaTiV is controlled predominantly by edge dislocations, whereas $Nb_{45}Ta_{25}Ti_{15}Hf_{15}$ features the motion of long, straight screw dislocations. The figure for NbTaTiV is adapted from Ref. [1].

mobility of edge dislocations in RCCAs, since edge dislocations can react strongly with the hydrostatic pressure field from local lattice distortion whereas screw dislocations are unaffected.

Edge dislocation glide control cannot fully explain the plateau behavior since it is thermally activated and still temperature dependent. Several alternative mechanisms have been considered to rationalize the plateau behavior. First, dynamic strain aging (DSA) through cross-core diffusion has been proposed by Maresca and Curtin [4], where tensile and compressive strain fields of the edge dislocation provide driving force for primary constituent atoms near the edge dislocation core with different atomic radii to diffuse across the core. Alternatively, He et al. [5] proposed the formation of superjogs on edge dislocations by vacancy nucleation. It is computed that the above two mechanisms are trivial unless the actual equilibrium vacancy concentration in the RCCA is several orders of magnitude higher than the equilibrium vacancy concentration calculated by using an average vacancy formation energy for different constituents. This research will directly probe the equilibrium vacancy concentration by diffraction-based techniques to elucidate the origin of the yield strength plateau.

Future Plans

We will evaluate multiple NbTaTi-based RCCA specimens alloyed with a gradient of V to achieve varying screw versus edge mobility as a function of vanadium concentration. The alloys will be arc melted, cold rolled, and for full homogenization and recrystallization. Tensile tests will be carried out at RT (~0.14 T_m) and 0.2-0.6 T_m (~ 400-1273 K) on an Instron 1331 hydraulic testing machine with a custom-built vacuum furnace that has the capability of high temperature testing up to 1873 K in vacuum. The tests will be interrupted at ~0.5% strain to preserve the near-yield microstructure and at a large strain of 10% for TEM examination. Diffraction contrast imaging scanning transmission electron microscopy (DCI-STEM) will be performed under different two-beam conditions and zone axes to examine the percentage of edge and mixed character dislocations compared to screw dislocations. Additional *in-situ* neutron scattering experiments will be conducted to provide a more representative analysis throughout a larger sample volume. Samples will be brought to the VULCAN neutron diffractometer at the Spallation Neutron Source (SNS) at Oak Ridge National Laboratory (ORNL) with the capability of performing neutron scattering during loading from RT up to 1273 K. Neutron scattering data will also be used to determine the average dislocation characters and the lattice distortion parameter in different alloys. The proposed research above will provide comprehensive experimental evidence to illustrate the transition from screw to edge dislocation control as a function of alloy composition (V content), lattice distortion, and temperature in relation to the yield strength plateau in RCCAs.

The research will also experimentally determine the equilibrium vacancy concentration in NbTaTiV by the Simmons and Balluffi experiment ($\Delta L/L-\Delta a/a$) via *in-situ* heating and neutron scattering on the VULCAN diffractometer at ORNL. The equilibrium vacancy concentration will be determined by the difference between the displacement of the material during heating and the expansion of the material's lattice constant. The displacement during heating will be measured by

an extensometer on the sample, and the lattice expansion will be calculated from neutron scattering data. This experiment will be repeated on several alloys with different V content to understand if there is an effect of increasing lattice distortion on the equilibrium vacancy concentration of the RCCA. It is also of great interest to understand whether vacancies can be localized to dislocations to facilitate core-core diffusion or superjog formation. The recent progress of 4D-STEM has enabled the Simmons and Balluffi experiment to be performed on TEMs with nanometer-level spatial resolution. *In-situ* heating specimens for the same materials will be prepared by focused ion beam (FIB) and transferred to a Protochip heating holder at NCEM, LBNL. 4D-STEM will be performed. We identify the potential limitation that the measurement of the absolute vacancy concentration can be complicated by thin sample, FIB damage during sample preparation, and electron beam damage related artifacts. Therefore, 4D-STEM scans will be performed in a high dislocation density region and a dislocation-free region immediately nearby, where the correlation between the relative vacancy concentration and dislocation density can be directly examined.

References

1. Lee, C., et al., Strength can be controlled by edge dislocations in refractory high-entropy alloys. Nature Communications, 2021. 12(1): p. 5474.
2. Mills, L.H., et al., Temperature-dependent tensile behavior of the HfNbTaTiZr multi-principal element alloy. Acta Materialia, 2023. 245: p. 118618.
3. Zhang, C., et al., Strong and ductile refractory high-entropy alloys with super formability. Acta Materialia, 2023. 245: p. 118602.
4. Maresca, F. and W.A. Curtin, Mechanistic origin of high strength in refractory BCC high entropy alloys up to 1900K. Acta Materialia, 2020. 182: p. 235-249.
5. He, S., et al., Thermal super-jogs control the high-temperature strength plateau in Nb-Mo-Ta-W alloys. Acta Materialia, 2023. 244: p. 118539.

Publications

This is a new project.

Author Index